SAPIENZA
UNIVERSITÀ DI ROMA

Diffuse interface modelling of micro/nano cavitation bubbles and their interactions with elastoplastic walls

Mechanical and Aerospace Engineering Department

PhD Program in Theoretical and Applied Mechanics – Cycle XXXIII

Candidate

Dario Abbondanza
ID number 1560753

Thesis Advisors

Prof. Carlo Massimo Casciola
Dr. Francesco Magaletti
Dr. Mirko Gallo

2021

Thesis defended on 21 May 2021
in front of a Board of Examiners composed by:

Prof. Sergio Chibbaro
Prof. Nicola Pio Belfiore
Prof. Giorgio Figliolini

Diffuse interface modelling of micro/nano cavitation bubbles and their interactions with elastoplastic walls
Ph.D. thesis. Sapienza – University of Rome

This thesis has been typeset by LaTeX and the Sapthesis class.

Author's email: dario.abbondanza@uniroma1.it

Abstract

The cavitation phenomenon, namely the appearance and collapse of vapour/gas bubbles surrounded by their liquid, has been of great interest in the past decades.

The reason behind this interest is related to the large variety of possible applications in which the dynamics of small bubbles is involved and play a relevant role in the generation of significant macroscopic effects. Examples of these applications can be found in many different disciplines, such as biomedicine, industrial engineering and industrial cleaning processes. Most of the applications aim to control the cavitation phenomenon in order to take advantage of its power and, at the same time, limit its destructiveness.

In this thesis, in which a Diffuse Interface model is used to physically describe and capture the dynamic behavior of bubbles, I analyse the results of many numerical simulations designed to gain insights and knowledge in both the nature of the cavitation phenomenon itself, and the effects resulting from a number of possible circumstances and applications. The core of the thesis can be summarized in two main topics: bubble growth due to laser (energy) deposition, and bubble collapse near solid boundaries and the effects generated on them.

In the former part, the Diffuse Interface model capabilities of describing a thermodynamically consistent evolution of a two-phase flow are exploited, to simulate the nucleation, growth and subsequent rebounds dynamic occurring when a bubble is generated through laser deposition. The results suggest that the model is able to capture the phase change and the breakdown wave emission occurring when the vapour bubble is forming. The latter is focused on a typical effect observed on mechanical objects interacting with liquid flows in which cavitation occurs. Bubble collapse is a highly energetic process, which is capable of damaging nearby objects. In this thesis, the aim is to numerically reproduce the first stages of this phenomenon, by coupling a Diffuse Interface model for the description of the fluid dynamics with an elastoplastic model for the description of the solid mechanics. The presence of a solid boundary near a collapsing bubble influences the dynamics of the fluid and allows for greater energy transmission from the fluid to the wall, resulting in larger deformations and deeper plastic indentation.

Contents

Chapter 1

Introduction

With the term cavitation one usually refers to the phenomenon of appearance and collapse of vapour/gas bubbles within a liquid phase, mainly driven by the thermodynamic state, and in particular by the pressure of the fluid. Cavitation is traditionally and infamously associated with damage and erosion of mechanical objects such as ship propellers and hydraulic turbomachinery. Still, cavitation effects cannot be circumscribed to damage and erosion only. But there is much more, and many applications from extremely different disciplines aim to understand cavitation, to control and mitigate his destructiveness, but also to reproduce it and take advantage of its power. The aim of the present thesis is to gain a better knowledge and understanding of cavitation phenomena and bubbles dynamics by adopting a multidisciplinary approach, coupling fluid dynamics simulation of collapsing bubbles with solid mechanics simulations of elastic and elastoplastic materials reacting to the impacts exerted by these bubbles as a consequence of their powerful dynamics.

In recent years, the study of cavitation has become one of the most interesting and challenging in the field of theoretical, experimental and computational fluid dynamics. Large numbers of different models have been developed, to capture different aspects of cavitation phenomena, and have been implemented in numerical codes. At the same time, experiments have shown how wide the range of possible cavitation applications is, and have gained more and more insights on the physical behavior of bubbles, in a large variety of conditions.

The most classical cavitation application, as mentioned above, is well known to the marine, aerospace and mechanical engineering community, and is related to the study of cavitation damage to mechanical components of ships, engines and turbomachineries. This damage, which in actual operative conditions consists of many different types of damage (corrosion, erosion, pitting, plastic deformations, wear), is usually characterized by the presence of pits in the material, as it is clearly visible from Figure 1.1 (a), where the implosion of clusters of bubbles near the shape of the propeller of a watercraft has caused loss of material. An example of the destructive power of cavitation is visible in Figure 1.1 (b), where the blades of the rotor of a Francis turbine are highly damaged, result-

ing in the complete loss of functionality of the turbine. During the operation of these mechanical components surrounded by liquid, many vapour/gas bubbles are formed, due to the pressure conditions in the fluid around the objects, and when those bubbles collapse near a solid boundary, they are able to permanently damage it, by mechanisms that will be explained through the thesis. Other more

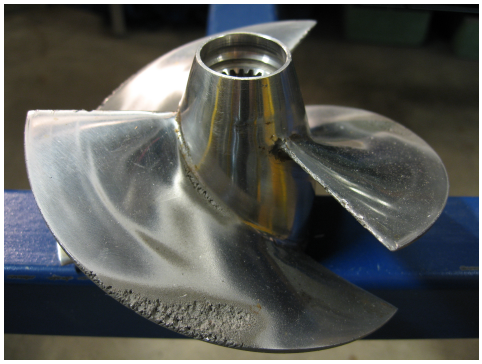

(a) Propeller of a watercraft.

(b) Rotor of a Francis turbine.

Figure 1.1. Cavitation damage in mechanical components. Source of the images: `https://en.wikipedia.org/wiki/Cavitation`.

recent applications of cavitation have been studied in many diverse fields, such as biomedicine (Christopher Earls Brennen 2015). One of the most innovative and promising application in the field consists in efficiently use cavitation effects to enhance drug delivery (Peruzzi et al. 2018; T. Sun et al. 2015), in particular for those cases where drug delivery is inhibited by the poor permeability and high selectivity of endothelial cells, such as in the case of the blood-brain barrier (BBB). Microbubbles can be injected into the bloodstream, and their dynamics can be controlled with localized ultrasound, with the possibility to increase the permeability of the endothelial barrier and enhance the delivery of drugs. In this context, the two types of dynamical behavior exploited are referred to as *stable* and *inertial* cavitation, respectively obtained with a lower and a higher excitation of the bubbles through ultrasounds. Stable cavitation is essentially the oscillating behavior of bubbles around their equilibrium condition, while inertial cavitation implies bubble collapse, with subsequent shock wave emission and microjets of liquid impacting the endothelial cells (these mechanisms will be clarified and described through the thesis). Advances on this technology and on the physics involved may help in the treatment of cancers or degenerative disorders. Cavitation can also be used for the sonoporation of single living cell membranes (Le Gac et al. 2007; Li et al. 2011), an acoustic technique constituting an alternative to electroporation, which is a frequently used method in enzymology, stem cell research, pharmaceutics and food industry to introduce foreign substances in a cell (e.g. DNA fragments); or for fragmentation of kidney stones in shock wave lithotripsy (SWL) (Zhu et al. 2002), where cavitation was found to be necessary to produce fine passable fragments, to succeed in the clinical treatment and disintegration of

renal calculi. Other worth mentioning applications, from completely different contexts, relate to the treatment of water pollution (Adewuyi 2005), where cavitation is used to destroy or accelerate the destruction of liquid-phase contaminants; and to enhanced mixing in biochemistry applications (R. H. Liu et al. 2003), thanks to the microstream induced in their surroundings, by cavitation bubbles vibrating in their stable regime.

Most of the actual applications of cavitation have a common need, that of studying and understanding the dynamical behavior of bubbles and the interaction between these bubbles and their surroundings, therefore the author of this thesis concentrated his attention and efforts on the classical problem of cavitation in mechanical engineering presented above, that of the interaction between a cavitating bubble and a solid surface placed nearby. Although this project is focused on a very specific application, which has not been fully characterized and clarified yet, gaining insights and knowledge regarding this classical problem may lead to important advances in all the above mentioned fields. In particular, the application the author has in mind is that of a single cavitating bubble expanding and imploding near a solid boundary, representing the solid surface. To properly introduce the mathematical models used and the approach adopted, few physical insights on cavitation and its interaction with nearby solids will be given in the following.

When the pressure in a liquid (for instance water) drops below a certain threshold, which is called the *vapour saturation pressure*, a vapour nucleus may form and, if its energetic content is large enough, it grows until this new phase is stable within the surrounding liquid. When this happens, a macroscopic vapour bubble is created and visible, we say that nucleation occurred. With reference to Figure 1.2, where the pressure of the fluid is represented as a function of the thermodynamic state, identified by density and temperature, it is possible to identify those zones relevant for the description of a two-phase system such the one we are interested in. The region on the right, in white, represents the stable liquid region (where liquid is the stable phase), which is confined by the critical isothermal curve denoted by $\hat{T} = 1$ and the binodal curve $\mathcal{C}$, defining the two-phase region (the wider dome). If, following an isothermal curve, for instance the one at $\hat{T} = 0.85$, the pressure drops below the saturation pressure at that temperature, identified by the corresponding dashed line spanning the two-phase region, the fluid enters the metastable liquid region, that represents a necessary condition for the formation of a vapour nucleus (nucleation). The vapour thus formed is in the stable or metastable vapour region, below the critical isothermal curve, in the white or light grey zone on the left. If vapour or liquid phase is heated up above the critical isothermal line $\hat{T} = 1$, then gas is formed (G region in the figure). The two internal curves denoted by S, delimiting the metastable regions and the *coexistence* region (dark grey) are called the *spinodal* curves, and are the loci of relative maxima and minima of the pressure.

This phenomenon of nucleation is a stochastic process occurring when the

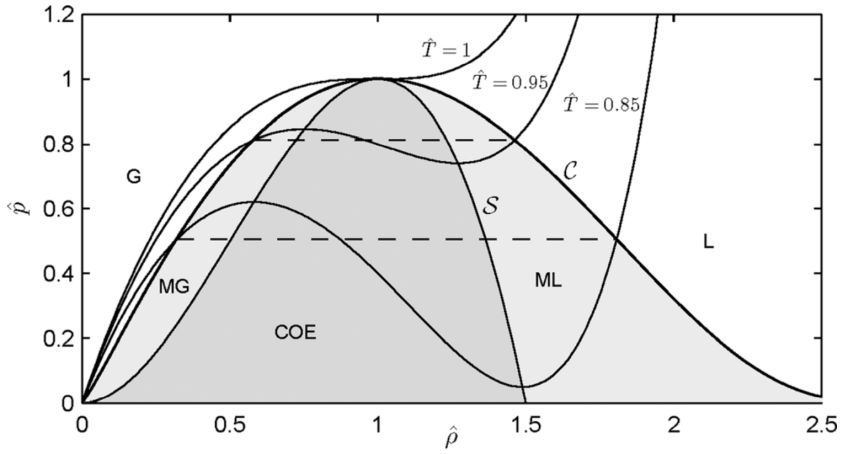

Figure 1.2. van der Waals equation of state (EOS), from (Zhao et al. 2011)

liquid is in metastable conditions, and a certain energy barrier is overcome, leading to the formation of a vapour nucleus. The Classical Nucleation Theory (CNT) provides a way, based on macroscopic considerations, to compute the value of the energy required to activate this stochastic process and to obtain an estimate of the nucleation rates in homogeneous conditions (Blander and Katz 1975), which can be generalized to heterogeneous conditions, i.e. to situations where the nucleus formation happens near a solid boundary (Ward et al. 1983). The energy required for the formation of those nuclei is split into two contributions, one connected to the formation of the liquid-vapour interface, which is represented by the product between the surface tension and the interface area, the other related to the formation of the new vapour phase within the liquid, which is proportional to the volume of the bubble to be formed.

In the cases of our interest, once the bubble nucleation has occurred and the bubbles reach a stable radius, they are transported by the fluid. If the bubbles reach zones in the liquid where the pressure is higher than the saturation pressure at that temperature, the collapse of the bubbles is triggered, and if the pressures involved during this process are sufficiently large, the bubble implodes, emitting a shock wave which travels through the liquid and could hit near objects, potentially damaging them. This is the complete process that, once repeated over time, leads to those damages visible in Figure 1.1, which are the result of millions of cycles of cavitating bubbles implosion (Christopher E Brennen 2014; Pereira et al. 1998).

From an experimental standpoint, the bubble dynamics and their interaction with solid boundaries has been studied extensively. In particular, the results to which we will be focusing our attention in the thesis are those obtained for the dynamics of expansion and collapse of single bubbles of vapour/gas (Dular, Požar, et al. 2019; Philipp and Lauterborn 1998; Tomita and Shima 1986; Vogel et al. 1999). To make the experiments reproducible, the bubbles are usually spark or laser generated into a closed box filled with liquid water. This gives the possibility to generate the bubbles always in the same spot, and to follow their dynamical be-

havior with high frame rate cameras. The experiments showed how complicated and fascinating cavitation is, implying a large number of different interacting phenomena, such as plasma formation and sonoluminescence when the bubble is generated; phase changes and transitions to and from supercritical states during the bubbles dynamics; shock wave emission and propagation, large bubble deformation and topological changes and extremely high peaks in the liquid in terms of temperatures (thousands ok K) and pressures (dozens of GPa) during the collapse stage. This is completed, in our main focus and application, by the interaction with solid boundaries, which is an extremely complicated phenomenon by itself, and is challenging by both theoretical and numerical viewpoints. In some of the researches mentioned, in particular (Dular, Požar, et al. 2019; Philipp and Lauterborn 1998), it is evident how the first stages of cavitation damage due to the action of a single collapsing bubble are not characterized by loss of material, hence it cannot be strictly classified as *damage*. It is rather a plastic deformation, which is a particular form of permanent deformation often occurring in metals, when some relevant quantities are exceeded (an extensive description on the phe-

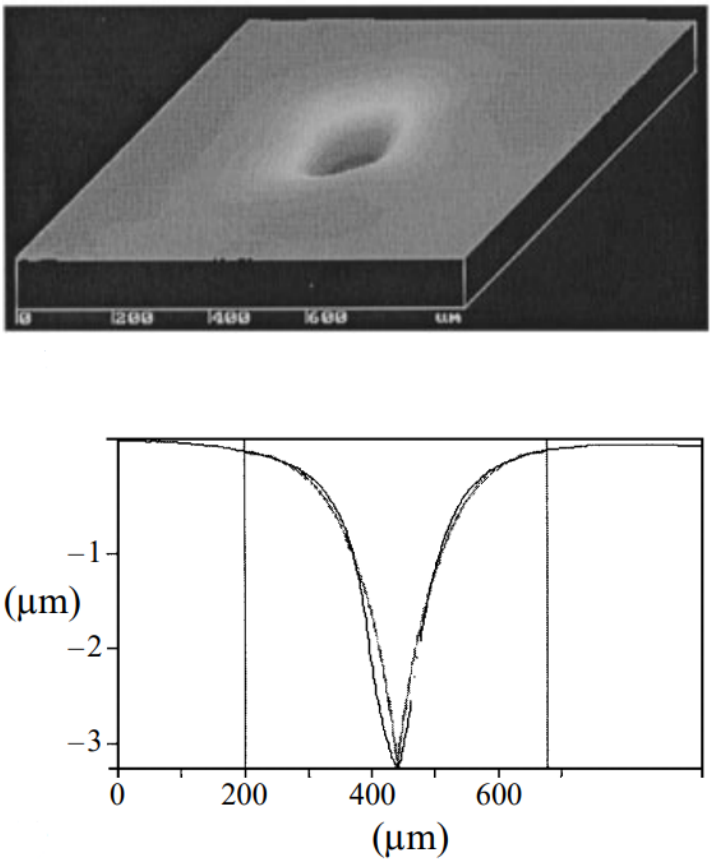

Figure 1.3. Plastic permanent deformation on an Aluminium specimen due to the collapse of a single cavitation bubble. Three dimensional view and two-dimensional surface profiles. Image from (Philipp and Lauterborn 1998).

nomenology of plasticity and its mathematical modelling takes a large part of this thesis). An example of plastic indentation resulting from the collapse of a single bubble on an Aluminium specimen is displayed in Figure 1.3.

The system that will be studied theoretically and numerically in this thesis is exactly the one analyzed in the experiments carried out in the above mentioned works. The dynamics of a single cavitation bubble is inspected, and the interaction taking place during the collapse stage between the fluid and a solid boundary is considered. At the current state of the implementation, only one-way coupling between fluid and solid has been achieved, where the fluid dynamics acts as an external force on the solid. Further developments are considering to complete this study by adopting a two-way coupling between fluid and solid, where the response of the solid has an influence on the subsequent dynamic of the fluid, as it happens in real applications. The model adopted for the description of the fluid is the *diffuse interface model* described below (Didier Jamet 2001; Magaletti, Gallo, et al. 2016; Magaletti, Marino, et al. 2015), which is a continuum model well suited for the description of mesoscale systems. The model chosen by the author to describe the solid mechanical and dynamical response to the fluid dynamics lives in the context of the *classical rate-independent plasticity theory*. It has been adopted as a starting point for such a study, given its ability to describe and reproduce the evolution of macroscopic quantities relevant in the physics of elastoplastic materials, and the fact that it is the most known and accepted theory in the field.

Structure of the thesis

Chapter 1 was the introduction of the thesis.

Chapter 2 is where the fluid dynamic model for the description of a two-phase fluid is introduced. The diffuse interface model is a continuum model suitable for the description of mesoscale systems, and has been recently shown to successfully describe bubble nucleation and dynamics (Gallo, Magaletti, and Casciola 2018; Gallo, Magaletti, Cocco, et al. 2020; Magaletti, Gallo, et al. 2016). In the same chapter, the equation of state adopted for the description of liquid-vapour systems is described, and an equation for the evolution of vorticity is derived, which will be useful in later analysis.

Chapter 3 is introduced by a brief discussion on linear elasticity, and then is entirely devoted to the introduction, description and full characterization of classical plasticity models. Chapter 3 takes a large part of the thesis since it required a lot of work by the author to be able to successfully synthesize all the relevant features of the theory, and to present them in a way it is possible for readers unfamiliar with those concepts to approach them more easily and directly. For this reason, all the assumptions made are justified and deeply explained, in a form that tries to be as self-contained as possible. Thermodynamics principles are recalled and the classical theory of plasticity, with all its components, is build upon them. Then,

the theory is particularized to the von Mises plasticity theory, that is the one used in the thesis and numerical investigations.

Chapter 4 is where the numerical formulations adopted for the implementation of mathematical models are described and analyzed. Particular emphasis is given, again, to the plasticity integration algorithm, which consists in the *return mapping algorithm*, a predictor-corrector scheme to solve the constrained problem of elasto-plasticity. The codes have been developed using two well known libraries, the first one being a linear algebra library for the solution of partial differential equations, PETSc; the second one being a general purpose finite element library with many relevant features explained through the thesis, deal.II.

Chapter 5 consist in the results obtained from numerical simulations regarding the cavitation bubble expansion and rebounds dynamics. The objectives of the study are extensively explained in the chapter itself.

Chapter 6 is where the main results of this thesis are. The problem of bubble collapse and interaction with a solid boundary is introduced in details, and the numerical strategy adopted is clarified.

Chapter 7 presents the conclusions of the work and some future developments, some of which are already under construction.

Results and new contributions

This thesis aims at opening and defining a new line of research related to the theoretical study and numerical implementation of the problem of interaction between a collapsing bubble and an elastic-plastic wall. Even though it is possible to find in the literature works where this interaction problem is considered (see for instance (Cao et al. n.d.; Chahine and Hsiao 2015; Joshi 2018; Lechner, Koch, et al. 2017; Lechner, Werner Lauterborn, et al. 2020; Shan et al. 2016)) none of these studies have been carried out by using the models adopted in this thesis, which have been shown to be the natural framework where to study the cavitation problem when dealing with small bubbles (nanometric up to micrometric) ((Magaletti, Gallo, et al. 2016; Magaletti, Marino, et al. 2015)).

The recognition that thermodynamically consistent models, such as the Diffuse Interface model and the plasticity model adopted in this thesis, have an important role in the dynamics of the interaction problem - composed by bubble dynamics, phase changes, transition to supercritical states, shock-wave emission and propagation and solid dynamics - is a key contribution of this thesis

The results described in Chapter 5 and 6 were possible thanks to the use of the open source finite element library deal.II (Arndt et al. 2020), but to the best of the author's knowledge, no open source codes were available to solve the problem tackled in this thesis. The development of high performance parallel codes

based on both deal.II and PETSc libraries, to solve the one-way coupled interaction problem between a fluid described by the Diffuse Interface model and a solid wall described by the non-stationary elasto-plasticity equations is the main new contribution of this thesis, together with the recognition that automatic grid refinement could be efficiently used to simulate up to micrometric bubbles while still adopting a phase-field model such as the Diffuse Interface one.

A new contribution of this thesis is also the energetic analysis described in Chapter 5 and applied to the breakdown stage of cavitation bubbles. The analysis carried out were made possible thanks to the model adopted, which is consistent with the law of thermodynamics and allows the identification of the different energies involved in the bubble dynamics. No similar studies are currently present in the literature.

The development of the codes has been done for most of the part by the author of the thesis, and also the choice of the mathematical and physical models to adopt was mainly a decision of the author (particularly for what concerns the solid dynamic model).

All the characteristics mentioned above contributed to results that were not available before in the scientific literature, and could potentially constitute a starting point for novel analysis on the topic and for new lines of research.

Publications

Submitted papers:

- **Vapor Nucleation in Metastable Liquids - The Continuum Description**
  M. Gallo, F. Magaletti, D. Abbondanza, C. M. Casciola

  Abstract Liquid-vapor phase change is of importance across a wide spectrum of fundamental and applied disciplines. The phenomenology of vapor formation is very complex due to the large range of spatio-temporal scales involved. Here the microscopic features of vapor embryos nucleation coexist with the macroscopic bubble dynamics. This multiscale nature of the phenomenon makes nucleation challenging both from a theoretical and experimental point of view. In this work we aim to retrace the state of art of continuum description of liquid-vapor phase change, starting from the Classical Nucleation Theory which provides a basic description of the phenomenon up to the phase field-description and fluctuating hydrodynamics theory.

In preparation papers:

- **Numerical investigation of cavitation-induced plastic deformation: Coupling the diffuse interface model with plasticity**
  D. Abbondanza, M. Gallo, F. Magaletti, C. M. Casciola

Abstract The cavitation phenomenon, namely the appearance and collapse of vapor/gas bubbles surrounded by their liquid, has been of great interest in the past decades. The reason behind this interest is related to the large variety of possible applications in which the dynamics of small bubbles is involved and play a relevant role in the generation of significant macroscopic effects. In particular, many efforts have been put in the observation of bubbles dynamics and the effects of collapsing bubbles near solid surfaces. On the other hand, recent studies have shown the ability of the Diffuse Interface model to numerically reproduce the dynamics of a collapsing vapor bubble surrounded by its liquid, both in presence and absence of solid boundaries. In our study, we present the numerical investigation of a one-way coupled fluid-structure interaction between a collapsing bubble, described by a Diffuse Interface model, and a solid wall, with a non-stationary elasto-plastic behavior. Our aim is to capture the effects of a single bubble collapse on a near wall, and quantify the plastic deformation and indentation in the first stages of cavitation. Automatic grid refinement is used in the fluid solver to simulate micrometric bubbles without artificially thickening the interface, reaching dimensions never observed before with a Diffuse Interface model.

Chapter 2

Fluid Dynamics Modelling of Cavitation

2.1 Introduction

The study of cavitation phenomena and cavitating bubbles dynamics has been of great interest, and is continuously growing, in the past few decades, due to the important physical, biomedical and engineering applications outlined in the introduction of this thesis, as well as for its intrinsic fascinating physics and its challenging theoretical modelling. Our interest here is mainly focused on the physical description and numerical simulation of single or few interacting bubbles dynamics. In this context, the most used model, which is one of the first to ever be adopted, and is still in use today for benchmark and testing, as well as for research, is the Rayleigh-Plesset model (Plesset 1949), which prescribes a law for the evolution in time of the radius of an empty cavity immersed in an incompressible fluid. When considering viscous effects and capillary forces, the equation reads

$$\frac{P_B(t) - P_\infty(t)}{\rho_L} = R\ddot{R} + \frac{3}{2}\dot{R}^2 + \frac{4\nu_L}{R}\dot{R} + \frac{2\sigma}{\rho_L R}, \tag{2.1}$$

where $P_B(t)$ is the bubble pressure, ν_L is the kinematic viscosity of the surrounding liquid and σ is the surface tension. Equation (2.1) can be easily recovered by taking the one-dimensional spherical incompressible Navier-Stokes equations, and expressing the mechanical balance at the bubble interface considering the capillary effects giving rise to the surface tension term. Many authors have studied modifications to the Rayleigh-Plesset equations to account for gas presence in the bubble, or compressible fluids, and have studied analytical and numerical solutions to those equations (Kudryashov and Sinelshchikov 2014; Van Gorder 2016). Important results can be obtained on the acoustics of the system composed by an oscillating empty or gas filled bubble, in a confined rigid or elastic medium, with Rayleigh-Plesset-like approach (Doinikov et al. 2018; Drysdale et al. 2017).

Recent advances have been made in the study of single and multiple bubbles dynamics and collapse, with many differences in the models adopted and

in the numerical techniques. Worth mentioning are the results obtained with Lattice Boltzmann methods (LBM) and modified LBM, as in (Peng et al. 2019, 2020; Shan et al. 2016; Sukop and Or 2005). Among the continuum models used, one the most adopted is the *single fluid* equation, where the density field is assumed to be a superposition of the gas and liquid density, and equations of state for the gas and liquid pressures are required (Lechner, Koch, et al. 2017; Lechner, Werner Lauterborn, et al. 2020). This model though, which is implemented in the open source library OpenFoam and is widely spread and used, lacks a consistent thermodynamic framework. As a result, no mass transfer between the two phases is allowed, and no phase change can occur. In principle, this is a severe limitation for the model, which may not be reliable in conditions where the thermodynamics of the system plays a relevant role, affecting the dynamical behavior of the bubbles, as it is the case during cavitation.

The model adopted in this thesis is a continuum phase-field model, thermodynamically consistent, that has been recently validated by various studies in the description and simulations of bubbles dynamics at the mesoscale (nm to μm) (Gallo, Magaletti, Cocco, et al. 2020; Jamet et al. 2001; Didier Jamet 2001; Magaletti, Gallo, et al. 2016; Magaletti, Marino, et al. 2015). The model is usually referred to as the *Diffuse Interface* model, which leads to the *Navier-Stokes-Korteweg* equations for a fluid with capillarity, and it is included in the much broader class of phase-field models.

2.2 Diffuse interface model

The diffuse interface model originates by an idea of the physicist Johannes Diderik van der Waals (Waals 1979), who identified the need of non-local terms in the definition of the Helmholtz free energy functional, to describe inhomogeneous systems in which two different phases are separated by a finite interface with non-zero thickness, as it is the case for bubbles. Such a non-local term should be added to the classical local free energy density functional, to account for a thermodynamic consistent description of a fluid with non-negligible capillary effects.

Van der Waals theory can now be justified in the context of a modern physical theory that goes by the name of *Density Functional Theory* (Lutsko 2011). According to this theory, the general form of the Helmholtz free energy functional F, as a function of temperature θ and a generic phase indicator Φ takes the form

$$F\left[\Phi,\theta\right] = \int_V \left[f_b(\Phi,\theta) + f_s(\nabla\Phi, \nabla\Phi \otimes \cdots \otimes \nabla\Phi)\right] \mathrm{d}V, \tag{2.2}$$

where f_b is the classical bulk free energy, corresponding to the free energy contribution of the bulk homogeneous phases, and f_s is the gradient contribution to the total free energy functional, which depends on the spatial gradients of the phase indicator field Φ. In equation (2.2), the boundary contribution term has been disregarded, since it is not used nor required throughout the thesis.

Finding the extremal points of this functional corresponds to finding the equilibrium condition. At fixed temperature $\theta = \theta_0$, the first variation of the functional (2.2), with respect to the field Φ is

$$\frac{\delta F}{\delta \Phi} = \frac{\partial f_b}{\partial \Phi} + \sum_{k=1}^{N} (-1)^k \nabla^{(k)} : \frac{\partial f_s}{\partial \left(\nabla^{(k)} \Phi\right)} = 0, \tag{2.3}$$

where the superscript $\cdot^{(k)}$ denotes rank k tensor operator defined as the n-fold tensor product of ∇ with itself.

Van der Waals assumption in (Waals 1979), in the present framework, consists in considering the density of the fluid as the phase indicator, $\Phi = \rho$. This leads to a set of equations which are capable of describing the equilibrium conditions for a fluid with two miscible phases, with their bulk, and a finite interface where all the relevant fields vary smoothly. The model is able to reproduce phase changes within the fluid, and the values of relevant physical quantities such as the surface tension, once a meaningful equation of state is specified (in our case it will be the van der Waals EoS). The definition of the total free energy functional can then be used in conjunction with the Navier-Stokes equation for a compressible fluid, to get thermodynamic consistent constitutive relations for the stress tensor, leading to the well known Navier-Stokes-Korteweg equations.

The first step is to rewrite eq. (2.2) for a fluid with $\Phi = \rho$, in the van der Waals assumption of second gradient free energy approximation, and obtain the Euler-Lagrange equation (2.3). For a closed system with mass M_0, the Helmholtz free energy functional with second gradient approximation reads,

$$F[\rho, \theta] = \int_V f(\rho, \theta) \, \mathrm{d}V = \int_V \left[f_b(\rho, \theta) + \frac{\lambda}{2} |\nabla \rho|^2 \right] \mathrm{d}V + \beta \left(M_0 - \int_V \rho \, \mathrm{d}V \right), \tag{2.4}$$

where β is a Lagrange multiplier associated with the constraint of fixed mass (we are looking at a closed system). The coefficient λ, the *capillary coefficient* is a function of the thermodynamic state (ρ, θ), and incorporates all the information and properties of the interfacial liquid-vapour system. Rewriting eq. (2.3) for a free energy functional of the form (2.4), we get the Euler-Lagrange equations, or equilibrium conditions

$$\begin{cases} \theta = \theta^{eq} = \text{const.}, \\ \mu_b - \nabla \cdot (\lambda \nabla \rho) = \beta = \mu^{eq}, \end{cases} \tag{2.5}$$

indicating that, at the equilibrium, the temperature is constant and the bulk chemical potential defined by

$$\mu_b = \frac{\partial f_b}{\partial \rho} \tag{2.6}$$

satisfies equation (2.5), corresponding to the definition of the generalized chemical potential μ_c, which is constant at the equilibrium, and takes into account capillary contributions. In the bulk regions, where the density gradient vanishes, far from the interface, we get the bulk equilibrium condition $\mu_b(\rho_v, \theta_0) = \mu^{eq} = \mu_b(\rho_l, \theta_0)$.

2.2.1 One dimensional solution and surface tension

For the illustration of the above mentioned equilibrium conditions, and the consequences of adopting the assumption of a free energy functional of the form (2.4), it is instructive to analyze a one-dimensional case, where a single planar interface divides two bulk phases, say liquid and vapour, and the variation of all the fields is smooth along the interface thickness. Assuming a constant value for the capillary coefficient λ, equation (2.5) transforms into

$$\mu_c = \mu_b(\rho) - \lambda \frac{\mathrm{d}^2\rho}{\mathrm{d}x^2} = \mu^{eq}. \tag{2.7}$$

A solution to equation (2.7) can be obtained by integrating the equation along the x direction, after having it multiplied by the density gradient $\frac{\partial \rho}{\partial x}$,

$$\left(\mu_b(\rho) - \mu^{eq}\right) \frac{\mathrm{d}\rho}{\mathrm{d}x} = \lambda \frac{\mathrm{d}^2\rho}{\mathrm{d}x^2} \frac{\mathrm{d}\rho}{\mathrm{d}x} = \frac{\lambda}{2} \frac{\mathrm{d}}{\mathrm{d}x} \left[\left(\frac{\mathrm{d}\rho}{\mathrm{d}x} \right)^2 \right], \tag{2.8}$$

$$\int_{x_0}^{x} \left(\mu_b(\rho) - \mu^{eq}\right) \frac{\mathrm{d}\rho}{\mathrm{d}x'} \, \mathrm{d}x' = \int_{x_0}^{x} \frac{\lambda}{2} \frac{\mathrm{d}}{\mathrm{d}x'} \left[\left(\frac{\mathrm{d}\rho}{\mathrm{d}x'} \right)^2 \right] \mathrm{d}x', \tag{2.9}$$

assuming $\rho(x_0) = \rho_v$, a change of variables leads to

$$\int_{\rho_v}^{\rho} \left(\frac{\partial f_b}{\partial \rho'}(\rho') - \mu^{eq} \right) \mathrm{d}\rho' = \int_{\rho_v}^{\rho} \frac{\lambda}{2} \, \mathrm{d} \left[\left(\frac{\mathrm{d}\rho'}{\mathrm{d}x'} \right)^2 \right], \tag{2.10}$$

$$f_b(\rho) - f_b(\rho_v) - \mu^{eq}(\rho - \rho_v) = \frac{\lambda}{2} \left(\frac{\mathrm{d}\rho}{\mathrm{d}x} \right)^2, \tag{2.11}$$

where, in the latter relation, the density gradient computed in correspondence with the vapour phase vanishes, since it is assumed to be a bulk phase.

Equation (2.11) can be conveniently rewritten in terms of a new thermodynamic potential, whose definition is in (2.11) itself. It is the *grand potential* density per unit volume, or Landau free energy, and is the characteristic state function for the grand canonical ensemble,

$$\omega(\rho) = f(\rho) - \mu^{eq}\rho, \qquad \omega_b(\rho) = f_b(\rho) - \mu^{eq}\rho. \tag{2.12}$$

Using eq. (2.12), eq. (2.11) reads

$$\omega_b(\rho) - \omega_b(\rho_v) = \frac{\lambda}{2} \left(\frac{\mathrm{d}\rho}{\mathrm{d}x} \right)^2, \tag{2.13}$$

from which it is evident how the grand potential itself must be equal, at equilibrium, in the bulk phases, for the same argument used above during the integration

$$\omega_b(\rho_l) = \omega_b(\rho_v). \tag{2.14}$$

The grand potential is in fact intimately linked to the Helmholtz free energy, being its Legendre transform,

$$\Omega = F - \int_V \rho \frac{\delta F}{\delta \rho} \, \mathrm{d}V = \int_V \omega \, \mathrm{d}V. \tag{2.15}$$

Thus, once the expression of the Helmholtz free energy is assigned, so is the grand potential and its density per unit volume. Consequently, it is possible to integrate equation (2.13) to get an implicit expression for the equilibrium density profile,

$$x = \sqrt{\frac{\lambda}{2}} \int_{\rho_v}^{\rho} \frac{\mathrm{d}\rho}{\sqrt{\omega_b(\rho) - \omega_b(\rho_v)}} + \text{const.} \tag{2.16}$$

The interface thickness can then be estimated to be

$$\epsilon \simeq \mathcal{O}\left(\frac{\rho_l - \rho_v}{\max\left[\frac{\mathrm{d}\rho}{\mathrm{d}x}\right]} \right), \tag{2.17}$$

and consequently, by taking the square root of equation (2.13),

$$\epsilon = (\rho_l - \rho_v) \sqrt{\frac{\lambda}{2(\omega_b(\bar{\rho}) - \omega_b(\rho_v))}}, \tag{2.18}$$

where $\bar{\rho}$ is taken such that

$$\left.\frac{\mathrm{d}\rho}{\mathrm{d}x}\right|_{\bar{\rho}} = \max\left[\frac{\mathrm{d}\rho}{\mathrm{d}x}\right]. \tag{2.19}$$

Finally, the surface tension can be defined as the excess of grand potential, in both the liquid and vapour phase,

$$\sigma = \int_{-\infty}^{s} (\omega(\rho) - \omega_b(\rho_v)) \, \mathrm{d}x + \int_{s}^{+\infty} (\omega(\rho) - \omega_b(\rho_l)) \, \mathrm{d}x, \tag{2.20}$$

where s is considered to be the spatial location of the interface center. Recalling that, for liquid bulk and vapour bulk phases, the grand potential is the same, we can merge together the two contributions, obtaining

$$\sigma = \int_{-\infty}^{+\infty} (\omega(\rho) - \omega_b(\rho_v)) \, \mathrm{d}x. \tag{2.21}$$

By using the grand potential density definition (2.12) and the generalized chemical potential definition (2.7), equation (2.21) can be further simplified to get to

$$\sigma = \int_{-\infty}^{\infty} \left[f_b + \frac{\lambda}{2} \left(\frac{\mathrm{d}\rho}{\mathrm{d}x} \right)^2 - \mu^{eq} \rho - \omega(\rho_v) \right] \mathrm{d}x \tag{2.22}$$

$$= \int_{-\infty}^{\infty} \left[w_b(\rho) + \frac{\lambda}{2} \left(\frac{\mathrm{d}\rho}{\mathrm{d}x} \right)^2 - \omega(\rho_v) \right] \mathrm{d}x, \tag{2.23}$$

that, using (2.13), can be expressed in one of the following equivalent forms

$$\sigma = \int_{-\infty}^{\infty} \lambda \left(\frac{\mathrm{d}\rho}{\mathrm{d}x} \right)^2 \mathrm{d}x, \tag{2.24}$$

$$= \int_{\rho_v}^{\rho_l} \lambda \frac{\mathrm{d}\rho}{\mathrm{d}x} \mathrm{d}\rho, \tag{2.25}$$

$$= \int_{\rho_v}^{\rho_l} \sqrt{2\lambda(\omega_b(\rho) - \omega_b(\rho_v))} \, \mathrm{d}\rho. \tag{2.26}$$

In particular, the latter expression (2.26) can be used to compute the surface tension of a substance whose thermodynamics is known, through its Helmholtz or Landau free energy, without knowledge of the spatial density profile. If one applies the above calculation to a spherically symmetric one-dimensional domain, it is possible to obtain the famous Young-Laplace equation.

2.2.2 Navier-Stokes-Korteweg equations of motion

Once the static equilibrium has been studied in the previous section, we shall now face the problem of dynamical equilibrium. The easiest way we have to get thermodynamically consistent equations of motion is to substitute the van der Waals assumption on the Helmholtz free energy functional in the equations of motion of a generic continuum, in the eulerian formulation. By doing this, we will obtain a system of equations with constitutive relations to be prescribed. We can assign those constitutive equations on the basis of the second principle of thermodynamics, following the Noll procedure and principles (Noll 2012).

We start from the basic Navier-Stokes system of equations, in its conservative formulation, formed by the continuity equation (2.27a), the momentum equations (2.27b), and the energy equation (2.27c). These equations are the PDE corresponding to the physical principles of conservation of mass, momentum and energy. Disregarding body forces, which are negligible at the scales we are interested to, we get

$$\frac{\partial \rho}{\partial t} + \nabla \cdot (\rho \mathbf{u}) = 0, \tag{2.27a}$$

$$\frac{\partial \rho \mathbf{u}}{\partial t} + \nabla \cdot (\rho \mathbf{u} \otimes \mathbf{u}) = \nabla \cdot T, \tag{2.27b}$$

$$\frac{\partial E}{\partial t} + \nabla \cdot (E \mathbf{u}) = \nabla \cdot (T \cdot \mathbf{u}) - \nabla \cdot \mathbf{q}_e; \tag{2.27c}$$

where ρ is the density, $\mathbf{u}$ the velocity vector, E the total energy of the system (internal + kinetic energy), T the stress tensor and $\mathbf{q}_e$ is the energy flux across the boundaries. The next step is to include the capillary contributions in the system of PDEs (2.27). To do this, we shall first obtain an equation representative of the second principle of thermodynamics, in local form. By scalar multiplying (2.27b) times the velocity vector $\mathbf{u}$, and subtracting the resulting equation from the conservation of energy equation (2.27c), recalling the fact that $\nabla \cdot (T \cdot \mathbf{u}) =$

$\mathbf{u} \cdot \nabla \cdot T + T : \nabla \mathbf{u}$, we get an evolution equation for the internal energy $\hat{u}$,

$$\rho \frac{\mathrm{D}\hat{u}}{\mathrm{D}t} = T : \mathbf{u} - \nabla \cdot \mathbf{q}_e; \tag{2.28}$$

where the *material derivative* operator is expressed by the following relation,

$$\frac{\mathrm{D}(\bullet)}{\mathrm{D}t} = \frac{\partial(\bullet)}{\partial t} + \mathbf{u} \cdot \nabla(\bullet). \tag{2.29}$$

In (2.28), $\hat{u}$ is the internal energy per unit mass of the system, which is related to the internal energy per unit volume, and to the Helmholtz free energy per unit mass by the relations

$$\hat{u}(v, \hat{s}) = \frac{1}{\rho} u(\rho, s), \qquad \hat{f} = \hat{u} - \theta \hat{s}, \tag{2.30}$$

where θ is the absolute temperature field and $\hat{s}$ the entropy per unit mass. Similarly, the Helmholtz free energy per unit mass $\hat{f}(v, \theta)$ is related to the Helmholtz free energy per unit volume $f(\rho, \theta)$ by

$$\hat{f}(v, \theta) = \frac{1}{\rho} f(\rho, \theta). \tag{2.31}$$

Since we are interested in expressing the internal energy in (2.28) as a function of the Helmholtz free energy per unit volume, which is the one appearing in the assumption (2.4), we shall rewrite it as

$$\hat{u} = \hat{f} + \theta \hat{s} = \frac{1}{\rho} f(\rho, \theta) + \theta \hat{s}. \tag{2.32}$$

However, in our formulation $f = f(\rho, \nabla\rho, \theta)$, therefore eq. (2.32) reads

$$\hat{u} = \frac{1}{\rho} f(\rho, \nabla\rho, \theta) + \theta \hat{s} = \frac{1}{\rho} \left(f_b(\rho, \theta) + \frac{\lambda}{2} |\nabla\rho|^2 \right) + \theta \hat{s}. \tag{2.33}$$

Differentiating the latter, we obtain a way to pass from the internal energy equation (2.28) to an equation of evolution for the entropy, which is useful to apply the second principle of thermodynamics and find consistent constitutive relation for the fluid behavior.

$$\begin{aligned} \mathrm{d}\hat{u} &= \frac{\partial \hat{f}(v, \theta)}{\partial \rho} \mathrm{d}\rho + \frac{\partial}{\partial \rho} \left(\frac{\lambda}{2\rho} |\nabla\rho|^2 \right) \mathrm{d}\rho + \frac{\partial}{\partial \nabla\rho} \left(\frac{\lambda}{2\rho} |\nabla\rho|^2 \right) \cdot \mathrm{d}\nabla\rho + \theta \mathrm{d}\hat{s} = \\ &= \frac{1}{\rho^2} \left(-\frac{\partial \hat{f}(v, \theta)}{\partial v} - \frac{\lambda}{2} |\nabla\rho|^2 \right) \mathrm{d}\rho + \frac{\lambda}{\rho} \nabla\rho \cdot \mathrm{d}\nabla\rho + \theta \mathrm{d}\hat{s} = \\ &= \frac{1}{\rho^2} \left(p_0 - \frac{\lambda}{2} |\nabla\rho|^2 \right) \mathrm{d}\rho + \frac{\lambda}{\rho} \nabla\rho \cdot \mathrm{d}\nabla\rho + \theta \mathrm{d}\hat{s}. \end{aligned} \tag{2.34}$$

Thus, we have an expression for the material derivative of the internal energy per unit mass, which reads

$$\rho\frac{\mathrm{D}\hat{u}}{\mathrm{D}t} = -\left(p_0 - \frac{\lambda}{2}\left|\nabla\rho\right|^2\right)\nabla\cdot\mathbf{u} + \lambda\nabla\rho\cdot\frac{\mathrm{D}\nabla\rho}{\mathrm{D}t} + \rho\theta\frac{\mathrm{D}\hat{s}}{\mathrm{D}t}, \tag{2.35}$$

where the divergence of velocity appears as the result of a substitution where the continuity equation (2.27a) has been used. The only term of the latter equation to be further arranged and specified is $\lambda\nabla\rho\cdot\frac{\mathrm{D}\nabla\rho}{\mathrm{D}t}$. We can easily obtain such a relation by applying the gradient operator to the mass or continuity equation (2.27a), in its non-conservative form,

$$\frac{\partial\rho}{\partial t} + \rho\nabla\cdot\mathbf{u} + \mathbf{u}\cdot\nabla\rho = 0 \tag{2.36}$$

$$\Downarrow$$

$$\frac{\partial\nabla\rho}{\partial t} + \nabla\left(\rho\nabla\cdot\mathbf{u}\right) + \nabla\mathbf{u}\cdot\nabla\rho + \mathbf{u}\cdot\nabla\otimes\nabla\rho = 0 \tag{2.37}$$

Hence,

$$\frac{\mathrm{D}\nabla\rho}{\mathrm{D}t} = \frac{\partial\nabla\rho}{\partial t} + \mathbf{u}\cdot\nabla\otimes\nabla\rho = -\nabla\left(\rho\nabla\cdot\mathbf{u}\right) - \nabla\mathbf{u}\cdot\nabla\rho. \tag{2.38}$$

By scalar multiplying equation (2.38) times $\lambda\nabla\rho$, we obtain

$$\lambda\nabla\rho\cdot\frac{\mathrm{D}\nabla\rho}{\mathrm{D}t} = -\lambda\nabla\rho\cdot\nabla\left(\rho\nabla\cdot\mathbf{u}\right) - \lambda\nabla\rho\otimes\nabla\rho : \nabla\mathbf{u}. \tag{2.39}$$

Finally, we have been able to specify an evolution equation for the entropy density per unit mass of the system, where all the terms arising from the van der Waals assumption on the free energy functional appear.

$$\begin{aligned}\rho\theta\frac{\mathrm{D}\hat{s}}{\mathrm{D}t} = T : \nabla\mathbf{u} - \nabla\cdot\mathbf{q}_e + \left(p_0 - \frac{\lambda}{2}\left|\nabla\rho\right|^2\right)\nabla\cdot\mathbf{u} + \\ + \lambda\nabla\rho\cdot\nabla\left(\rho\nabla\cdot\mathbf{u}\right) + \lambda\nabla\rho\otimes\nabla\rho : \nabla\mathbf{u}.\end{aligned} \tag{2.40}$$

Rearranging the terms in equation (2.40), we get to the final form

$$\begin{aligned}\rho\frac{\mathrm{D}\hat{s}}{\mathrm{D}t} =& \nabla\cdot\left(\frac{\lambda\rho\nabla\rho\nabla\cdot\mathbf{u} - \mathbf{q}_e}{\theta}\right) + \frac{\lambda\rho\nabla\rho\nabla\cdot\mathbf{u} - \mathbf{q}_e}{\theta^2}\cdot\nabla\theta + \\ &+ \frac{1}{\theta}\left[T + \left(p_0 - \frac{\lambda}{2}\left|\nabla\rho\right|^2 - \rho\nabla\cdot\left(\lambda\nabla\rho\right)\right)I + \lambda\nabla\rho\otimes\nabla\rho\right] : \nabla\mathbf{u}.\end{aligned} \tag{2.41}$$

Integrating equation (2.41) all over the domain, the divergence term in the rhs of the equation can be transformed into a boundary integral. It represents indeed the entropy flux across the boundary, meaning that it does not contribute directly to the entropy production, and can be positive or negative, depending on the flux velocity relative to the boundary of the domain. The remaining contributions on

the rhs, those with $\nabla\theta$ and $\nabla\mathbf{u}$, are the so-called entropy production terms, and must be positive-definite to respect the second principle of thermodynamics. This can be used as a criterion to find thermodynamically consistent constitutive equations. By following the Noll procedure (Noll 2012) and principles of determinism, locality and frame indifference, together with the Onsager reciprocal relations in irreversible processes (Onsager 1931), one possible choice is made by asking for the terms

$$\frac{\lambda\rho\nabla\rho\nabla\cdot\mathbf{u}-\mathbf{q}_e}{\theta^2},\quad \frac{1}{\theta}\left[T+\left(p_0-\frac{\lambda}{2}\left|\nabla\rho\right|^2-\rho\nabla\cdot(\lambda\nabla\rho)\right)I+\lambda\nabla\rho\otimes\nabla\rho\right], \tag{2.42}$$

which are referred to as the thermodynamic fluxes, to be linear in the respective conjugate thermodynamic forces.

$$\nabla\theta,\qquad \nabla\mathbf{u}.$$

As a result, we get to the final expression for the stress tensor and the energy flux,

$$\begin{aligned}T=&-\left(p_0-\frac{\lambda}{2}\left|\nabla\rho\right|^2-\rho\nabla\cdot(\lambda\nabla\rho)\right)I+\\&-\lambda\nabla\rho\otimes\nabla\rho+\mu(\nabla\mathbf{u}+(\nabla\mathbf{u})^T)-\frac{2}{3}\mu(\nabla\cdot\mathbf{u})I,\end{aligned} \tag{2.43}$$

$$\mathbf{q}_e=\lambda\rho\nabla\rho\nabla\cdot\mathbf{u}-k\nabla\theta. \tag{2.44}$$

The former is the usual viscous stress tensor and pressure plus terms depending on the density gradient, which is representative of capillary effects, and partially determines a new generalized pressure. The latter, the energy flux, is the usual Fourier model for heat conduction, to which we add a new capillary contribution, to form a new generalized energy flux.

2.2.3 Van der Waals equation of state

The system of equations is now complete, and the only physical quantity that needs to be specified is the pressure. In compressible Navier-Stokes formulation, an equation of state (EoS) is required, to express the thermodynamic pressure as a function of the thermodynamic state, identified by the couple (ρ,θ) of density and temperature.

throughout the whole thesis, the van der Waals equation of state is adopted, which is one of the possible choices to describe two phase flows, where miscibility and phase changes may occur. The van der Waals pressure can be expressed as (see (Zhao et al. 2011))

$$p=\frac{R\rho\theta}{1-b\rho}-a\rho^2, \tag{2.45}$$

with R the gas constant. By introducing the dimensionless or reduced variables

$$\rho^*=\frac{\rho}{\rho_c},\qquad p^*=\frac{p}{p_c},\qquad \theta^*=\frac{\theta}{\theta_c}, \tag{2.46}$$

where the *critical values* of density, pressure and temperature are those at the *critical point*,

$$\rho_c = \frac{1}{3b}, \qquad p_c = \frac{a}{27b^2}, \qquad \theta_c = \frac{8a}{27Rb}, \tag{2.47}$$

we can rewrite equation (2.45) as

$$p^* = \frac{8\rho^*\theta^*}{3-\rho^*} - 3\rho^{*2}, \tag{2.48}$$

which is the one used in numerical simulations.

2.2.4 Initial and boundary condition

System (2.27) completed with the constitutive relations (2.43), (2.44) and a suitable equation of state, e.g. the Van der Waals EOS (2.45), holds in the flow domain $\Omega \subset \mathbb{R}^3$ for time $t \in [0, T]$. Initial conditions need to be specified for the density, velocity and energy fields, $\rho(\mathbf{x}, 0) = \rho_0(\mathbf{x})$, $\mathbf{u}(\mathbf{x}, 0) = \mathbf{u}_0(\mathbf{x})$, and $E(\mathbf{x}, 0) = E_0(\mathbf{x})$, respectively.

We shall also assign suitable boundary conditions on $\partial\Omega$. Throughout this thesis, boundary conditions of the following form will be assumed,

$$\mathbf{u}(\mathbf{x}, t) = \hat{\mathbf{u}}(\mathbf{x}, t), \tag{2.49}$$

$$\mathbf{q}_e(\mathbf{x}, t) \cdot \mathbf{n} = f(\mathbf{x}, t), \qquad \text{for } \mathbf{x} \in \partial\Omega \tag{2.50}$$

$$\nabla\rho(\mathbf{x}, t) \cdot \mathbf{n} = \cos\left[\varphi(\mathbf{x}, t)\right]. \tag{2.51}$$

The first one is a Dirichlet type condition on the velocity vector $\mathbf{u}$, whereas the other two are Neumann boundary conditions on the energy flux and contact angle ($\mathbf{n}$ is the unit normal to the domain pointing outwards). The latter condition can be interpreted as an interface contact angle condition, where the angle φ is the one defined by the normal to the domain and the density gradient.

2.2.5 Vorticity equation

An equation for the evolution of the vorticity, i.e. the rotor of the velocity field $\boldsymbol{\omega} = \nabla \times \mathbf{u}$, can be obtained by taking the rotor of the momentum equation (2.27b), having in mind the stress tensor constitutive equation derived above, eq. (2.43),

$$\begin{aligned}\frac{\partial\rho\mathbf{u}}{\partial t} + \nabla\cdot(\rho\mathbf{u}\otimes\mathbf{u}) &= \nabla\cdot T \\ &= \nabla\cdot(-p\mathbf{I} - \lambda\nabla\rho\otimes\nabla\rho) + \mu\nabla\cdot\left(\nabla\mathbf{u} + \nabla^T\mathbf{u}\right) - \frac{2}{3}\mu\nabla\left(\nabla\cdot\mathbf{u}\right) \\ &= -\nabla p - \lambda\nabla\cdot(\nabla\rho\otimes\nabla\rho) + \mu\nabla\cdot\left(\nabla\mathbf{u} + \nabla^T\mathbf{u}\right) - \frac{2}{3}\mu\nabla\left(\nabla\cdot\mathbf{u}\right)\end{aligned} \tag{2.52}$$

where p is the generalized pressure, which takes into account the capillary terms,

$$p = p_{vdw} - \lambda\rho\nabla^2\rho - \frac{\lambda}{2}\left|\nabla\rho\right|^2, \tag{2.53}$$

With this in mind, by noting that

$$\nabla p + \lambda \nabla \cdot (\nabla \rho \otimes \nabla \rho) = \rho \nabla \mu^g + s \nabla \theta, \tag{2.54}$$

one can rewrite the above equation as follows (s being the entropy per unit volume and μ^g being the generalized chemical potential)

$$\frac{\partial \rho \mathbf{u}}{\partial t} + \nabla \cdot (\rho \mathbf{u} \otimes \mathbf{u}) = -\rho \nabla \mu^g - s \nabla \theta + \mu \nabla \cdot \left(\nabla \mathbf{u} + \nabla^T \mathbf{u} \right) - \frac{2}{3} \mu \nabla (\nabla \cdot \mathbf{u}) \tag{2.55}$$

By using the continuity equation, and dividing by the density ρ, we get to

$$\frac{\partial \mathbf{u}}{\partial t} + \mathbf{u} \cdot \nabla \mathbf{u} = \frac{D\mathbf{u}}{Dt} = -\nabla \mu^g - \frac{s}{\rho} \nabla \theta + \nu \nabla \cdot \left(\nabla \mathbf{u} + \nabla^T \mathbf{u} \right) - \frac{2}{3} \nu \nabla (\nabla \cdot \mathbf{u}) \tag{2.56}$$

To obtain an equation for the evolution of the vorticity for a NSK fluid, is necessary to apply the curl operator to (2.56). This leads us to

$$\frac{D\boldsymbol{\omega}}{Dt} + \boldsymbol{\omega} \nabla \cdot \mathbf{u} - (\boldsymbol{\omega} \cdot \nabla) \mathbf{u} = -\nabla \left(\frac{s}{\rho} \right) \times \nabla \theta + \nabla \times \left(\frac{1}{\rho} \nabla \cdot D(\mathbf{u}) \right) \tag{2.57}$$

where the fact that

$$\frac{D\mathbf{u}}{Dt} = \frac{\partial \mathbf{u}}{\partial t} + \nabla \left(\frac{|\mathbf{u}|^2}{2} \right) + \boldsymbol{\omega} \times \mathbf{u} \tag{2.58}$$

has been used. With further considerations, it's easy to rearrange equation (2.57) to get to the final form of the equation:

$$\frac{D}{Dt} \left(\frac{\boldsymbol{\omega}}{\rho} \right) = \left(\frac{\boldsymbol{\omega}}{\rho} \cdot \nabla \right) \mathbf{u} - \frac{1}{\rho} \nabla \left(\frac{s}{\rho} \right) \times \nabla \theta + \frac{1}{\rho} \nabla \times \left(\frac{1}{\rho} \nabla \cdot D(\mathbf{u}) \right), \tag{2.59}$$

where the first term in the rhs of (2.59) is called the *stretching and tilting* term, and the second is a generalized *baroclinic* term. The latter is responsible for the vorticity production in the field, while the former is responsible for stretching and tilting of vortex. The last term in the rhs of (2.59) is the dissipative terms.

2.2.6 Dimensionless form of the equations

By introducing dimensionless parameters for all the variables appearing in the NSK equations (2.27), it is possible to obtain the dimensionless form of the NSK equations for a fluid with capillarity. In particular, the relevant dimensionless group appear in the definition of the constitutive relations, i.e. in the definitions of the stress tensor T and of the energy flux $\mathbf{q}_e$. By considering the parameters λ and μ constants, as it is assumed throughout the thesis, the dimensionless stress tensor T and energy flux $\mathbf{q}_e$ assume the following form (where all the variables

are already dimensionless variables):

$$T = -\left(p_0 - \frac{Cn}{2}|\nabla\rho|^2 - Cn\rho\nabla^2\rho\right)I + \\ - Cn\nabla\rho\otimes\nabla\rho + \frac{1}{Re}(\nabla\mathbf{u} + (\nabla\mathbf{u})^T) - \frac{2}{3Re}(\nabla\cdot\mathbf{u})I, \tag{2.60}$$

$$\mathbf{q}_e = Cn\rho\nabla\rho\nabla\cdot\mathbf{u} - \frac{1}{Pe}\nabla\theta. \tag{2.61}$$

In the above equations, Cn is the Cahn number,

$$Cn = \frac{\lambda\rho_c^2}{p_c L_{ref}^2};$$

Re is the Reynolds number

$$Re = \frac{L_{ref}\sqrt{p_c\rho_c}}{\mu};$$

and Pe is the Péclet number defined by

$$Pe = \frac{3L_{ref}\sqrt{p_c\rho_c}R}{8k},$$

where R is the gas constant, p_c and ρ_c are the values of pressure and density at the critical point of water and L_{ref} is the reference value for the spatial dimension.

Chapter 3

Elements of Solid Mechanics

This chapter presents the most relevant theoretical aspects extensively described in many books (Morton E Gurtin et al. 2010; Han and Reddy 2012; Lubliner 2008; Souza Neto et al. 2011), which have been synthesized and unified for the reader. A particular attention is given to the physical explanations and justifications of all the assumptions in the model, to allow for a complete understanding of the theory. The first two sections of the chapter are focused on the theory of linear elasticity and the thermodynamics of a solid continuum, both being the basis for the development of a theory of plasticity. Then, Section 3.3 is where the classical plasticity theory is introduced and discussed in its fundamentals, and Section 3.4 is where it is particularized for our cavitation applications. The choice of a plasticity theory is suggested and motivated by the results obtained from experimental observations both in past decades (Philipp and Lauterborn 1998) and in recent years (Dular, Požar, et al. 2019). The von Mises plasticity model outlined in Section 3.4 is suitable for the description of ductile metals, which are of great interest in cavitation applications.

3.1 Theory of linear elasticity

The theory of linear elasticity can be obtained from the theory of Elasticity by linearizing appropriate relations, i.e. neglecting higher-order terms. A linear theory of elasticity is suitable for the description of solids undergoing small deformations when subjected to loads. In mathematical words, this corresponds to a situation where the symmetric gradient of the displacement $\nabla^s \mathbf{u}$ is small and, as a consequence, the eulerian and lagrangian description correspond, since there is no more need to differentiate between a reference and an actual configuration.

The basic equation of the linear theory of elasticity is the local momentum balance,

$$\rho \ddot{\mathbf{u}} = \nabla \cdot \boldsymbol{\sigma} + \mathbf{b}, \qquad \rho \ddot{u}_i = \frac{\partial \sigma_{ij}}{\partial X_j} + b_i \tag{3.1}$$

where $\ddot{\mathbf{u}}$ is the double derivative in time of the displacement vector (acceleration), $\boldsymbol{\sigma}$ is the Cauchy stress tensor and $\mathbf{b}$ is the body force vector per unit volume.

The Cauchy stress tensor is linked to the displacement through the *strain-displacement* relation and the *stress-strain* relation. The former is the definition of the strain tensor,

$$\boldsymbol{\epsilon} = \frac{1}{2}\left(\nabla \mathbf{u} + \nabla \mathbf{u}^T\right) = \nabla^s \mathbf{u}, \qquad \epsilon_{ij} = \frac{1}{2}\left(\frac{\partial u_i}{\partial X_j} + \frac{\partial u_j}{\partial X_i}\right). \tag{3.2}$$

The latter connects the Cauchy stress tensor with the strain tensor, representing the deformations. It is the constitutive equation

$$\boldsymbol{\sigma} = \mathbf{C}^{el} : \boldsymbol{\epsilon}, \qquad \sigma_{ij} = C^{el}_{ijkl}\epsilon_{kl}. \tag{3.3}$$

In (3.3), $\mathbf{C}^{el}$ is the *elasticity tensor* and characterizes the behavior of an elastic material, relating unknown stresses and strains.

3.1.1 Constitutive equation: the elasticity tensor

The constitutive model used in this thesis is the one for a *hyperelastic* material. For such a material the stress-strain relation is derived from a **Strain Energy Density Function**. Although the hyperelastic model is a generalization, usually used to describe non-linear elastic material behaviors, the classical linear elasticity constitutive relation can actually be derived from an internal energy density function, sometimes referred to as strain energy. Once a strain energy W has been defined, the stress-strain relation (3.3) comes from the derivative of the energy with respect to the strain tensor $\boldsymbol{\epsilon}$,

$$\boldsymbol{\sigma}(\mathbf{x}) = \frac{\partial W(\mathbf{x}, \boldsymbol{\epsilon}(\mathbf{x}))}{\partial \boldsymbol{\epsilon}}, \qquad \sigma_{ij} = \frac{\partial W}{\partial \epsilon_{ij}} \tag{3.4}$$

The elasticity tensor is then

$$\mathbf{C}^{el} = \frac{\partial^2 W(\mathbf{x}, \boldsymbol{\epsilon}(\mathbf{x}))}{\partial \boldsymbol{\epsilon}^2}, \qquad C^{el}_{ijkl} = \frac{\partial^2 W}{\partial \epsilon_{ij} \partial \epsilon_{kl}} \tag{3.5}$$

Since the strain tensor $\boldsymbol{\epsilon}$ is, by definition, a second-order symmetric tensor, the elasticity tensor possesses the following symmetries:

$$C^{el}_{ijkl} = C^{el}_{klij} = C^{el}_{ijlk} = C^{el}_{jilk}. \tag{3.6}$$

When dealing with the *linear* theory of elasticity, the positive-definiteness of $\mathbf{C}^{el}$ restricted to the space of second-order symmetric tensors is always assumed,

$$\mathbf{A} : \mathbf{C}^{el} : \mathbf{A} := A_{ij} C^{el}_{ijkl} A_{kl} > 0, \tag{3.7}$$

which is equivalent to postulating that the strain energy W is *convex* on the same vector space.

If we then ask for the strain energy to not depend on the points of the body we are considering, and to be rotationally invariant, it means we are considering

a *homogeneous* and *isotropic* material, which is the case studied in this thesis when dealing with purely elastic materials. Finally, assuming $\mathbf{C}^{el}$ is constant, we get the classical result for linear elasticity, which comes from a representation theorem for isotropic linear tensor functions (Morton E Gurtin 1982):

$$\mathbf{C}^{el} = \lambda \mathbf{I} \otimes \mathbf{I} + 2\mu \mathbb{S}, \tag{3.8}$$

where $\mathbf{I}$ is the second-order identity tensor with components

$$\mathbf{I}_{ij} = \delta_{ij}, \qquad (\mathbf{I} \otimes \mathbf{I})_{ijkl} = \delta_{ij}\delta_{kl}, \tag{3.9}$$

and $\mathbb{S}$ is the fourth-order symmetric identity tensor, that maps each second-order tensor into its symmetric part. Its components are

$$\mathbb{S}_{ijkl} = \frac{1}{2}\left(\delta_{ik}\delta_{jl} + \delta_{il}\delta_{jk}\right). \tag{3.10}$$

In (3.8) λ and μ are the Lamé parameters, that characterize the material behavior as will be more clear in subsequent sections. For such a model, the strain energy density function is

$$W = \frac{1}{2}\boldsymbol{\epsilon} : \mathbf{C}^{el} : \boldsymbol{\epsilon} \tag{3.11}$$

and it represents the energy stored by a system undergoing deformation.

When we let the elasticity tensor act on the strain tensor we get the stress-strain relation, which takes the form

$$\boldsymbol{\sigma} = \mathbf{C}^{el} : \boldsymbol{\epsilon} = \lambda\,(\mathrm{tr}\boldsymbol{\epsilon})\,\mathbf{I} + 2\mu\boldsymbol{\epsilon}, \qquad \sigma_{ij} = \lambda\epsilon_{kk}\delta_{ij} + 2\mu\epsilon_{ij} \tag{3.12}$$

Conditions on Lamé parameters

We must use the positive-definiteness assumption on the elasticity tensor to derive conditions on the Lamé parameters for this to happen. The positive-definiteness of the elasticity tensor with respect to the space of second-order symmetric tensors requires (3.7). In particular, since the strain tensor $\boldsymbol{\epsilon}$ is a second-order symmetric tensor, it must be

$$\boldsymbol{\epsilon} : \mathbf{C}^{el} : \boldsymbol{\epsilon} = \boldsymbol{\epsilon} : \boldsymbol{\sigma} > 0.$$

By using the constitutive equation (3.12), it's easy to get to the inequality

$$2\mu\,\|\boldsymbol{\epsilon}\|^2 + \lambda\,(\mathrm{tr}\boldsymbol{\epsilon})^2 > 0. \tag{3.13}$$

Any second-order tensor can be decoupled in its deviatoric and hydrostatic part, so that

$$\boldsymbol{\epsilon} = \boldsymbol{\epsilon}^d + \frac{1}{3}\,(\mathrm{tr}\boldsymbol{\epsilon})\,\mathbf{I}, \qquad \mathrm{tr}\boldsymbol{\epsilon}^d = 0.$$

By substituting this decomposition into (3.13) one gets

$$2\mu\|\boldsymbol{\epsilon}^d\|^2 + k\,(\mathrm{tr}\boldsymbol{\epsilon})^2 > 0, \qquad k = \frac{2}{3}\mu + \lambda, \tag{3.14}$$

where k is called bulk modulus.

Since the first term in (3.14) is related to the deviator of the strain tensor, while the second term to the hydrostatic one, both of them must verify the inequality independently. This means that we have a condition on the two Lamé parameters to satisfy the positive-definiteness assumption,

$$\mu > 0, \qquad 2\mu + 3\lambda > 0. \tag{3.15}$$

3.1.2 Displacement form of the equation of motion

A useful form of the equation of motion (3.1) which is not seen often when dealing with finite element approximations, is the so called displacement form. It can be used to derive some important notions and quantities regarding the dynamical behavior of an elastic material. Substituting equation (3.12) in (3.1), we have

$$\rho\ddot{\mathbf{u}} = \nabla \cdot (\lambda \,(\mathrm{tr}\boldsymbol{\epsilon})\, \mathbf{I} + 2\mu\boldsymbol{\epsilon}) + \mathbf{b} \tag{3.16}$$

using the definition of strain tensor (3.2) into (3.16) we can easily get to the final form

$$\rho\ddot{\mathbf{u}} = \mu\Delta\mathbf{u} + (\lambda + \mu)\nabla\,(\nabla \cdot \mathbf{u}) + \mathbf{b} \tag{3.17}$$

3.1.3 Progressive elastic waves

The equation of motion in the form (3.17) is a wave equation, even though it has a rather unfamiliar structure. In fact, it describes the propagation of two different waves at once.

To see this, by taking the curl of the PDE in (3.17), having in mind the fact that the curl of a gradient vanishes, so that

$$\frac{\partial^2}{\partial t^2}\nabla \times \mathbf{u} = c_S^2 \Delta\,(\nabla \times \mathbf{u})\,. \tag{3.18}$$

This is now clearly a wave equation for the propagation of the quantity $\nabla \times \mathbf{u}$. The wave velocity is

$$c_S = \sqrt{\frac{\mu}{\rho}}. \tag{3.19}$$

The corresponding waves are called *S waves* or shear waves or rotation waves, and they are indeed related to the curl of displacement, which is itself linked to rotations.

We now take the divergence of equation (3.17). This gives rise to a new wave equation, related to the propagation of the $\nabla \cdot \mathbf{u}$,

$$\frac{\partial^2}{\partial t^2}\nabla \cdot \mathbf{u} = c_P^2 \Delta\,(\nabla \cdot \mathbf{u})\,. \tag{3.20}$$

These are called *P waves* or compression/expansion waves or pressure waves, since are related to the propagation of volume change. Their velocity is

$$c_P = \sqrt{\frac{\lambda + 2\mu}{\rho}}. \tag{3.21}$$

In a homogeneous and isotropic medium, only two types of progressive waves are possible: S and P waves (sometimes also referred to as longitudinal and transverse waves). Their velocity is real, as a consequence of the positive-definiteness of the elasticity tensor.

3.1.4 Dimensionless form of the time-dependent elasticity problem

In this subsection, the scaling approach presented in (Petter Langtangen and Pedersen 2016) is followed, to derive a dimensionless form of the equation of motion (3.17), which will be useful to distinguish cases in which the inertial term can be neglected, from cases in which it may play a relevant role. This treatment also allows a deeper understanding of the relevant parameters in the elasticity problem.

Starting from the equation of motion in the displacement form (3.17), it is possible to define the following dimensionless variables:

$$\bar{\mathbf{u}} = \frac{\mathbf{u}}{u_c}, \quad \bar{x} = \frac{x}{L}, \quad \bar{y} = \frac{y}{L}, \quad \bar{z} = \frac{z}{L}, \quad \bar{t} = \frac{t}{t_c}$$

Inserting now these dimensionless variables in the equation of motion, neglecting the body forces and considering the material parameters (ρ, λ, μ) as constants (as we will throughout the whole thesis), we get to the following equations:

$$\frac{\rho u_c}{t_c^2}\frac{\partial^2 \bar{\mathbf{u}}}{\partial \bar{t}^2} = \frac{u_c}{L^2}(\lambda+\mu)\bar{\nabla}\left(\bar{\nabla}\cdot\bar{\mathbf{u}}\right) + \frac{u_c\mu}{L^2}\bar{\nabla}\cdot\left(\bar{\nabla}\bar{\mathbf{u}}\right)$$

$$\frac{\partial^2 \bar{\mathbf{u}}}{\partial \bar{t}^2} = \frac{t_c^2(\lambda+\mu)}{\rho L^2}\bar{\nabla}\left(\bar{\nabla}\cdot\bar{\mathbf{u}}\right) + \frac{t_c^2\mu}{\rho L^2}\bar{\nabla}\cdot\left(\bar{\nabla}\bar{\mathbf{u}}\right)$$

$$\frac{\partial^2 \bar{\mathbf{u}}}{\partial \bar{t}^2} = \frac{t_c^2\mu(\beta+1)}{\rho L^2}\bar{\nabla}\left(\bar{\nabla}\cdot\bar{\mathbf{u}}\right) + \frac{t_c^2\mu}{\rho L^2}\bar{\nabla}\cdot\left(\bar{\nabla}\bar{\mathbf{u}}\right), \qquad \beta = \frac{\lambda}{\mu} \tag{3.22}$$

From (3.22) one may choose che characteristic time t_c in order to make the dimensionless terms equal to unity,

$$t_c = \sqrt{\frac{\rho}{\mu}}. \tag{3.23}$$

In this situation, the only dimensionless parameter is $\beta = \lambda/\mu$.

Suppose we now have a time-varying load (i.e. a boundary condition) with a frequency ω, so that its characteristic time scale would be $t_c = 1/\omega$. In this situation, equation (3.22) becomes

$$\gamma\frac{\partial^2 \bar{\mathbf{u}}}{\partial \bar{t}^2} = (\beta+1)\bar{\nabla}\left(\bar{\nabla}\cdot\bar{\mathbf{u}}\right) + \bar{\nabla}\cdot\left(\bar{\nabla}\bar{\mathbf{u}}\right), \tag{3.24}$$

with the dimensionless coefficient γ given by

$$\gamma = \frac{\rho L^2\omega^2}{\mu} = \left(\frac{L\sqrt{\rho/\mu}}{1/\omega}\right)^2. \tag{3.25}$$

It is evident that $\sqrt{\gamma}$ is the ratio between the time scale for the shear waves and the time scale for the time-varying load applied at the boundaries. This analysis clearly shows that the lhs of the equation of motion, the inertial term, can therefore be neglected only when $\gamma \ll 1$, when the time scale t_c, at which the forced boundary movement happens, is way larger than the time scale for the S waves to travel through the elastic medium.

3.1.5 The quasi-static elastic problem

In many different applications, the speed at which the S and P waves propagate is much larger than the velocity of the moving load on the boundary. In these cases, as described above with (3.24), it is possible to neglect the acceleration, and so the inertial term, from the equation of motion. This leads to the so called *quasi-static* formulation for the elastic problem, sometimes also referred to as the problem of *elastostatics*, since all the dynamical effects are absent. A quasi-static problem could be time dependent, in the sense that the boundary condition could depend on time. In this situation, the underlying assumption is that between two different times and states, say t_1 and t_2, the material had enough time to respond to the load and reach the equilibrium, so that at all times there is a *static equilibrium*.

The boundary-value problem for elastostatics is:

$$\nabla \cdot \boldsymbol{\sigma} + \mathbf{b} = 0 \tag{3.26}$$

$$\boldsymbol{\sigma} = \mathbf{C}^{el} : \boldsymbol{\epsilon} \tag{3.27}$$

$$\boldsymbol{\epsilon} = \nabla^s \mathbf{u} \tag{3.28}$$

$$\mathbf{u} = \hat{\mathbf{u}} \qquad \text{on } \partial\mathcal{B}_{\mathbf{u}} \tag{3.29}$$

$$\boldsymbol{\sigma}\mathbf{n} = \mathbf{t} \qquad \text{on } \partial\mathcal{B}_{\sigma} \tag{3.30}$$

In (3.26) the displacement field is the unknown. For the mixed problem of elastostatics there is a unique solution (Morton E Gurtin et al. 2010).

3.2 Thermodynamics of a continuum

It is useful to write down the first and second law of Thermodynamics for a general three-dimensional continuum whose motion is governed by (3.1). The equations presented in this section can be adopted with no differences for an elastic material as well as for a plastic or viscoplastic material.

3.2.1 Firs law of thermodynamics

The first law of Thermodynamics postulates the *conservation of energy*. It means that energy can be transformed from one form to another, but can never be destroyed nor created. The total energy of a system, which is composed by its kinetic energy and its internal energy, can be increased by the means of mechanical work done on the system by the surroundings and of energy supplied to the system as

heat. Without loss of generality, we will assume that no heat transfer is occurring within the material bulk, but only at its boundaries. Thus, for a three dimensional continuum, the equation for the conservation of energy takes the form

$$\frac{\mathrm{d}}{\mathrm{d}t}\int_{\mathcal{B}} e\,\mathrm{d}V = \int_{\mathcal{B}} \mathbf{b}\cdot\mathbf{v}\,\mathrm{d}V + \int_{\partial\mathcal{B}} \mathbf{t}(\mathbf{n})\cdot\mathbf{v}\,\mathrm{d}S - \int_{\partial\mathcal{B}} \mathbf{q}_e\cdot\mathbf{n}\,\mathrm{d}S. \tag{3.31}$$

In equation (3.31), e is the total energy per unit volume of the system, $\mathbf{v}$ is the velocity vector, $\mathbf{b}$ is the density of body forces, $\mathbf{t}(\mathbf{n})$ is the traction vector oriented as the normal to the boundary of the body, $\mathbf{q}_e$ is the thermal flux outflow per unit time per unit surface area and $\mathbf{n}$ is the outward unit normal. First two terms of the rhs represent the mechanical power, while the latter represents the rate of heat transferred. All the integrals are taken on the reference configuration of the body and on its boundaries. Note that reference and actual configuration correspond, since we are considering a problem with small deformations, i.e. small $\nabla\mathbf{u}$. By making use of the divergence theorem and (3.30), it is possible to obtain a local energy conservation law, which is

$$\dot{e} = \mathbf{b}\cdot\mathbf{v} + \nabla\cdot(\boldsymbol{\sigma}\mathbf{v}) - \nabla\cdot\mathbf{q}_e \tag{3.32}$$

Recalling the fact that the total energy is composed by the internal energy and the kinetic energy, it is possible to get an equation for the internal energy evolution by subtracting a kinetic energy evolution equation from (3.32). To do so, we first need an equation for the evolution of the kinetic energy, which is straightforward to obtain from the local equation of motion (3.1). By scalar multiplying equation (3.1) times the velocity vector we get

$$\mathbf{v}\cdot\rho\frac{\mathrm{d}\mathbf{v}}{\mathrm{d}t} = \mathbf{v}\cdot\nabla\cdot\boldsymbol{\sigma} + \mathbf{v}\cdot\mathbf{b}$$

$$\frac{1}{2}\rho\frac{\mathrm{d}}{\mathrm{d}t}(\mathbf{v}\cdot\mathbf{v}) = \nabla\cdot(\boldsymbol{\sigma}\mathbf{v}) - \boldsymbol{\sigma}:\nabla\mathbf{v} + \mathbf{b}\cdot\mathbf{v} \tag{3.33}$$

In the lhs of the equation, we recognize the time derivative of the kinetic energy density, so that it is an equation for its evolution.

We can now obtain an equation for the evolution of the internal energy density $u = e - \frac{1}{2}\rho\,|\mathbf{v}|^2$ by subtracting eq. (3.33) from eq. (3.32):

$$\dot{u} = \boldsymbol{\sigma}:\nabla\mathbf{v} - \nabla\cdot\mathbf{q}_e. \tag{3.34}$$

3.2.2 Second law of thermodynamics

The second law of Thermodynamics postulates the *irreversibility of entropy production*, and can be expressed in a variety of formulations, all equivalent to each other. The one we will be using throughout this section is the *Clausius-Duhem Inequality*, which is a convenient way of expressing the second law of Thermodynamics when dealing with continuum media, because it allows the determination

of thermodynamically consistent or physically acceptable constitutive relations. In its local form, the Clausius-Duhem inequality can be written as

$$\dot{s} + \nabla \cdot \left(\frac{\mathbf{q}_e}{\theta} \right) \geq 0, \tag{3.35}$$

where s is the entropy density per unit volume and $\theta > 0$ is the absolute temperature. Equation (3.35) is equivalent to asking for the entropy production terms to be non-negative. Let us see why by deriving an equation for the evolution of entropy.

It is possible to obtain an evolution equation for entropy from eq. (3.34) for the internal energy evolution, by using the definition of *Helmholtz free energy* density per unit volume.

$$f = u - \theta s \tag{3.36}$$

Substituting eq. (3.36) in (3.34) one gets the following,

$$\begin{aligned} \dot{u} &= \dot{f} + \dot{\theta} s + \theta \dot{s} \\ \theta \dot{s} &= \boldsymbol{\sigma} : \nabla \mathbf{v} - \nabla \cdot \mathbf{q}_e - (\dot{f} + s\dot{\theta}) \\ \dot{s} &= \frac{1}{\theta} \boldsymbol{\sigma} : \nabla \mathbf{v} - \frac{1}{\theta} \nabla \cdot \mathbf{q}_e - \frac{1}{\theta} (\dot{f} + s\dot{\theta}) \\ \dot{s} &= \frac{1}{\theta} \boldsymbol{\sigma} : \nabla \mathbf{v} - \nabla \cdot \left(\frac{\mathbf{q}_e}{\theta} \right) - \frac{\mathbf{q}_e}{\theta^2} \cdot \nabla \theta - \frac{1}{\theta} (\dot{f} + s\dot{\theta}) \end{aligned} \tag{3.37}$$

Requiring the Clausius-Duhem inequality to hold corresponds to asking for the entropy production term to be non-negative, i.e. applying (3.35) to (3.37),

$$\boldsymbol{\sigma} : \nabla \mathbf{v} - \frac{\mathbf{q}_e}{\theta} \cdot \nabla \theta - (\dot{f} + \dot{\theta} s) \geq 0 \tag{3.38}$$

Equation (3.38) allows for the determination of whether or not a constitutive relation is thermodynamically acceptable. The only difference between purely elastic material and elastoplastic or viscoplastic materials depends on the definition of the Helmholtz free energy, as we will see in the following sections. In particular, the Helmholtz free energy could depend on the strain tensor and temperature, or on a set of relevant *internal variables* in addition to strain and temperature, as it is the case in classical plasticity.

In the context of linear elasticity, the Helmholtz free energy density function depends on the strain tensor and the absolute temperature, $f = f(\boldsymbol{\epsilon}, \theta)$. Its total derivative is

$$\dot{f}(\boldsymbol{\epsilon}, \theta) = \frac{\partial f}{\partial \boldsymbol{\epsilon}} : \dot{\boldsymbol{\epsilon}} + \frac{\partial f}{\partial \theta} \dot{\theta}. \tag{3.39}$$

Substituting the latter expression in (3.38) one gets

$$\left(\boldsymbol{\sigma} - \frac{\partial f}{\partial \boldsymbol{\epsilon}} \right) : \dot{\boldsymbol{\epsilon}} - \frac{\mathbf{q}_e}{\theta} \cdot \nabla \theta - \left(\frac{\partial f}{\partial \theta} + s \right) \dot{\theta} \geq 0. \tag{3.40}$$

Keeping in mind the entropy definition in terms of thermodynamic potentials

$$s = -\frac{\partial f}{\partial \theta}, \tag{3.41}$$

we are left with the choice of two constitutive relations for the stress tensor and the thermal flux. The two terms left in (3.40) must verify the inequality independently, due to a famous result in (Truesdell 1984). In particular, since we are dealing with a linear elastic material, the stress-strain contribution must vanish, because elastic deformation is a reversible process, hence it does not take part in the production of entropy. For this reason we must require

$$\sigma = \frac{\partial f}{\partial \epsilon} \tag{3.42}$$

In the case of linear elasticity, the Helmholtz free energy indeed corresponds to the strain energy (3.11).

The only term left in (3.40), which is responsible for the whole entropy production in a thermo-elastic body, is

$$-\frac{\mathbf{q}_e}{\theta} \cdot \nabla\theta \geq 0. \tag{3.43}$$

In solid mechanics as well as in fluid dynamics, the Coleman-Noll (Coleman and Noll 1974) procedure to find constitutive equation is usually adopted. The basic principles leading this procedure, introduced by (Truesdell 1969) are the *Thermodynamics Determinism* and the *Frame Indifference*. The former postulates that "it is the history of the process to which a neighborhood of a point $\mathbf{x}$ of the body $\mathcal{B}$ has been subjected, to determine the behavior of the same point $\mathbf{x}$" (principle of local determinism), and the latter requires the constitutive equations to be invariant under changes of frame, meaning that the material response must be independent of the observer. The Coleman–Noll procedure is based on the premise that the second law be satisfied in all conceivable processes, irrespective of the difficulties involved in producing such processes in the laboratory. It prescribes, in its simplest form, which will be used in this thesis, the constitutive relation for each independent *thermodynamic flux* acting against its conjugate or dual *thermodynamic force*, to be linear with respect to the conjugate thermodynamic force, and to satisfy the dissipation inequality derived from the *Clausius-Duhem* inequality. In the case of (3.43), the thermodynamic force is $\nabla\theta$, so we shall assume a constitutive equation for the thermal flux of the form

$$\mathbf{q}_e = -k\nabla\theta \qquad k > 0. \tag{3.44}$$

which is the usual Fourier law for heat transfer. This choice, which is not the only possible, is thermodynamically consistent, meaning that is consistent with the first and second law of thermodynamics, and is physically acceptable. Indeed,

$$-\frac{\mathbf{q}_e}{\theta} \cdot \nabla\theta = \frac{k}{\theta} |\nabla\theta|^2 \geq 0.$$

3.3 Classical theory of small deformation plasticity

We usually use the term *plastic* to indicate the property that many materials, such as metals, can be deformed, by the action of some forces, up to a point where

they keep the new shape acquired during deformation, even upon removal of such forces. Plastic behavior, at least that of metals, to which we focus our attention in this thesis, can be partially explained by means of *microscopic* theories, such as the crystal theory of solids and the dislocation theory. Most of the macroscopic effects that can be observed when a solid undergoes a *plastic deformation*, can be explained in terms of such theories, and in particular in terms of defects movement in crystals. All the macroscopic effects described below are caused by the movement of specific crystal defects, that can be classified in: *point defects*, when they involve only few atoms; *line defects*, when are extended to entire rows of atoms; and *planar defects*, covering whole planes of atoms in the crystal. Mathematical models accounting for the description of crystals and defects are microscopic models suitable for molecular dynamics simulations, and mesoscale models.

In the following, we will not deal with any of these concepts, since our interest is mainly focused on the *macroscopic response* of a solid plastic structure to an external loading. In this context, the term macroscopic response means that we are not interested in the description and analysis of metal crystals or dislocation movement, but only in determining the macroscopic effects in terms of stresses and deformations attained during the process.

Macroscopic theories of plasticity, such as the *classical theory of plasticity* (reviewed and analysed in subsequent sections), are based on a macroscopic characterization of materials by means of tensile tests. These tests are carried out on cylindrical specimens of materials, that are stretched or compressed at a constant or variable deformation rate. The condition in which the rate of application of the deformation is kept constant is called *rate-independent*, because the material response is not characterized by the rate at which the applied deformation varies (this is the framework of the model applied in this thesis, since rate-dependency has not been taken into consideration). The aim of these tests is usually to get information on the constitutive behavior of materials in the form of stress-strain σ-ϵ curves, with σ the longitudinal Cauchy stress, and ϵ the applied deformation at one end of the specimen. Some of these curves are represented for a variety of materials in Figure 3.1, from (Lubliner 2008). By looking at the curves, some important information can be drawn. The first type of behavior exhibited by all the materials in the figure, which is not even visible on the scale of deformation adopted, is the linear elastic behavior. All the materials in Figure 3.1, except annealed copper and soft brass, have a linear elastic behavior that ends at very small deformation values, leaving the place to a highly non-linear response, that is actually the plastic behavior we want to characterize. As seen in the previous section, linear elastic materials can be characterized by only two Lamé parameters λ and μ. Plastic behavior instead requires more attention to the particular aspects we want our model to be able to capture and describe. The following quantities and phenomena are fundamental for the study of plastic behavior of materials, in particular metals, and have their mathematical counterpart in concepts that will be

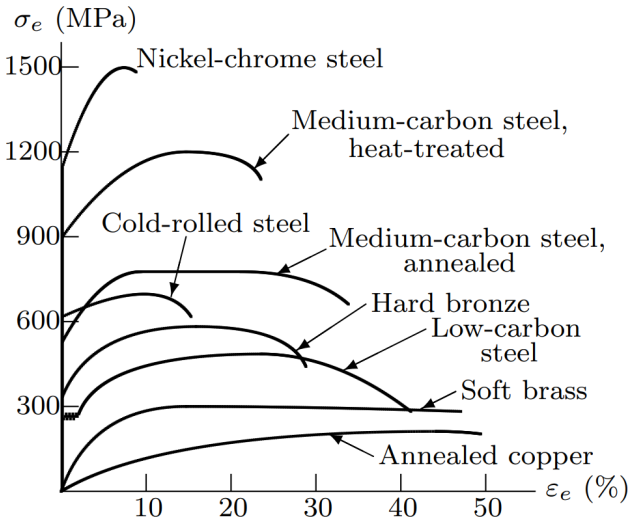

Figure 3.1. From (Lubliner 2008), stress-strain (engineering) curves for various materials. The elastic behavior is not visible since is vertical at this strain-scale. Most of them exhibit a *strain-hardening* behavior.

introduced in the next section, thus a phenomenological explanation is required, and is provided here. The most essentials concept in a theory of macroscopic plasticity are:

- The *elastic range*, that is the interval, in terms of stress σ or strain ϵ, in which the linear elastic Hooke law holds, i.e. the one-dimensional relation $\sigma = E\epsilon$, with E the Young Modulus;

- The *yield stress* is the limit value of the tensile stress above which the response of the material is no more elastic, and *plastic deformation* occurs. The material has overcome its *elastic limit* and, once the stress is reduced to zero (the unload phase is always linear elastic), the strain at the end of the process is different from zero, because the material has gained a *permanent strain*. The permanent strain, that is the plastic residual deformation, is a reflection of the fact that the material structure is rearranged to find a new local equilibrium in its energetic configuration. For many materials, it is not possible to uniquely define a yield stress, since the transition between elastic and plastic behavior does not occur abruptly but continuously. In those cases, a conventional value is adopted, and for such materials the yield stress is indicated as the value of the stress that produces a conventional permanent strain (often 0.2%);

- When the specimen is loaded the first time, it follows the *virgin curves* in Figure 3.1. If at a certain point the loading process is interrupted, and the specimen is unloaded, the unloading curve is linear, with slope E the Young modulus, hence elastic. When the specimen is reloaded, it follows the virgin

curve again up to the stress at which the loading was interrupted the first time, which acts as a new yield stress. This increase of stress with plastic deformation is called *work-hardening* or *strain-hardening*, and it can occur up until a point called *ultimate tensile strength*, which is the maximum attainable stress in a tensile test;

- Suppose we have a material with equal tensile and compressive yield stresses. If the same procedure of loading-unloading outlined above is applied, but after the unloading the specimen is compressed, it is found that the yield stress in compression is lower than expected. This fact is known as *Bauschinger effect*, and appears mainly in metals. It is particularly relevant when cyclic loads are involved, whilst can be neglected otherwise.

Many other phenomena can be observed during tensile and compressions tests, such as discontinuous yielding, thermal effects and rate dependent effects. These are not of our interest in the theory and applications presented in this thesis, and for this reason are not introduced.

3.3.1 Thermodynamics with internal variables and constitutive equations

To characterize the behavior of a plastic material, we need some additional quantities with respect to the theory of elasticity. In particular, as we have seen in the introduction, we must be able to describe whether or not the material exhibits *hardening*, or if some phenomena such as the *Bauschinger effect* take place. The behavior of the material in the so called plastic region, outside of the elastic domain, where the material behaves as a purely elastic one, depends on some additional quantities that should be able to reproduce the macroscopic effects of some phenomena occurring at the microscopic scale, which are responsible for the actual plastic deformation of a solid. We may call these quantities *hidden* or *internal variables* and label them $\boldsymbol{\alpha}$. These functions could be scalar, vectorial or tensorial functions, and are exclusively related to plasticity, meaning that are the only quantities characterizing the non-elastic behavior of the material. For this reason, these functions are implicitly related to irreversible processes. Once we have introduced some generic internal variables, it is possible to build a consistent thermodynamic framework taking into account their presence. The concept of thermodynamics with internal variables has been introduced by Onsager in (Onsager 1931) and applied to continuum mechanics by Coleman and Gurtin (Coleman and Morton E Gurtin 1967). To introduce the thermodynamics with internal variables, it is convenient to assume that at any time t, the thermodynamic state at a point in the material, is determined by a certain number of state variables, such as $\{\boldsymbol{\epsilon}, \theta, \boldsymbol{\alpha}\}$, with θ being the absolute temperature[1]. Among these state variables, there are the internal variables $\boldsymbol{\alpha} = \{\alpha_k\}$. This vector may contain,

[1]The dependence on the temperature gradient is disregarded as it contradicts the second principle of thermodynamics (Coleman and Morton E Gurtin 1967)

as we mentioned above, scalar quantities as well as vectorial and tensorial entities. In addition, we must prescribe some constitutive equation on the vector of internal variables, in the form of evolution equation. Here, we will assume that the constitutive equations for the internal variables take the following form, which is equivalent to asking that their evolutions depends solely on the past histories of stress and temperature (Lubliner 1972)

$$\dot{\boldsymbol{\alpha}} = \boldsymbol{F}\left(\boldsymbol{\sigma}, \theta, \boldsymbol{\alpha}\right). \tag{3.45}$$

We then assume a specific free energy of the form

$$f = f\left(\boldsymbol{\epsilon}, \theta, \boldsymbol{\alpha}\right). \tag{3.46}$$

In the present framework, by having in mind the constitutive equation for the stress in an elastic solid, derived as a consequence of the second law of thermodynamics, it is possible to deduce a decomposition for the strain tensor $\boldsymbol{\epsilon}$ which goes under the name of *additive decomposition*. This derivation has been shown originally in (ibid.), and is also present in (Han and Reddy 2012). First of all, let us recall the constitutive equation for the stress tensor,

$$\boldsymbol{\sigma} = \frac{\partial f}{\partial \boldsymbol{\epsilon}}.$$

By introducing the *gibbs free energy* function as the Legendre transformation of the Helmholtz free energy,

$$g\left(\boldsymbol{\sigma}, \theta, \boldsymbol{\alpha}\right) = \boldsymbol{\sigma} : \boldsymbol{\epsilon} - f\left(\boldsymbol{\epsilon}, \theta, \boldsymbol{\alpha}\right), \tag{3.47}$$

the strain tensor is, as a result of derivation,

$$\boldsymbol{\epsilon}(\boldsymbol{\sigma}, \theta, \boldsymbol{\alpha}) = \frac{\partial g(\boldsymbol{\sigma}, \theta, \boldsymbol{\alpha})}{\partial \boldsymbol{\sigma}}. \tag{3.48}$$

As a result of (3.48), we can write, for the strain rate,

$$\dot{\boldsymbol{\epsilon}}(\boldsymbol{\sigma}, \theta, \boldsymbol{\alpha}) = \frac{\partial \boldsymbol{\epsilon}}{\partial \boldsymbol{\sigma}} : \dot{\boldsymbol{\sigma}} + \frac{\partial \boldsymbol{\epsilon}}{\partial \theta}\dot{\theta} + \frac{\partial \boldsymbol{\epsilon}}{\partial \boldsymbol{\alpha}} \cdot \dot{\boldsymbol{\alpha}}.$$

The terms $\frac{\partial \boldsymbol{\epsilon}}{\partial \boldsymbol{\sigma}}$ and $\frac{\partial \boldsymbol{\epsilon}}{\partial \theta}$ are, in general, functions of the whole state $(\boldsymbol{\sigma}, \theta, \boldsymbol{\alpha})$, but for crystalline solids are largely determined by the primary crystal structure and are insensitive to irreversible processes, so that their dependence on the internal variables $\boldsymbol{\alpha}$ can be neglected (Lubliner 1972). Following this assumption,

$$\frac{\partial}{\partial \boldsymbol{\alpha}}\frac{\partial \boldsymbol{\epsilon}}{\partial \boldsymbol{\sigma}} = \frac{\partial}{\partial \boldsymbol{\alpha}}\frac{\partial \boldsymbol{\epsilon}}{\partial \theta} = 0,$$

and, as a consequence, the latter term is a function of the internal variables only,

$$\frac{\partial}{\partial \boldsymbol{\sigma}}\frac{\partial \boldsymbol{\epsilon}}{\partial \boldsymbol{\alpha}} = \frac{\partial}{\partial \theta}\frac{\partial \boldsymbol{\epsilon}}{\partial \boldsymbol{\alpha}} = 0.$$

Thus, we deduced a decomposition for the total strain which is an additive decomposition, [2]

$$\boldsymbol{\epsilon}(\boldsymbol{\sigma}, \theta, \boldsymbol{\alpha}) = \boldsymbol{\epsilon}^e(\boldsymbol{\sigma}, \theta) + \boldsymbol{\epsilon}^p(\boldsymbol{\alpha}), \tag{3.49}$$

were the elastic strain and the plastic strain appear. The elastic strain is linked to the stress via the linear elastic constitutive relation $\boldsymbol{\epsilon}^e = \mathbf{C}^{el\,-1} : \boldsymbol{\sigma}$, whilst the plastic strain $\boldsymbol{\epsilon}^p = \boldsymbol{\epsilon} - \boldsymbol{\epsilon}^e$ is defined for the first time in (3.49) and is one of the basic ingredient of the classical theory of plasticity, which needs a constitutive relation of the form (3.45), that will be determined in the following sections. Even though the additive decomposition can be formally derived as we did above, it is usually assumed to be valid without explanations.

As shown in (Lubliner 1972) and (Han and Reddy 2012), the choice of an additive decomposition of the form (3.49), is compatible with the existence of a free energy density $f(\boldsymbol{\epsilon}, \theta, \boldsymbol{\alpha})$ if and only if f can be decomposed as

$$\begin{aligned} f = f(\boldsymbol{\epsilon}, \boldsymbol{\epsilon}^p, \theta, \boldsymbol{\alpha}) &= f^e(\boldsymbol{\epsilon} - \boldsymbol{\epsilon}^p, \theta) + f^p(\theta, \boldsymbol{\alpha}) \\ &= f^e(\boldsymbol{\epsilon}^e, \theta) + f^p(\theta, \boldsymbol{\alpha}). \end{aligned} \tag{3.50}$$

in fact, using (3.48) and (3.49), we obtain the following relations,

$$\frac{\partial \epsilon^e_{ij}}{\partial \sigma_{kl}} = \frac{\partial \epsilon_{ij}}{\partial \sigma_{kl}} = \frac{\partial}{\partial \sigma_{kl}} \frac{\partial g}{\partial \sigma_{ij}} = \frac{\partial}{\partial \sigma_{ij}} \frac{\partial g}{\partial \sigma_{kl}} = \frac{\partial \epsilon_{kl}}{\partial \sigma_{ij}} = \frac{\partial \epsilon^e_{kl}}{\partial \sigma_{ij}},$$

$$\frac{\partial \epsilon^e_{ij}}{\partial \sigma_{kl}} = \frac{\partial \epsilon^e_{kl}}{\partial \sigma_{ij}}.$$

The latter is a sufficient condition for the existence of a potential, thus we can write

$$\boldsymbol{\epsilon}^e(\boldsymbol{\sigma}, \theta) = \frac{\partial g^e(\boldsymbol{\sigma}, \theta)}{\partial \boldsymbol{\sigma}}. \tag{3.51}$$

Once a potential has been found, we are allowed to make use of the Legendre transformation again, to get

$$f^e(\boldsymbol{\epsilon}^e, \theta) = \boldsymbol{\sigma} : \boldsymbol{\epsilon}^e - g^e(\boldsymbol{\sigma}, \theta), \qquad \boldsymbol{\sigma} = \frac{\partial f^e}{\partial \boldsymbol{\epsilon}^e}. \tag{3.52}$$

By substituting (3.52) into (3.47), using (3.49), one has the decomposition for the gibbs free energy

$$\begin{aligned} g(\boldsymbol{\sigma}, \theta, \boldsymbol{\alpha}) &= g^e(\boldsymbol{\sigma}, \theta) + \boldsymbol{\sigma} : \boldsymbol{\epsilon}^p + f^e(\boldsymbol{\epsilon}^e, \theta) - f(\boldsymbol{\epsilon}, \theta, \boldsymbol{\alpha}) \\ &= g^e(\boldsymbol{\sigma}, \theta) + \boldsymbol{\sigma} : \boldsymbol{\epsilon}^p - f^p(\theta, \boldsymbol{\alpha}), \end{aligned} \tag{3.53}$$

where a non-elastic contribution $f^p(\theta, \boldsymbol{\alpha})$ to the Helmholtz free energy has been defined, leading us to the above mentioned decomposition for the Helmholtz free

[2] This is not the only possible decomposition. In the more general context of large or finite deformation plasticity, the multiplicative decomposition is often used, where the total deformation gradient $\mathbf{F}$ takes the form $\mathbf{F} = \mathbf{F}^e\mathbf{F}^p$. This is usually referred to as *Kröner decomposition* (Morton E Gurtin et al. 2010).

energy (3.50). The function $f^p(\theta, \boldsymbol{\alpha})$ indeed depends only on the internal variables and absolute temperature, since

$$\boldsymbol{\epsilon} = \frac{\partial g}{\partial \boldsymbol{\sigma}} = \frac{\partial g^e}{\partial \boldsymbol{\sigma}} + \boldsymbol{\epsilon}^p - \frac{\partial f^p}{\partial \boldsymbol{\sigma}} = \boldsymbol{\epsilon}^e + \boldsymbol{\epsilon}^p$$

implies

$$\frac{\partial f^p}{\partial \boldsymbol{\sigma}} = 0.$$

The entropy definition in terms of thermodynamic potential (3.41) still holds with no differences,

$$s = -\frac{\partial f(\boldsymbol{\epsilon}, \theta, \boldsymbol{\alpha})}{\partial \theta}. \tag{3.54}$$

Before continuing our analysis, we rewrite the Helmholtz free energy decomposition here, which is the basis of what follows:

$$\begin{aligned} f = f(\boldsymbol{\epsilon}, \boldsymbol{\epsilon}^p, \theta, \boldsymbol{\alpha}) &= f^e(\boldsymbol{\epsilon} - \boldsymbol{\epsilon}^p, \theta) + f^p(\theta, \boldsymbol{\alpha}) \\ &= f^e(\boldsymbol{\epsilon}^e, \theta) + f^p(\theta, \boldsymbol{\alpha}). \end{aligned} \tag{3.55}$$

In the rhs of (3.55), the former term is the classical free energy for a thermo-elastic material, f^e, depending only on elastic strains and temperature; while the latter is the one carrying information about irreversible processes, f^p.

Our objective is now to derive a dissipation inequality for a material with internal variables, to be able to apply the Coleman-Noll procedure presented in section 3.2.2 and obtain physically acceptable constitutive equations for the evolution of the internal variables and the plastic strain (3.45), (3.49). To this aim, we shall apply the second law of Thermodynamics in the form of Clausius-Duhem inequality (3.38). Let us first recall equation (3.38):

$$\boldsymbol{\sigma} : \boldsymbol{\epsilon} - \frac{\mathbf{q}_e}{\theta} \cdot \nabla\theta - (\dot{f} + \dot{\theta} s) \geq 0. \tag{3.56}$$

we need a way to express the total derivative $\dot{f}$,

$$\begin{aligned} \dot{f}(\boldsymbol{\epsilon}, \boldsymbol{\epsilon}^p, \theta, \boldsymbol{\alpha}) &= \frac{\partial f^e}{\partial \boldsymbol{\epsilon}} : \dot{\boldsymbol{\epsilon}} + \frac{\partial f^e}{\partial \boldsymbol{\epsilon}^p} : \dot{\boldsymbol{\epsilon}^p} + \frac{\partial f^p}{\partial \boldsymbol{\alpha}} \cdot \dot{\boldsymbol{\alpha}} + \frac{\partial f}{\partial \theta}\dot{\theta} \\ &= \frac{\partial f^e}{\partial \boldsymbol{\epsilon}^e} : \frac{\partial \boldsymbol{\epsilon}^e}{\partial \boldsymbol{\epsilon}} : \dot{\boldsymbol{\epsilon}} + \frac{\partial f^e}{\partial \boldsymbol{\epsilon}^e} : \frac{\partial \boldsymbol{\epsilon}^e}{\partial \boldsymbol{\epsilon}^p} : \dot{\boldsymbol{\epsilon}^p} + \frac{\partial f^p}{\partial \boldsymbol{\alpha}} \cdot \dot{\boldsymbol{\alpha}} + \frac{\partial f}{\partial \theta}\dot{\theta} \\ &= \frac{\partial f^e}{\partial \boldsymbol{\epsilon}^e} : \dot{\boldsymbol{\epsilon}} - \frac{\partial f^e}{\partial \boldsymbol{\epsilon}^e} : \dot{\boldsymbol{\epsilon}^p} + \frac{\partial f^p}{\partial \boldsymbol{\alpha}} \cdot \dot{\boldsymbol{\alpha}} + \frac{\partial f}{\partial \theta}\dot{\theta}. \end{aligned} \tag{3.57}$$

After substituting (3.57) in (3.56) we get to the inequality

$$\left(\boldsymbol{\sigma} - \frac{\partial f^e}{\partial \boldsymbol{\epsilon}^e}\right) : \boldsymbol{\epsilon} - \frac{1}{\theta}\mathbf{q}_e \cdot \nabla\theta + \frac{\partial f^e}{\partial \boldsymbol{\epsilon}^e} : \dot{\boldsymbol{\epsilon}^p} - \frac{\partial f^p}{\partial \boldsymbol{\alpha}} \cdot \dot{\boldsymbol{\alpha}} - \left(\frac{\partial f}{\partial \theta} + s\right) \geq 0. \tag{3.58}$$

Here, applying the Coleman-Noll procedure and invoking the constitutive axioms introduced by Truesdell, we can immediately recognize the fact that some constitutive relations are already known, so that it is possible to substitute them in the inequality (3.58). In particular, we know from Section 3.2.2 and (3.52)

$$\boldsymbol{\sigma} = \frac{\partial f^e}{\partial \boldsymbol{\epsilon}^e}. \tag{3.59}$$

Then, from standard Thermodynamics relations mentioned before, we know

$$s = -\frac{\partial f}{\partial \theta}. \tag{3.60}$$

Finally, adopting Fourier law for the heat flux,

$$\mathbf{q}_e = -k\nabla\theta. \tag{3.61}$$

Thus, we end up with the final form of the Clausius-Duhem inequality for a thermo-elastoplastic material with internal variables

$$\frac{k}{\theta}\left|\nabla\theta\right|^2 + \boldsymbol{\sigma} : \dot{\boldsymbol{\epsilon}}^p - \mathbf{A}\cdot\dot{\boldsymbol{\alpha}} \geq 0, \tag{3.62}$$

where we have defined

$$\mathbf{A} = \frac{\partial f^p}{\partial \boldsymbol{\alpha}}. \tag{3.63}$$

In case it is possible to neglect thermal effects, as we will assume throughout the remainder of the thesis, (3.62) becomes

$$\mathcal{D}^p\left(\boldsymbol{\sigma}, \mathbf{A}; \dot{\boldsymbol{\epsilon}}^p, \dot{\boldsymbol{\alpha}}\right) = \boldsymbol{\sigma} : \dot{\boldsymbol{\epsilon}}^p - \mathbf{A}\cdot\dot{\boldsymbol{\alpha}} \geq 0. \tag{3.64}$$

From eq. (3.64), which is the definition of the *plastic dissipation function*, it is evident how $\boldsymbol{\sigma}$ and $\mathbf{A}$ are both thermodynamic forces associated respectively with the plastic strain and the internal variables. The difference between the actual case and the previously analyzed ones, is that here we do not have to prescribe some constitutive equations for the thermodynamic forces $\boldsymbol{\sigma}$ and $\mathbf{A}$, which are already determined by previous relations. Instead, we must find an expression for the evolution of the internal variables and the plastic strain, $\dot{\boldsymbol{\alpha}}$ and $\dot{\boldsymbol{\epsilon}}^p$. This is the reason why we are looking for constitutive equations in the form

$$\dot{\boldsymbol{\epsilon}}^p = \mathbf{R}(\boldsymbol{\sigma}, \mathbf{A}), \tag{3.65}$$

$$\dot{\boldsymbol{\alpha}} = \mathbf{H}(\boldsymbol{\sigma}, \mathbf{A}). \tag{3.66}$$

In general, we cannot disregard the dependence of the functions (3.65)-(3.66) on both the associated thermodynamic forces $\boldsymbol{\sigma}$ and $\mathbf{A}$, so that our choice of $\mathbf{R}(\boldsymbol{\sigma}, \mathbf{A})$ and $\mathbf{H}(\boldsymbol{\sigma}, \mathbf{A})$ must both satisfy the *dissipation inequality* (3.64) at once. As a consequence of this fact, the plastic work rate $\boldsymbol{\sigma} : \dot{\boldsymbol{\epsilon}}^p$ in (3.64) may be negative, without violating the second law of thermodynamics, if the term $-\mathbf{A}\cdot\dot{\boldsymbol{\alpha}}$ is large enough to compensate for that. This is a situation which usually takes place in biochemical processes, as noted in Chapter 1 of (Lubliner 2008). In the literature, the constitutive equations in rate form (3.65)-(3.66) are usually referred to as *Flow rule* and *Hardening law*, respectively.

Before entering the discussion regarding the constitutive modeling of an elasto-plastic material, we shall note that both the plastic strain rate $\dot{\boldsymbol{\epsilon}}^p$ and the rate of internal variables $\dot{\boldsymbol{\alpha}}$ should be non-zero only when plastic deformation occurs,

i.e. when the material behaves no more as a linear elastic one, and vanish otherwise. For this reason, we have to define an elastic domain, in which the material behaves elastically, and a region, which will be the boundary of the elastic domain, where plastic flow occurs and both plastic strain and internal variables are non-zero functions.

3.3.2 The yield function and elastic domain

In classical plasticity, the states which are admissible by the material are only those included in the elastic range, or elastic domain, and its boundary. The elastic domain is in fact defined as the interior of the set of all the admissible states, and its boundary is called yield function. In many practical applications involving ductile materials, such as metals, the von Mises yield function is used, which is related to the well known criterion for ductile materials.

In the elastic domain, the linear elasticity equations hold, while the *plastic flow*, as stated in the previous Section 3.3.1 takes place only when the state of the material, characterized by its stresses and *hardening thermodynamic forces* $\mathbf{A}$, lies on the yield function.

Let us start introducing the state of a material as characterized by a pair $(\boldsymbol{\sigma}, \mathbf{A}) \in \mathbb{S} \times \mathbb{R}^m$, where $\mathbb{S}$ is the space of second-order tensors and $\mathbb{R}^m$ is the vectorial space where the vector of internal variables $\boldsymbol{\alpha}$ and the hardening thermodynamic forces $\mathbf{A}$ live. We then define *yield function* a generic function

$$\Phi\left(\boldsymbol{\sigma}, \mathbf{A}\right) : \mathbb{S} \times \mathbb{R}^m \to \mathbb{R}, \tag{3.67}$$

and the set of *admissible states* as the **closed** set of states that verify the condition $\Phi(\boldsymbol{\sigma}, \boldsymbol{\alpha}) \leq 0$,

$$\mathbb{E}_{\boldsymbol{\sigma},\mathbf{A}} := \left\{(\boldsymbol{\sigma}, \mathbf{A}) \in \mathbb{S} \times \mathbb{R}^m \,|\, \Phi(\boldsymbol{\sigma}, \mathbf{A}) \leq 0\right\}. \tag{3.68}$$

The *elastic domain* is therefore defined as the interior of the set of admissible states,

$$\text{int}(\mathbb{E}_{\boldsymbol{\sigma},\mathbf{A}}) := \left\{(\boldsymbol{\sigma}, \mathbf{A}) \in \mathbb{S} \times \mathbb{R}^m \,|\, \Phi(\boldsymbol{\sigma}, \mathbf{A}) < 0\right\}. \tag{3.69}$$

Finally, the boundary of the elastic domain is called *yield surface*, and is the set of all states that satisfy the equality $\Phi(\boldsymbol{\sigma}, \mathbf{A}) = 0$,

$$\partial\mathbb{E}_{\boldsymbol{\sigma},\mathbf{A}} := \left\{(\boldsymbol{\sigma}, \mathbf{A}) \in \mathbb{S} \times \mathbb{R}^m \,|\, \Phi(\boldsymbol{\sigma}, \mathbf{A}) = 0\right\}. \tag{3.70}$$

All the states outside $\mathbb{E}_{\boldsymbol{\sigma},\mathbf{A}}$ are *non-admissible* and are ruled out in classical plasticity.

3.3.3 The principle of maximum plastic dissipation

Since now, we have introduced some basic concepts for the theory of classical plasticity. In the first Section 3.3.1, we have described the general framework of thermodynamics with internal variables, deriving a decomposition for both the total strain tensor and the Helmholtz free energy density function, that allowed

us to obtain a form of the second principle of thermodynamics suitable for solving the problem of finding a constitutive relation. Then, we defined those quantities which are responsible for the inelastic behavior of material, the plastic strain $\boldsymbol{\epsilon}^p$ and the hardening variables $\boldsymbol{\alpha}$, and we realized the need of a constitutive equation for them, in the form of evolution equations. Finally, in Section 3.3.2, we introduced the notion of yield function, yield surface and elastic domain, as fundamental components of the set of admissible states. We have not yet discussed about any real assumption regarding the inelastic and irreversible behavior of solids, and it is time to do it. The fundamental principle in our exposition of the classical theory of plasticity is the *postulate of maximum plastic dissipation*. It has been historically obtained as a consequence of other alternative postulates, in particular the one on stability due to Drucker (Drucker 1957), but we decided to take it as a postulate in this thesis, thanks to its generality, and the possibility to conveniently apply it to our framework. It can also be justified on physical grounds by appealing to the behavior of crystals undergoing plastic deformation.

The *postulate of maximum plastic dissipation* states that:
For a given and fixed couple $\{\dot{\boldsymbol{\epsilon}}^p, \dot{\boldsymbol{\alpha}}\}$*, among all the* ***admissible*** *states* $\{\boldsymbol{\tau}, \mathcal{A}\}$*, the plastic dissipation function* (3.64) *attains its maximum for the actual state* $\{\boldsymbol{\sigma}, \mathbf{A}\}$*,*

$$\mathcal{D}^p\left(\boldsymbol{\sigma}, \mathbf{A}; \dot{\boldsymbol{\epsilon}}^p, \dot{\boldsymbol{\alpha}}\right) = \max_{(\boldsymbol{\tau}, \mathcal{A}) \in \mathbb{E}_{\sigma, \mathbf{A}}} \left\{\mathcal{D}^p\left(\boldsymbol{\tau}, \mathcal{A}; \dot{\boldsymbol{\epsilon}}^p, \dot{\boldsymbol{\alpha}}\right)\right\}, \tag{3.71}$$

where $\mathbb{E}_{\sigma, \mathbf{A}}$ is the closure of the elastic domain, i.e. the set of all admissible states.

Solving this maximization problem leads to fundamental results in the theory of plasticity. It can be regarded as an optimization problem with constraints expressed with inequalities (the set of admissible states), and can be transformed into an unconstrained minimization problem of some generalized lagrangian functional whose optimal point is a saddle point. These kind of optimization problems have been studied for the first time by Karush (Karush 1939) and Kuhn and Tucker (Kuhn and Tucker 2014), and the procedure to solve them is indeed a generalization of the method of Lagrange multipliers. The Karush–Kuhn–Tucker (KKT) conditions are necessary conditions for the optimization problem introduced above. Additional information can be found in Chapter 11 of (Luenberger, Ye, et al. 1984).

Introducing the KKT multipliers $\gamma \geq 0$, it is possible to transform the constrained maximization problem into an unconstrained minimization problem by defining a lagrangian functional

$$\mathcal{L}^p\left(\boldsymbol{\tau}, \mathcal{A}, \gamma; \dot{\boldsymbol{\epsilon}}^p, \dot{\boldsymbol{\alpha}}\right) := -\boldsymbol{\tau} : \dot{\boldsymbol{\epsilon}}^p + \mathcal{A} \cdot \dot{\boldsymbol{\alpha}} + \gamma \Phi(\boldsymbol{\tau}, \mathcal{A}), \tag{3.72}$$

where $\Phi(\boldsymbol{\tau}, \mathcal{A})$ is the yield function and we are searching for a solution in the set of all admissible states, which satisfy the condition $\Phi(\boldsymbol{\tau}, \mathcal{A}) \leq 0$. The KKT

procedure leads to the following results,

$$\frac{\partial \mathcal{L}^p\left(\boldsymbol{\sigma}, \mathbf{A}, \gamma; \dot{\boldsymbol{\epsilon}^p}, \dot{\boldsymbol{\alpha}}\right)}{\partial \boldsymbol{\tau}} = -\dot{\boldsymbol{\epsilon}^p} + \gamma \nabla_{\boldsymbol{\tau}} \Phi(\boldsymbol{\sigma}, \mathbf{A}) = 0 \tag{3.73}$$

$$\frac{\partial \mathcal{L}^p\left(\boldsymbol{\sigma}, \mathbf{A}, \gamma; \dot{\boldsymbol{\epsilon}^p}, \dot{\boldsymbol{\alpha}}\right)}{\partial \mathcal{A}} = \dot{\boldsymbol{\alpha}} + \gamma \nabla_{\mathcal{A}} \Phi(\boldsymbol{\sigma}, \mathbf{A}) = 0 \tag{3.74}$$

$$\begin{aligned} \gamma &\geq 0 \\ \Phi(\boldsymbol{\sigma}, \mathbf{A}) &\leq 0 \\ \gamma \Phi(\boldsymbol{\sigma}, \mathbf{A}) &= 0. \end{aligned} \tag{3.75}$$

Hence, the implications of the principle of maximum plastic dissipation are:

1. *Associativity* of the flow rule and hardening law (3.73)-(3.74).
2. The three Karush–Kuhn–Tucker necessary conditions (3.75), which are usually referred to as the *loading-unloading conditions*, as will be clear in subsequent sections.
3. The *convexity* of the closed set of admissible states $\mathbb{E}_{\sigma,\mathbf{A}}$.

Associativity of the constitutive equations

From (3.73) and (3.74) follow the two constitutive relations for the evolution of plastic strain and the internal variables:

$$\dot{\boldsymbol{\epsilon}^p} = \gamma \frac{\partial \Phi}{\partial \boldsymbol{\sigma}}, \tag{3.76}$$

$$\dot{\boldsymbol{\alpha}} = -\gamma \frac{\partial \Phi}{\partial \mathbf{A}}. \tag{3.77}$$

The former is usually called flow rule, whilst the latter is referred to as hardening law. This particular choice of constitutive equations, which in our case is a consequence of the postulate of maximum plastic deformation, is very often assumed *a priori*, since it is a very convenient form. In general, this choice is part of a broader class of constitutive relations derived from a *plastic potential*. The starting point of such an approach is to postulate the existence of a plastic potential with the form

$$\Psi = \Psi(\boldsymbol{\sigma}, \mathbf{A}) : \mathbb{S} \times \mathbb{R}^m \to \mathbb{R} \tag{3.78}$$

such that,

$$\dot{\boldsymbol{\epsilon}^p} = \mathbf{R}(\boldsymbol{\sigma}, \mathbf{A}) = \gamma \frac{\partial \Psi}{\partial \boldsymbol{\sigma}}, \tag{3.79}$$

$$\dot{\boldsymbol{\alpha}} = \mathbf{H}(\boldsymbol{\sigma}, \mathbf{A}) = -\gamma \frac{\partial \Psi}{\partial \mathbf{A}}. \tag{3.80}$$

In this context, the flow potential is required to be a non-negative convex function of both $\boldsymbol{\sigma}$ and $\mathbf{A}$, and have zero value at the origin, $\Psi(\mathbf{0}, \mathbf{0}) = 0$. These conditions are sufficient to ensure that the Clausius-Duhem inequality (3.64) is satisfied by

the evolution equations. In this framework, a convenient choice for the plastic potential is

$$\Psi = \Phi, \tag{3.81}$$

where Φ is the yield function. The corresponding model is then called an *associative plasticity* model, because it *associates* the plastic potential with the yield function. This is the constitutive relation that we will adopt for the evolution of plastic quantities throughout this thesis, since it works particularly well for ductile metals, but it is not the only possible choice. We recall the fact that postulating the maximum plastic dissipation, the associative flow rules have been derived as a consequence.

Karush-Kuhn-Tucker (KKT) conditions

The equations (3.75) are necessary conditions for the Karush-Kuhn-Tucker theorem. In mathematical optimization theory they are usually presented as:

1. *primal feasibility* condition
$$\Phi(\boldsymbol{\sigma}, \mathbf{A}) \leq 0, \tag{3.82}$$
in our context is the set of admissible states expressed by means of he yield function, which represents the constraint.

2. *dual feasibility* condition
$$\gamma \geq 0, \tag{3.83}$$
which states that the Lagrange or KKT multipliers, in our framework called *consistency parameter plastic multiplier*, being non-negative.

3. *Complementary slackness*
$$\gamma \Phi(\boldsymbol{\sigma}, \mathbf{A}) = 0. \tag{3.84}$$
This is the complementarity condition for a plastic material, and states that the plastic multiplier γ and, consequently due to (3.76) and (3.77), the plastic strain rate $\dot{\boldsymbol{\epsilon}}^p$ and the rate of internal variables $\dot{\boldsymbol{\alpha}}$ vanish within the elastic domain
$$\Phi(\boldsymbol{\sigma}, \mathbf{A}) < 0 \implies \gamma = 0 \implies \dot{\boldsymbol{\epsilon}}^p = \dot{\boldsymbol{\alpha}} = \mathbf{0},$$
and conversely, the plastic flow may occur only when the state lives on the yield surface, the boundary of the set of admissible states,
$$\Phi(\boldsymbol{\sigma}, \mathbf{A}) = 0 \implies \gamma > 0$$

In addition to the necessary conditions for the KKT theorem, the following consistency condition may be established

$$\gamma \dot{\Phi}(\boldsymbol{\sigma}, \mathbf{A}) = 0, \qquad \text{if} \quad \Phi(\boldsymbol{\sigma}, \mathbf{A}) = 0. \tag{3.85}$$

The consistency condition (3.85) follows from the fact that, if the current state $\{\boldsymbol{\sigma}, \mathbf{A}\}$ lies on the yield surface and plastic flow occurs, $\Phi(\boldsymbol{\sigma}, \mathbf{A}) = 0$, then the time derivative of $\Phi(\boldsymbol{\sigma}, \mathbf{A})$ cannot be positive (Simo and Hughes 2006),

$$\dot{\Phi}(\boldsymbol{\sigma}, \mathbf{A}) \leq 0. \tag{3.86}$$

Furthermore, when yielding is occurring, $\gamma \neq 0$,

$$\dot{\Phi}(\boldsymbol{\sigma}, \mathbf{A}) = 0, \tag{3.87}$$

since the state keeps living instantaneously on the yield surface $\partial \mathbb{E}_{\boldsymbol{\sigma}, \mathbf{A}}$.

Let us now analyze the previous results in terms of elastoplastic behavior of solids, identifying more in detail all possible scenarios that could occur:

- In case the state $(\boldsymbol{\sigma}, \mathbf{A})$ is in the elastic domain, then $\Phi(\boldsymbol{\sigma}, \mathbf{A}) < 0$ holds, and the plastic multiplier $\gamma = 0$, in fact from (3.84)

  $$\gamma \Phi = 0 \quad \text{and} \quad \Phi < 0 \implies \gamma = 0 \tag{3.88}$$

  In this case the state is actually elastic and there is no plastic flow, so that

  $$\dot{\boldsymbol{\epsilon}}^p = \mathbf{0}, \quad \dot{\boldsymbol{\alpha}} = \mathbf{0}. \tag{3.89}$$

  This response is called *instantaneously elastic*.

- If the stress state lies on the yield surface, on the boundary of the admissibility range, then $\Phi(\boldsymbol{\sigma}, \mathbf{A}) = 0$. The complementarity condition (3.84) is automatically satisfied even if $\gamma > 0$. Two situations can arise, leading to a positive or null value for the plastic multiplier γ.

  – If $\dot{\Phi}(\boldsymbol{\sigma}, \mathbf{A}) < 0$, from the consistency condition (3.85) we can conclude that

  $$\gamma \dot{\Phi} = 0 \quad \text{and} \quad \dot{\Phi} < 0 \implies \gamma = 0. \tag{3.90}$$

  Thus again no plastic deformation occurs and $\dot{\boldsymbol{\epsilon}}^p = \dot{\boldsymbol{\alpha}} = 0$, but since we are on the boundary of the admissibility range, this response is called *unloading from a plastic state*.

  – If $\dot{\Phi}(\boldsymbol{\sigma}, \mathbf{A}) = 0$, the consistency condition (3.85) is automatically satisfied, and we have again two possibilities. One in which $\gamma > 0$ and there occurs plastic flow so that $\dot{\boldsymbol{\epsilon}}^p \neq 0$ and $\dot{\boldsymbol{\alpha}} \neq 0$ and the situation is called *plastic loading*. The other one when $\gamma = 0$ goes under the name of *neutral loading*.

All these cases can be efficiently summarized in the following table:

$$\begin{cases} \Phi < 0 \iff (\boldsymbol{\sigma}, \mathbf{A}) \in \operatorname{int}(\mathbb{E}_{\boldsymbol{\sigma}, \mathbf{A}}) \implies \gamma = 0 \\ \Phi = 0 \iff (\boldsymbol{\sigma}, \mathbf{A}) \in \partial \mathbb{E}_{\boldsymbol{\sigma}, \mathbf{A}} \begin{cases} \dot{\Phi} < 0 \implies \gamma = 0 \\ \dot{\Phi} = 0 \text{ and } \gamma = 0 \\ \dot{\Phi} = 0 \text{ and } \gamma > 0 \end{cases} \end{cases} \tag{3.91}$$

Convexity of the set of admissible states

The final result of the postulate of maximum plastic dissipation is the convexity of the yield function and of the set of admissible states $\mathbb{E}_{\sigma,\mathbf{A}}$. The proof of this is given in (Simo and Hughes 2006), and we will briefly summarize some details. The postulate of maximum plastic dissipation implies, for the actual state $\{\boldsymbol{\sigma}, \mathbf{A}\} \in \partial\mathbb{E}_{\sigma,\mathbf{A}}$ occurring in the material ($\{\boldsymbol{\tau}, \mathcal{A}\} \in \mathbb{E}_{\sigma,\mathbf{A}}$)

$$\mathcal{D}^p\left(\boldsymbol{\sigma}, \mathbf{A}; \dot{\boldsymbol{\epsilon}}^p, \dot{\boldsymbol{\alpha}}\right) \geq \mathcal{D}^p\left(\boldsymbol{\tau}, \mathcal{A}; \dot{\boldsymbol{\epsilon}}^p, \dot{\boldsymbol{\alpha}}\right), \tag{3.92}$$

$$\boldsymbol{\sigma} : \dot{\boldsymbol{\epsilon}}^p - \mathbf{A} \cdot \dot{\boldsymbol{\alpha}} \geq \boldsymbol{\tau} : \dot{\boldsymbol{\epsilon}}^p - \mathcal{A} \cdot \dot{\boldsymbol{\alpha}}, \tag{3.93}$$

$$(\boldsymbol{\tau} - \boldsymbol{\sigma}) : \dot{\boldsymbol{\epsilon}}^p - (\mathcal{A} - \mathbf{A}) \cdot \dot{\boldsymbol{\alpha}} \leq 0, \tag{3.94}$$

which can be arranged, having in mind the the associative flow rules developed in Section 3.3.3, as

$$(\boldsymbol{\tau} - \boldsymbol{\sigma}) : \gamma \frac{\partial \Phi}{\partial \boldsymbol{\sigma}} + (\mathcal{A} - \mathbf{A}) \gamma \frac{\partial \Phi}{\partial \mathbf{A}} \leq 0. \tag{3.95}$$

By using then the complementarity condition (3.84), the latter inequality can be expressed as

$$(\boldsymbol{\tau} - \boldsymbol{\sigma}) : \gamma \frac{\partial \Phi}{\partial \boldsymbol{\sigma}} + (\mathcal{A} - \mathbf{A}) \gamma \frac{\partial \Phi}{\partial \mathbf{A}} \leq \gamma \Phi(\boldsymbol{\tau}, \mathcal{A}) \tag{3.96}$$

If $\gamma = 0$, the inequality is satisfied trivially. On the other hand, if $\gamma > 0$, it is possible to cancel γ from (3.96). Then, since $\Phi(\boldsymbol{\sigma}, \mathbf{A}) = 0$, we get to

$$(\boldsymbol{\tau} - \boldsymbol{\sigma}) : \frac{\partial \Phi}{\partial \boldsymbol{\sigma}} + (\mathcal{A} - \mathbf{A}) \frac{\partial \Phi}{\partial \mathbf{A}} \leq \Phi(\boldsymbol{\tau}, \mathcal{A}) - \Phi(\boldsymbol{\sigma}, \mathbf{A}), \tag{3.97}$$

which we shall re-write as

$$\Phi(\boldsymbol{\tau}, \mathcal{A}) \geq \Phi(\boldsymbol{\sigma}, \mathbf{A}) + (\boldsymbol{\tau} - \boldsymbol{\sigma}) : \frac{\partial \Phi}{\partial \boldsymbol{\sigma}} + (\mathcal{A} - \mathbf{A}) \frac{\partial \Phi}{\partial \mathbf{A}}, \tag{3.98}$$

to make evident the fact that (3.98) coincides with the definition of convexity of a multivariable functions. In fact, by recalling the definition of *tangent plane* to a function $f(x, y)$ in a point (x_0, y_0),

$$z = f(x_0, y_0) + \frac{\partial f}{\partial x}(x - x_0) + \frac{\partial f}{\partial y}(y - y_0), \tag{3.99}$$

it is evident how the inequality (3.98) expresses the fact that the yield function, calculated in the generic state $\{\boldsymbol{\tau}, \mathcal{A}\} \in \mathbb{E}_{\sigma,\mathbf{A}}$, is always greater or at least equal to the value of the tangent plane at the same point, which is a necessary and sufficient condition for convexity.

Now that we have discussed all the results and consequences of adopting the postulate of maximum plastic dissipation, it is convenient to clarify that this postulate, and all the corresponding results, are *not* universal. Even though it is true that maximum dissipation has been shown to hold in crystal plasticity and is very successful when applied to metals description, it is not the only possible choice, and in many cases non-associative flow rules are required (for instance, when dealing with soils and granular materials).

3.3.4 The plastic multiplier and the elastoplastic tangent operator

Now that we have determined some thermodynamically consistent constitutive equations for the plastic variables, we shall focus our attention on the determination of the plastic multiplier γ, which is still an unknown function, and on the determination of an *elastoplastic tangent operator*, which will allow us to write a relation valid even under plastic load,

$$\dot{\boldsymbol{\sigma}} = \mathbf{C}^{ep} : \dot{\boldsymbol{\epsilon}} \tag{3.100}$$

with $\mathbf{C}^{ep}$ the above mentioned elastoplastic tangent operator or elastoplastic modulus. Let us start with the determination of the plastic multiplier γ by assuming the state of the material $(\boldsymbol{\sigma}, \mathbf{A})$ lying on the yield surface, such that it is in a plastic state, characterized by $\gamma \neq 0$. We can use the consistency condition (3.85) which, together with the fact that the plastic multiplier is non-zero while yielding occurs, implies the *consistency condition* (3.87)

$$\dot{\Phi} = 0. \tag{3.101}$$

By differentiating the yield function, and considering the consistency condition (3.101), we get

$$\dot{\Phi}\left(\boldsymbol{\sigma}, \mathbf{A}\right) = \frac{\partial \Phi}{\partial \boldsymbol{\sigma}} : \dot{\boldsymbol{\sigma}} + \frac{\partial \Phi}{\partial \mathbf{A}} \cdot \dot{\mathbf{A}} = 0. \tag{3.102}$$

Now, having in mind the stress-strain constitutive equation for an elastic solid

$$\boldsymbol{\sigma} = \mathbf{C}^{el} : \boldsymbol{\epsilon}^{e} \tag{3.103}$$

and the additive decomposition of strain (3.49), recalling the fact that $\mathbf{C}^{el}$ is constant and the associative law (3.76), we obtain

$$\dot{\boldsymbol{\sigma}} = \mathbf{C}^{el} : \left(\dot{\boldsymbol{\epsilon}} - \dot{\boldsymbol{\epsilon}}^{p}\right) = \mathbf{C}^{el} : \left(\dot{\boldsymbol{\epsilon}} - \gamma \partial_{\sigma} \Phi\right). \tag{3.104}$$

In addition, thanks to the definition of $\mathbf{A}$ in terms of the free energy potential (3.63), we can write

$$\dot{\mathbf{A}} = \frac{\partial}{\partial \boldsymbol{\alpha}} \frac{\partial f^{p}}{\partial \boldsymbol{\alpha}} \cdot \dot{\boldsymbol{\alpha}} = -\gamma \frac{\partial}{\partial \boldsymbol{\alpha}} \frac{\partial f^{p}}{\partial \boldsymbol{\alpha}} \cdot \frac{\partial \Phi}{\partial \mathbf{A}}. \tag{3.105}$$

Putting all these relations together into (3.102), we find

$$\dot{\Phi} = \partial_{\sigma} \Phi : \mathbf{C}^{el} : \left(\dot{\boldsymbol{\epsilon}} - \gamma \partial_{\sigma} \Phi\right) - \gamma \partial_{\mathbf{A}} \Phi \cdot \frac{\partial^{2} f^{p}}{\partial \boldsymbol{\alpha}^{2}} \cdot \partial_{\mathbf{A}} \Phi = 0 \tag{3.106}$$

where we used the compact notation

$$\partial_{*}(\cdot) = \frac{\partial(\cdot)}{\partial *}$$

Finally, from (3.106) it is straightforward to obtain a closed analytical expression for the plastic multiplier in case of plastic flow,

$$\gamma = \frac{\left\langle \partial_{\sigma} \Phi : \mathbf{C}^{el} : \dot{\boldsymbol{\epsilon}} \right\rangle}{\partial_{\sigma} \Phi : \mathbf{C}^{el} : \partial_{\sigma} \Phi + \partial_{\mathbf{A}} \Phi \cdot \frac{\partial}{\partial \boldsymbol{\alpha}} \frac{\partial f^{p}}{\partial \boldsymbol{\alpha}} \cdot \partial_{\mathbf{A}} \Phi} \tag{3.107}$$

where the brackets $\langle(\cdot)\rangle$ denote the fact that the plastic multiplier is positive when plastic deformation occurs and vanishes when plastic flow is absent and the material behaves elastically. We use these brackets to denote indeed the ramp function, defined as

$$\langle x \rangle = \frac{x + |x|}{2} \tag{3.108}$$

From eq. (3.107), it is worth noting that

$$\gamma \geq 0 \iff \partial_\sigma \Phi : \mathbf{C}^{el} : \dot{\boldsymbol{\epsilon}} \geq 0 \tag{3.109}$$

which means plastic flow can occur if and only if the angle defined by the inner product between the strain tensor and the normal $\partial_\sigma \Phi$ to the yield surface through the elastic modulus is $\leq 90°$.

Finally, it is possible to derive a general equation for the elastoplastic tangent operator in the case of associative plasticity. In fact, by simply substituting the expression for the plastic multiplier γ (3.107) into the elastic stress-strain equation in rate form (3.104), we get

$$\begin{aligned}
\dot{\boldsymbol{\sigma}} &= \mathbf{C}^{el} : (\dot{\boldsymbol{\epsilon}} - \gamma \partial_\sigma \Phi) \\
&= \mathbf{C}^{el} : \dot{\boldsymbol{\epsilon}} - \gamma \mathbf{C}^{el} : \partial_\sigma \Phi \\
&= \mathbf{C}^{el} : \dot{\boldsymbol{\epsilon}} - \frac{\mathbf{C}^{el} : \partial_\sigma \Phi \otimes \mathbf{C}^{el} : \partial_\sigma \Phi}{\partial_\sigma \Phi : \mathbf{C}^{el} : \partial_\sigma \Phi + \partial_{\mathbf{A}} \Phi \cdot \frac{\partial}{\partial \boldsymbol{\alpha}} \frac{\partial f^p}{\partial \boldsymbol{\alpha}} \cdot \partial_{\mathbf{A}} \Phi} : \dot{\boldsymbol{\epsilon}}
\end{aligned} \tag{3.110}$$

So that the elastoplastic tangent operator is given by

$$\mathbf{C}^{ep} = \begin{cases} \mathbf{C}^{el} & \text{if} \quad \gamma = 0 \\ \mathbf{C}^{el} - \dfrac{\mathbf{C}^{el} : \partial_\sigma \Phi \otimes \mathbf{C}^{el} : \partial_\sigma \Phi}{\partial_\sigma \Phi : \mathbf{C}^{el} : \partial_\sigma \Phi + \partial_{\mathbf{A}} \Phi \cdot \frac{\partial}{\partial \boldsymbol{\alpha}} \frac{\partial f^p}{\partial \boldsymbol{\alpha}} \cdot \partial_{\mathbf{A}} \Phi} & \text{if} \quad \gamma > 0 \end{cases} \tag{3.111}$$

and we can adopt the following rate equation to characterize the behavior of an elastoplastic material,

$$\dot{\boldsymbol{\sigma}} = \mathbf{C}^{ep} : \dot{\boldsymbol{\epsilon}} \tag{3.112}$$

In our case, since we chose an associative law for the evolution of plastic variables, the elastoplastic tangent operator is also symmetric, due to the symmetries of $\mathbf{C}^{el} = \frac{\partial}{\partial \boldsymbol{\epsilon}^e} \frac{\partial f^e}{\partial \boldsymbol{\epsilon}^e}$.

3.4 Von Mises plasticity

Until now we have determined a thermodynamically consistent procedure to characterize the plastic behavior of a material. In addition to this, we made use of the postulate of maximum plastic dissipation to find a precise form for the constitutive relations called *flow rules*. The Karush-Kuhn-Tucker necessary conditions (3.75) associated with the maximization problem of plastic dissipation express some constraint that our problem must satisfy, and this allowed us to characterize

all possible plastic behavior that could occur. We found a way to determine the plastic multiplier γ and, consequently, the elastoplastic tangent modulus which correlates the total strain occurring in the material with the resulting total stress. It is convenient to summarize the main results of our analysis in the following box:

Additive strain tensor decomposition

$$\boldsymbol{\epsilon}(\boldsymbol{\sigma}, \boldsymbol{\alpha}) = \boldsymbol{\epsilon}^e(\boldsymbol{\sigma}) + \boldsymbol{\epsilon}^p(\boldsymbol{\alpha})$$

Helmholtz free energy density decomposition

$$f(\boldsymbol{\epsilon} - \boldsymbol{\epsilon}^p, \boldsymbol{\alpha}) = f^e(\boldsymbol{\epsilon}^e) + f^p(\boldsymbol{\alpha})$$

Set of admissible states and yield function

$$\mathbb{E}_{\sigma,\mathbf{A}} := \{(\boldsymbol{\sigma}, \mathbf{A}) \in \mathbb{S} \times \mathbb{R}^m \,|\, \Phi(\boldsymbol{\sigma}, \mathbf{A}) \leq 0\}$$
$$\Phi(\boldsymbol{\sigma}, \mathbf{A}) \leq 0$$

Associative flow rule and hardening law (for the plastic strain and internal variable evolutions)

$$\dot{\boldsymbol{\epsilon}}^p = \gamma \frac{\partial \Phi}{\partial \boldsymbol{\sigma}} \qquad \dot{\boldsymbol{\alpha}} = -\gamma \frac{\partial \Phi}{\partial \mathbf{A}}$$

Thermodynamic forces constitutive equations

$$\boldsymbol{\sigma} = \frac{\partial f^e}{\partial \boldsymbol{\epsilon}^e} \qquad \mathbf{A} = \frac{\partial f^p}{\partial \boldsymbol{\alpha}}$$

Plastic multiplier

$$\gamma = \frac{\langle \partial_\sigma \Phi : \mathbf{C}^{el} : \dot{\boldsymbol{\epsilon}} \rangle}{\partial_\sigma \Phi : \mathbf{C}^{el} : \partial_\sigma \Phi + \partial_{\mathbf{A}} \Phi \cdot \frac{\partial}{\partial \boldsymbol{\alpha}} \frac{\partial f^p}{\partial \boldsymbol{\alpha}} \cdot \partial_{\mathbf{A}} \Phi}$$

Elastic stress-strain equation

$$\boldsymbol{\sigma} = \mathbf{C}^{el} : \boldsymbol{\epsilon}^e$$
$$\mathbf{C}^{el} = \lambda \mathbf{I} \otimes \mathbf{I} + 2\mu \mathbb{S}$$

Elastoplastic stress-strain rate equation

$$\dot{\boldsymbol{\sigma}} = \mathbf{C}^{ep} : \dot{\boldsymbol{\epsilon}}$$

$$\mathbf{C}^{ep} = \begin{cases} \mathbf{C}^{el} & \text{if} \quad \gamma = 0 \\ \mathbf{C}^{el} - \dfrac{\mathbf{C}^{el} : \partial_\sigma \Phi \otimes \mathbf{C}^{el} : \partial_\sigma \Phi}{\partial_\sigma \Phi : \mathbf{C}^{el} : \partial_\sigma \Phi + \partial_{\mathbf{A}} \Phi \cdot \frac{\partial}{\partial \boldsymbol{\alpha}} \frac{\partial f^p}{\partial \boldsymbol{\alpha}} \cdot \partial_{\mathbf{A}} \Phi} & \text{if} \quad \gamma > 0 \end{cases}$$

By looking at the box, it is evident how the elastoplastic problem is closed once

the total Helmholtz free energy and the yield function are prescribed. The aim of this section is to describe a convenient choice for the yield function, suitable for the description of ductile metals, and some related forms for the free energy. It will lead us to the modeling of the von Mises flow theory of plasticity, with mixed isotropic-kinematic hardening.

3.4.1 The von Mises yield criterion

We shall start our discussion about von Mises plasticity, sometimes also called $\mathcal{J}_2$ flow theory (this name will be clear in a moment), by introducing the von Mises yield criterion. In 1913, Richard von Mises described a criterion to asses when plastic yielding begins, and the subsequent deformation cannot be fully recovered (Mises 1913). According to von Mises, *plastic yielding takes place when the $\mathcal{J}_2$ stress deviator invariant reaches a critical value*. mathematically, this is expressed by

$$\mathcal{J}_2(\boldsymbol{\sigma}_d) = \frac{1}{2}\boldsymbol{\sigma}_d : \boldsymbol{\sigma}_d = R(\alpha), \tag{3.113}$$

where R is the critical value, as a function of a scalar hardening variable α. The physical interpretation underlying the von Mises criterion is that plastic yielding occurs once the *distortional* contribution to the strain energy (i.e. the Helmholtz free energy) reaches a critical value. This is equivalent to assuming that for ductile metals the *volumetric* contribution to the strain energy does not play any role in plastic flow, and only the distortional portion is responsible for that. To clarify why this criterion is connected with the *distortional* strain energy of a linear elastic material, let us decompose the Helmholtz free energy of a linear elastic material (3.11) in its volumetric and distortional contributions. First, we shall recall that every second-order tensor can be decomposed in two parts, the volumetric and deviatoric ones, and that the following holds,

$$\mathbf{T} = \mathbf{T}_v + \mathbf{T}_d, \qquad \mathbf{T}_d = \mathbf{T} - \frac{1}{3}\mathrm{tr}\,(\mathbf{T})\,\mathbf{I} \tag{3.114}$$

$$\mathrm{tr}\,(\mathbf{T}_d) = 0. \tag{3.115}$$

From this follows

$$\begin{aligned} f^e &= \frac{1}{2}\boldsymbol{\epsilon}^e : \mathbf{C}^{el} : \boldsymbol{\epsilon}^e \\ &= \frac{1}{2}\boldsymbol{\sigma} : \boldsymbol{\epsilon}^e \\ &= \frac{1}{2}(\boldsymbol{\sigma}_v + \boldsymbol{\sigma}_d) : (\boldsymbol{\epsilon}^e_v + \boldsymbol{\epsilon}^e_d) \\ &= \frac{1}{2}\left(\boldsymbol{\sigma}_d : \boldsymbol{\epsilon}^e_d + \boldsymbol{\sigma}_v : \boldsymbol{\epsilon}^e_v\right). \end{aligned} \tag{3.116}$$

Now, by using the elastic stress-strain equation (3.12) it is possible to derive, after a few manipulations involving the relations (3.114),

$$\boldsymbol{\sigma}_d = 2\mu\boldsymbol{\epsilon}^e_d, \qquad \mathrm{tr}(\boldsymbol{\sigma}) = (3\lambda + 2\mu)\mathrm{tr}(\boldsymbol{\epsilon}^e). \tag{3.117}$$

Substituting then (3.117) in (3.116), we get

$$\begin{aligned} f^e &= \frac{1}{2}\left(\boldsymbol{\sigma}_d : \boldsymbol{\epsilon}_d^e + \boldsymbol{\sigma}_v : \boldsymbol{\epsilon}_v^e\right) \\ &= \frac{1}{2}\left(\frac{\boldsymbol{\sigma}_d : \boldsymbol{\sigma}_d}{2\mu} + \frac{1}{3}\mathrm{tr}(\boldsymbol{\sigma})\mathrm{tr}(\boldsymbol{\epsilon})\right) \\ &= \frac{\boldsymbol{\sigma}_d : \boldsymbol{\sigma}_d}{4\mu} + \frac{1}{6}\frac{\mathrm{tr}(\boldsymbol{\sigma})^2}{(3\lambda + 2\mu)} = f_d^e + f_v^e \end{aligned} \tag{3.118}$$

with the distortional and volumetric contributions

$$f_d^e = \frac{\boldsymbol{\sigma}_d : \boldsymbol{\sigma}_d}{4\mu} = \frac{1}{2\mu}\mathcal{J}_2(\boldsymbol{\sigma}_d), \qquad f_v^e = \frac{1}{6}\frac{\mathrm{tr}(\boldsymbol{\sigma})^2}{(3\lambda + 2\mu)}. \tag{3.119}$$

The von Mises yield criterion can then be rewritten as

$$f_{d\,crit}^e = \frac{R(\alpha)}{2\mu}. \tag{3.120}$$

This means, assuming the von Mises criterion, that as long as

$$\mathcal{J}_2 - R(\alpha) < 0$$

the material behaves elastically. It defines indeed an elastic range and, consequently, a yield function, which can be written as

$$\Phi(\boldsymbol{\sigma}) = \sqrt{\mathcal{J}_2(\boldsymbol{\sigma}_d)} - \sqrt{R} \leq 0. \tag{3.121}$$

When considering the von Mises criterion, one often refers to uniaxial stress states where $\boldsymbol{\sigma} = \sigma \mathrm{e}_1 \otimes \mathrm{e}_1$. In this framework, the yield function (3.121) is rewritten as

$$\Phi(\boldsymbol{\sigma}) = \sqrt{3\mathcal{J}_2(\boldsymbol{\sigma}_d)} - \sigma_y \leq 0, \tag{3.122}$$

where σ_y is the uniaxial yield stress. It is worth noting that the yield function as defined in (3.121) and (3.122) is *pressure-insensitive*, meaning that, given a pressure p_0, the following relation holds,

$$\Phi(\boldsymbol{\sigma} + p_0\mathbf{I}) = \Phi(\boldsymbol{\sigma}). \tag{3.123}$$

This is true because only the deviator of the stress tensor influences plastic yielding in von Mises plasticity. For this reason, such a model is called *pressure-insensitive* or *plastically incompressible*[3]. The yield function (3.122), which defines the closed set of admissible states, is a cylinder in the stress space, and no hardening variables have been defined yet. This means that the radius of the cylinder is constant,

[3]Plastic incompressibility is a characteristic observed also in the experiments. In particular, in metal forming applications, plastic deformation does not affect the volume of materials (Lubliner 2008).

proportional to σ_y. Since we want to describe situations where the material may exhibit hardening behaviors, we shall allow for the radius of the yield function in stress space to increase while plastic flow is occurring. In addition to this, we may also want to consider phenomena such as the Bauschinger effect, which can be modeled as a translation of the yield function in stress space. All these modifications to the actual yield function (3.122) will be tackled in the next sections. Before entering the discussion about hardening behavior, we shall derive an equation of evolution for the plastic strain, the *flow rule*.

3.4.2 The Prandtl-Reuss associative flow rule

Assuming the von Mises criterion as the yield function, and following the consequences of the postulate of maximum plastic dissipation, we know that the evolution equation for the plastic strain is (3.76)

$$\dot{\boldsymbol{\epsilon}^p} = \gamma \frac{\partial \Phi}{\partial \boldsymbol{\sigma}}. \tag{3.124}$$

The resulting evolution equation is called the Prandtl-Reuss plasticity law (Prandtl 1925)-(Reuss 1932), and can be obtained by taking the derivative of the von Mises yield function (3.122) with respect to the stress tensor,

$$\begin{aligned}
\frac{\partial \Phi}{\partial \boldsymbol{\sigma}} &= \frac{\partial}{\partial \boldsymbol{\sigma}} \sqrt{3 \mathcal{J}_2(\boldsymbol{\sigma}_d(\boldsymbol{\sigma}))} \\
&= \sqrt{\frac{3}{2}} \frac{\partial}{\partial \boldsymbol{\sigma}} \sqrt{\boldsymbol{\sigma}_d : \boldsymbol{\sigma}_d} \\
&= \sqrt{\frac{3}{2}} \frac{\partial \left\| \boldsymbol{\sigma}_d \right\|}{\partial \boldsymbol{\sigma}_d} : \frac{\partial \boldsymbol{\sigma}_d}{\partial \boldsymbol{\sigma}}.
\end{aligned}$$

The derivative of the norm of a second-order tensor $\|\mathbf{T}\| = \sqrt{\mathbf{T} : \mathbf{T}}$ is

$$\frac{\partial \left\| \mathbf{T} \right\|}{\partial \mathbf{T}} = \frac{\mathbf{T}}{\left\| \mathbf{T} \right\|}, \tag{3.125}$$

so that

$$\begin{aligned}
\frac{\partial \Phi}{\partial \boldsymbol{\sigma}} &= \sqrt{\frac{3}{2}} \frac{\boldsymbol{\sigma}_d}{\left\| \boldsymbol{\sigma}_d \right\|} : \frac{\partial \boldsymbol{\sigma}_d}{\partial \boldsymbol{\sigma}} \\
&= \sqrt{\frac{3}{2}} \frac{\boldsymbol{\sigma}_d}{\left\| \boldsymbol{\sigma}_d \right\|} : \frac{\partial}{\partial \boldsymbol{\sigma}} \left(\boldsymbol{\sigma} - \frac{1}{3} \mathrm{tr}(\boldsymbol{\sigma}) \mathbf{I} \right) \\
&= \sqrt{\frac{3}{2}} \frac{\boldsymbol{\sigma}_d}{\left\| \boldsymbol{\sigma}_d \right\|} : \frac{\partial}{\partial \boldsymbol{\sigma}} \left(\boldsymbol{\sigma} - \frac{1}{3} (\boldsymbol{\sigma} : \mathbf{I}) \mathbf{I} \right).
\end{aligned}$$

The derivative of a second-order symmetric tensor with respect to itself is the fourth-order symmetric identity tensor $\mathbb{S}$ (3.10) which maps second-order symmetric tensors to themselves, and whose components are

$$\mathbb{S}_{ijkl} = \frac{1}{2} \left(\delta_{ik} \delta_{jl} + \delta_{il} \delta_{jk} \right). \tag{3.126}$$

With this in mind, and the fact that the second-order identity tensor $\mathbf{I}$ is a constant with respect to σ, we obtain

$$\begin{aligned}\frac{\partial \Phi}{\partial \sigma} &= \sqrt{\frac{3}{2}}\frac{\sigma_d}{\|\sigma_d\|} : \frac{\partial}{\partial \sigma}\left(\sigma - \frac{1}{3}(\sigma : \mathbf{I})\mathbf{I}\right) \\ &= \sqrt{\frac{3}{2}}\frac{\sigma_d}{\|\sigma_d\|} : \left(\mathbb{S} - \frac{1}{3}\frac{\partial(\sigma : \mathbf{I})}{\partial \sigma} \otimes \mathbf{I}\right) \\ &= \sqrt{\frac{3}{2}}\frac{\sigma_d}{\|\sigma_d\|} : \left(\mathbb{S} - \frac{1}{3}\mathbf{I} \otimes \mathbf{I}\right).\end{aligned}$$

In the latter expression, it is possible to recognize, between round brackets, the fourth-order deviator tensor which maps second-order symmetric tensors to their deviatoric part. Since the deviator of the deviatoric stress tensor is the deviatoric stress tensor itself, we obtain

$$\frac{\partial \Phi}{\partial \sigma} = \sqrt{\frac{3}{2}}\frac{\sigma_d}{\|\sigma_d\|} \tag{3.127}$$

$$\dot{\boldsymbol{\epsilon}}^p = \gamma\sqrt{\frac{3}{2}}\frac{\sigma_d}{\|\sigma_d\|}. \tag{3.128}$$

The constitutive associative equation (3.128), and the associative flow rules in general, implies that the plastic strain rate is a tensor *normal to the yield surface* in the space of stresses. In addition, the plastic strain rate and the plastic strain itself are deviatoric tensor, as a consequence of the pressure-insensitivity of the von Mises yield function:

$$\mathrm{tr}\,(\boldsymbol{\epsilon}^p) = 0. \tag{3.129}$$

This condition is referred to as *plastic incompressibility*.

3.4.3 Hardening laws

Once we have determined the evolution equation for the plastic strain, we shall focus our attention in defining some proper internal variables which should be representative of the hardening behavior. In the three-dimensional theory, hardening is represented by changes in the thermodynamic forces $\mathbf{A}$ during plastic yielding. All these changes usually effect the size, shape, orientation and position of the yield surface in the stress space, which, we recall, is defined by the equation $\Phi(\sigma, \mathbf{A}) = 0$

Isotropic hardening

A plasticity model is said to be *isotropic hardening* if the yield surface evolves in such a way that it undergoes an isotropic expansion with respect to the initial yield surface, without translation. The expansion rate may be linear or non-linear. From a physical point of view, the internal variable representing isotropic hardening is intrinsically connected with the density of dislocations, which pile up

and as a result increase the resistance of the material to plastic flow. Generally, the internal variable responsible for this isotropic expansion behavior is a single scalar variable.

We indicate with $\boldsymbol{\alpha} = \alpha^p$ this scalar internal variable, called *equivalent* or *accumulated plastic strain*, and with $\mathbf{A} = \kappa$ the associated thermodynamic force, so that

$$\kappa = \frac{\partial f^p}{\partial \alpha^p}, \tag{3.130}$$

$$\dot{\alpha^p} = -\gamma \frac{\partial \Phi(\boldsymbol{\sigma}, \kappa)}{\partial \kappa}. \tag{3.131}$$

This leads us to defining the plastic potential, which is a function of the internal variables. The simplest form of the plastic potential, which is the plastic portion of the total Helmholtz free energy,

$$f^p(\boldsymbol{\alpha}) = f(\boldsymbol{\epsilon}, \boldsymbol{\epsilon}^p, \boldsymbol{\alpha}) - f^e(\boldsymbol{\epsilon} - \boldsymbol{\epsilon}^p),$$

is a positive-definite quadratic function of the scalar internal variable α^p, for example

$$f^p(\alpha^p) = \frac{1}{2} k_1 \alpha^{p2}, \tag{3.132}$$

with k_1 a constant.

In addition to the definition of the plastic free energy density function, we shall modify our yield function to account for isotropic expansions in the stress space. We do so by allowing for the radius of the yield surface to be a function of the thermodynamic force κ, modifying the uniaxial yield stress as

$$\sigma_y(\kappa) = \sigma_{y0} + \kappa(\alpha^p), \tag{3.133}$$

such that the von Mises yield function becomes

$$\Phi(\boldsymbol{\sigma}, \kappa) = \sqrt{3\mathcal{J}_2(\boldsymbol{\sigma}_d)} - \sigma_y(\kappa). \tag{3.134}$$

After these rather general and simple assumption, we get the final hardening law from equations (3.130)-(3.131),

$$\kappa = k_1 \alpha^p \tag{3.135}$$

$$\sigma_y(\kappa) = \sigma_{y0} + k_1 \alpha^p \tag{3.136}$$

$$\begin{aligned} \dot{\alpha^p} &= -\gamma \frac{\partial \Phi(\boldsymbol{\sigma}, \kappa)}{\partial \kappa}, \\ &= -\gamma \frac{\partial \left(\sqrt{3\mathcal{J}_2(\boldsymbol{\sigma}_d(\boldsymbol{\sigma}))} - \sigma_y(\kappa) \right)}{\partial \kappa}, \\ \dot{\alpha^p} &= \gamma \end{aligned} \tag{3.137}$$

In this context, as mentioned above, the scalar internal variable α^p is called *accumulated plastic strain* because it is actually equivalent to the integral over time of the norm of the plastic strain rate:

$$\dot{\alpha^p} = \gamma \implies \alpha^p(t) = \int_0^t \gamma(\tau)\,\mathrm{d}\tau,$$

and using (3.128),

$$\alpha^p(t) = \int_0^t \sqrt{\frac{2}{3}}\,\|\dot{\epsilon}^p(\tau)\|\,\mathrm{d}\tau. \tag{3.138}$$

It is evident how, given the particular choice of plastic potential (3.132), the resulting model is a *linear hardening* model, with the evolution of the radius of the yield surface which goes linearly with the evolution of the internal variable α^p. More general forms of the plastic potential (3.132) may account for non-linear behavior and hardening limit or saturation, without losing the property of being associative laws.

One possible choice for the plastic potential which leads to a non-linear hardening law (3.133) is the following:

$$f^p(\alpha^p) = \frac{1}{2}k_1\alpha^{p2} + (k_\infty - k_2)(\alpha^p + \delta^{-1}e^{-\delta\alpha^p}). \tag{3.139}$$

The hardening law which can be derived from (3.139) is a non-linear law with a saturation hardening term of the exponential type, as presented in (Voce 1955),

$$\kappa = \frac{\partial f^p}{\partial \alpha^p} = k_1\alpha^p + (k_\infty - k_2)(1 - e^{-\delta\alpha^p}). \tag{3.140}$$

The hardening law (3.137) still holds, since

$$\sigma_y(\kappa) = \sigma_{y0} + \kappa = \sigma_{y0} + k_1\alpha^p + (k_\infty - k_2)(1 - e^{-\delta\alpha^p}),$$
$$\dot{\alpha^p} = -\gamma\frac{\partial\Phi(\sigma,\kappa)}{\partial\kappa} = \gamma.$$

When the isotropic hardening law is absent and $\kappa = 0$, $\dot{\alpha^p} = 0$ the model represents a *perfectly plastic* material, where there is no isotropic hardening and the stress-strain relation is flat, because the radius of the yield surface is fixed and constant.

Kinematic hardening and the Bauschinger effect

A totally different hardening behavior occurs when the material is loaded and hardened in one direction, and then loaded in the opposite direction. Many materials show a decreased resistance to plastic yielding after this operation, with respect to the one they would have had before the experiment. This phenomenon is known as the *Bauschinger effect* and is modelled with the introduction of the kinematic hardening. In the three-dimensional stress space, where the yield function lives, the kinematic hardening is modelled as a translation of the yield surface, with preservation of its shape and without expansion. This corresponds to

the generalization of the motion of the stress-strain curve in a uniaxial test. For this reason, it is justified a yield function of the form

$$\Phi(\sigma, \beta) = \sqrt{3\mathcal{J}_2(\eta(\sigma, \beta))} - \sigma_y \tag{3.141}$$

$$\eta(\sigma, \beta) = \sigma^d - \beta \tag{3.142}$$

derived by the original von Mises yield function by introducing the *relative stress* tensor, as the difference between the stress deviator and the second-order tensor β, which is known with the name of *back-stress* tensor. By definition (3.142), the back-stress tensor is deviatoric, and it is assumed to be the thermodynamic force associated with kinematic hardening $\mathbf{A} = \beta$, representing the translation of the yield surface in stress space. As a result of this adoption, the yield function is now an isotropic function of the *relative stress* η, and when no kinematic hardening occurs, i.e. $\beta = \mathbf{0}$, the von Mises yield function is recovered.

The Prandtl-Reuss flow rule is then generalized to account for kinematic hardening, and takes the form (compare with the calculation made above to derive the classical Prandtl-Reuss equation)

$$\dot{\epsilon^p} = \gamma \frac{\partial \Phi}{\partial \sigma} = \gamma \frac{\partial \Phi}{\partial \eta} = \gamma \sqrt{\frac{3}{2}} \frac{\eta}{\|\eta\|}, \tag{3.143}$$

which is essentially equivalent to equation (3.128), since it prescribes the plastic strain rate being normal to the yield surface in the *relative stress space*, and coincides with (3.128) when $\beta = \mathbf{0}$.

Following the same procedure outlined above when dealing with isotropic hardening modeling, we need to identify a suitable form for the plastic free energy density, to derive an associative kinematic hardening law for the evolution of the internal variable conjugate to the thermodynamic force β. Let us indicate with χ this new internal variable, such that

$$\beta = \frac{\partial f^p}{\partial \chi}, \tag{3.144}$$

$$\dot{\chi} = -\gamma \frac{\partial \Phi(\sigma, \beta)}{\partial \beta}. \tag{3.145}$$

The simplest choice for a plastic potential is given, as before, by a quadratic form in the internal variable χ, except for the fact that now those variables are second-order tensors:

$$f^p(\chi) = \frac{1}{2} k_3 \chi : \chi = \frac{1}{2} k_3 \|\chi\|^2, \tag{3.146}$$

with $k3$ a constant. The kinematic hardening evolution law is then given by

$$\dot{\chi} = -\gamma \frac{\partial \Phi(\sigma, \beta)}{\partial \beta} = \gamma \frac{\partial \Phi(\sigma, \beta)}{\partial \sigma} = \gamma \sqrt{\frac{3}{2}} \frac{\eta}{\|\eta\|}, \tag{3.147}$$

which is equivalent to (3.143), so that $\boldsymbol{\chi} = \boldsymbol{\epsilon}^p$. From (3.146), the equation defining the back-stress tensor is

$$\boldsymbol{\beta} = k_3 \boldsymbol{\chi},$$

and the resulting evolution equation for the back-stress is

$$\dot{\boldsymbol{\beta}} = k_3 \gamma \sqrt{\frac{3}{2}} \frac{\boldsymbol{\eta}}{\|\boldsymbol{\eta}\|}. \tag{3.148}$$

By comparing this result with experimental results for uniaxial tests, the constant k_3 in (3.148) is usually assumed to take the form

$$k_3 = \frac{2}{3} H,$$

with H a material constant called *linear kinematic hardening modulus*, such that, finally

$$\dot{\boldsymbol{\beta}} = \gamma \sqrt{\frac{2}{3}} H \frac{\boldsymbol{\eta}}{\|\boldsymbol{\eta}\|} = \frac{2}{3} H \dot{\boldsymbol{\epsilon}}^p. \tag{3.149}$$

The material constant k_3 or, equivalently, H, may be substituted with a constant positive-definite kinematic hardening fourth-order tensor, containing material constants. This would result in a plastic potential of the form

$$f^p(\boldsymbol{\chi}) = \frac{1}{2} \boldsymbol{\chi} : \mathbf{H} : \boldsymbol{\chi},$$

which adds complexity but does not change the physical linear response of the material. Other non-linear kinematic hardening laws may be used, such as Armstrong-Frederick or nonlinear Prager's rules, but will not be covered in this thesis because they are *non-associative* laws, although they can be derived from a flow potential different from the yield function.

Combined isotropic and kinematic hardening

A mixed model with both isotropic and kinematic hardening can be derived by combining together the results of the two previous sections. The resulting model is able to reproduce both isotropic expansions and translations of the yield surface in the stress space. In addition, to keep the flow rules associative, linear and non-linear isotropic hardening models may be chosen, and the linear kinematic hardening model of Prager can be assumed.

The combined isotropic and kinematic hardening model can be derived as follows:
We assume the hardening internal variables vector to be $\boldsymbol{\alpha} = \{\alpha^p, \boldsymbol{\chi}\}$, where α^p is a scalar representing the accumulated plastic strain of Section 3.4.3, and $\boldsymbol{\chi}$ is a second-order tensor, as in 3.4.3. The conjugate thermodynamic forces vector $\mathbf{A} = \{\kappa, \boldsymbol{\beta}\}$ is then composed by a scalar κ, representing the isotropic expansion of the yield surface in the relative stress space, and a second-order deviatoric tensor $\boldsymbol{\beta}$, the back-stress.

The yield function is a combination of (3.134) and (3.141), and depends on all the thermodynamic forces defined

$$\Phi(\boldsymbol{\sigma}, \boldsymbol{\beta}, \kappa) = \sqrt{3\mathcal{J}_2(\boldsymbol{\eta}(\boldsymbol{\sigma}, \boldsymbol{\beta}))} - \sigma_y(\kappa), \tag{3.150}$$

where the relative stress $\boldsymbol{\eta}$ is, as before, $\boldsymbol{\eta}(\boldsymbol{\sigma}, \boldsymbol{\beta}) = \boldsymbol{\sigma}^d - \boldsymbol{\beta}$. In addition to (3.150), which represents the potential for the flow rules and hardening laws, we can obtain a mixed plastic Helmholtz free energy by combining (3.132) or (3.139) and (3.146). The results would be

$$f^p(\alpha^p, \boldsymbol{\chi}) = \frac{1}{2}k_1\alpha^{p2} + \frac{1}{3}H\,\|\boldsymbol{\chi}\|^2 \tag{3.151}$$

$$f^p(\alpha^p, \boldsymbol{\chi}) = \frac{1}{2}k_1\alpha^{p2} + \frac{1}{3}H\,\|\boldsymbol{\chi}\|^2 + (k_\infty - k_2)(\alpha^p + \delta^{-1}e^{-\delta\alpha^p}) \tag{3.152}$$

Once the key ingredients of the combined isotropic and kinematic hardening have been defined, the constitutive relations come with the usual derivation procedure resulting form the postulate of maximum plastic dissipation. For the flow rule and the hardening laws, we have:

$$\dot{\boldsymbol{\epsilon}}^p = \gamma\frac{\partial\Phi(\boldsymbol{\sigma}, \mathbf{A})}{\partial\boldsymbol{\sigma}}, \qquad \dot{\boldsymbol{\alpha}} = -\gamma\frac{\partial\Phi(\boldsymbol{\sigma}, \mathbf{A})}{\partial\mathbf{A}}, \qquad \mathbf{A} = \frac{\partial f^p}{\partial\boldsymbol{\alpha}}.$$

Resulting in the Prandtl-Reuss equation

$$\dot{\boldsymbol{\epsilon}}^p = \gamma\frac{\partial\Phi(\boldsymbol{\sigma}, \boldsymbol{\beta}, \kappa)}{\partial\boldsymbol{\sigma}} = \gamma\frac{\partial\Phi(\boldsymbol{\sigma}, \boldsymbol{\beta}, \kappa)}{\partial\boldsymbol{\eta}} = \gamma\sqrt{\frac{3}{2}}\frac{\boldsymbol{\eta}}{\|\boldsymbol{\eta}\|}, \tag{3.153}$$

the combined hardening laws

$$\dot{\boldsymbol{\chi}} = -\gamma\frac{\partial\Phi(\boldsymbol{\sigma}, \boldsymbol{\beta}, \kappa)}{\partial\boldsymbol{\beta}} = \gamma\frac{\partial\Phi(\boldsymbol{\sigma}, \boldsymbol{\beta}, \kappa)}{\partial\boldsymbol{\sigma}} = \gamma\sqrt{\frac{3}{2}}\frac{\boldsymbol{\eta}}{\|\boldsymbol{\eta}\|},$$

$$\dot{\alpha^p} = -\gamma\frac{\partial\Phi(\boldsymbol{\sigma}, \boldsymbol{\beta}, \kappa)}{\partial\kappa} = \gamma,$$

and the definition of the thermodynamic forces

$$\boldsymbol{\beta} = \frac{\partial f^p(\alpha^p, \boldsymbol{\chi})}{\partial\boldsymbol{\chi}} = \frac{2}{3}H\boldsymbol{\chi},$$

$$\kappa = \frac{\partial f^p(\alpha^p, \boldsymbol{\chi})}{\partial\alpha^p} = k_1\alpha^p,$$

or

$$\kappa = k_1\alpha^p + (k_\infty - k_2)(1 - e^{-\delta\alpha^p}).$$

Chapter 4

Numerical Formulation

4.1 Introduction

In this chapter, some details regarding the current implementation in numerical codes of the previously described mathematical and physical models is provided. The results presented in following chapters are obtained with finite difference and finite element codes whose structure is outlined in the next sections. The computational modelling of phase-transition problems and general phase-field models is a very challenging task and has been of great interest in the past decades due to the enormous amount of applications related to such models.

The Diffuse Interface model used in this thesis belongs to this framework, and has the same computational issues and characteristics of many other phase-field models, such as the Cahn-Hilliard model. Extensive reviews on computational modelling of phase-field models can be found at (Gomez, Bures, et al. 2019; Gomez and Zee 2018), where the authors analysed, among the others, the Navier-Stokes-Korteweg system of equations. This model suffers from the same main problems present in most of the phase-field theories, that of the spatial discretization and approximation of higher-order terms. The Diffuse Interface model includes in fact third-order spatial derivatives of the density field, that one should take care of in appropriate finite difference and finite element schemes.

From the viewpoint of finite difference approximations, the presence of higher order terms is not a real problem, since the equations are solved directly in their strong formulation, and all possible numerical artifacts vanish once an appropriate scheme is adopted (for a reference on this, see (Didier Jamet et al. 2002)). When dealing with finite element approximations instead, the presence of higher-order terms would formally require a higher degree of continuity on the basis functions (C^1 basis functions for fourth-order problems such as the Cahn-Hilliard model). Meeting this requirement using standard finite element basis can be extremely difficult or even impossible, depending on the dimensionality of the problem and on the domain complexity. For this reason, many different strategies to circumvent the problem can be found in literature. One of the most used in practice is that of splitting the high-order equation into different second-order equations,

resulting in a *mixed finite element method*. This is the strategy adopted in this thesis, and is supported by the literature on high-order problems (such as the bi-harmonic equation, see e.g. (Boffi et al. 2013; Scholz 1978)), general phase-field models (Gomez and Zee 2018) and the Cahn-Hilliard equation (Du and Nicolaides 1991; Elliott et al. 1989). The method has the advantage of being very simple, since it consists in the addition of an equation to the original system, with the only objective of reducing its high-order in spatial derivatives, resulting in a system of PDEs suitable for classical C^0-continuous finite element spaces. The drawbacks of such a treatment is the increase in degrees of freedom related to the addition of a new equation, which can be dramatic for systems with a very large number of DOFs and unknowns, resulting in an overall increase in the computational cost.

Consequently, other procedures have been developed and tested in the years. To solve the Cahn-Hilliard equation, finite volume methods (Cueto-Felgueroso and Jaume Peraire 2008), discontinuous Galerkin formulations (Wells et al. 2006), iso-geometric analysis (Gómez et al. 2008) and meshless methods (Rajagopal et al. 2010) have been adopted. The simulations of isothermal and non-isothermal Navier-Stokes-Korteweg equations have been carried out in a similar way, by using discontinuous Galerkin methods (Diehl 2007; Tian et al. 2015), iso-geometric analysis (Gomez, Hughes, et al. 2010; J. Liu et al. 2015) and finite volume methods with convex-concave energy splitting techniques (Kou and S. Sun 2018). The time discretization adopted in this thesis for the fluid solver is the Crank-Nicolson scheme, a second order scheme to ensure unconditional stability.

For what concerns the finite element discretization of the elasto-plasticity equations, a standard procedure with C^0-continuous basis function was already possible thanks to the nature of the elasticity equations, which is completed by an *elastic predictor-plastic corrector* algorithm for solving the non-linearity introduced by the classical plasticity theory. Details on the numerical implementations are provided in this chapter, which is based on the widely accepted literature on the topic (Lubliner 2008; Simo and Hughes 2006; Souza Neto et al. 2011). The inertial contribution, when present, is treated with a fully implicit Newmark method to ensure unconditional stability (details can be found at (Newmark 1959; Zienkiewicz and Robert L Taylor 2005)).

4.2 Finite difference discretization for fluid dynamics

The technique introduced in this section is the one used in the applications and results presented in Chapter 5.

Finite difference discretization is a widely adopted and accepted technique for solving the Navier-Stokes equations, particularly suitable for problems where the domain has simple geometries and is fixed. In this section, a brief outline of the method used in this thesis and in some numerical simulations, is provided.

The finite difference method aims at solving directly the strong, or local, form of the partial differential equations adopted to model a particular phenomenon.

In our case, since we are interested in the description of a two-phase mixture of a fluid with capillarity, the model used is the Diffuse Interface model introduced in Chapter 2, and the corresponding NS equations are the system of equations (2.27), which we report below for the reader convenience:

$$\frac{\partial \rho}{\partial t} + \nabla \cdot (\rho \mathbf{u}) = 0, \tag{4.1a}$$

$$\frac{\partial \rho \mathbf{u}}{\partial t} + \nabla \cdot (\rho \mathbf{u} \otimes \mathbf{u}) = \nabla \cdot T, \tag{4.1b}$$

$$\frac{\partial E}{\partial t} + \nabla \cdot (E \mathbf{u}) = \nabla \cdot (T \cdot \mathbf{u}) - \nabla \cdot \mathbf{q}_e, \tag{4.1c}$$

with the constitutive relations discussed in the same chapter,

$$\begin{aligned} T = &- \left(p_0 - \frac{\lambda}{2} |\nabla \rho|^2 - \rho \nabla \cdot (\lambda \nabla \rho) \right) I + \\ &- \lambda \nabla \rho \otimes \nabla \rho + \mu (\nabla \mathbf{u} + (\nabla \mathbf{u})^T) - \frac{2}{3} \mu (\nabla \cdot \mathbf{u}) I, \end{aligned} \tag{4.2}$$

$$\mathbf{q}_e = \lambda \rho \nabla \rho \nabla \cdot \mathbf{u} - k \nabla \theta. \tag{4.3}$$

By directly discretizing the derivatives in the above equations over a cartesian grid, as it is the case in this thesis, and by adopting an appropriate time scheme, it is possible to solve the NS equations in time and space.

The time discretization scheme used in this simulations is the second order Runge-Kutta method with two stages, which is already implemented in the PETSc library used for the solution of our problem. PETSc is, as mentioned in the homepage of the project itself, "a suite of data structures and routines for the scalable (parallel) solution of scientific applications modeled by partial differential equations".

The actual finite difference approximation adopted goes by the name of *staggered* finite difference scheme. A staggered finite difference scheme is a numerical scheme where the quantities involved in the calculations are not considered to be placed all in the same position with respect to a grid. Rather, some of these quantities are positioned with respect to different grids. The reasons behind this technique lie in multiple advantages with respect to the use of *collocated* grids, where all the variables share the same grid. In particular, several terms that would require interpolation in collocated grids can be evaluated without interpolation, and staggered arrangements can be shown to directly conserve the energy.

In the case of spherically symmetric one-dimensional simulations analyzed in the subsequent chapter, the one-dimensional grid can be represented as a line with nodes where the variables are computed. With reference to Figure 4.1, where such a grid is represented, all the scalar quantities appearing in the system of equations (4.1) are calculated at the nodal points •, corresponding to the centers of the cells defined by the grid space, whereas vectorial and tensorial components (which are

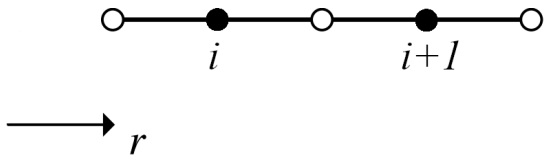

Figure 4.1. Finite difference 1D staggered grid

also scalars in this one-dimensional application, but pertain to a different group) are computed at the nodes ○ delimiting the cells.

The situation slightly differs when dealing with two-dimensional applications, no matter the symmetries involved. The grid adopted in this case is depicted in Figure 4.2, where all the scalars are again computed at the centers • of the cells, all the vector components along the radial direction r are calculated at the nodes ▷ identifying the vertical faces of the cells, all the vector components along the z direction are calculated at the nodes △ on the horizontal faces. Finally, tensor components are calculated at different places, depending on the position they occupy in the tensor itself. The components along the diagonal of the stress tensor (τ_{rr}, $\tau_{\theta\theta}$, τ_{zz}) are computed at the central nodes •, as is done for the scalars, while the out-of-diagonal components, the ones implying mixed derivatives, are located at the vertices ○ of the cells.

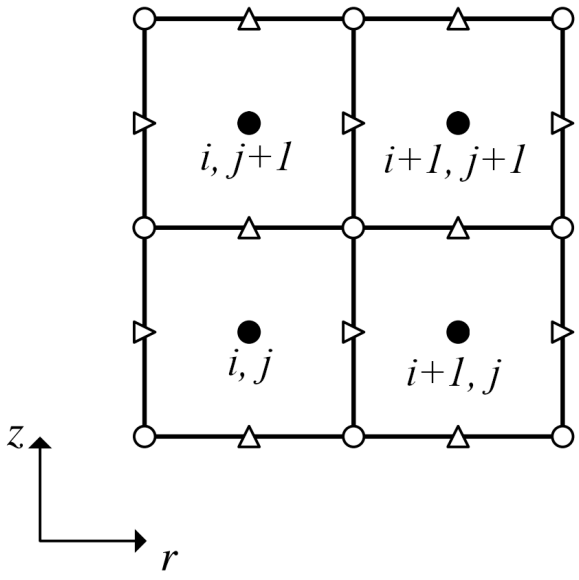

Figure 4.2. Finite difference 2D staggered grid

4.3 Weak form of the equations

4.3.1 Motivations for the introduction of a mixed finite element formulation for fluid dynamics

In the introduction of this chapter we provided the framework and context in which the NSK system of equations is considered for the numerical solution through finite elements. Here, we explain more in details the motivations that lead us to a mixed finite element method for the numerical solution of the NSK system of equations, investigating the relations between the model adopted in this thesis and some of the works recalled in the introduction, constituting the state of the art in the numerical treatment of phase field models and problems with high-order spatial derivatives.

The simplest problem pertaining to the latter class is the bi-harmonic problem

$$\nabla^2\left(\nabla^2 u\right) = f \qquad \text{in} \quad \Omega, \tag{4.4}$$

$$u = \nabla u \cdot \mathbf{n} = 0 \qquad \text{on} \quad \partial\Omega, \tag{4.5}$$

where fourth-order partial derivatives are present. This PDE is extensively analysed in literature, particularly in (Boffi et al. 2013). In the book, the problem is rephrased in terms of a mixed finite element method, where an auxiliary variable is added, and the overall system consists of two second-order PDEs in space:

$$\nabla^2 u_2 = f \qquad \text{in} \quad \Omega, \tag{4.6}$$

$$\nabla^2 u_1 = u_2 \qquad \text{in} \quad \Omega, \tag{4.7}$$

$$u_1 = \nabla u_1 \cdot \mathbf{n} = 0 \qquad \text{on} \quad \partial\Omega, \tag{4.8}$$

where $u_1 = u$ of the previously defined problem (4.4). A weak formulation of equation (4.6) can be obtained integrating it against some test functions $(\phi_1, \phi_2) \in \mathscr{V} \times \mathscr{V}$, where $\mathscr{V}$ is a suitable space. If $(\cdot, \cdot)$ indicates the usual inner product on L^2, we have

$$(\nabla u_2, \nabla \phi_1) + (f, \phi_1) = 0 \qquad \text{in} \quad \Omega, \tag{4.9}$$

$$(\nabla u_1, \nabla \phi_2) + (u_2, \phi_2) = 0 \qquad \text{in} \quad \Omega, \tag{4.10}$$

and the boundary terms vanish thanks to the boundary conditions. If $\mathscr{V} = H^1$, it is possible to find a solution to (4.9), (4.10) which is a weak solution to the bi-harmonic problem, and the error estimates are given in (ibid.) for the case where the finite element basis functions are polynomial of degree $r \geq 2$, and in (Glowinski 2008; Scholz 1978) for the case of piecewise linear basis functions.

To show how the NSK system of equations is related to problem (4.4) we shall consider equations (4.24), (4.25), with the momentum equation expressed in the form (2.56), recalled here for the reader convenience, together with the

conservation of mass equation:

$$\frac{\partial \rho}{\partial t} + \nabla \cdot (\rho \mathbf{u}) = 0, \tag{4.11}$$

$$\frac{\partial \mathbf{u}}{\partial t} + \mathbf{u} \cdot \nabla \mathbf{u} = -\nabla \mu_g - \frac{s}{\rho} \nabla \theta + \nu \nabla \cdot \left(\nabla \mathbf{u} + \nabla^T \mathbf{u} \right) - \frac{2}{3} \nu \nabla \left(\nabla \cdot \mathbf{u} \right); \tag{4.12}$$

where $\mu_g = \mu_b - \lambda \nabla^2 \rho$ is the generalized chemical potential (2.5). If we now examine the case of a non-viscous ($\nu = 0$) and non-conductive ($\nabla \theta = 0$) flow, the previous system reads

$$\frac{\partial \rho}{\partial t} + \nabla \cdot (\rho \mathbf{u}) = 0, \tag{4.13}$$

$$\frac{\partial \mathbf{u}}{\partial t} + \mathbf{u} \cdot \nabla \mathbf{u} = -\nabla (\mu_b - \lambda \nabla^2 \rho). \tag{4.14}$$

To further proceed in our analysis, let us assume the fluid is initially at rest, and a small disturbance $\tilde{\rho}$ acts on the initial density field ρ_0, such that the entire density field can be considered as $\rho = \rho_0 + \tilde{\rho}$, with $\frac{\tilde{\rho}}{\rho} << 1$. In such conditions, we can assume the velocity arising in the domain to be of the order of magnitude of $\tilde{\rho}$ and we will indicate that velocity as $\mathbf{u} = \tilde{\mathbf{u}}$. Linearizing eqs. (4.13) and (4.14), i.e. neglecting second-order terms in $\tilde{\rho}$, $\tilde{\mathbf{u}}$, the following system of equations is obtained:

$$\frac{\partial \tilde{\rho}}{\partial t} + \rho_0 \nabla \cdot \tilde{\mathbf{u}} = 0, \tag{4.15}$$

$$\frac{\partial \tilde{\mathbf{u}}}{\partial t} = -\nabla (\mu_b - \lambda \nabla^2 \tilde{\rho}) = -\left. \frac{\partial^2 f_b}{\partial \rho^2} \right|_{\rho_0} \nabla \tilde{\rho} + \lambda \nabla \left(\nabla^2 \tilde{\rho} \right), \tag{4.16}$$

where we have also used the fact that $\mu_b = \frac{\partial f_b}{\partial \rho}$. After taking the divergence of eq. (4.16), it is possible to substitute eq. (4.15) in (4.16) to obtain a single wave equation for the evolution of the density disturbance field $\tilde{\rho}$,

$$\frac{\partial^2 \tilde{\rho}}{\partial t^2} = \rho_0 \left. \frac{\partial^2 f_b}{\partial \rho^2} \right|_{\rho_0} \nabla^2 \tilde{\rho} - \rho_0 \lambda \nabla^2 \left(\nabla^2 \tilde{\rho} \right), \tag{4.17}$$

which can be further manipulated by introducing a wave speed $c_0 = \sqrt{\rho_0 \left. \frac{\partial^2 f_b}{\partial \rho^2} \right|_{\rho_0}}$ as

$$\frac{\partial^2 \tilde{\rho}}{\partial t^2} = c_0^2 \nabla^2 \tilde{\rho} - \rho_0 \lambda \nabla^2 \left(\nabla^2 \tilde{\rho} \right). \tag{4.18}$$

Taking the Fourier transform of (4.18) to treat the second-order term in time,

$$\mathcal{F}\{\tilde{\rho}\}(\mathbf{x}, \omega) = \hat{\rho}(\mathbf{x}, \omega),$$

we obtain

$$-\omega^2 \hat{\rho} = c_0^2 \nabla^2 \hat{\rho} - \rho_0 \lambda \nabla^2 \left(\nabla^2 \hat{\rho} \right). \tag{4.19}$$

It is at this point that we can introduce a mixed finite element formulation, motivated by the bi-harmonic problem analysed above. By introducing a new variable

$g = \nabla^2\hat{\rho}$, it is indeed possible to rephrase equation (4.19) as the following system of equations:

$$\nabla^2 g = \frac{c_0^2}{\rho_0\lambda} g + \frac{\omega^2}{\rho_0\lambda}\hat{\rho}, \tag{4.20}$$

$$\nabla^2\hat{\rho} = g, \tag{4.21}$$

whose weak formulation, by taking the same test functions as before $(\phi_1, \phi_2) \in \mathscr{V} \times \mathscr{V}$, is

$$(\nabla g, \nabla\phi_1) + \left(\frac{c_0^2}{\rho_0\lambda} g + \frac{\omega^2}{\rho_0\lambda}\hat{\rho}, \phi_1\right) = 0, \tag{4.22}$$

$$(\nabla\rho, \nabla\phi_2) + (g, \phi_2) = 0. \tag{4.23}$$

By defining

$$f = \frac{c_0^2}{\rho_0\lambda} g + \frac{\omega^2}{\rho_0\lambda}\hat{\rho},$$

it can be seen that system (4.22)-(4.23) has the exact same formal structure as system (4.9)-(4.10), thus motivated the use of this procedure, and also the adoption of the vector space $\mathscr{V} = H^1$, since the results presented in the works mentioned in the introduction have been demonstrated in this setting for bi-harmonic and Cahn-Hilliard equations. Additionally, convergence has been shown also for the case of piecewise linear basis, the ones used throughout the thesis.

Once the equation for the density disturbance is solved in this way, the remaining system is composed by the compressible Navier-Stokes equations, whose inviscid and non-conductive simplification is known as Euler system of equations for compressible flows. In this thesis, the author adopted the same regularity choice on all the variables of the problem, asking for all the components of the weak solution to belong to the same Sobolev space H^1, and to be approximated by piecewise linear finite element basis functions. This is supported by the literature on compressible Euler equations, where a common choice is to interpolate the entire solution vector with C^0 shape functions (see for instance (Hughes et al. 1986; Le Beau and Tezduyar 1991; Jaime Peraire et al. 1988)).

4.3.2 Weak form of the Navier-Stokes-Korteweg equations

This section is focused on deriving the weak form of the Navier-Stokes-Korteweg system of equations (2.27) which is the starting point for the finite element discretization. The system can be conveniently rewritten in terms of a single vector unknown including all the vector and scalar fields as

$$\frac{\partial \boldsymbol{\Phi}}{\partial t} + \nabla \cdot \mathbf{F}(\tilde{\mathbf{U}}, \nabla\tilde{\mathbf{U}}, \nabla^2\tilde{\mathbf{U}}) = 0, \tag{4.24}$$

where

$$\boldsymbol{\Phi} = \begin{pmatrix} \rho \\ \rho\mathbf{u} \\ E \end{pmatrix}, \qquad \mathbf{F} = \begin{pmatrix} \rho\mathbf{u} \\ \rho\mathbf{u}\otimes\mathbf{u} - T \\ E\mathbf{u} - T\cdot\mathbf{u} + \mathbf{q}_e \end{pmatrix}, \qquad \tilde{\mathbf{U}} = \begin{pmatrix} \rho \\ \mathbf{u} \\ E \end{pmatrix} \tag{4.25}$$

with the definition of the stress tensor T and the energy flux $\mathbf{q}_e$ provided in (2.43) and (2.44). After noticing that T includes the Laplacian of the density field, $g = \nabla^2\rho$, by following the same procedure outlined in the previous section, the system can be split in the form

$$\begin{aligned} \frac{\partial \boldsymbol{\Phi}}{\partial t} + \nabla \cdot \mathbf{F}(\mathbf{U}, \nabla\mathbf{U}) = 0, \\ g = \nabla^2\rho, \end{aligned} \tag{4.26}$$

where the augmented vector of unknown is

$$\mathbf{U} = (\rho, \mathbf{u}, E, g)^T. \tag{4.27}$$

Accordingly, the constitutive relations now read

$$\begin{aligned} T = &- \left(p_0 - \frac{\lambda}{2}|\nabla\rho|^2 - \rho\lambda g\right) I + \\ &- \lambda \nabla\rho \otimes \nabla\rho + \mu(\nabla\mathbf{u} + (\nabla\mathbf{u})^T) - \frac{2}{3}\mu(\nabla\cdot\mathbf{u})I, \end{aligned} \tag{4.28}$$

$$\mathbf{q}_e = \lambda\rho\nabla\rho\nabla\cdot\mathbf{u} - k\nabla\theta. \tag{4.29}$$

The system must then be completed with appropriate boundary conditions as presented in 2.2.4. These conditions will then be explicitly specified in the result Chapters 5 and 6.

We must also introduce an initial condition for the solution vector

$$\mathbf{U}(\mathbf{x}, 0) = \mathbf{U}_o(\mathbf{x}). \tag{4.30}$$

By simply integrating over the fluid domain the system (4.26) multiplied by *test functions* $(\tilde{\mathbf{V}}, \tilde{g})$, we obtain the following system of equations:

$$\int_\Omega \left[\frac{\partial \boldsymbol{\Phi}}{\partial t} + \nabla \cdot \mathbf{F}(\mathbf{U}, \nabla\mathbf{U})\right] \cdot \tilde{\mathbf{V}}\, \mathrm{d}V = 0, \qquad \forall\, \tilde{\mathbf{V}} \in \mathscr{V}^d, \tag{4.31}$$

$$\int_\Omega \left[g - \nabla^2\rho\right] \tilde{g}\, \mathrm{d}V = 0, \qquad \forall\, \tilde{g} \in \mathscr{V}, \tag{4.32}$$

where the test functions are sufficiently regular functions living in an appropriate vectorial space $\mathscr{V}$ (the superscript d indicates the dimension of vectors $\boldsymbol{\Phi}$ and $\tilde{\mathbf{V}}$).

As a further step, we could make use of the divergence theorem, to take advantage of the regularity required on the test functions $\tilde{\mathbf{V}}$ and $\tilde{g}$,

$$\begin{aligned} &\int_\Omega \left[\frac{\partial \boldsymbol{\Phi}}{\partial t} \cdot \tilde{\mathbf{V}} - \mathbf{F}(\mathbf{U}, \nabla\mathbf{U}) : \nabla\tilde{\mathbf{V}}\right] \mathrm{d}V + \int_{\partial\Omega} \tilde{\mathbf{V}} \cdot \mathbf{F}(\mathbf{U}, \nabla\mathbf{U})\mathbf{n}\, \mathrm{d}S = 0, \qquad \forall\, \tilde{\mathbf{V}} \in \mathscr{V}, \\ &\int_\Omega \left[g\tilde{g} + \nabla\rho \cdot \nabla\tilde{g}\right] \mathrm{d}V - \int_{\partial\Omega} \tilde{g}\nabla\rho \cdot \mathbf{n}\, \mathrm{d}S = 0, \qquad \forall\, \tilde{g} \in \mathscr{V}, \end{aligned} \tag{4.33}$$

This description is indeed adopted to move the high-order derivatives to the test functions, thus requiring less regularity on the solution vector. This is the reason why this final formulation is called *weak form*, and the corresponding solution is named *weak solution*.

When completed with the appropriate initial and boundary conditions (4.30), (2.49), the system of equations (4.33), together with constitutive relations (4.28), (4.29) and an equation of state as indicated in Chapter 2, constitutes the initial boundary value problem (IBVP) for the dynamics of a capillary two-phase fluid.

The objective of the finite element discretization of such a problem is to find a vector $\mathbf{U}$ satisfying (4.33). Formally, the vectorial space $\mathscr{V}$ we are considering in our analysis coincides with the Sobolev space H^1, thus $\mathscr{V} = H^1(\Omega)$. Sobolev space H^1 is the space of square-integrable functions whose gradient is also square-integrable, and in which an inner product and a norm can be naturally defined with these integrals. From a numerical point of view, requiring each variable of our vector solution and test function to live in H^1 is equivalent to asking to find an approximated solution expanded on a continuous finite element basis. A suitable choice can be the basis of polynomials of order r. In this thesis, we will restrict our attention to the case $r = 1$, thus selecting the basis of piecewise linear functions. As a result, we are asking our numerical solution to be C^0 continuous.

We shall clarify that the above outlined procedure and the adoption of a mixed finite element formulation based on the augmented system in (4.33), has been motivated by the discussion in the previous Section 4.3.1, where we showed how our problem can be related to well known mathematical aspects of the bi-harmonic equation.

4.3.3 Weak form of the elastoplasticity equations

As we have done for the fluid dynamic problem, we now focus our attention on the weak formulation for the elastoplastic dynamic equations. The weak equilibrium comes directly from the *principle of virtual work*, and will lead us to the definition of the *initial boundary value problem* for elastoplasticity. The analysis presented here follows schematically the concepts shown in (Souza Neto et al. 2011).

First of all, let us recall the *strong form* of the momentum balance for a general non-linear material, with generic equations of state for the stress tensor and the internal variable evolution, as stated below:

$$\rho\ddot{\mathbf{u}} = \nabla \cdot \boldsymbol{\sigma} + \mathbf{b}, \tag{4.34}$$

$$\begin{aligned} \boldsymbol{\sigma} &= \hat{\boldsymbol{\sigma}}(\boldsymbol{\epsilon}, \boldsymbol{\alpha}), \\ \dot{\boldsymbol{\alpha}} &= f(\boldsymbol{\epsilon}, \boldsymbol{\alpha}), \\ \boldsymbol{\epsilon} &= \nabla^s \mathbf{u}, \end{aligned} \tag{4.35}$$

with the following boundary conditions, prescribed in terms of tractions and dis-

placements on the corresponding boundaries, and initial conditions,

$$\mathbf{u} = \bar{\mathbf{u}} \quad \text{on } \partial\mathcal{B}_{\mathbf{u}} \qquad \mathbf{u}(\mathbf{x}, 0) = \mathbf{u}_0, \tag{4.36}$$

$$\boldsymbol{\sigma}\mathbf{n} = \mathbf{t} \quad \text{on } \partial\mathcal{B}_t \qquad \dot{\mathbf{u}}(\mathbf{x}, 0) = \mathbf{v}_0. \tag{4.37}$$

In the infinitesimal, or small deformation case, the *principle of virtual work* states that the body $\mathscr{B}$ is in equilibrium if and only if the Cauchy stress in the material, $\boldsymbol{\sigma}$, satisfies the weak equilibrium

$$\int_{\mathcal{B}} [\boldsymbol{\sigma} : \nabla\tilde{\boldsymbol{v}} - (\mathbf{b} - \rho\ddot{\mathbf{u}}) \cdot \tilde{\boldsymbol{v}}] \, \mathrm{d}V - \int_{\partial\mathcal{B}} \mathbf{t} \cdot \tilde{\boldsymbol{v}} \, \mathrm{d}S = 0, \qquad \forall\, \tilde{\boldsymbol{v}} \in \mathscr{V}, \tag{4.38}$$

where $\mathbf{b}$ and $\mathbf{t}$ are, respectively, the body force per unit deformed volume and the traction at the boundary, per unit deformed area. $\mathscr{V}$ is the *space of virtual displacements*, which is the space of sufficiently regular *arbitrary* displacements $\tilde{\boldsymbol{v}}$.

It can be easily shown that one can derive the weak formulation of the momentum balance from the strong form of the equations. First, we recall the product rule

$$\boldsymbol{\sigma} : \nabla\tilde{\boldsymbol{v}} = \nabla \cdot (\boldsymbol{\sigma}\tilde{\boldsymbol{v}}) - (\nabla \cdot \boldsymbol{\sigma}) \cdot \tilde{\boldsymbol{v}}, \tag{4.39}$$

where the symmetry of $\boldsymbol{\sigma}$ has been used. Using (4.39) in conjunction with (4.38), we get

$$\int_{\mathcal{B}} [\nabla \cdot (\boldsymbol{\sigma}\tilde{\boldsymbol{v}}) - (\nabla \cdot \boldsymbol{\sigma} + \mathbf{b} - \rho\ddot{\mathbf{u}}) \cdot \tilde{\boldsymbol{v}}] \, \mathrm{d}V - \int_{\partial\mathcal{B}} \mathbf{t} \cdot \tilde{\boldsymbol{v}} \, \mathrm{d}S = 0, \qquad \forall\, \tilde{\boldsymbol{v}} \in \mathscr{V}. \tag{4.40}$$

Then, by making use of the divergence theorem, the first term in (4.40) can be transformed and moved to the boundary, as

$$\int_{\mathcal{B}} \nabla \cdot (\boldsymbol{\sigma}\tilde{\boldsymbol{v}}) \, \mathrm{d}V = \int_{\partial\mathcal{B}} \boldsymbol{\sigma}\tilde{\boldsymbol{v}} \cdot \mathbf{n} \, \mathrm{d}S. \tag{4.41}$$

Finally, using again the symmetry of the stress tensor $\boldsymbol{\sigma}$, we obtain

$$\int_{\mathcal{B}} (\nabla \cdot \boldsymbol{\sigma} + \mathbf{b} - \rho\ddot{\mathbf{u}}) \cdot \tilde{\boldsymbol{v}} \, \mathrm{d}V + \int_{\partial\mathcal{B}} (\mathbf{t} - \boldsymbol{\sigma}\mathbf{n}) \cdot \tilde{\boldsymbol{v}} \, \mathrm{d}S = 0, \qquad \forall\, \tilde{\boldsymbol{v}} \in \mathscr{V}. \tag{4.42}$$

This equation holds for all virtual displacement fields $\tilde{\boldsymbol{v}}$, hence, each term between parenthesis must vanish locally (M. Gurtin 1972). By noting this, we just recovered the local or strong form of the momentum balance equation, showing the equivalence between weak and strong form.

The initial boundary value problem (IBVP) for elastoplasticity

We are now able to define the weak form of the initial boundary value problem for elastoplasticity, in the general framework with inertial contribution, which may be neglected later when the conditions outlined in Section 3.1.4 are met. The numerical solution to this problem will be addressed in the following sections.

Let us assume the body is subjected to some prescribed forces active over time,

$$\mathbf{b}(\mathbf{x}, t), \qquad t \in [t_0, T].$$

In addition, also the natural and essential boundary conditions are prescribed, each on the specific part of the boundary they are acting on:

$$\mathbf{t}(\mathbf{x}_b, t), \qquad t \in [t_0, T]$$

is the traction vector acting on a surface occupying a region $\partial\mathcal{B}_t$ of the body. It is defined as the *natural boundary condition*.

The *essential boundary condition* is instead the motion prescribed at the boundary occupying the region $\partial\mathcal{B}_u$ of the body,

$$\mathbf{u}(\mathbf{x}_b, t) = \bar{\mathbf{u}}(\mathbf{x}_b, t).$$

In addition to the essential boundary condition, we define the *kinematically admissible displacements* of $\mathscr{B}$ as the set of all displacements satisfying the essential boundary condition,

$$\mathscr{K} = \{\mathbf{u} \mid \mathbf{u}(\mathbf{x}_b, t) = \bar{\mathbf{u}}(\mathbf{x}_b, t),\ t \in [t_0, T],\ \mathbf{x}_b \in \partial\mathcal{B}_u\}\,. \tag{4.43}$$

If the body evolution is then assumed to be influenced by some internal variable evolution, as it is in our case, their value at the initial time is also prescribed,

$$\boldsymbol{\alpha}(\mathbf{x}, t) = \boldsymbol{\alpha}_0(t).$$

The infinitesimal transient non-linear initial boundary value problem is thus stated as: *Find a kinematically admissible displacement* $\mathbf{u} \in \mathscr{K}$*, such that, for* $t \in [t_0, T]$,

$$\int_{\mathcal{B}} [\boldsymbol{\sigma}(\boldsymbol{\epsilon}(\mathbf{u}), \boldsymbol{\alpha}) : \nabla\tilde{\boldsymbol{v}} - (\mathbf{b} - \rho\ddot{\mathbf{u}}) \cdot \tilde{\boldsymbol{v}}]\, \mathrm{d}V - \int_{\partial\mathcal{B}_t} \mathbf{t} \cdot \tilde{\boldsymbol{v}}\, \mathrm{d}S = 0, \qquad \forall\, \tilde{\boldsymbol{v}} \in \mathscr{V}, \tag{4.44}$$

where the space of virtual displacements is defined as

$$\mathscr{V} = \{\tilde{\boldsymbol{v}} \mid \tilde{\boldsymbol{v}} = \mathbf{0}\ \text{on}\ \partial\mathcal{B}_u\}\,. \tag{4.45}$$

4.4 Finite element discretization

To numerically solve for the problems defined above, we use the finite element method, which consists of replacing the functional sets of virtual displacements or test functions $\mathscr{V}$ (4.45), and of kinematically admissible displacements $\mathscr{K}$ (4.43) with discrete subsets to be defined later, ${}^{h}\mathscr{V}$ and ${}^{h}\mathscr{K}$, generated by a finite element discretization h of the domain $\mathcal{B}$. A Lagrange finite element e is defined by a certain number n_{nodes} of nodes, and a *shape* or *interpolation function* $N_i^{(e)}(\mathbf{x})$ for each node i with coordinates $\mathbf{x}^i$.

The shape functions are defined in a way they are 0 at every node, except at the one they are associated with, such that

$$N_i^{(e)}(\mathbf{x}^j) = \delta_{ij}, \tag{4.46}$$

where δ_{ij} is the kronecker's delta and the shape function is defined over each single element, such that it is called *element shape function*. Consequently, any generic function defined over the element domain $\mathcal{B}^e$ can be interpolated within the element itself, leading to

$$ {}^h a(\mathbf{x}) = \sum_{i=1}^{n_{node}} a^i N_i^{(e)}(\mathbf{x}), \tag{4.47} $$

$$ a^i = a(\mathbf{x}^i). \tag{4.48} $$

If we now let the function $a(\mathbf{x})$ be defined over the whole domain $\mathcal{B}$, we can extend the above definition of the interpolated function ${}^h a(\mathbf{x})$. By first defining an approximate domain, as the union of all the element domains,

$$ {}^h\mathcal{B} = \bigcup_{e=1}^{n_{elem}} \mathcal{B}^{(e)}, \tag{4.49} $$

the final interpolation of $a(\mathbf{x})$ takes the form

$$ {}^h a(\mathbf{x}) = \sum_{i=1}^{n_{point}} a^i N_i^g(\mathbf{x}), \tag{4.50} $$

where N_i^g is a piecewise polynomial function defined over the entire domain, called the *global shape function*, and n_{point} is the total number of nodal points in the finite element mesh. The global shape function N_i^g is associated with each global node i.

4.4.1 The finite element method in fluid dynamics

At this point, to particularize the method for the solution of the IBVP (4.33), we can introduce the finite-dimensional set of test functions $\mathscr{V}$:

$$ {}^h\mathscr{V} = \left\{ {}^h\tilde{\boldsymbol{v}}(\mathbf{x}) = \sum_{i=1}^{n_{point}} \tilde{\boldsymbol{v}}^i N_i^g(\mathbf{x}) \right\} \tag{4.51} $$

$$ {}^h\mathscr{V} \subset \mathscr{V} = H^1 \tag{4.52} $$

This subsets will substitute the functional sets in our finite element framework.

Before deriving a discretized form for the IBVP (4.33), we define the *global interpolation matrix* $\mathbf{N}^g$ and the *global vector of nodal solutions* $\mathbf{U}$, to obtain a more compact and standard notation. The former is obtained by assembling together all the global shape functions, and the latter is a vector whose generic element U_i^j is the i-component of the solution vector at the global node j. After these definitions, each element ${}^h\mathbf{U}(\mathbf{x})$ can be expressed as

$$ {}^h\mathbf{U} = \mathbf{N}^g\mathbf{U}. \tag{4.53} $$

An analogous formulation is possible for the test function approximation ${}^h\tilde{\mathbf{V}} \in \mathscr{V}$,

$$ {}^h\tilde{\mathbf{V}} = \mathbf{N}^g \tilde{\mathbf{V}}, \tag{4.54} $$

where $\tilde{\mathbf{V}}$ is the *global vector of test nodal solutions*. We finally introduce the *discrete gradient operator* $\mathbf{B}^g$, which is a matrix whose elements are the gradients of the global shape functions,

$$ B^g_{ij} = \frac{\partial N^g_i}{\partial x_j}. \tag{4.55} $$

Since the problem we want to solve is the IBVP (4.33), which is a system of PDEs with different natures and characteristics, it is worth introducing the following notation, to make the equations more easily readable,

$$ {}^h\mathbf{U}_i = \mathbf{N}^g_i \mathbf{U}_i, \qquad i = (\rho,\, \mathbf{u},\, E,\, g), \tag{4.56} $$

$$ {}^h\tilde{\mathbf{V}}_i = \mathbf{N}^g_i \tilde{\mathbf{V}}_i, \qquad i = (\rho,\, \mathbf{u},\, E,\, g). \tag{4.57} $$

The same can be done for the discrete gradient operator $\mathbf{B}^g$, thus we will refer to $\mathbf{B}^g_i$ with $i = (\rho,\, \mathbf{u},\, E,\, g)$. The components of the vector $\boldsymbol{\Phi}$ and of the second-order tensor $\mathbf{F}$ will be indicated in the same way.

The discrete IBVP

Applying the definitions made above to the IBVP (4.33), we get its discretized version,

$$ \int_{{}^h\mathcal{B}} \left[\frac{\partial \boldsymbol{\Phi}}{\partial t} \cdot \mathbf{N}^g \tilde{\mathbf{V}} - \mathbf{F} : \mathbf{B}^g \tilde{\mathbf{V}} \right] \mathrm{d}V = 0, \qquad \forall\, \tilde{\mathbf{V}} \in {}^h\mathscr{V}^d, \tag{4.58} $$

which can be rearranged as

$$ \tilde{\mathbf{V}}^T \left[\int_{{}^h\mathcal{B}} \mathbf{N}^g_i \frac{\partial \boldsymbol{\Phi}_i}{\partial t} - \mathbf{B}^{gT}_i \mathbf{F}_i \, \mathrm{d}V \right] = 0, \qquad \forall\, \tilde{\mathbf{V}} \in {}^h\mathscr{V}^d, \quad i = (\rho,\, \mathbf{u},\, E,\, g) \tag{4.59} $$

Equation (4.59) must be satisfied for all possible virtual displacements $\tilde{\mathbf{V}} \in {}^h\mathscr{V}^d$, which is equivalent to ask the term within square bracket to vanish.

Time scheme and the Newton-Raphson procedure

The time scheme chosen for the integration of the discrete fluid dynamic problem (4.59) is the Crank-Nicolson method (Thomas 2013), which is an implicit second-order method in time and is numerically stable. With reference to the eq. (4.26), the Crank-Nicolson time discretization reads

$$ \frac{\boldsymbol{\Phi}_{n+1} - \boldsymbol{\Phi}_n}{\Delta t} = \frac{1}{2} \left(\nabla \cdot \mathbf{F}_{n+1} + \nabla \cdot \mathbf{F}_n \right), \tag{4.60} $$

$$ \boldsymbol{\Phi}_{n+1} - \boldsymbol{\Phi}_n = \frac{\Delta t}{2} \left[\nabla \cdot \mathbf{F}(\mathbf{U}_{n+1}, \nabla \mathbf{U}_{n+1}) + \nabla \cdot \mathbf{F}(\mathbf{U}_n, \nabla \mathbf{U}_n) \right]. \tag{4.61} $$

where Δt is the timestep chosen in the simulation.

This time approximation can be then used in conjunction with the procedure that lead to equations (4.59), to derive the final computational scheme

$$\int_{h\mathcal{B}} \mathbf{N}^g \left(\boldsymbol{\Phi}_{n+1} - \boldsymbol{\Phi}_n\right) \mathrm{d}V - \frac{\Delta t}{2} \int_{h\mathcal{B}} \mathbf{B}^{gT} \left(\mathbf{F}_{n+1} + \mathbf{F}_n\right) \mathrm{d}V = 0. \tag{4.62}$$

Since our aim is to find the global solution vector at the new time $\mathbf{U}_{n+1}$, whose components are

$$\mathbf{U}_{n+1} = \begin{pmatrix} \rho_{n+1} \\ \mathbf{u}_{n+1} \\ E_{n+1} \\ g_{n+1} \end{pmatrix}, \tag{4.63}$$

by recalling the definition of $\boldsymbol{\Phi}$ and $\mathbf{F}$, and computing them at the new time

$$\boldsymbol{\Phi}_{n+1} = \begin{pmatrix} \rho_{n+1} \\ \rho_{n+1}\mathbf{u}_{n+1} \\ E_{n+1} \end{pmatrix}, \qquad \mathbf{F}_{n+1} = \begin{pmatrix} \rho_{n+1}\mathbf{u}_{n+1} \\ \rho_{n+1}\mathbf{u}_{n+1} \otimes \mathbf{u}_{n+1} - T_{n+1} \\ E_{n+1}\mathbf{u}_{n+1} - T_{n+1} \cdot \mathbf{u}_{n+1} + \mathbf{q}_{e_{n+1}} \end{pmatrix}, \tag{4.64}$$

it is evident how this problem is strongly nonlinear (part of the non-linearities being present in the definition of the capillary stress tensor and the energy flux). Thus, an iterative procedure is required. It consists in a linearization of the problem, which is then solved iteratively, until certain convergence criterion is met. The procedure used in this thesis is the usual Newton-Raphson method.

The starting point for such a scheme is the definition of the residual, which corresponds to the discrete global equilibrium (4.62). Suppose we know the solution of the problem at a certain timestep t_n and we are solving for the solution at time t_{n+1}, then the general requirement is that the solution satisfies the residual being equal to zero, i.e. the discrete global equilibrium equation (4.62)

$$\Psi_{n+1} = \int_{h\mathcal{B}} \mathbf{N}^g \left(\boldsymbol{\Phi}_{n+1} - \boldsymbol{\Phi}_n\right) \mathrm{d}V - \frac{\Delta t}{2} \int_{h\mathcal{B}} \mathbf{B}^{gT} \left(\mathbf{F}_{n+1} + \mathbf{F}_n\right) \mathrm{d}V = 0. \tag{4.65}$$

The linearization procedure of the residual Ψ_{n+1} around the current k-th iteration leads then to

$$\Psi_{n+1}^{k+1} \approx \Psi_{n+1}^{k} + \left.\frac{\partial \Psi}{\partial \mathbf{U}_{n+1}}\right|_{n+1}^{k} \left(\mathbf{U}_{n+1}^{k+1} - \mathbf{U}_{n+1}^{k}\right) = 0, \tag{4.66}$$

and to the final formulation of the problem,

$$\left.\frac{\partial \Psi}{\partial \mathbf{U}_{n+1}}\right|_{n+1}^{k} \Delta \mathbf{U}_{n+1}^{k+1} = -\Psi_{n+1}^{k}, \tag{4.67}$$

Each iteration, once the problem is solved, provides the incremental solution $\Delta \mathbf{U}_{n+1}^{k+1}$, that can be used to update the global solution vector, The above procedure is then repeated until the residual computed at the m-th iteration is lower than a certain prescribed value,

$$\left\|\Psi_{n+1}^{m}\right\| \leq \epsilon \left\|\Psi_{n+1}^{1}\right\|, \tag{4.68}$$

where ϵ is a sufficiently small specified equilibrium convergence tolerance. Once the *convergence criterion* (4.68) is satisfied, the corresponding solution is accepted as the solution at the new timestep t_{n+1},

$$\mathbf{U}_{n+1} = \mathbf{U}^m_{n+1}.$$

Automatic grid refinement

The above derived and discussed equations for the finite element discretization of the NSK system of equations have been implemented by the author of this thesis with the use of a HPC library called *deal.II* (Arndt et al. 2020). The library allows for automatic grid refinement thanks to an *a posteriori* error estimation. This was the main motivation that lead to the use of this library, since mesh adaptivity is a very interesting feature to take advantage of, when dealing with multiscale and mesoscale problems that can be described with phase field models. In particular, the model used in this thesis to describe the fluid behavior is a continuum model where the liquid-vapor interface is a very narrow zone in the domain where the fields vary smoothly and continuously. For this reason, from a computational viewpoint, this interface must be numerically resolved by having a sufficient amount of computational points in the interface width. Mesh adaptivity and automatic grid refinement allow for this and can efficiently follow the dynamics of the system (and of the interface).

In the finite element code, a cell is refined or coarsen based on the Kelly error estimator (Ainsworth and Oden 2011; Kelly et al. 1983). This error indicator tries to approximate the error per cell by integration of the jump of the gradient of the solution along the faces of each cell, and it is based on the analysis of the generalized Poisson equation

$$-\nabla \cdot (a(x)\nabla u) = 0,$$

with either Dirichlet or Neumann boundary conditions.

At each timestep of the numerical scheme introduced in the previous sections, the error per cell is computed, and a certain amount of cells with higher error are refined. On the contrary, a portion of cells with lower error is coarsen. This procedure is not applied to the whole solution vector, but to the density field only, since numerical experiments carried out during the thesis have shown that the best convergence and stability of the solution is achieved when the whole mesh is refined according to this field only. As explicitly stated in Chapter 6, the automatic grid refinement strategy adopted allowed for the numerical solution of systems with micrometric bubbles, that would not be feasible with a structured uniform grid and the Diffuse Interface model used in the thesis.

4.4.2 The finite element method in dynamic nonlinear mechanics

As it has been done above for the NSK equations, to introduce the discretized problem of dynamic elastoplasticity we first need to define the finite-dimensional

sets of kinematically admissible displacements and virtual displacement, $\mathscr{K}$ and $\mathscr{V}$ respectively:

$$ {}^h\mathscr{K} = \left\{ {}^h\mathbf{u}(\mathbf{x}) = \sum_{i=1}^{n_{point}} \mathbf{u}^i N_i^g(\mathbf{x}) \mid \mathbf{u}^i = \bar{\mathbf{u}}(\mathbf{x}^i) \text{ if } \mathbf{x}^i \in \partial\mathcal{B}_u \right\}, \tag{4.69} $$

$$ {}^h\mathscr{V} = \left\{ {}^h\tilde{\boldsymbol{v}}(\mathbf{x}) = \sum_{i=1}^{n_{point}} \tilde{\boldsymbol{v}}^i N_i^g(\mathbf{x}) \mid \tilde{\boldsymbol{v}}^i = \mathbf{0} \text{ if } \mathbf{x}^i \in \partial\mathcal{B}_u \right\}. \tag{4.70} $$

$$ {}^h\mathscr{K} \subset \mathscr{K} = H^1(\mathcal{B}), \qquad {}^h\mathscr{V} \subset \mathscr{V} = H_0^1(\mathcal{B}) \tag{4.71} $$

These subsets will substitute the functional sets in our finite element framework.

We again recall the definition of *global interpolation matrix* $\mathbf{N}^g$ and the *global vector of nodal displacements* $\mathbf{u}$, to obtain a more compact and standard notation, for both the element displacement vector

$$ {}^h\mathbf{u} = \mathbf{N}^g\mathbf{u}. \tag{4.72} $$

and the virtual displacement approximation ${}^h\tilde{\boldsymbol{v}} \in \mathscr{V}$,

$$ {}^h\tilde{\boldsymbol{v}} = \mathbf{N}^g\tilde{\boldsymbol{v}}, \tag{4.73} $$

where $\tilde{\boldsymbol{v}}$ is the *global vector of virtual nodal displacement*. We finally introduce the *discrete symmetric gradient operator* $\mathbf{B}^g$, which is a matrix whose elements are the gradients of the global shape functions,

$$ B_{ij}^g = \frac{\partial N_i^g}{\partial x_j} \tag{4.74} $$

The discrete IBVP

Applying the definitions made above to the IBVP (4.44), we get the discretized version of the virtual work,

$$ \int_{{}^h\mathcal{B}} [\boldsymbol{\sigma}^T \mathbf{B}^g \tilde{\boldsymbol{v}} - (\mathbf{b} - \rho\mathbf{N}^g\ddot{\mathbf{u}}) \cdot \mathbf{N}^g\tilde{\boldsymbol{v}}] \, \mathrm{d}V - \int_{{}^h\partial\mathcal{B}_t} \mathbf{t} \cdot \mathbf{N}^g\tilde{\boldsymbol{v}} \, \mathrm{d}S = 0, \qquad \forall\, \tilde{\boldsymbol{v}} \in^h \mathscr{V} \tag{4.75} $$

which can be rearranged as

$$ \tilde{\boldsymbol{v}}^T \left[\int_{{}^h\mathcal{B}} \mathbf{N}^{gT}\rho\mathbf{N}^g \, \mathrm{d}V\ddot{\mathbf{u}} + \int_{{}^h\mathcal{B}} \mathbf{B}^{gT}\boldsymbol{\sigma} \, \mathrm{d}V - \int_{{}^h\mathcal{B}} \mathbf{N}^{gT}\mathbf{b} \, \mathrm{d}V - \int_{{}^h\partial\mathcal{B}_t} \mathbf{N}^{gT}\mathbf{t} \, \mathrm{d}S \right] = 0, \quad \forall\, \tilde{\boldsymbol{v}} \in {}^h\mathscr{V} \tag{4.76} $$

Equation (4.76) must be satisfied for all possible virtual displacements $\tilde{\boldsymbol{v}} \in^h \mathscr{V}$, which is equivalent to ask the term within parenthesis to vanish. Since the stress

tensor $\boldsymbol{\sigma}$ depends on the actual strain $\boldsymbol{\epsilon}$, which depends on the displacement vector $\mathbf{u}$, the finite element discrete initial boundary value problem can be formulated as:

Find the global vector of nodal displacements $\mathbf{u}$ *such that*

$$\mathbf{M}\ddot{\mathbf{u}} + \mathbf{F}^{\text{int}}(\mathbf{u}) - \mathbf{F}^{\text{ext}} = \mathbf{0}, \tag{4.77}$$

where we have defined the following quantities, namely the *mass matrix* and the *internal* and *external global forces vectors*, all in their *global* form

$$\mathbf{M} = \int_{{}^h\mathcal{B}} \mathbf{N}^{g\,T} \rho \mathbf{N}^g \, \mathrm{d}V \tag{4.78}$$

$$\mathbf{F}^{\text{int}}(\mathbf{u}) = \int_{{}^h\mathcal{B}} \mathbf{B}^{g\,T} \boldsymbol{\sigma} \, \mathrm{d}V \tag{4.79}$$

$$\mathbf{F}^{\text{ext}} = \int_{{}^h\mathcal{B}} \mathbf{N}^{g\,T} \mathbf{b} \, \mathrm{d}V + \int_{{}^h\partial\mathcal{B}_t} \mathbf{N}^{g\,T} \mathbf{t} \, \mathrm{d}S \tag{4.80}$$

The element force vectors and mass matrix

In the actual finite element program, the mass matrix and the internal and external global forces vectors (4.78)-(4.80) are obtained as the assemblies of the corresponding element matrix and vectors through the linear finite element *assembly operator* A,

$$\mathbf{M} = \mathop{\mathrm{A}}_{e=1}^{n_{elem}} \left(\mathbf{M}_{(e)} \right) \qquad \mathbf{F}^{\text{int}} = \mathop{\mathrm{A}}_{e=1}^{n_{elem}} \left(\mathbf{F}^{\text{int}}_{(e)} \right) \qquad \mathbf{F}^{\text{ext}} = \mathop{\mathrm{A}}_{e=1}^{n_{elem}} \left(\mathbf{F}^{\text{ext}}_{(e)} \right)$$

where the element mass matrix and vectors of internal and external forces are

$$\mathbf{M}_{(e)} = \int_{\mathcal{B}^{(e)}} \mathbf{N}^T \rho \mathbf{N} \, \mathrm{d}V \tag{4.81}$$

$$\mathbf{F}^{\text{int}}_{(e)} = \int_{\mathcal{B}^{(e)}} \mathbf{B}^T \boldsymbol{\sigma} \, \mathrm{d}V \tag{4.82}$$

$$\mathbf{F}^{\text{ext}}_{(e)} = \int_{\mathcal{B}^{(e)}} \mathbf{N}^T \mathbf{b} \, \mathrm{d}V + \int_{\partial\mathcal{B}^{(e)}_t} \mathbf{N}^T \mathbf{t} \, \mathrm{d}S \tag{4.83}$$

with $\mathbf{N}$ a matrix composed by all the element shape functions $N_i^{(e)}$, and $\mathbf{B}$ with components

$$B^g_{ij} = \frac{\partial N_i^{(e)}}{\partial x_j} \tag{4.84}$$

Numerical integration

All the integrals in the finite element codes are computed and numerically evaluated with *Gaussian quadrature formulas*. Suppose we want to integrate a function $g(\mathbf{x})$ over the element domain $\mathcal{B}^{(e)}$. We can approximate the integral with a sum-

mation,

$$\int_{\mathcal{B}^{(e)}} g(\boldsymbol{x})\,\mathrm{d}\boldsymbol{x} = \int_{\Gamma} g(\boldsymbol{x}(\boldsymbol{\xi}))j(\boldsymbol{\xi})\,\mathrm{d}\boldsymbol{\xi} \approx \sum_{i=1}^{n_{gauss}} w_i g_i j_i, \tag{4.85}$$

$$j(\boldsymbol{\xi}) = \det\left(\frac{\partial \boldsymbol{x}}{\partial \boldsymbol{\xi}}\right) \tag{4.86}$$

$$j_i = j(\boldsymbol{\xi}_i) \qquad g_i = g(\boldsymbol{x}(\boldsymbol{\xi}_i))$$

where a change of variables has been applied, to move the integral from the actual domain to the standard integration domain Γ, such that the $\boldsymbol{\xi}_i$ are the positions of the Gauss points in Γ and the w_i are the corresponding weights. In (4.85), $j(\boldsymbol{\xi})$ is the determinant of the Jacobian of the transformation.

A similar result is applied to approximate integrals over the boundaries of the computational domain $\partial\mathcal{B}^{(e)}$

$$\int_{\partial\mathcal{B}^{(e)}} g(\boldsymbol{x}^b)\,\mathrm{d}\boldsymbol{x}^b = \int_{\partial\Gamma} g(\boldsymbol{x}^b(\boldsymbol{\xi}^b))j^b(\boldsymbol{\xi}^b)\,\mathrm{d}\boldsymbol{\xi}^b \approx \sum_{i=1}^{n_{gaussb}} w_i^b g_i j_i^b \tag{4.87}$$

4.4.3 Dynamic nonlinear mechanics: Newton-Raphson scheme and Newmark implicit method

We shall now discuss about the time discretization of the IBVP (4.44). The spatial discretization of the IBVP (4.44) led to the global discretized equilibrium (4.77), which is a non-linear equation to be solved for the variable $\mathbf{u}$, with all the non-linearity being present in the constitutive law defining the stress tensor σ in terms of the internal variables and the displacement vector. Thus, we need an iterative procedure to get to the final form of (4.77). The linearization of equation (4.77) is performed by adopting a Newton-Raphson procedure (as we have done for the fluid dynamics problem), which leads us to an incremental linear equation to be solved for the incremental displacement $\Delta\mathbf{u}$. It is particularly suited to solve non-linear problems thanks to its quadratic rate of asymptotic convergence and its robustness and efficiency.

In addition to that, we also need a time discretization scheme to advance the solution in time and express the second derivative of the displacement vector, the acceleration $\ddot{\mathbf{u}} = \mathbf{a}$, in terms of the displacement vector itself. To this aim, we adopt a fully implicit Newmark scheme (Newmark 1959; Zienkiewicz and Robert L Taylor 2005), which works well in combination with an incremental procedure such as the Newton-Raphson approximation. As described above, in Section 4.4.1, the starting point for such a scheme is the definition of the residual, which corresponds to the discrete global equilibrium (4.77). Suppose we know the solution of the problem at a certain timestep t_n and we are solving for the solution at time t_{n+1}, then the general requirement is that the solution satisfies the residual being equal to zero, i.e. the discrete global equilibrium equation

$$\Psi_{n+1} = \mathbf{M}\mathbf{a}_{n+1} + \mathbf{F}^{\text{int}}(\mathbf{u}_{n+1}) - \mathbf{F}^{\text{ext}}_{n+1} = 0, \tag{4.88}$$

where

$$\mathbf{F}^{\text{int}}_{n+1} = \int_{{}^h\mathcal{B}} \mathbf{B}^{g\,T} \boldsymbol{\sigma}_{n+1}\, \mathrm{d}V = \int_{{}^h\mathcal{B}} \mathbf{B}^{g\,T} \boldsymbol{\sigma}(\boldsymbol{\alpha}_n, \boldsymbol{\epsilon}(\mathbf{u}_{n+1}))\, \mathrm{d}V \tag{4.89}$$

$$\mathbf{F}^{\text{ext}}_{n+1} = \int_{{}^h\mathcal{B}} \mathbf{N}^{g\,T} \mathbf{b}_{n+1}\, \mathrm{d}V + \int_{{}^h\partial\mathcal{B}_t} \mathbf{N}^{g\,T} \mathbf{t}_{n+1}\, \mathrm{d}S. \tag{4.90}$$

First, we approximate the displacement and velocity vectors at the next timestep $\mathbf{u}_{n+1}$, $\mathbf{v}_{n+1}$ with the Newmark β method formulation, in terms of the new acceleration $\mathbf{a}_{n+1}$

$$\mathbf{u}_{n+1} = \mathbf{u}_n + \Delta t \mathbf{v}_n + \left(\frac{1}{2} - \beta\right) \Delta t^2 \mathbf{a}_n + \beta \Delta t^2 \mathbf{a}_{n+1} = \hat{\mathbf{u}}_{n+1} + \beta \Delta t^2 \mathbf{a}_{n+1}, \tag{4.91}$$

$$\mathbf{v}_{n+1} = \mathbf{v}_n + (1-\gamma)\Delta t \mathbf{a}_n + \gamma \Delta t \mathbf{a}_{n+1} = \hat{\mathbf{v}}_{n+1} + \gamma \Delta t \mathbf{a}_{n+1}. \tag{4.92}$$

Here, β and γ are constant parameters, and the common choice $\gamma = 2\beta = \frac{1}{2}$ leads to the *trapezoidal rule*. With this approximation, the discrete global equilibrium (4.88) reads

$$\Psi_{n+1} = \frac{c}{\beta \Delta t^2} \mathbf{M}(\mathbf{u}_{n+1} - \hat{\mathbf{u}}_{n+1}) + \mathbf{F}^{\text{int}}(\mathbf{u}_{n+1}) - \mathbf{F}^{\text{ext}}_{n+1} = 0, \tag{4.93}$$

where we have introduced a parameter c which is null when considering quasi-static processes, and is the unity when dealing with transient or dynamic problems. Since equation (4.93) is a non-linear equation for the variable $\mathbf{u}$, as anticipated before, an incremental Newton-Raphson procedure is required. The linearization procedure of the residual Ψ_{n+1} around the current k-th iteration leads then to

$$\Psi^{k+1}_{n+1} \approx \Psi^k_{n+1} + \left.\frac{\partial \Psi}{\partial \mathbf{u}_{n+1}}\right|^k_{n+1} (\mathbf{u}^{k+1}_{n+1} - \mathbf{u}^k_{n+1}) = 0, \tag{4.94}$$

where the derivative of the residual with respect to the displacement, computed at the current iteration, is

$$\left.\frac{\partial \Psi}{\partial \mathbf{u}_{n+1}}\right|^k_{n+1} = \frac{c}{\beta \Delta t^2} \mathbf{M} + \left.\frac{\partial \mathbf{F}^{\text{int}}(\mathbf{u}_{n+1})}{\partial \mathbf{u}_{n+1}}\right|^k_{n+1}. \tag{4.95}$$

As a result, the incremental problem for elastoplasticity (4.94) is formulated as

$$\left(\frac{c}{\beta \Delta t^2} \mathbf{M} + \left.\frac{\partial \mathbf{F}^{\text{int}}(\mathbf{u}_{n+1})}{\partial \mathbf{u}_{n+1}}\right|^k_{n+1}\right) \Delta \mathbf{u}^{k+1}_{n+1} = -\Psi^k_{n+1}, \tag{4.96}$$

$$\left(\frac{c}{\beta \Delta t^2} \mathbf{M} + \mathbf{K}_T\right) \Delta \mathbf{u}^{k+1}_{n+1} = -\Psi^k_{n+1}, \tag{4.97}$$

where $\mathbf{K}_T$ is an important quantity to be computed during the assemble of the system, and is usually referred to as the *global tangent stiffness matrix*. It can be

derived as follows:

$$\begin{aligned}\mathbf{K}_T &= \left.\frac{\partial \mathbf{F}^{\text{int}}(\mathbf{u}_{n+1})}{\partial \mathbf{u}_{n+1}}\right|_{n+1}^{k} = \int_{{}^h\mathcal{B}} \mathbf{B}^{g\,T} \frac{\partial \boldsymbol{\sigma}_{n+1}}{\partial \mathbf{u}_{n+1}}\,\mathrm{d}V \\ &= \int_{{}^h\mathcal{B}} \mathbf{B}^{g\,T} \frac{\partial \boldsymbol{\sigma}_{n+1}}{\partial \boldsymbol{\epsilon}_{n+1}} \frac{\partial \boldsymbol{\epsilon}_{n+1}}{\partial \mathbf{u}_{n+1}}\,\mathrm{d}V \\ &= \int_{{}^h\mathcal{B}} \mathbf{B}^{g\,T} \frac{\partial \boldsymbol{\sigma}_{n+1}}{\partial \boldsymbol{\epsilon}_{n+1}} \mathbf{B}^{g}\,\mathrm{d}V \\ &= \int_{{}^h\mathcal{B}} \mathbf{B}^{g\,T} \mathbf{C} \mathbf{B}^{g}\,\mathrm{d}V. \end{aligned} \tag{4.98}$$

In the latter expression, the corresponding *consistent tangent matrix* has been defined,

$$\mathbf{C} = \frac{\partial \boldsymbol{\sigma}_{n+1}}{\partial \boldsymbol{\epsilon}_{n+1}}. \tag{4.99}$$

Each iteration, solving the problem (4.97) provides the incremental displacement $\Delta\mathbf{u}_{n+1}^{k+1}$, that can be used to update the global solution vectors of displacement, acceleration and velocity,

$$\mathbf{u}_{n+1}^{k+1} = \mathbf{u}_{n+1}^{k} + \Delta\mathbf{u}_{n+1}^{k+1}, \tag{4.100}$$

$$\mathbf{a}_{n+1}^{k+1} = \frac{1}{\beta\Delta t^2}(\mathbf{u}_{n+1}^{k+1} - \hat{\mathbf{u}}_{n+1}), \tag{4.101}$$

$$\mathbf{v}_{n+1}^{k+1} = \hat{\mathbf{v}}_{n+1} + \gamma\Delta t \mathbf{a}_{n+1}^{k+1}. \tag{4.102}$$

The above procedure is then repeated each iteration, until the residual computed at the m-th iteration is lower than a certain prescribed value,

$$\left\|\Psi_{n+1}^{m}\right\| \leq \epsilon \left\|\Psi_{n+1}^{1}\right\|, \tag{4.103}$$

where ϵ is a sufficiently small specified equilibrium convergence tolerance. Once the *convergence criterion* (4.103) is satisfied, the corresponding displacement is accepted as the solution at the new timestep t_{n+1}.

$$\mathbf{u}_{n+1} = \mathbf{u}_{n+1}^{m}$$

All the solution vectors are then updated and a new initial guess is made to solve the problem at the subsequent timestep. Usually, the initial guess for displacement is taken as the converged value of the displacement vector,

$$\mathbf{u}_{n+1}^{1} = \mathbf{u}_{n},$$

and the initial guesses for velocity and acceleration follow from (4.102) and (4.101).

4.5 The elastic predictor/plastic corrector algorithm

The procedure outlined in Section 4.4.2 is not sufficient to find the solution to (4.44), the reason being the fact that the non-linear function $\sigma(\boldsymbol{\epsilon}(\mathbf{u}, \boldsymbol{\alpha}))$ depends

on the path followed during the process, it is said to be *path dependent* or *history dependent*, because it depends on the particular successions of states that have been visited by the body during the simulation. In the particular case analyzed here, the stress depends on the history of strains occurring in the material. The solution to the IBVP for elastoplasticity is still given numerically by the Newmark-Newton-Raphson (NNR) algorithm described in 4.4.2, but, in addition to that, we must address the computation of all the elastoplastic quantities, the stress and the consistent tangent matrix (4.99) within each iteration of the NNR method. However, the general numerical constitutive law for a path dependent material is non-linear and path-*independent* within each increment, meaning that the stress tensor solution of (4.77) is considered to be a function of the actual 'solution' strain $\boldsymbol{\epsilon}_{n+1}$ and of a constant (within the timestep) internal variables vector $\boldsymbol{\alpha}_n$, such that the stress-strain relation is analogous to a non-linear elastic law. Thus, the additional problem for a path-dependent material requires the determination of the quantities

$$\boldsymbol{\sigma}_{n+1} = \hat{\boldsymbol{\sigma}}(\boldsymbol{\alpha}_n, \boldsymbol{\epsilon}_{n+1}) \tag{4.104}$$

$$\boldsymbol{\alpha}_{n+1} = \hat{\boldsymbol{\alpha}}_n(\boldsymbol{\alpha}_n, \boldsymbol{\epsilon}_{n+1}) \tag{4.105}$$

to be updated before starting a new iteration of the global NNR problem (4.97). The *Return Mapping Algorithm* discussed in this section represents an example of numerical integration scheme for path-dependent constitutive laws.

The problem we have just introduced is called the *elastoplastic constitutive initial value problem*. Given initial values for the elastic strain $\boldsymbol{\epsilon}_0^e$ and for the list of internal variables $\boldsymbol{\alpha}_0$, and given the history of the strain tensor $\boldsymbol{\epsilon}(t)$, find the function $\boldsymbol{\epsilon}^e$, $\boldsymbol{\alpha}$ and γ that satisfy the elastoplastic associative constitutive equations and the KKT conditions

$$\dot{\boldsymbol{\epsilon}}^e(t) = \dot{\boldsymbol{\epsilon}} - \gamma(t)\frac{\partial \Phi(\boldsymbol{\sigma}(t), \mathbf{A}(t))}{\partial \boldsymbol{\sigma}}, \tag{4.106}$$

$$\dot{\boldsymbol{\alpha}}(t) = -\gamma(t)\frac{\partial \Phi(\boldsymbol{\sigma}(t), \mathbf{A}(t))}{\partial \mathbf{A}} \tag{4.107}$$

$$\gamma(t) \geq 0, \quad \Phi(\boldsymbol{\sigma}(t), \mathbf{A}(t)) \leq 0, \quad \gamma(t)\Phi(\boldsymbol{\sigma}(t), \mathbf{A}(t)) = 0, \tag{4.108}$$

with

$$\boldsymbol{\sigma}(t) = \frac{\partial f}{\partial \boldsymbol{\epsilon}^e}(t), \quad \mathbf{A}(t) = \frac{\partial f}{\partial \boldsymbol{\alpha}}(t). \tag{4.109}$$

Once the solution to this problem is obtained, one can easily get the plastic strain history through the additive decomposition of strains

$$\boldsymbol{\epsilon}^p(t) = \boldsymbol{\epsilon}(t) - \boldsymbol{\epsilon}^e(t).$$

Since an analytical solution to equations (4.106)-(4.109) is not always possible, an incremental constitutive problem suitable for the numerical approximation and solution of (4.106)-(4.109) must be defined. It takes the name of *incremental elasto-plastic constitutive problem*, and is obtained from (4.106)-(4.109) by applying a backward Euler scheme to those equations. It can be formulated as follows:

Given the values for the elastic strain and internal variables list at the beginning of a discrete timestep $[t_n, t_{n+1}]$, namely $\boldsymbol{\epsilon}^e_n$ and $\boldsymbol{\alpha}_n$, and given a prescribed incremental strain $\Delta\boldsymbol{\epsilon}$, obtained from the solution of the NNR problem (4.97) as $\Delta\boldsymbol{\epsilon} = \mathbf{B}\Delta\mathbf{u}$, solve the system of algebraic equations for $\boldsymbol{\epsilon}^e_{n+1}$, $\boldsymbol{\alpha}_{n+1}$ and $\Delta\gamma$,

$$\boldsymbol{\epsilon}^e_{n+1} = \boldsymbol{\epsilon}^e_n + \Delta\boldsymbol{\epsilon} - \Delta\gamma \frac{\partial \Phi(\boldsymbol{\sigma}_{n+1}, \mathbf{A}_{n+1})}{\partial \boldsymbol{\sigma}}, \tag{4.110}$$

$$\boldsymbol{\alpha}_{n+1} = \boldsymbol{\alpha}_n - \Delta\gamma \frac{\partial \Phi(\boldsymbol{\sigma}_{n+1}, \mathbf{A}_{n+1})}{\partial \mathbf{A}}, \tag{4.111}$$

$$\Delta\gamma \geq 0, \quad \Phi(\boldsymbol{\sigma}_{n+1}, \mathbf{A}_{n+1}) \leq 0, \quad \Delta\gamma\Phi(\boldsymbol{\sigma}_{n+1}, \mathbf{A}_{n+1}) = 0, \tag{4.112}$$

with

$$\boldsymbol{\sigma}_{n+1} = \left.\frac{\partial f}{\partial \boldsymbol{\epsilon}^e}\right|_{n+1}, \quad \mathbf{A}_{n+1} = \left.\frac{\partial f}{\partial \boldsymbol{\alpha}}\right|_{n+1}. \tag{4.113}$$

Due to the presence of the discrete complementarity conditions (4.112), the solution procedure of the incremental problem (4.110)-(4.113) must be considered carefully. In particular, equations (4.112) give rise to two mutually exclusive possibilities:

1. The incremental plastic multiplier vanishes

   $$\Delta\gamma = 0.$$

   As a consequence, no plastic flow occurs within the timestep $[t_n, t_{n+1}]$. It means the material behaves purely elastically, the constraint $\Delta\gamma\Phi = 0$ is automatically satisfied, and the update procedure leads to

   $$\boldsymbol{\epsilon}^e_{n+1} = \boldsymbol{\epsilon}^e_n + \Delta\boldsymbol{\epsilon},$$
   $$\boldsymbol{\alpha}_{n+1} = \boldsymbol{\alpha}_n,$$

   where the elastic strain increment coincides with the total strain increment, and the internal variables are frozen within the timestep.

   In addition, the constraint

   $$\Phi(\boldsymbol{\sigma}_{n+1}, \mathbf{A}_{n+1}) \leq 0$$

   must hold.

2. The incremental plastic multiplier is strictly positive

   $$\Delta\gamma > 0,$$

   in which case $\boldsymbol{\epsilon}^e_{n+1}$, $\boldsymbol{\alpha}_{n+1}$ are given by equations (4.110) and (4.111), and the complementarity conditions reduce to the constraint

   $$\Phi(\boldsymbol{\sigma}_{n+1}, \mathbf{A}_{n+1}) = 0$$

The method used to solve for this incremental problem with complementarity conditions is called *Elastic Predictor/Plastic Corrector* algorithm, where it is first assumed that the material behaves as a purely elastic material, and, if some conditions are met, a correction is adopted to consider plastic flow. The plastic corrector step is usually referred to as the *Return Mapping Algorithm*.

1. During the *Elastic Trial Step*, the material is assumed to behave elastically. It implies considering $\Delta\gamma = 0$, such that the incremental solution is

$$\boldsymbol{\epsilon}^{\text{e trial}}_{n+1} = \boldsymbol{\epsilon}^{e}_{n} + \Delta\boldsymbol{\epsilon}, \tag{4.114}$$

$$\boldsymbol{\alpha}^{\text{trial}}_{n+1} = \boldsymbol{\alpha}_{n}, \tag{4.115}$$

and it is called *elastic trial solution*. Then, the *elastic trial stress* and the *elastic trial hardening forces* are computed as

$$\boldsymbol{\sigma}^{\text{trial}}_{n+1} = \left.\frac{\partial f}{\partial \boldsymbol{\epsilon}^{e}}\right|^{\text{trial}}_{n+1}, \quad \mathbf{A}^{\text{trial}}_{n+1} = \left.\frac{\partial f}{\partial \boldsymbol{\alpha}}\right|^{\text{trial}}_{n+1}.$$

The yield function is then estimated at the *elastic trial state*.

If

$$\Phi^{\text{trial}} = \Phi(\boldsymbol{\sigma}^{\text{trial}}_{n+1}, \mathbf{A}^{\text{trial}}_{n+1}) \leq 0,$$

then, by definition, the *elastic trial state* lies within the elastic domain, and the solution (4.114), (4.115) is accepted. In this case, all the incremental quantities are updated,

$$(\cdot)_{n+1} = (\cdot)^{\text{trial}}_{n+1}.$$

Otherwise, the elastic trial state is non-admissible, and the *plastic corrector* comes in.

2. The idea of the *Plastic Corrector/Return Mapping Algorithm* is to solve a reduced form of the algebraic system (4.110)-(4.111), where the constraint is modified by taking into account the fact that $\Delta\gamma \neq 0$, $\Delta\gamma > 0$. The reduced system takes the form

$$\boldsymbol{\epsilon}^{e}_{n+1} = \boldsymbol{\epsilon}^{\text{e trial}}_{n+1} + \Delta\boldsymbol{\epsilon} - \Delta\gamma \frac{\partial \Phi(\boldsymbol{\sigma}_{n+1}, \mathbf{A}_{n+1})}{\partial \boldsymbol{\sigma}}, \tag{4.116}$$

$$\boldsymbol{\alpha}_{n+1} = \boldsymbol{\alpha}^{\text{trial}}_{n} - \Delta\gamma \frac{\partial \Phi(\boldsymbol{\sigma}_{n+1}, \mathbf{A}_{n+1})}{\partial \mathbf{A}}, \tag{4.117}$$

$$\Phi(\boldsymbol{\sigma}_{n+1}, \mathbf{A}_{n+1}) = 0 \tag{4.118}$$

$$\boldsymbol{\sigma}_{n+1} = \left.\frac{\partial f}{\partial \boldsymbol{\epsilon}^{e}}\right|_{n+1}, \quad \mathbf{A}_{n+1} = \left.\frac{\partial f}{\partial \boldsymbol{\alpha}}\right|_{n+1}. \tag{4.119}$$

The aim is then to find a solution to the reduced system of algebraic equations, which satisfies $\Delta\gamma > 0$. Since this is, in general, a non-linear problem, it is solved first, without taking into consideration the constraint $\Delta\gamma > 0$ or $\Phi(\boldsymbol{\sigma}_{n+1}, \mathbf{A}_{n+1}) = 0$, then an iteration procedure ensures that the constraint is satisfied within a certain prescribed tolerance.

4.5.1 The return mapping algorithm for associative plasticity

The model implemented in the following discussion regarding the return mapping algorithm is the combined isotropic and kinematic hardening for associative infinitesimal plasticity, fully described in Sections 3.3.3 and 3.4.3. We recall the constitutive equations adopted here:

The associative flow rule (3.76) and hardening law (3.77) for the evolution of the plastic strain $\boldsymbol{\epsilon}^p$ and of the set of internal variables $\boldsymbol{\alpha}$,

$$\dot{\boldsymbol{\epsilon}}^p = \gamma \frac{\partial \Phi}{\partial \boldsymbol{\sigma}}, \qquad \dot{\boldsymbol{\alpha}} = -\gamma \frac{\partial \Phi}{\partial \mathbf{A}}. \tag{4.120}$$

The constitutive equations for the thermodynamic forces conjugated to the elastic and plastic strain, and the internal variables, derived from the Helmholtz free energy, (3.42), (3.63)

$$\boldsymbol{\sigma} = \frac{\partial f}{\partial \boldsymbol{\epsilon}^e}, \qquad \mathbf{A} = \frac{\partial f}{\partial \boldsymbol{\alpha}}. \tag{4.121}$$

The resulting linear elastic stress-strain equation (3.103)

$$\boldsymbol{\sigma} = \mathbf{C}^{el} : \boldsymbol{\epsilon}^e \tag{4.122}$$

$$\mathbf{C}^{el} = \lambda \mathbf{I} \otimes \mathbf{I} + 2\mu \mathbb{S} \tag{4.123}$$

The internal variables chosen to describe isotropic and kinematic hardening, namely the accumulated plastic strain α^p and the internal variable associated with the back-stress, $\boldsymbol{\chi}$, as well as their respectively conjugate thermodynamic forces κ and the back-stress $\boldsymbol{\beta}$

$$\boldsymbol{\alpha} = \{\alpha^p, \boldsymbol{\chi}\}, \qquad \mathbf{A} = \{\kappa, \boldsymbol{\beta}\}. \tag{4.124}$$

A yield function suitable for the description of ductile metals, namely the von Mises yield function with combined isotropic and kinematic hardening (3.150),

$$\Phi(\boldsymbol{\sigma}, \boldsymbol{\beta}, \kappa) = \sqrt{3\mathcal{J}_2(\boldsymbol{\eta}(\boldsymbol{\sigma}, \boldsymbol{\beta}))} - \sigma_y(\kappa), \quad \boldsymbol{\eta} = \boldsymbol{\sigma}^d - \boldsymbol{\beta}, \tag{4.125}$$

with $\boldsymbol{\eta}$ the relative deviatoric stress. It results in the standard associative flow rule (3.153)

$$\dot{\boldsymbol{\epsilon}}^p = \gamma \sqrt{\frac{3}{2}} \frac{\boldsymbol{\eta}}{\|\boldsymbol{\eta}\|} = \gamma \sqrt{\frac{3}{2}} \hat{\mathbf{N}}, \tag{4.126}$$

where we have defined the unit normal tensor to the yield surface in the space of relative deviatoric stresses

$$\hat{\mathbf{N}} = \frac{\boldsymbol{\eta}}{\|\boldsymbol{\eta}\|}. \tag{4.127}$$

Then we adopt a general form for the plastic part of the Helmholtz free energy f^p, which leads to non-linear associative isotropic hardening laws and to linear associative kinematic hardening, as (3.152). As seen in Section 3.4.3, the resulting evolution laws for the internal variables, and the constitutive equations for the

associated thermodynamic forces, from (4.120) and (4.121), are

$$\dot{\boldsymbol{\chi}} = \gamma\sqrt{\frac{3}{2}}\frac{\boldsymbol{\eta}}{\|\boldsymbol{\eta}\|} = \dot{\boldsymbol{\epsilon}}^p, \quad \boldsymbol{\beta} = \frac{2}{3}H\boldsymbol{\chi}, \tag{4.128}$$

$$\dot{\alpha}^p = \gamma, \qquad \kappa = k_1\alpha^p + (k_\infty - k_2)(1 - e^{-\delta\alpha^p}). \tag{4.129}$$

Since the evolution equation for $\boldsymbol{\chi}$ does not really add information, we shall get rid of it and consider an evolution equation for the back-stress $\boldsymbol{\beta}$, derived from the evolution equation for $\boldsymbol{\chi} = \boldsymbol{\epsilon}^p$. Hence, we will make use of

$$\dot{\boldsymbol{\beta}} = \frac{2}{3}H\dot{\boldsymbol{\chi}} = \gamma\sqrt{\frac{2}{3}}H\frac{\boldsymbol{\eta}}{\|\boldsymbol{\eta}\|}. \tag{4.130}$$

The elastic predictor step in details

The first step to the solution of the system (4.110)-(4.113) is the elastic predictor introduced above. Let us see, in the present framework of combined isotropic and kinematic hardening for associative infinitesimal plasticity, how it works in details.

In the following, for a notation convenience, we shall indicate the deviatoric stress tensor $\boldsymbol{\sigma}^d$ as $\boldsymbol{s}$

The solution of the global NNR iterative problem (4.97), where the global tangent stiffness matrix $\mathbf{K}_T$ is firstly assembled with the assumption of elastic behavior, is given by $\mathbf{u}_{n+1}$. The corresponding incremental strains are then obtained by using the discrete symmetric gradient operator $\mathbf{B}$ as $\Delta\boldsymbol{\epsilon} = \boldsymbol{\epsilon}_{n+1} - \boldsymbol{\epsilon}_n = \mathbf{B}\Delta\mathbf{u}_{n+1}$. The elastic trial state is then calculated assuming that no plastic flow occurs, such that $\Delta\gamma = 0$, and the internal variables are frozen. As a result, we have the following

$$\begin{aligned} \boldsymbol{\epsilon}_{n+1}^{\text{e trial}} &= \boldsymbol{\epsilon}_n^e + \Delta\boldsymbol{\epsilon} \\ \alpha_{n+1}^{p\ \text{trial}} &= \alpha_n^p \\ \boldsymbol{\beta}_{n+1}^{\text{trial}} &= \boldsymbol{\beta}_n \end{aligned} \tag{4.131}$$

The trial stress is then computed through the linear elastic stress-strain relation

$$\boldsymbol{\sigma}_{n+1}^{\text{trial}} = \mathbf{C}^{el} : \boldsymbol{\epsilon}_{n+1}^{\text{e trial}}. \tag{4.132}$$

Since we are using a yield function which is pressure insensitive, meaning that the only portion of the stress tensor having an influence on plastic flow is the deviatoric one, we shall use a slightly different form of the elasticity tensor, which automatically decomposes the resulting stress tensor in its volumetric and deviatoric parts. This is obtained by substituting the Lamé parameter λ with the bulk modulus k

$$\mathbf{C}^{el} = \lambda\mathbf{I}\otimes\mathbf{I} + 2\mu\mathrm{S} = k\mathbf{I}\otimes\mathbf{I} + 2\mu\mathbf{I}_{\mathrm{d}}, \qquad \lambda = k - \frac{2}{3}\mu, \tag{4.133}$$

where the fourth-order deviator tensor $\mathbf{I}_{\mathrm{d}}$ is defined as the difference between the fourth-order symmetric identity tensor $\mathbb{S}$ and the fourth-order tensor $\frac{1}{3}\mathbf{I}\otimes\mathbf{I}$

$$\mathbf{I}_{\mathrm{d}} = \mathbb{S} - \frac{1}{3}\mathbf{I}\otimes\mathbf{I}, \tag{4.134}$$

and maps second-order tensors into their deviatoric part, such that (4.132) is rewritten as

$$\begin{aligned}\boldsymbol{\sigma}_{n+1}^{\text{trial}} &= (k\mathbf{I}\otimes\mathbf{I} + 2\mu\mathbf{I}_{\mathrm{d}}) : \boldsymbol{\epsilon}_{n+1}^{\mathrm{e\ trial}} \\ &= k\mathrm{tr}(\boldsymbol{\epsilon}_{n+1}^{\mathrm{e\ trial}})\mathbf{I} + 2\mu\boldsymbol{\epsilon}_{d\ n+1}^{e\ \mathrm{trial}} \qquad (4.135)\\ \boldsymbol{s}_{n+1}^{\text{trial}} &= 2\mu\boldsymbol{\epsilon}_{d\ n+1}^{e\ \mathrm{trial}}. \qquad (4.136)\end{aligned}$$

Thus, the trial yield stress and the trial relative stress are

$$\sigma_{y\ n+1}^{\text{trial}} = \sigma_y(k(\alpha_n^p)), \tag{4.137}$$

$$\boldsymbol{\eta}_{n+1}^{\text{trial}} = \boldsymbol{s}_{n+1}^{\text{trial}} - \boldsymbol{\beta}_n. \tag{4.138}$$

The final step is the computation of the trial yield function. If the stress state lies inside the elastic domain, i.e. if

$$\Phi(\boldsymbol{\eta}_{n+1}^{\text{trial}}, \sigma_y(\alpha_n^p)) < 0, \tag{4.139}$$

then the process is actually elastic, and all the quantities calculated above can be accepted and updated,

$$(\cdot)_{n+1} = (\cdot)_{n+1}^{\text{trial}}.$$

Otherwise, the process is elastoplastic within the discrete timestep $[t_n, t_{n+1}]$ and the plastic corrector step, which in this thesis is chosen to be the return mapping algorithm, is applied.

The plastic corrector - implicit return mapping

When the trial state does not satisfy the requirement (4.139), the plastic corrector algorithm is involved. The method used in this thesis is the implicit return mapping algorithm, which provides a solution to the following incremental problem:

$$\begin{aligned}\Phi_{n+1} &= \sqrt{\frac{3}{2}}\left\|\boldsymbol{\eta}_{n+1}\right\| - \sigma_y(\alpha_{n+1}^p) = 0,\\ \boldsymbol{\epsilon}_{n+1}^p &= \boldsymbol{\epsilon}_n^p + \Delta\gamma\sqrt{\frac{3}{2}}\frac{\boldsymbol{\eta}_{n+1}}{\left\|\boldsymbol{\eta}_{n+1}\right\|},\\ \alpha_{n+1}^p &= \alpha_n^p + \Delta\gamma,\\ \boldsymbol{\beta}_{n+1} &= \boldsymbol{\beta}_n + \Delta\gamma\sqrt{\frac{2}{3}}H\frac{\boldsymbol{\eta}_{n+1}}{\left\|\boldsymbol{\eta}_{n+1}\right\|}.\end{aligned} \tag{4.140}$$

Since we will be focusing our attention on the elastic strain $\boldsymbol{\epsilon}^e$, it is useful to substitute the incremental equation for the plastic strain with one for $\boldsymbol{\epsilon}^e_{n+1}$. Using the additive decomposition,

$$\boldsymbol{\epsilon}_{n+1} = \boldsymbol{\epsilon}^e_{n+1} + \boldsymbol{\epsilon}^p_{n+1} \tag{4.141}$$

$$\begin{aligned}\boldsymbol{\epsilon}^e_{n+1} &= \boldsymbol{\epsilon}_{n+1} - \left(\boldsymbol{\epsilon}^p_n + \sqrt{\frac{3}{2}}\Delta\gamma\frac{\boldsymbol{\eta}_{n+1}}{\|\boldsymbol{\eta}_{n+1}\|}\right), \\ &= \boldsymbol{\epsilon}^{\text{e trial}}_{n+1} - \sqrt{\frac{3}{2}}\Delta\gamma\frac{\boldsymbol{\eta}_{n+1}}{\|\boldsymbol{\eta}_{n+1}\|}.\end{aligned} \tag{4.142}$$

An equation to update the actual stress is obtained by using the stress-strain constitutive equation for linear elasticity,

$$\boldsymbol{\sigma}_{n+1} = \mathbf{C}^{el} : \boldsymbol{\epsilon}^e_{n+1} = \mathbf{C}^{el} : \boldsymbol{\epsilon}^{\text{e trial}}_{n+1} - \Delta\gamma\sqrt{\frac{3}{2}}\mathbf{C}^{el} : \frac{\boldsymbol{\eta}_{n+1}}{\|\boldsymbol{\eta}_{n+1}\|}, \tag{4.143}$$

which can be further developed recalling the form of the elasticity tensor mentioned above in (4.133) and the fact that $\boldsymbol{\sigma}^{\text{trial}}_{n+1} = \mathbf{C}^{el} : \boldsymbol{\epsilon}^{\text{e trial}}_{n+1}$,

$$\begin{aligned}\boldsymbol{\sigma}_{n+1} &= \boldsymbol{\sigma}^{\text{trial}}_{n+1} - \Delta\gamma\sqrt{\frac{3}{2}}\left[\lambda\text{tr}\left(\frac{\boldsymbol{\eta}_{n+1}}{\|\boldsymbol{\eta}_{n+1}\|}\right)\mathbf{I} + 2\mu\frac{\boldsymbol{\eta}_{n+1}}{\|\boldsymbol{\eta}_{n+1}\|}\right], \\ \boldsymbol{\sigma}_{n+1} &= \boldsymbol{\sigma}^{\text{trial}}_{n+1} - 2\mu\Delta\gamma\sqrt{\frac{3}{2}}\frac{\boldsymbol{\eta}_{n+1}}{\|\boldsymbol{\eta}_{n+1}\|},\end{aligned} \tag{4.144}$$

where the latter relation is obtained recalling that the relative stress tensor $\boldsymbol{\eta}$ is a deviatoric and symmetric second-order tensor, so that its trace vanishes. By taking the deviator of equation (4.144), and recalling the definition of trial deviatoric stress (4.136), one gets

$$\boldsymbol{s}_{n+1} = \boldsymbol{s}^{\text{trial}}_{n+1} - 2\mu\Delta\gamma\sqrt{\frac{3}{2}}\frac{\boldsymbol{\eta}_{n+1}}{\|\boldsymbol{\eta}_{n+1}\|}. \tag{4.145}$$

The basic idea of the algorithm is to reduce the system of equations (4.140) to a single equation for the determination of $\Delta\gamma$, which as it is evident from (4.140), is necessary to update all the plastic quantities. At the same time, the constraint which requires the stress state to lie on the yield surface must be verified. For this reason, the algorithm is built in such a way that the equation for the determination of the discrete plastic multiplier $\Delta\gamma$ also enforces the constraint $(4.140)_1$. To this aim, we will substitute to equation $(4.140)_1$ the expressions for the updated relative stress $\boldsymbol{\eta}_{n+1}$. The incremental equation for $\boldsymbol{\eta}_{n+1}$ can be derived from the equations for the deviatoric stress tensor (4.144) and the incremental equation for the back-stress $(4.140)_4$ as

$$\boldsymbol{\eta}_{n+1} = \boldsymbol{\eta}^{\text{trial}}_{n+1} - \Delta\gamma\sqrt{\frac{3}{2}}\left[2\mu + \frac{2}{3}H\right]\frac{\boldsymbol{\eta}_{n+1}}{\|\boldsymbol{\eta}_{n+1}\|}, \tag{4.146}$$

where we used the fact that

$$\boldsymbol{\eta}_{n+1}^{\text{trial}} = \boldsymbol{s}_{n+1}^{\text{trial}} - \boldsymbol{\beta}_n$$

By rearranging equation (4.146) into

$$\left[1 + \frac{\Delta\gamma}{\left\|\boldsymbol{\eta}_{n+1}\right\|}\sqrt{\frac{3}{2}}\left(2\mu + \frac{2}{3}H\right)\right]\boldsymbol{\eta}_{n+1} = \boldsymbol{\eta}_{n+1}^{\text{trial}} \tag{4.147}$$

the fact that $\boldsymbol{\eta}_{n+1}^{\text{trial}}$ and $\boldsymbol{\eta}_{n+1}$ are *colinear* is evident, since the former is a scalar multiple of the latter. It means

$$\frac{\boldsymbol{\eta}_{n+1}}{\left\|\boldsymbol{\eta}_{n+1}\right\|} = \frac{\boldsymbol{\eta}_{n+1}^{\text{trial}}}{\left\|\boldsymbol{\eta}_{n+1}^{\text{trial}}\right\|}, \tag{4.148}$$

thus, the above expression can be rearranged as

$$\boldsymbol{\eta}_{n+1} = \left[1 - \frac{\Delta\gamma}{\sqrt{\frac{3}{2}}\left\|\boldsymbol{\eta}_{n+1}^{\text{trial}}\right\|}\left(3\mu + H\right)\right]\boldsymbol{\eta}_{n+1}^{\text{trial}}. \tag{4.149}$$

To make this equation, and the following, more easily readable, we introduce the *relative effective stress* q_{n+1}^{trial}, defined as

$$q_{n+1}^{\text{trial}} := \sqrt{\frac{3}{2}}\left\|\boldsymbol{\eta}_{n+1}^{\text{trial}}\right\| = \sqrt{3\mathcal{J}_2(\boldsymbol{\eta}_{n+1}^{\text{trial}})}. \tag{4.150}$$

With this in mind, (4.149) reads

$$\boldsymbol{\eta}_{n+1} = \sqrt{\frac{2}{3}}\left[q_{n+1}^{\text{trial}} - \Delta\gamma\left(3\mu + H\right)\right]\frac{\boldsymbol{\eta}_{n+1}^{\text{trial}}}{\left\|\boldsymbol{\eta}_{n+1}^{\text{trial}}\right\|}. \tag{4.151}$$

We can now substitute this expression, together with the incremental law for the accumulated plastic strain $(4.140)_3$ into the expression of the yield surface $(4.140)_1$, to get at one time both the constraint satisfaction and an equation to determine the plastic multiplier,

$$g(\Delta\gamma) = q_{n+1}^{\text{trial}} - \Delta\gamma\left(3\mu + H\right) - \sigma_y(\alpha_n^p + \Delta\gamma) = 0. \tag{4.152}$$

This is a non-linear scalar equation for $\Delta\gamma$, and can be recursively solved by means of the usual Newton-Raphson procedure. The first order approximation for $g(\Delta\gamma)$, with the requirement of setting the next iteration to zero, results in

$$g(\Delta\gamma^{k+1}) = g(\Delta\gamma^k) + \frac{\mathrm{d}g(\Delta\gamma^k)}{\mathrm{d}\Delta\gamma}\left(\Delta\gamma^{k+1} - \Delta\gamma^k\right) = 0, \tag{4.153}$$

which can be inverted to get an equation for the recursive approximation of $\Delta\gamma$, which can be initially assumed to be zero,

$$\Delta\gamma^{k+1} = \Delta\gamma^k - \left(\frac{\mathrm{d}g(\Delta\gamma^k)}{\mathrm{d}\Delta\gamma}\right)^{-1} g(\Delta\gamma^k). \tag{4.154}$$

The derivative appearing in the latter equation can be calculated, and is, for the present case

$$\frac{\mathrm{d}g(\Delta\gamma^k)}{\mathrm{d}\Delta\gamma} = -3\mu - H - \sigma_y'(\alpha_n^p + \Delta\gamma^k), \tag{4.155}$$

where $\sigma_y'(\alpha_n^p + \Delta\gamma^k)$ is the derivative of the yield stress with respect to the accumulated plastic strain, calculated in the last converged iteration. Once the plastic multiplier has been found, it projects the state of the material onto the yield surface, since the equation for the determination of $\Delta\gamma$ coincides with the yield locus. Consequently, all the quantities in (4.140) can be updated, as well as the Cauchy stress tensor (4.144). The elastoplastic problem within a single iteration of the global NNR procedure has been solved, and the next global iteration can take place.

The equation (4.144) can be further rearranged using (4.148) and the definition of relative effective stress (4.150), to express the Cauchy stress tensor in the form (4.104)

$$\boldsymbol{\sigma}_{n+1} = \hat{\boldsymbol{\sigma}}(\alpha_n^p, \boldsymbol{\beta}_n, \boldsymbol{\epsilon}_{n+1}^{\text{e trial}}) \tag{4.156}$$

$$= \mathbf{C}^{el} : \boldsymbol{\epsilon}_{n+1}^{\text{e trial}} - 2\mu\Delta\gamma\sqrt{\frac{3}{2}}\frac{\boldsymbol{\eta}_{n+1}^{\text{trial}}}{\|\boldsymbol{\eta}_{n+1}^{\text{trial}}\|} \tag{4.157}$$

$$= \mathbf{C}^{el} : \boldsymbol{\epsilon}_{n+1}^{\text{e trial}} - \frac{3\mu\Delta\gamma}{q_{n+1}^{\text{trial}}}\left(\boldsymbol{s}_{n+1}^{\text{trial}} - \boldsymbol{\beta}_n\right) \tag{4.158}$$

which can then be reduced, using (4.136),to

$$\boldsymbol{\sigma}_{n+1} = \left(\mathbf{C}^{el} - \frac{3\mu\Delta\gamma}{q_{n+1}^{\text{trial}}}2\mu\mathbf{I}_{\mathrm{d}}\right) : \boldsymbol{\epsilon}_{n+1}^{\text{e trial}} + \frac{3\mu\Delta\gamma}{q_{n+1}^{\text{trial}}}\boldsymbol{\beta}_n. \tag{4.159}$$

This form for the update of the stress tensor is extremely important, since it serves also as a basis for the derivation of the *consistent elastoplastic tangent modulus* (4.99), which is necessary for the assembly operation of the global tangent stiffness matrix (4.98) that appears in the global NNR iterative procedure. The problem of derivation of a consistent algorithmic tangent modulus will be tackled in the following section

Linearization of the consistent elastoplastic tangent

Here we describe the solution to the problem of finding an appropriate algorithmic consistent form of the elastoplastic tangent modulus (4.99) appearing in the assembly of the global system. The starting point will be the algorithmic incremental constitutive relation (4.159), together with the rate equation which defines the algorithmic elastoplastic tangent,

$$\mathrm{d}\boldsymbol{\sigma}_{n+1} = \frac{\partial\boldsymbol{\sigma}_{n+1}}{\partial\boldsymbol{\epsilon}_{n+1}^{\text{e trial}}} : \mathrm{d}\boldsymbol{\epsilon}_{n+1}^{\text{e trial}} = \mathbf{C}^{ep} : \mathrm{d}\boldsymbol{\epsilon}_{n+1}^{\text{e trial}}. \tag{4.160}$$

Let us rewrite (4.159) in a more easily readable form,

$$\boldsymbol{\sigma}_{n+1} = \mathbf{C}^{el} : \boldsymbol{\epsilon}^{\text{e trial}}_{n+1} - \frac{3\mu\Delta\gamma}{q^{\text{trial}}_{n+1}} 2\mu \mathbf{I}_{\text{d}} : \boldsymbol{\epsilon}^{\text{e trial}}_{n+1} + \frac{3\mu\Delta\gamma}{q^{\text{trial}}_{n+1}} \boldsymbol{\beta}_n, \tag{4.161}$$

where it is evident that the first term in the lhs of (4.161) contributes with one term, corresponding to the elasticity tensor, to the elastoplastic tangent modulus. The second term in the lhs also contributes trivially, but, together with the third term, contributes with two additional members, obtained as the derivatives of the plastic multiplier and the relative effective stress, so that

$$\begin{aligned} \frac{\partial \boldsymbol{\sigma}_{n+1}}{\partial \boldsymbol{\epsilon}^{\text{e trial}}_{n+1}} = \left(\mathbf{C}^{el} - \frac{3\mu\Delta\gamma}{q^{\text{trial}}_{n+1}} 2\mu \mathbf{I}_{\text{d}} \right) - \frac{3\mu}{q^{\text{trial}}_{n+1}} \frac{\partial \Delta\gamma}{\partial \boldsymbol{\epsilon}^{\text{e trial}}_{n+1}} \otimes \boldsymbol{\eta}^{\text{trial}}_{n+1} \\ + \frac{3\mu\Delta\gamma}{(q^{\text{trial}}_{n+1})^2} \frac{\partial q^{\text{trial}}_{n+1}}{\partial \boldsymbol{\epsilon}^{\text{e trial}}_{n+1}} \otimes \boldsymbol{\eta}^{\text{trial}}_{n+1} \end{aligned} \tag{4.162}$$

Let us focus on the latter term first, since it is needed also in the derivation of the one involving the plastic multiplier. By rearranging the definition of the relative effective stress, we know

$$q^{\text{trial}}_{n+1} = \sqrt{\frac{3}{2}} \left\| \boldsymbol{\eta}^{\text{trial}}_{n+1} \right\| = \sqrt{\frac{3}{2}} \left\| 2\mu \mathbf{I}_{\text{d}} : \boldsymbol{\epsilon}^{\text{e trial}}_{n+1} - \boldsymbol{\beta}_n \right\|. \tag{4.163}$$

As a result, recalling the derivation of the norm of a second-order tensor with respect to itself, (3.125), we have

$$\begin{aligned} \frac{\partial q^{\text{trial}}_{n+1}}{\partial \boldsymbol{\epsilon}^{\text{e trial}}_{n+1}} &= \sqrt{\frac{3}{2}} \frac{\partial \left\| 2\mu \mathbf{I}_{\text{d}} : \boldsymbol{\epsilon}^{\text{e trial}}_{n+1} - \boldsymbol{\beta}_n \right\|}{\partial \boldsymbol{\epsilon}^{\text{e trial}}_{n+1}} = \\ &= 2\mu \sqrt{\frac{3}{2}} \frac{2\mu \mathbf{I}_{\text{d}} : \boldsymbol{\epsilon}^{\text{e trial}}_{n+1} - \boldsymbol{\beta}_n}{\left\| 2\mu \mathbf{I}_{\text{d}} : \boldsymbol{\epsilon}^{\text{e trial}}_{n+1} - \boldsymbol{\beta}_n \right\|} = 2\mu \sqrt{\frac{3}{2}} \frac{\boldsymbol{\eta}^{\text{trial}}_{n+1}}{\left\| \boldsymbol{\eta}^{\text{trial}}_{n+1} \right\|} \\ &= 2\mu \sqrt{\frac{3}{2}} \hat{\mathbf{N}}_{n+1}, \end{aligned} \tag{4.164}$$

where the definition of the normal to the yield surface (4.127) and the collinearity of the relative stresses (4.148) have been used.

We shall now find a way to evaluate the derivative of the plastic multiplier with respect to the trial elastic strain tensor. Since the plastic multiplier is obtained through an iterative procedure, and is not an explicit function, we must manipulate equation (4.152) to get to the actual derivative. By noting that the function g corresponds with the yield surface constraint, which is set to zero, we can differentiate it, obtaining

$$g(\Delta\gamma) = 0 \implies \mathrm{d}g = 0. \tag{4.165}$$

Its differential is then

$$\mathrm{d}g = \mathrm{d}q^{\text{trial}}_{n+1} - (3\mu + H)\mathrm{d}\Delta\gamma - \sigma_y\prime(\alpha^p_{n+1})\mathrm{d}\Delta\gamma = 0, \tag{4.166}$$

and we can find a relation between the differential of $\Delta\gamma$ and the differential of q_{n+1}^{trial},

$$\mathrm{d}\Delta\gamma = \frac{1}{3\mu + H + \sigma_y{}'} \mathrm{d}q_{n+1}^{\text{trial}}. \tag{4.167}$$

As a consequence, the partial derivative of the plastic multiplier with respect to the relative effective stress is

$$\frac{\partial \Delta\gamma}{\partial q_{n+1}^{\text{trial}}} = \frac{1}{3\mu + H + \sigma_y{}'}, \tag{4.168}$$

which allows us to derive the required relation by means of the chain rule

$$\frac{\partial \Delta\gamma}{\partial \boldsymbol{\epsilon}_{n+1}^{\text{e trial}}} = \frac{\partial \Delta\gamma}{\partial q_{n+1}^{\text{trial}}} \frac{\partial q_{n+1}^{\text{trial}}}{\partial \boldsymbol{\epsilon}_{n+1}^{\text{e trial}}}, \tag{4.169}$$

where the derivative of the relative effective stress computed above appears, so that

$$\frac{\partial \Delta\gamma}{\partial \boldsymbol{\epsilon}_{n+1}^{\text{e trial}}} = \frac{2\mu}{3\mu + H + \sigma_y{}'} \sqrt{\frac{3}{2}} \hat{\boldsymbol{N}}_{n+1}. \tag{4.170}$$

Putting all the results together in (4.162), we obtain the final form of the *consistent algorithmic tangent modulus*, which reads

$$\frac{\partial \boldsymbol{\sigma}_{n+1}}{\partial \boldsymbol{\epsilon}_{n+1}^{\text{e trial}}} = \mathbf{C}^{el} - \frac{6\mu^2 \Delta\gamma}{q_{n+1}^{\text{trial}}} \mathbf{I}_{\text{d}} + 6\mu^2 \left(\frac{\Delta\gamma}{q_{n+1}^{\text{trial}}} - \frac{1}{3\mu + H + \sigma_y{}'} \right) \hat{\boldsymbol{N}}_{n+1} \otimes \hat{\boldsymbol{N}}_{n+1}. \tag{4.171}$$

Differences between the consistent and continuum elastoplastic tangent modulus

An important thing to notice when dealing with computational plasticity, is that the consistent tangent modulus derived in the previous section is slightly different from the continuum tangent modulus derived in Section 3.3.4. This is related to computational stability and convergence rate of the overall numerical scheme, as firstly noted in (Simo and Robert Leroy Taylor 1985).

For the sake of simplicity, let us restrict our analysis to the simpler case of linear isotropic hardening with no kinematic hardening. This case is extensively analysed in Section 3.4.3. In this framework, by setting the back-stress and the kinematic hardening modulus H to zero in (4.171), the consistent elastoplastic tangent modulus reads

$$\frac{\partial \boldsymbol{\sigma}_{n+1}}{\partial \boldsymbol{\epsilon}_{n+1}^{\text{e trial}}} = \mathbf{C}^{el} - \frac{6\mu^2 \Delta\gamma}{q_{n+1}^{\text{trial}}} \mathbf{I}_{\text{d}} + 6\mu^2 \left(\frac{\Delta\gamma}{q_{n+1}^{\text{trial}}} - \frac{1}{3\mu + k_1} \right) \hat{\boldsymbol{N}}_{n+1} \otimes \hat{\boldsymbol{N}}_{n+1}, \tag{4.172}$$

with k_1 the isotropic hardening modulus of Section 3.4.3, and where now

$$q_{n+1}^{\text{trial}} = \sqrt{\frac{3}{2}} \left\| \boldsymbol{s}_{n+1}^{\text{trial}} \right\|, \qquad \hat{\boldsymbol{N}}_{n+1} = \frac{\boldsymbol{s}_{n+1}^{\text{trial}}}{\left\| \boldsymbol{s}_{n+1}^{\text{trial}} \right\|}. \tag{4.173}$$

Adopting the same notation, the continuum elastoplastic tangent modulus (3.111), in the same framework of linear isotropic hardening, is

$$\mathbf{C}^{ep} = \mathbf{C}^{el} - \frac{\frac{3}{2}\mathbf{C}^{el} : \hat{\boldsymbol{N}} \otimes \mathbf{C}^{el} : \hat{\boldsymbol{N}}}{\frac{3}{2}\hat{\boldsymbol{N}} : \mathbf{C}^{el} : \hat{\boldsymbol{N}} + \partial_{\mathbf{A}}\Phi \cdot \frac{\partial}{\partial \boldsymbol{\alpha}} \frac{\partial f^p}{\partial \boldsymbol{\alpha}} \cdot \partial_{\mathbf{A}}\Phi}. \tag{4.174}$$

To further simplify this expression we need the relations from Section 3.4.3,

$$\begin{aligned} \frac{\partial \Phi}{\partial \mathbf{A}} &= \frac{\partial \Phi}{\partial \kappa} = -1, \\ \frac{\partial}{\partial \boldsymbol{\alpha}} \frac{\partial f^p}{\partial \boldsymbol{\alpha}} &= \frac{\partial (k_1 \alpha^p)}{\partial \alpha^p} = k_1. \end{aligned}$$

In addition, recalling the deviatoric nature of the normal to the yield surface $\hat{\boldsymbol{N}}$, we know that

$$\begin{aligned} \mathbf{C}^{el} : \hat{\boldsymbol{N}} &= 2\mu \hat{\boldsymbol{N}} \\ \hat{\boldsymbol{N}} : \mathbf{C}^{el} : \hat{\boldsymbol{N}} &= 2\mu. \end{aligned}$$

As a result, the continuum elastoplastic tangent modulus takes the final form:

$$\mathbf{C}^{ep} = \mathbf{C}^{el} - \frac{6\mu}{3\mu^2 + k_1} \hat{\boldsymbol{N}} \otimes \hat{\boldsymbol{N}}. \tag{4.175}$$

It is evident how the two expressions (4.172) and (4.175) do not coincide. Their difference is represented by those terms proportional to the plastic multiplier,

$$\frac{\partial \boldsymbol{\sigma}_{n+1}}{\partial \boldsymbol{\epsilon}^{\text{e trial}}_{n+1}} - \mathbf{C}^{ep} = -\frac{6\mu^2 \Delta\gamma}{q^{\text{trial}}_{n+1}} \left(\mathbf{I}_{\text{d}} - \hat{\boldsymbol{N}}_{n+1} \otimes \hat{\boldsymbol{N}}_{n+1} \right). \tag{4.176}$$

If $\Delta\gamma = 0$, or is very small, then the algorithmic tangent approaches the continuum tangent. This difference is a consequence of the consistency of the numerical method, and for very large steps, where $\Delta\gamma$ is large, it cannot be neglected, and the algorithmic tangent must be used to ensure the appropriate rate of convergence to the global NNR scheme.

Chapter 5

Energy Deposition Simulations

5.1 Introduction and motivations

The phenomenon of bubble growth and dynamics has been extensively studied in the past decades, due to its variety of applications, as mentioned in the introduction of this thesis. Although the macroscopic behavior of the cavitation bubbles has been well characterized in terms of the bubbles dynamics (Philipp and Lauterborn 1998), lots of questions are still open for what concerns their thermodynamics. The reasons behind this are related to the reproducibility of the experiments and the high difficulty of making accurate and meaningful experimental measurements in a system composed by a collapsing bubble with the surrounding water.

One of the most effective techniques to generate controlled cavitation bubbles is by means of a pulsed laser, as shown in Figure 5.1, (Sinibaldi et al. 2019). The bubble cavitation is induced by the a beam, which is focused in a very narrow spot in a chamber filled with water. As a result, plasma is formed, and the high energy density allows for the expansion of the bubble. During the bubble formation, a shock wave is emitted, the so-called breakdown shock wave, which radiates a portion of the energy deposited with the laser beam. This energy is then transformed in heat by means of thermal and viscous effects. The remaining energy is split into kinetic and internal, or potential, energy. When the bubble reaches its maximum radius, the expansion stage finishes, and the collapse stage takes place. understanding how the energy is transformed during this process and how much is radiated by the breakdown wave and then dissipated is a difficult task, that cannot be fully solved with a purely experimental approach, because of the difficulties arising when attempting measurements in the vicinity of the bubble and in the experimental setup in general (Vogel et al. 1999). Only pressure values can be easily accessed through hydrophones probing specific locations in the box, while the velocity and temperature fields remain unknown. This problem may be overcome with the aid of numerical simulations, and it is the motivation leading to the first study presented in this chapter, where the computation of all the energy involved in the process, as well as all the relevant fields, is performed and

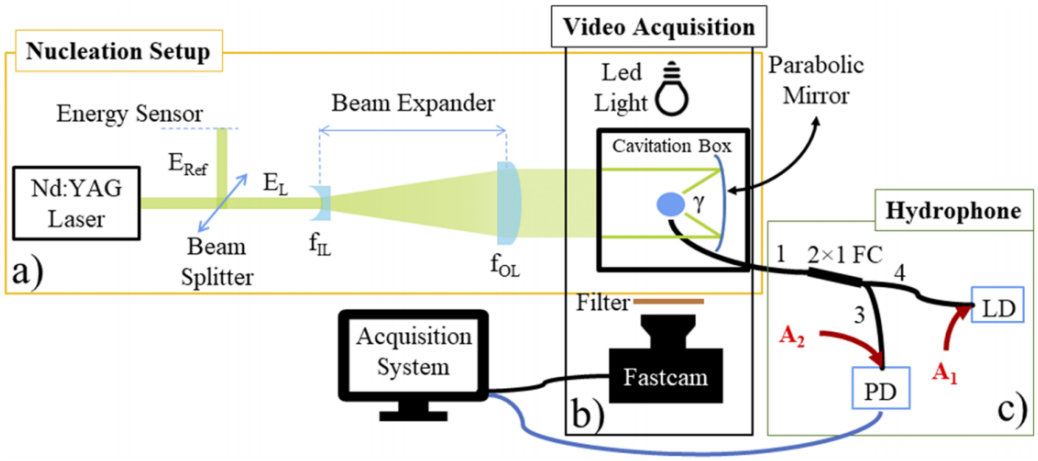

Figure 5.1. Experimental setup as shown in (Sinibaldi et al. 2019). a) The bubble is generated through a pulsed laser, which is expanded and then focused by a parabolic mirror in a chamber filled with water. b) A high-speed camera records the bubble dynamics, and c) some sensors may provide pressure or temperature measurements

analyzed. This study may lead to a better understanding of the energies involved in this process of formation, expansion and subsequent collapse and rebounds of a single vapor bubble, and, in general, of its thermodynamics.

Even though the laser induced cavitation technique is highly controllable, it has a few reproducibility limits, related to the fact that the focusing angle γ in Figure 5.1 has a relevant influence on the shape of the plasma and on its fragmentation. These irregularities in the plasma formation lead to small differences and asymmetries in the subsequent bubble dynamics, which may have a significant effect on measurement of physical quantities. The more the laser beam is expanded, the more the focusing angle γ is large, resulting in less irregularities in plasma shape, as showed in Figure 5.2 (Sinibaldi et al. 2019). When the focusing angle is maximum, the spot where plasma is formed is narrow and circular, and the successive bubble dynamics resemble the dynamics of the Rayleigh-Plesset model (Christopher E Brennen 2014; Plesset 1949). Conversely, when the focusing angle γ is small, the resulting plasma shape is far from spherical, and elongates along a direction perpendicular to the parabolic mirror. The following bubble expansion and dynamics, as well as the breakdown shock wave, are highly influenced by this shape. This fact motivates the second study presented in this chapter, which is focused on the understanding of the expansion stage of the dynamics of vapor bubbles, when such asymmetries in the plasma shape are involved. To this aim, axisymmetric cylindrical numerical simulations are performed and analyzed. The results presented in the corresponding sections are only preliminary results of a study which is still going on.

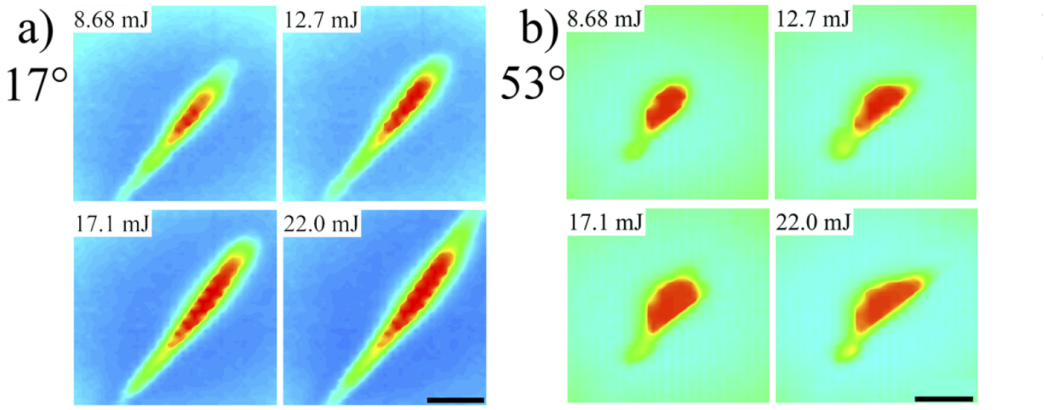

Figure 5.2. Non-spherical plasma formation in the laser deposition experiments in (Sinibaldi et al. 2019). When the deposition is achieved with small focusing angles γ, a highly non-spherical plasma spot is formed (a). When the focusing angle γ is maximum, the plasma shape is more spherical, and leads to spherical bubble dynamics.

5.2 Spherical simulations

Spherical simulations are performed to analyze the energy repartition during expansion of spherical bubbles. The equations solved are the Navier-Stokes with capillarity equations in spherical coordinates and spherical symmetry, meaning that the velocity vector is radial, and all the derivatives with respect to the polar and azimuthal angle are negligible. Hence, the resulting equations are those presented in appendix A.1.

The initial conditions are those of a liquid at rest, with a high energy gaussian spot in correspondence of the center of the sphere, at $r = 0$. These conditions are represented by the following fields:

$$\rho(r,0) = \rho_l, \qquad u_r(r,0) = 0, \qquad e(r,0) = 8\rho_l \left(\theta_0 + (\theta_{dep} - \theta_0)\mathrm{e}^{-\left(\frac{r}{a}\right)^2}\right) - 3\rho_l^2, \tag{5.1}$$

where ρ_l is a density corresponding to stable liquid conditions. The latter in (5.1) is the total energy at time 0 for a van der Waals fluid, when kinetic energy and capillary energy are set to zero, as it is the case here. Since the van der Waals internal energy reads

$$u = 8\rho\theta - 3\rho^2, \tag{5.2}$$

eq. (5.1) is consistent with an initial temperature field of the form

$$\theta(r,0) = \left(\theta_0 + (\theta_{dep} - \theta_0)\mathrm{e}^{-\left(\frac{r}{a}\right)^2}\right), \tag{5.3}$$

where θ_0 is the temperature of the unperturbed liquid, and θ_{dep} is the temperature corresponding to the laser deposition.

The equations are solved in their dimensionless form, with the following di-

mensionless parameters,

$$Re = 8.35, \qquad Cn = 0.00121, \qquad Pe = 0.67; \tag{5.4}$$

and the following reference values, which are computed based on the critical point of water, above which there cannot be coexistence of vapor and liquid phases:

$$\theta_c = 647.096\,\mathrm{K}, \qquad p_c = 22.064\,\mathrm{MPa}, \qquad \rho_c = 322\,\frac{\mathrm{kg}}{\mathrm{m}^3}, \tag{5.5}$$

$$\mathrm{L}_{ref} = 10^{-7}\,\mathrm{m}, \qquad v_{ref} = \sqrt{\frac{p_c}{\rho_c}}\,\frac{\mathrm{m}}{\mathrm{s}}, \qquad t_{ref} = \frac{L_{ref}}{v_{ref}}\,\mathrm{s}. \tag{5.6}$$

The grid used for discretization simulates a sphere with radius $R = 50\,\mathrm{L}_{ref}$, it is uniform with $N = 5000$ nodal points, corresponding to a grid space $\Delta r = R/N$. The time increment used to follow the dynamics of the system is $\Delta t = 10^{-5}\,t_{ref}$.

The study has been carried out with the variation of two parameters, the initial liquid density ρ_l, and the deposition temperature θ_{dep}, while the undisturbed liquid temperature θ_0 is kept constant, $\theta_0 = 0.75\,\theta_c$. Since the qualitative dynamical behavior is similar for all the conditions investigated, all the graphs shown below refer to a single case with $\theta_{dep} = 10\,\theta_c$ and $\rho_l = 2.1\,\rho_c$. The initial density ρ_l is slightly above the saturation density value at that temperature, such that we can also indicate this case as having an initial density of $\rho_l = 1.028\,\rho_l^{sat}(\theta_0)$.

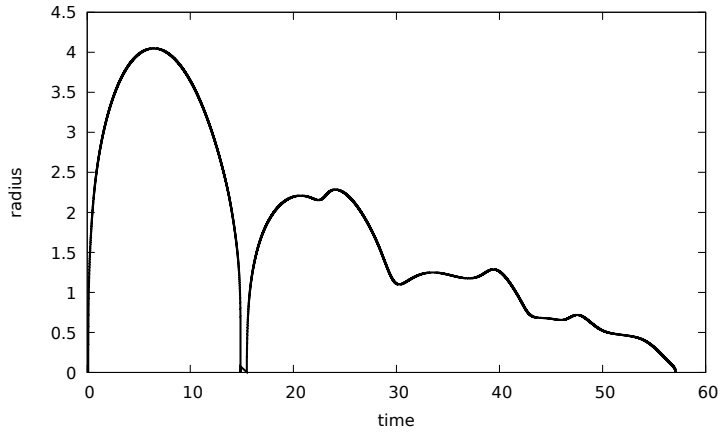

Figure 5.3. Radius evolution over time.

At each time, the radius of the bubble is computed through the relation in (Dell'Isola et al. 2009),

$$R_b = \frac{\int r \left(\frac{\partial \rho}{\partial r}\right)^2 r^2\,\mathrm{d}r}{\int \left(\frac{\partial \rho}{\partial r}\right)^2 r^2\,\mathrm{d}r}, \tag{5.7}$$

and its plot over time is represented in Figure 5.3. The first expansion stage ends when the bubble reaches its maximum radius R_{max}, and the collapse stage takes place. During collapse, the bubble condition become supercritical, and the gas inside the bubble behaves like a non-condensable gas. As a consequence, once the

minimum radius is attained, the bubble rebounds and starts the second expansion stage, which is less energetic. The subsequent dynamics is characterized by a series of rebounds until the bubble is absorbed by the liquid phase and vanishes. The dynamical behavior of spherical bubbles can be approximated with the Rayleigh-Plesset model, and a comparison between RP model and the diffuse interface model is provided in (Magaletti, Marino, et al. 2015).

The initial energy field per unit volume is represented in Figure 5.4, together with the energy field at the time of the first rebound. As it can be seen from the plot, most of the energy inserted through deposition is radiated away. Integration of the initial profile in Figure 5.4 over the volume of the sphere gives the initial energy deposited in the system.

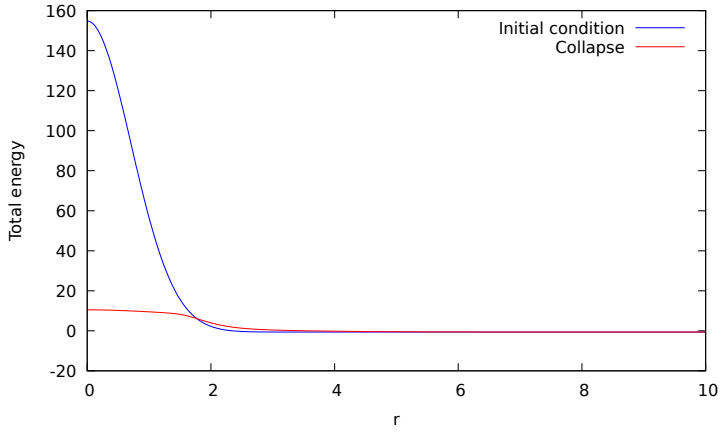

Figure 5.4. Initial total energy field: Two profiles are shown, the initial energy profile corresponding to eq. $(5.1)_3$ and a profile taken when the bubble is collapsing.

Figure 5.5 shows the density and velocity profiles during the expansion stage of the dynamics, when the vapor nucleus is formed and the breakdown wave has been emitted. The kinetic and capillary energy evolution in time is displayed in Figure 5.6. It is evident how the capillary energy does not play any relevant role in the energy balance, so that its contribution can be easily neglected. The kinetic energy evolution reaches a local minimum in time when the radius of the bubble attains its maximum. This happens because all the kinetic energy related to the bubble expansion is transformed into potential energy of the bubble itself. For this reason, we shall look at the kinetic energy evolution limited to the bubble. This can be computed, from the numerical simulation results, by limiting the integral of the kinetic energy density to the volume of the bubble, through the relation

$$K_b(t) = \int_0^{R_b} \frac{1}{2}\rho(r,t)u_r(r,t)^2 4\pi r^2 \,\mathrm{d}r. \tag{5.8}$$

The result of this calculation is plotted over time in Figure 5.7, and shows how the kinetic energy of the bubble vanishes when the expansion phase approaches the maximum radius. By applying a simple energy balance, when the kinetic energy

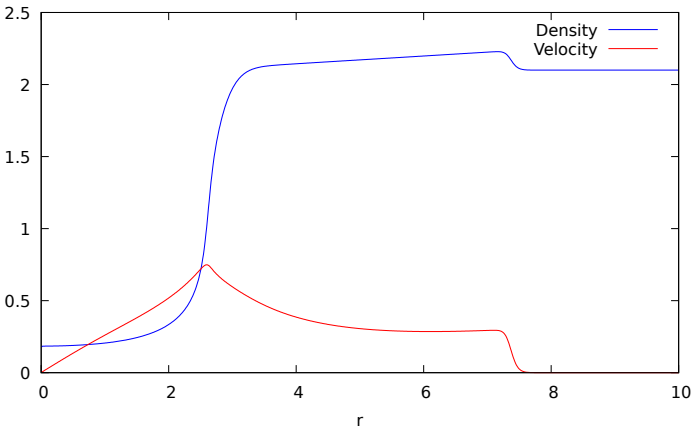

Figure 5.5. Density and velocity profiles at time $t = 1$, during the bubble expansion stage. It is clear how a vapor phase is forming in correspondence with the center of the domain at $r = 0$. It should be noted that the velocity profile has two peaks, corresponding to the interface velocity and the compression breakdown shock wave propagating within the liquid phase. The former indicates that the bubble is still expanding, while the latter shows that the breakdown wave has already been emitted.

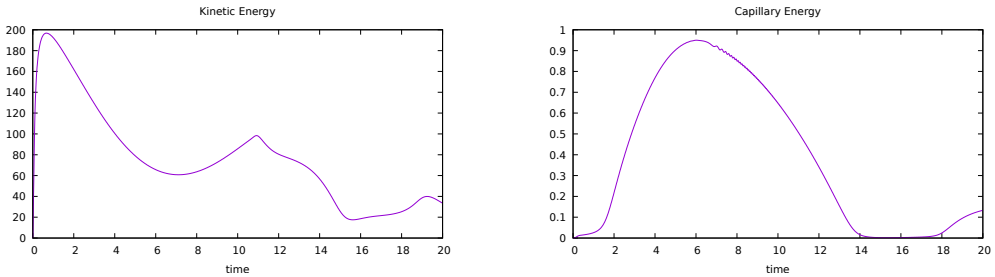

(a) **(b)**

Figure 5.6. Kinetic and capillary energy of the system as a function of time

of the bubble vanishes, its potential or internal energy attains its maximum, and corresponds to the total energy. From an experimental point of view, since the temperature and density of the fluid cannot be measured easily, the following relation is used to compute the value of the maximum potential energy:

$$E_b^{RP} = (p_l - p_v)\, V_b, \tag{5.9}$$

where p_l, p_v and V_b are, respectively, the unperturbed liquid pressure, the saturation pressure of vapor at the experiment temperature, and the bubble volume. This relation comes from the Rayleigh-Plesset model, and is often used in experimental works (Sinibaldi et al. 2019; Vogel et al. 1999). It represents the energy required to increase the bubble volume to V_b, and corresponds to the total energy required to form a bubble of volume V_b minus the energy required to form an interface whose surface tension is σ, from the classical nucleation theory (Christo-

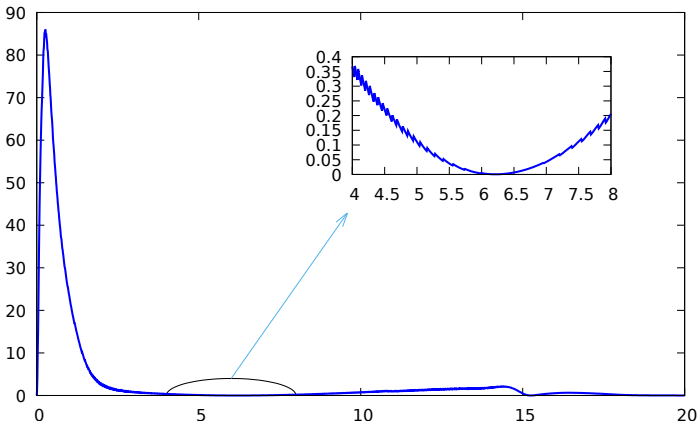

Figure 5.7. Bubble kinetic energy over time, computed as in (5.8). The inset clearly shows how the bubble kinetic energy approaches zero when the bubble radius is maximum, around $t = 6.4$.

pher E Brennen 2014). This expression has the drawback of not being sufficiently accurate, since the vapor pressure inside the bubble is far from the saturation pressure at the ambient temperature, the reason being the fact that high temperatures and phase changes are involved. Within the framework of numerical analysis, a more accurate estimate should consider the variation of pressure within the vapor phase, such that equation (5.9) transforms into

$$E_b^{\text{pot}} = (p_l - \bar{p})\, V_b, \qquad \bar{p} = \frac{\int p(r)\, \mathrm{d}V_b}{V_b}, \tag{5.10}$$

where $\bar{p}$ is the average pressure in the vapor bubble. A comparison of the two expressions is represented in Figure 5.8. In particular, the difference between the two is not negligible when the maximum radius is attained ($t \approxeq 6.4$).

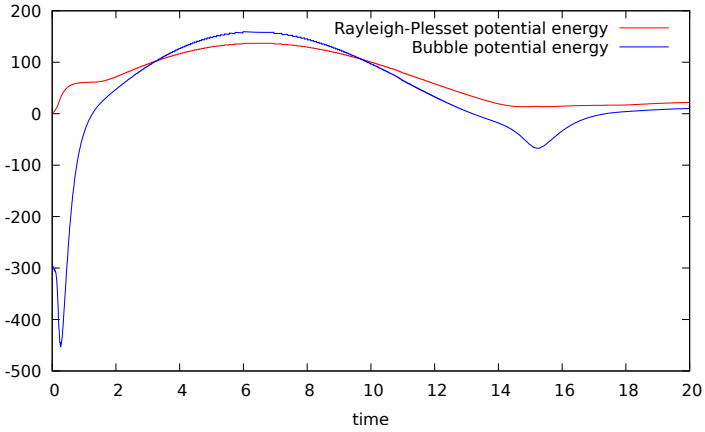

Figure 5.8. Comparison between the bubble potential energy from Rayleigh-Plesset or CNT (5.9), and the corrected potential energy (5.10) as plotted against time

A complete balance of the energies involved in the dynamic of growth and

collapse of bubbles should take into account the energy radiated away from the bubble by the breakdown shock wave. A way to compute this energy is illustrated in the book (Cole and Weller 1948), and used in the experimental work of Vogel (Vogel et al. 1999). The limits of the experimental approach concern the impossibility to probe locations near the spot where the laser is focused and the bubble is generated. For this reason, the hydrophones are quite far away from the bubbles, and an expression to account for the energy dissipated during the movement of the breakdown wave, before reaching the hydrophones, is needed. This problem can be easily overcome with the aid of numerical simulations. Locations near the hot spot can be probed and the pressure wave can be measured. As a result, it is possible to adopt directly the relation in (Cole and Weller 1948) for the energy radiated by a shock wave at a certain distance R_s from the breakdown center,

$$E_s = \frac{4\pi R_s^2}{\rho_l c_l} \int_0^\tau p(t)^2 \, \mathrm{d}t. \tag{5.11}$$

In this expression, c_l is the local thermodynamic speed of sound, and can be computed, for a van der Waals fluid, as (Zhao et al. 2011)

$$c = \sqrt{\left(\frac{\partial p}{\partial \rho}\right)_s} \tag{5.12}$$

$$= \sqrt{(1+\delta)\frac{p + a\rho^2}{\rho(1-b\rho)} - 2a\rho} \tag{5.13}$$

$$= \sqrt{\frac{32\theta}{(3-\rho)^2} - 6\rho}, \tag{5.14}$$

$$c_l = \sqrt{\frac{32\theta_0}{(3-\rho_l)^2} - 6\rho_l} \tag{5.15}$$

where $\delta = 1/3$ has been chosen. Probes located at different distances from the bubble center register the pressure of the shock wave during time. These pressures are represented in Figure 5.9. Once the pressure profiles are obtained, it is possible to compute the radiated energy through Eq. (5.11).

In what follows, results gathered from 12 different numerical simulations, obtained varying the initial conditions parameters ρ_l and θ_{dep}, are presented. A variation in the density of the liquid ρ_l is reflected in a variation of the external initial pressure p_l in the liquid phase, such that a density increase corresponds to a pressure increase. Figure 5.10 represents the influence of the initial conditions on the resulting maximum bubble radius at the end of the first expansion stage. The same behavior is observed in experimental studies, such as (Sinibaldi et al. 2019). The energy radiated by the initial breakdown wave, as a function of the initial liquid density (pressure) and the energy deposited is plotted in Figure 5.11, showing a quadratic trend. The portion of energy deposited through the laser, which goes into bubble potential energy at maximum expansion, as computed from the Rayleigh-Plesset potential energy (5.9), and based on data from

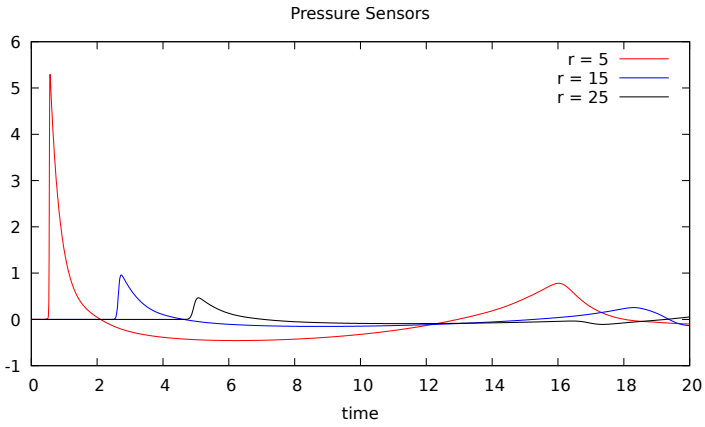

Figure 5.9. Pressure profiles as functions of time, for different radial distances from the bubble center. It it evident how the pressure wave dissipates its energy as it travels within the fluid

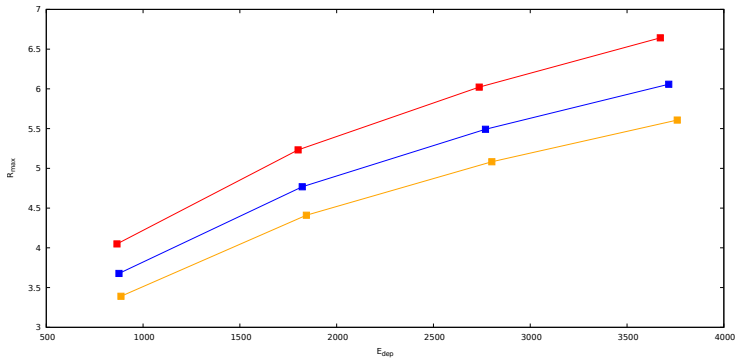

Figure 5.10. Maximum radius attained in the simulations during the first expansion stage, as a function of the energy deposited in the system and the initial density (pressure) in the liquid. The initial pressure in the fluid increases going from red to orange, and is reflected by the fact that larger radii are attained, at fixed energy deposition, for lower values of the external pressure.

the numerical simulations, together with their linear regressions, is represented in Figure 5.12. For increasing liquid density (from blue to green), the graph clearly shows an increasing percentage of deposited energy stored as potential energy by the bubble. At fixed liquid density, for increasing deposited energy, the potential energy stored in the bubble at maximum expansion increases linearly, with excellent accuracy.

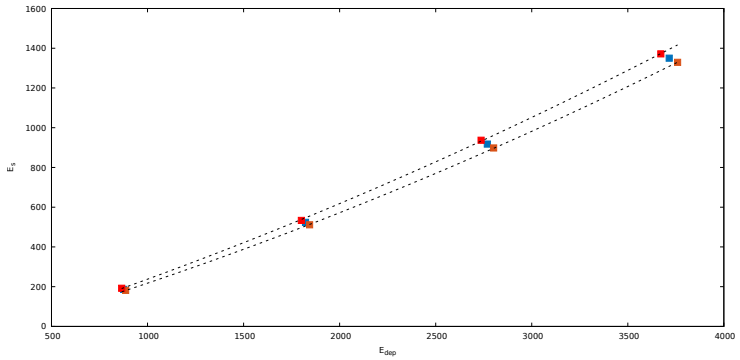

Figure 5.11. Energy radiated by the breakdown wave, obtained from (5.11). The energy values do not differ that much depending on the initial density (pressure) in the liquid (external pressure increases going from red to orange), but the graph shows a quadratic trend in the increase of radiated energy as a function of the initial energy deposited in the system.

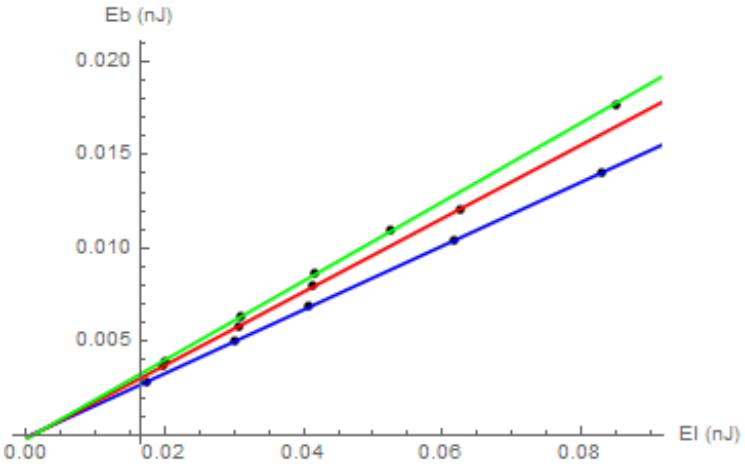

Figure 5.12. Bubble potential energy (E_b^{RP}) as a function of the initial energy deposited in the system, for different initial conditions. Blue to green shows increasing external liquid pressure.

5.3 Cylindrical axisymmetric simulations

To better understand the dynamics of growth and expansion stages of a cavitation bubble, in those situation presented in the introduction of this chapter, where the plasma inducing the vapor bubble nucleation has a shape far from spherical, and rather elongated in a direction perpendicular to the focusing mirror, we investigated these condition with axisymmetric cylindrical simulations. The revolution axis for these configurations will be the one along which the plasma shape is scattered.

In an axisymmetric cylindrical simulation, the equations solved are the usual Navier-Stokes-Korteweg equations, in cylindrical coordinates, with the assump-

tion of vanishing derivatives with respect to the revolution angle θ, and vanishing velocity along the same direction u_θ. The domain of simulation is indicated with the grid pattern in Figure 5.13, and consist in the z-r plane of symmetry. The

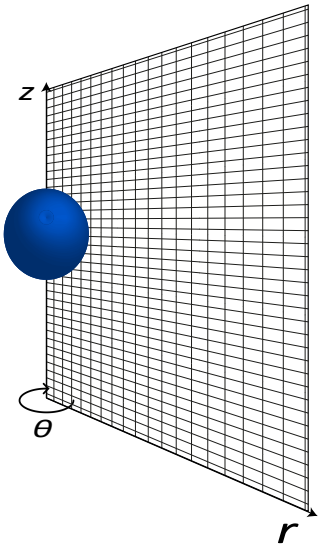

Figure 5.13. Axisymmetric cylindrical simulation configuration. All variations along θ direction are disregarded, and the velocity component $u_\theta = 0$. The simulated domain is only the z-r plane.

corresponding equations in cylindrical coordinates are written in the appendix A.2.

The configuration investigated are two, and they have similar initial conditions. In both cases, the dimensionless parameters and reference and critical values are the same, and equal to the ones used in the spherically symmetric simulations presented above,

$$Re = 8.35, \qquad Cn = 0.00121, \qquad Pe = 0.67; \tag{5.16}$$

and

$$\theta_c = 647.096\,\mathrm{K}, \qquad p_c = 22.064\,\mathrm{MPa}, \qquad \rho_c = 322\,\frac{\mathrm{kg}}{\mathrm{m}^3}, \tag{5.17}$$

$$\mathrm{L}_{ref} = 10^{-7}\,\mathrm{m}, \qquad v_{ref} = \sqrt{\frac{p_c}{\rho_c}}\,\frac{\mathrm{m}}{\mathrm{s}}, \qquad t_{ref} = \frac{L_{ref}}{v_{ref}}\,\mathrm{s}. \tag{5.18}$$

The initial density field is taken as uniform, with $\rho(r,z,0) = \rho_l = 2.1\,\rho_c$, and the fluid is at rest in both the configurations. The only difference is in the initial shape assumed for the temperature field, which mimics two different plasma configurations.

In the first case, three identical high temperature spots are initialized in the system. The three spots are located at different heights on the axis of revolution of the system, indicated with the direction $\hat{\mathbf{z}}$. As a result, the initial temperature field

is the summation of three non-overlapping gaussian functions with same variance and different location with respect to the axis.

In the second case, the three spots are located at different heights on the axis of revolution of the system, as in the case above, but, in addition, they have different dimensions (variance). The initial temperature field is then the superposition of three gaussian functions, partially overlapping, with different variance and different location with respect to the axis.

The subsequent dynamics is represented in the pictures in Figure 5.14 and Figure 5.15, where a Schlieren-like field is plotted. This field allows a better visualization of the breakdown shock wave propagating in the liquid, by magnification of the places where the density gradient norm is higher. This method, which allows a sort of numerical Schlieren visualization technique, is described in (Boukharfane et al. 2018; Hadjadj and Kudryavtsev 2005). The field plotted is

$$S = 0.8 \exp\left(-C\,|\nabla\rho|^2\right) \tag{5.19}$$

where the constant C is often related to the inverse of the maximum value of the density gradient norm in the domain.

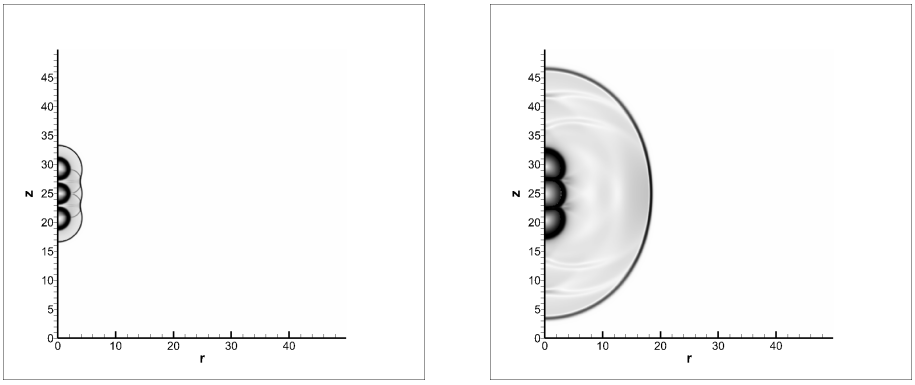

(a) **(b)**

Figure 5.14. Schlieren visualization of the breakdown wave for the first case, where the three high temperature spots are clearly visible in the inset (a). The breakdown waves of the single bubbles interact with each other and, after some time, their external envelope is merged, resulting in a quasi-spherical propagating wave. The internal waves arising from the single bubbles are trapped in the interior of this envelope and continue propagating within the liquid phase, until they dissipate their energy.

To identify the profile of the pressure wave moving within the liquid phase, 6 different locations are probed, and the relative pressure in the liquid is computed as a function of time. These results are represented in Figure 5.16 and Figure 5.17, for both the two cases described above. Analysis of the pressure profiles measured at prescribed distances and angles with respect to the plasma deposition axis could lead to a better understanding of the first stages of shock wave emission and propagation, and may serve as a support to reconstruct the initial bubbles

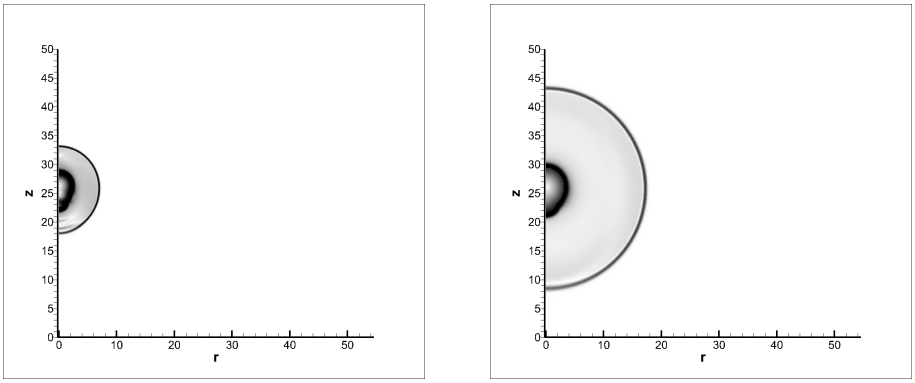

(a) **(b)**

Figure 5.15. Schlieren visualization of the breakdown wave for the second case, where the three different spots are close together. The resulting shock wave propagation is almost perfectly spherical, since its behavior is governed by the most intense breakdown, which is the one of the more energetic spots on the $\hat{\mathbf{z}}$ axis. In the panel (a) a small interaction between emerging waves is visible in the lowest part.

shape and disposition *a posteriori*, which are hard to determine from experiments, especially in those cases where the plasma deposition is highly non-spherical. Thus, this preliminary and qualitative results may serve as a starting point for a *reverse engineering* problem in which results from numerical simulations can help in the determination of the initial bubble shape in the experiments, by comparing the pressure profiles measured.

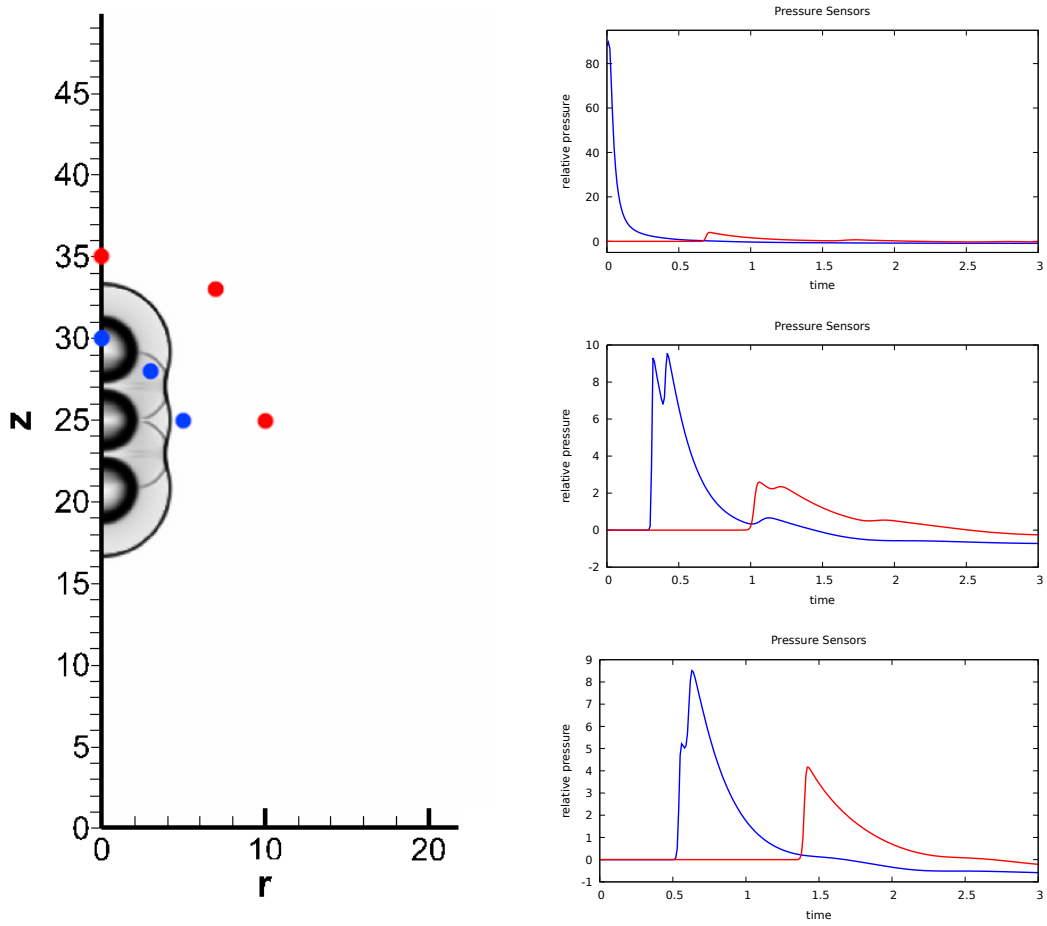

Figure 5.16. On the left, first stages of the breakdown emission and propagation, for the first case described above, with the probing locations where the pressure signals are measured in time. On the right, from top to bottom, the resulting pressure signals as functions of time, for the probes located at 90, 45 and 0 degrees with respect to the $\hat{\mathbf{r}}$ axis (counter-clockwise).

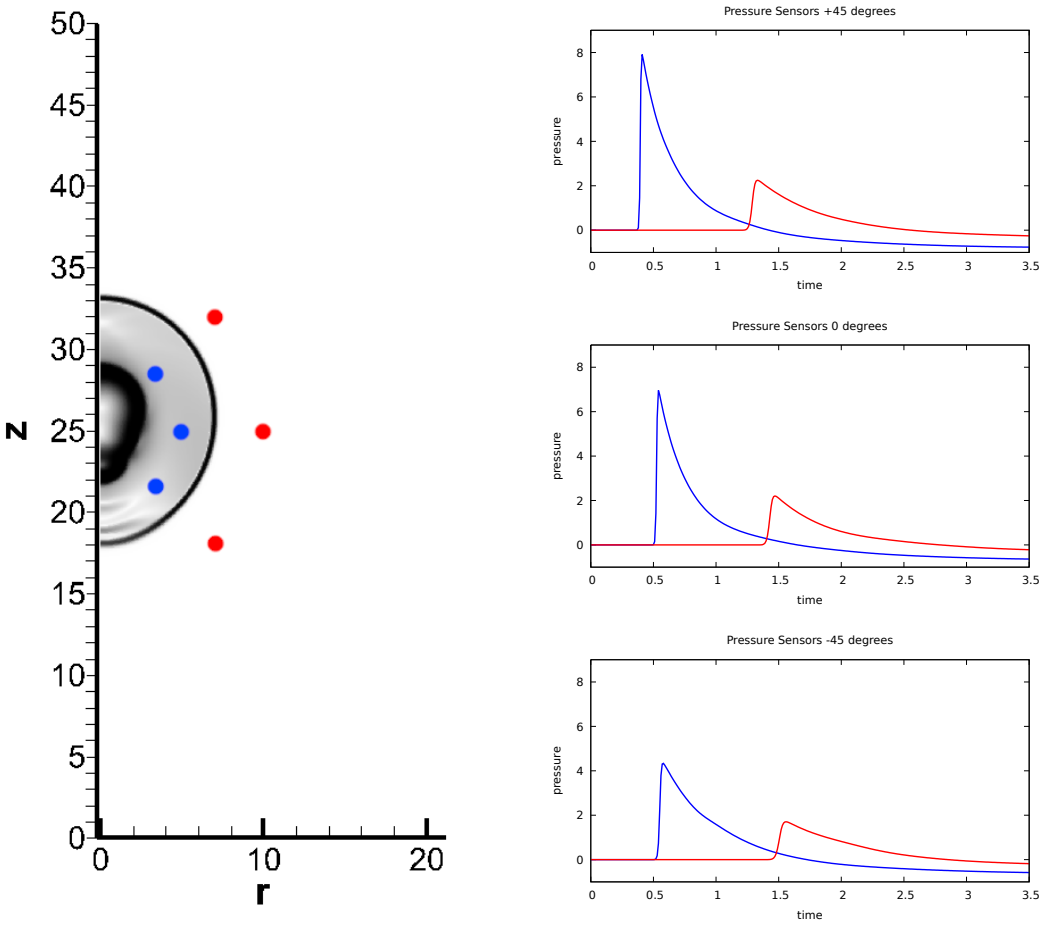

Figure 5.17. On the left, first stages of the breakdown emission and propagation, for the second case described above, with the probing locations where the pressure signals are measured in time. On the right, from top to bottom, the resulting pressure signals as functions of time, for the probes located at +45, 0 and -45 degrees with respect to the $\hat{\mathbf{r}}$ axis (counter-clockwise).

Chapter 6

Cavitation Bubble Implosion Near Solid Surfaces

6.1 Introduction and motivations

The cavitation problem introduced and outlined in previous sections will be now analyzed in details, and a complete description of the phenomenon will be provided, together with the results obtained. Bubble collapse near solid boundaries is an extremely complicated physical phenomenon, which involves high speeds, high energies and very small timescales and lengthscales. The interaction between a single collapsing bubble and a material surface has been extensively studied through experimental observation, which have some intrinsic problems and limitations (some of these have been discussed in previous Chapter 5), but served as a starting point for the work developed in this thesis. Although in the following we are mainly concerned with the interaction between a single bubble evolution and the presence of a solid metal surface, thus with the most classical of the problems related to cavitation, recent experimental advances showed how cavitation and its study could have a huge impact on many different applications. Among the others, it can be successfully used in industrial cleaning processes (Brems et al. 2013), to synthesize nanomaterials (Xu et al. 2013), to comminute kidney stones in shock wave lithotripsy (Zhong 2013) and enhance the drug permeability of human tissues or cell membranes (Christopher Earls Brennen 2015; Coussios and Roy 2008).

More specifically, for what concerns the study of bubble dynamics and implosion near solid boundaries, using both experimental and computational methods, different materials have been investigated in the past, including rigid walls (E. Brujan et al. 2002; Johnsen and Colonius 2009; Tomita and Shima 1986; Zhang et al. 1993), elastic solids (E.-A. Brujan et al. 2001), soft tissues (Kodama and Takayama 1998) and free liquid-gas interfaces (Robinson et al. 2001). Damage and plastic deformation occurring on the material surface due to cavitation has also been investigated (Dular, Delgosha, et al. 2013; Dular, Požar, et al. 2019; Philipp and Lauterborn 1998), and finally some works regarding the numerically coupled

dynamics of a fluid-solid system emerged in recent years and days (Cao et al. n.d.; Chahine and Hsiao 2015). The models used in the numerical simulations presented in the articles above though, are all macroscopic models, that are not accurate when dealing with small bubbles (nanometric up to micrometric). Moreover, they do not have a refined thermodynamic description, to account for phase changes, compressibility effects and capillary effects, all things playing a relevant role in the dynamics of bubbles and surrounding liquids.

In what follows, we analyze some numerical simulations, where the fluid behavior is described by the model outlined in Chapter 2, and the interaction with an elastoplastic solid wall (*cf.* Section 3.3) is treated in a one-way interaction framework, by letting the solid respond to the loads applied by the fluid on its surface.

6.2 Simulation setup

In experiments regarding a single bubble evolution, the bubble is spark or laser generated, which means it is formed due to the high energy focused in a very narrow zone in the water box. After its formation, the bubble expands up to a maximum radius and then the collapse phase starts, which ends when the bubble is finally absorbed by the liquid, and no vapor phase exists anymore. The simulations performed and analyzed in this chapter consider the bubble at maximum radius as the initial condition for the fluid dynamics, and let the collapse phase evolve as a result of the fact that the pressure in the liquid phase (water) is set to be much higher than the actual equilibrium pressure that can be found from thermodynamics. This condition in the system is usually referred to as *overpressure*, and the consequent bubble collapse is called an overpressure-induced bubble collapse, opposed to the numerical condition in which the collapse stage is triggered by a shock, for instance in (Magaletti, Gallo, et al. 2016).

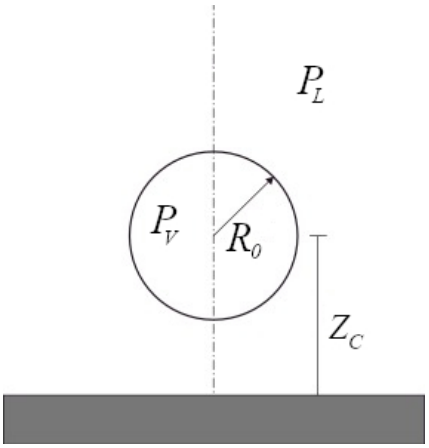

Figure 6.1. Initial 2D cylindrical configuration in the fluid domain. The bubble is initially located on the axis, at a certain height Z_c. The pressure in the liquid is p_L, whereas the pressure in the bubble is the vapor pressure p_v.

All the simulations are performed in a 2D cylindrical axisymmetric framework (*cf.* appendix A.2), the one already mentioned in the previous Section 5.3. Suppose our fluid domain is the square $\Omega = [0, R] \times [0, H] \in \mathbb{R}^2$, representing the two-dimensional domain in which axisymmetric cylindrical equations are discretized. Then the left vertical edge of the square would be the axis around which the domain should be revolved to obtain the three-dimensional solution, and we indicate this portion of the boundary as

$$\partial\Omega_{axis} := \partial\Omega \cap \left\{ \mathbf{x} \in \mathbb{R}^2 \,|\, x = 0 \right\}.$$

The remaining edges represent the boundaries of the cylindrical box obtained revolving the domain around the axis of symmetry $\partial\Omega_{axis}$, and we indicate them with $\partial\Omega_{ext} := \partial\Omega \backslash \partial\Omega_{axis}$. The boundary conditions adopted for the axisymmetric problem presented in Chapter 6 and complementing equations (4.26) are of the Dirichlet type for the velocity vector $\mathbf{u}$, of Neumann type for the energy and fluxes on $\partial\Omega_{ext}$, and of no normal flux on the axis of symmetry $\partial\Omega_{axis}$:

$$\mathbf{u} = 0 \quad \text{on } \partial\Omega_{ext} \qquad\qquad \mathbf{u} \cdot \mathbf{n} = 0 \quad \text{on } \partial\Omega_{axis}, \tag{6.1}$$

$$\mathbf{q}_e \cdot \mathbf{n} = 0 \quad \text{on } \partial\Omega \qquad\qquad \nabla\rho \cdot \mathbf{n} = 0 \quad \text{on } \partial\Omega; \tag{6.2}$$

where $\mathbf{n}$ identifies the outer normal to the boundary and the last condition $\nabla\rho \cdot \mathbf{n} = 0$ on $\partial\Omega$ is usually referred to as the *interface contact angle* condition in literature.

The initial condition in terms of fluid dynamic fields are the following,

$$\rho(r, z, 0) = \rho_v + \frac{1}{2}\left(1 + \tanh\left(\frac{\sqrt{(r - R_c)^2 + (z - Z_c)^2} - R_0}{h}\right)(\rho_l - \rho_v)\right), \tag{6.3}$$

$$\mathbf{u}(r, z, 0) = \mathbf{0}, \tag{6.4}$$

$$\theta(r, z, 0) = \theta_0, \tag{6.5}$$

with ρ_v and ρ_l the initial vapor and liquid density, respectively, R_c and Z_c the bubble center position, with $R_c = 0$ (bubble on the axis of symmetry), and θ_0 the initial temperature, taken as uniform in the domain. Since the density profile is initialized with an hyperbolic tangent function, h represents the width of the interface between liquid and vapor. The initial configuration is therefore as illustrated in Figure 6.1, with an initial radius R_0 and the bubble center located on the axis (radial distance $r = 0$) at a specific initial height Z_c. The pressure in the liquid $p_l(\rho_l, \theta_0)$, which is given by the van der Waals equation of state, as a function of density and temperature, is set to be higher than the equilibrium pressure, which is given by the Young-Laplace equation

$$p_v^{eq} - p_l^{eq} = \frac{2\sigma}{R_0}, \tag{6.6}$$

where σ is the surface tension.

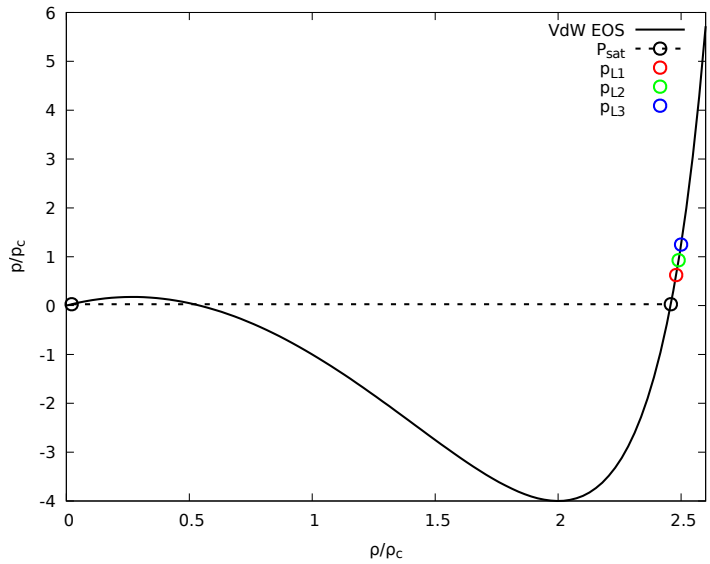

Figure 6.2. Initial overpressure conditions in the liquid represented on a pressure-density plane, with the corresponding van der Waals equation of state at the initial temperature of the system. Colors correspond to the three different conditions explored, red is the less energetic whereas blue is the most. The saturation pressure is also represented in the graph, while the equilibrium pressure in the liquid phase is not, since it approaches the saturation value for the cases considered.

The overpressure with respect to the equilibrium pressure derived from (6.6) is the quantity driving the process, which is also influenced by the initial distance from the wall Z_c. Thus, we classify the simulations performed by means of these two parameters, fixing the initial radius R_0 and varying the overpressure and the initial distance from the solid wall. The former is defined as the difference between the actual initial liquid pressure, which is a function of the initial density and temperature, and the equilibrium liquid pressure derived from (6.6), normalized with the equilibrium pressure $\frac{\Delta p}{p_l^{eq}} = \frac{p_l - p_l^{eq}}{p_l^{eq}}$. The more the overpressure, the more the collapse will be energetic, leading to higher loads at the wall. The three configurations examined within the presented simulations are characterized by the following values of overpressure, $\frac{\Delta p}{p_l^{eq}} \approx 28.5, 42.8, 58$. For a visual representation of the initial condition in terms of overpressure, in Figure 6.2 the van der Waals equation of state (EOS) used in the simulations is depicted. In this image, the three different values of actual initial pressure in the liquid are highlighted, together with the dashed line representing the saturation pressures at the temperature of simulation ($\theta_0 = 0.5$). The saturation pressure is the value of pressure below which a vapor phase could emerge within the liquid, at a given temperature, and it does not differ much from the equilibrium pressure, at the scales analyzed with this simulations ($R_0 = 1\mu$m).

The initial distance from the wall, instead, influences the dynamics of the bub-

ble in terms of topological and geometrical configurations assumed by the bubble during the collapse stage and subsequent rebounds. Two initial distances have been studied, corresponding to a dimensionless distance to initial radius ratio of $\frac{Z_c}{R_0} = 1.2, 1.5$.

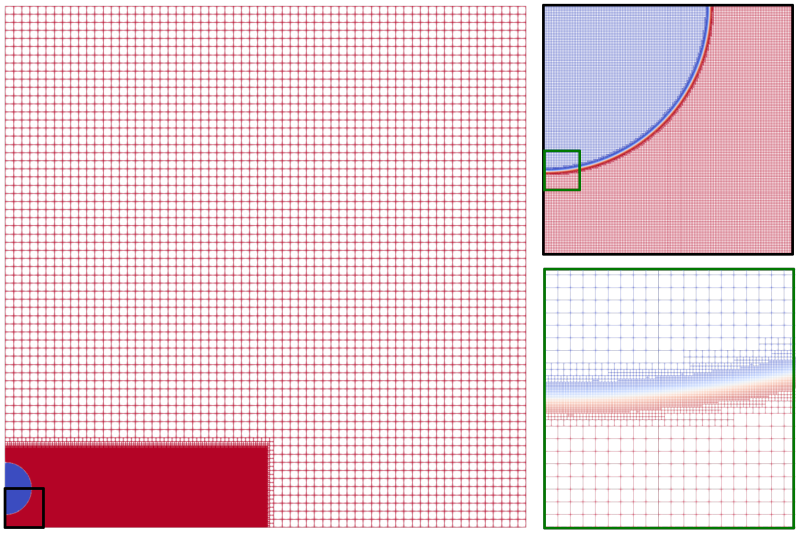

Figure 6.3. Initial grid configuration. In the left panel, the whole domain is visible, with the two zones with different maximum cell dimension. The zone where the bubble is located at the start is extended in the radial direction to account for a sufficiently high resolution to capture the pressure wave which radiates in the liquid phase. The two other panels on the right are progressive zooms of the view on the left. In the top right corner, half bubble is visible, while in the bottom right corner the interface is magnified, and the minimum grid dimension is clearly visible.

One of the major advances in this thesis has been the adoption of a diffuse interface method for the simulation of bubble dynamics in conjunction with a numerical technique called automatic grid refinement. This has been made possible thanks to the use of the high performance computing (HPC) finite element library deal.II (Arndt et al. 2020), that is a general purpose finite element library which has a feature (among the others) that allows automatic grid refinement, *i.e.* the possibility of automatically refine or coarsen the cells of a computational grid by following a user-defined criterion. This feature resulted to be fundamental in the simulation of bubbles through the diffuse interface model, since the smallest lengthscales to be solved in the computational grid is fixed across the scales, and is by orders of magnitude lower than the bubble dimensions, making the investigation of bubbles larger than few nanometers practically impossible or extremely computationally demanding. This approach permitted the investigation of micrometric bubbles dynamics in a decent time and with reasonable computational costs. The Initial grid configuration that was used in all the simulations described below is represented in Figure 6.3. Two zones with a fixed and prescribed maximum grid dimension are defined. The inner zone, the one in which

the bubble is located at the start, has also a minimum prescribed grid dimension, which is tuned to allow for the presence of enough grid points within the bubble interface, that constitutes the smallest lengthscale to be solved numerically. Once these threshold values are defined and the simulation is initialized, the library automatically deals with grid refinement, based on the criteria specified by the user. The general expression for the grid size in a square domain with length L is $\Delta x = L/2^n$, where n is the number of times a cell is refined. As a consequence, the maximum grid size allowed in the simulations is in the outer part, and corresponds to ($n = 6$, $L = 200$) 3.125, which in physical units is $\approx 0.3\,\mu$m, while the minimum grid, placed at the bubble interface, corresponds to ($n = 15$, $L = 200$) ≈ 0.006, which is $\approx 0.6\,$nm. Making a complete simulation with a uniform grid with the minimum grid size required by the physics of the problem, following the entire dynamics of the system, would be practically impossible, requiring more than 1 billion cells. In this case, this number has been reduced to 400000 (this number refers to the initial configuration, during collapse the number of cells required grows), leading to huge savings, and the possibility of actually simulating this phenomenon at such scales. As mentioned in 4.4.1, we used Kelly error estimator to evaluate which cells must be refined and coarsen. The refinement strategy has been applied to the density field only, since numerical experiments carried out during the thesis have shown that the best convergence and stability of the solution is achieved when the whole mesh is refined according to this field only.

The solver used in the numerical implementation of the Diffuse Interface model is GMRES (generalized minimal residual method) with a Block Jacobi preconditioner. The solution to the linear system is considered at convergence once a tolerance of 10^{-10} is met, whereas the Newton iteration is considered at convergence once the residual vector norm is less than 10^{-8}.

6.3 Results

In what follows, we will refer to the results of the numerical simulations whose configuration has been described in the latter section. Six total cases have been studied, and are classified in terms of relative height of the bubble center with respect to the wall, $Z_c^* = Z_c/R_b = 1.2, 1.5$, and of the overpressure value $p^* = \frac{\Delta p}{p_l^{eq}} \approx 28.5, 42.8, 58$ The initial temperature is always the same, and is uniform, $\theta_0 = 0.5$. The initial radius is $R_b = 1\,\mu$m and the initial vapor density ρ_v is the saturation density of vapor at the temperature θ_0.

The equations are solved in their dimensionless form, with the following dimensionless parameters,

$$Re = 8.35, \qquad Cn = 0.00121, \qquad Pe = 0.67; \tag{6.7}$$

and the following reference values, which are computed based on the critical point

of water, above which there cannot be coexistence of vapor and liquid phases:

$$\theta_c = 647.096\,\mathrm{K}, \qquad p_c = 22.064\,\mathrm{MPa}, \qquad \rho_c = 322\,\frac{\mathrm{kg}}{\mathrm{m}^3}, \tag{6.8}$$

$$\mathrm{L}_{ref} = 10^{-7}\,\mathrm{m}, \qquad v_{ref} = \sqrt{\frac{p_c}{\rho_c}}\,\frac{\mathrm{m}}{\mathrm{s}}, \qquad t_{ref} = \frac{L_{ref}}{v_{ref}}\,\mathrm{s}. \tag{6.9}$$

The following results are categorized by physical phenomena.

Topology change comparison

The first characteristic behavior to be observed is the topology change occurring during the collapse phase. This phenomenon has been widely described and analyzed in both experimental and numerical studies. During the collapse stage of the bubble dynamics, the liquid velocity field is directed towards the center of the bubble. In free-space conditions, where there are no disturbances near the collapsing bubble, the whole dynamic has a spherical symmetry, whereas in the case in which a wall is put nearby the bubble, the velocity field between the bubble and the wall, due to the presence of the wall itself, acting as a physical obstacle, is way lower in magnitude than the velocity field above the bubble. This latter condition leads to a dynamic that loses, in general, its symmetries, but can be simplified and treated as axisymmetric. As a consequence of the presence of the wall, a liquid jet is developed within the domain, and is directed vertically towards the wall surface. Therefore, it pierces the vapor/gas bubble, changing its topology from spherical to toroidal, passing through different quasi-spherical geometries. This behavior is also representative of the simulations carried out in this thesis, where the collapse stage is triggered by an overpressure. It would not have been possible to observe such a phenomenon if the bubble dimensions were lower than the used ones, because at smaller scales (nm) the surface tension is so strong that it keeps the bubble geometry spherical, even in the case where very high pressures are involved, as in this cases.

The topology change phenomenon is depicted in Figure 6.4 and Figure 6.5, where two different simulations are compared. The two cases differ for the initial height, which is the most relevant parameter to take into account when observing this behavior, as noted in the experimental work (Philipp and Lauterborn 1998). It is indeed the initial bubble distance from the wall that influences the non-sphericity of the collapse, in terms of velocity field in the liquid. In the Figure 6.5 in fact, which is the case with higher initial distance, the topology change is slower and smoother, and the toroidal topology of the vapor bubble is hardly reached only at the end of the dynamics.

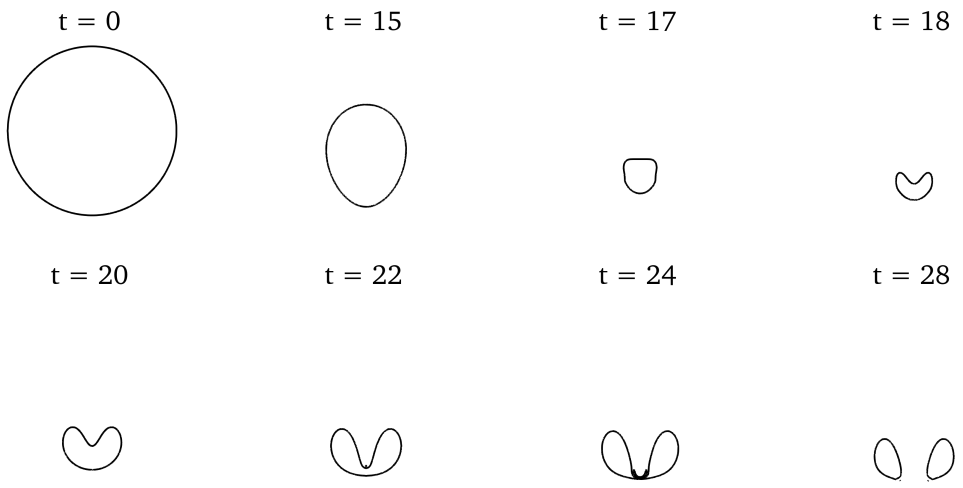

Figure 6.4. Change of geometry and topology during collapse for the case with overpressure $p^* = 42.8$ and initial bubble distance ratio from the wall $Z_c^* = 1.2$. Snapshots taken at different times.

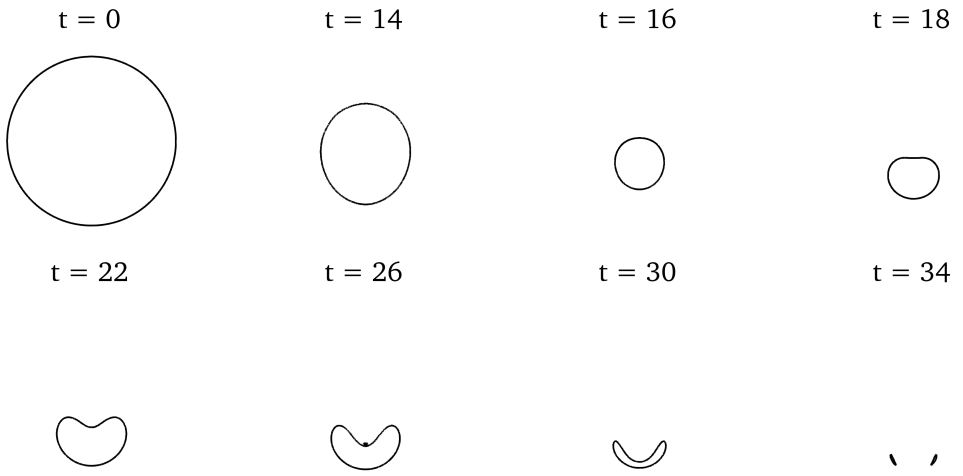

Figure 6.5. Change of geometry and topology during collapse for the case with overpressure $p^* = 42.8$ and initial bubble distance ratio from the wall $Z_c^* = 1.5$. Snapshots taken at different times.

Liquid jet comparison

The liquid jet developed during the collapse phase of the bubble dynamics, due to the presence of the wall, is observed in the simulations performed. The liquid jet is clearly more intense when the bubble is nearer to the wall, because the asymmetry in the domain is more pronounced, and the relative velocity between the lowest and the highest portion of the bubble is larger. A comparison on the jet geometry is provided in Figure 6.6, where two simulations with different overpressures but same initial distance from the wall are presented ($Z_c = 1.2$). On the

left panel of each picture, a Schlieren-like visualization (5.19) of the bubble allows the magnification of those zones where the density gradient is high, namely the bubble interface, and the vectors are representative of the velocity vector field, with the vector length proportional to the velocity magnitude. On the right, the density contour plot is represented, together with a solid black contour line, delimiting the zone where the temperature is greater than the critical temperature, and therefore the fluid is supercritical. It means the bubble, at this stage, is totally composed by gas. By comparing the two pictures, it is noticeable that the evolution corresponding to the higher overpressure leads to a more energetic dynamic of the bubble, where the velocity magnitude is clearly greater and the jet is developed faster. Moreover, as a result of the high pressures generated during collapse, a compression wave has travelled within the bubble interiors; this is visible in the Schlieren plot of the second picture, where a pressure wave is interacting with the bubble interface in the lowest part of the bubble, and also in the contour plot of the same image, where the density field has been perturbed by the action of such wave. Overall, the evolution corresponding to the lower overpressure (left picture) is smoother.

To assess whether or not the pressure wave propagating from the bubble towards the wall, as a result of the above described dynamic of collapse and liquid jet appearance, is actually a shock wave, we should look at the Mach number at each point of the domain. The Mach number indeed helps in determining those

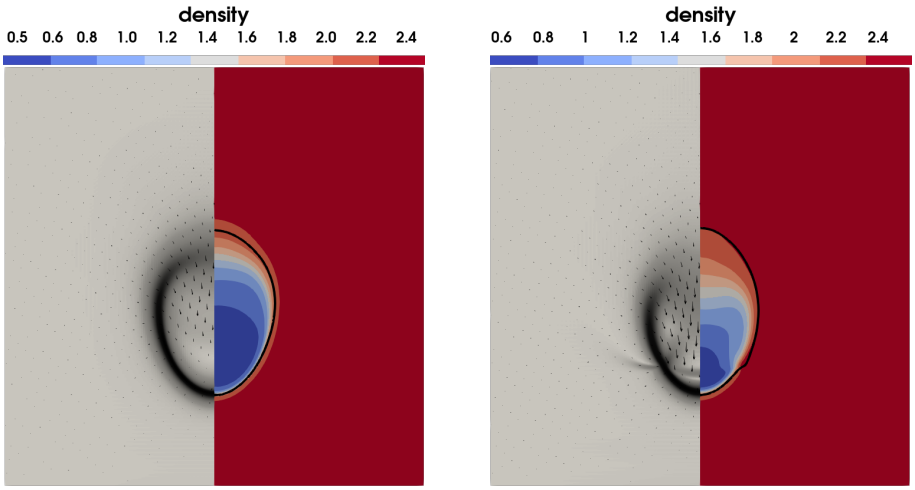

(a) ($p^* = \Delta p / p_l^{eq} = 28.5$) Bubble configuration at $t^* = 21$, during the collapse. The liquid jet is clearly visible.

(b) ($p^* = \Delta p / p_l^{eq} = 58$) Bubble configuration at $t^* = 14.5$, during the collapse. The liquid jet is clearly visible.

Figure 6.6. On the left of each inset, Schlieren visualization technique to highlight zones where the density gradient is large (i.e. interfaces and pressure waves), on the right, density contour plot, with a contour line identifying the supercritical region where the temperature is $\theta > \theta_c$

places in the domain where the velocity is greater than the local speed of sound in those thermodynamical conditions. If the pressure waves propagate at a velocity higher than the local speed of sound, we can properly speak of a shock wave, otherwise we would refer to those waves as simple pressure waves. Since the Mach number, intended as a field in the domain (or local Mach number), is the ratio between the magnitude of the velocity field and the local speed of sound, we shall first find a way to express the speed of sound of a van der Waals fluid, as a function of the local density and temperature. The speed of sound for a van der Waals fluid is, from (Zhao et al. 2011), and recalling the van der Waals EOS (2.45),

$$\begin{aligned} c(\rho,\theta) =& \sqrt{\left(\frac{\partial p}{\partial \rho}\right)_s} \\ =& \sqrt{(1+\delta)\frac{p+a\rho^2}{\rho(1-b\rho)} - 2a\rho} \\ =& \sqrt{\frac{40\theta}{(3-\rho)^2} - 6\rho}, \end{aligned} \tag{6.10}$$

where a value $\delta = 2/3$ has been used, to simulate the behavior of a diatomic gas. The local Mach number is therefore

$$\mathrm{Ma}(r,z,t) = \frac{|\mathbf{u}|}{c} \tag{6.11}$$

These quantities just introduced are plotted in Figure 6.7, where the case corresponding to the maximum overpressure simulated is examined. On the left picture of Figure 6.7, the velocity vectors are now uniform, but colored with the local Mach number value, to highlight those zones of the jet with larger velocity. A small spherical zone, delimited by the solid black contour line on the left panel is at a local Mach number $\mathrm{Ma} > 0.9$. As a consequence, that portion is almost in supersonic condition, but does not actually reach $\mathrm{Ma} = 1$, hence it would not be appropriate to speak of proper shock wave. Instead we will refer to the consequent wave radiated in the domain as a pressure wave. Since the case depicted in Figure 6.7 is the most energetic among all the simulations performed, no actual shock wave has been observed in the study, although all these pressure waves carry with them high energy and high damage capabilities, as it will be evident in subsequent sections. The image on the right of Figure 6.7 is instead a comparison, for the same configuration, of the speed of sound field and the local Mach number field. It allows to identify those zones where the speed of sound is higher, mainly due to high compressions in the liquid phase. The one with the highest values is indeed in correspondence with the propagation of the pressure wave emerging from the interior of the bubble. The high Mach number zone is instead, as noted above, in the interior of the bubble, where the lower density contributes to keep the speed of sound to reasonable values.

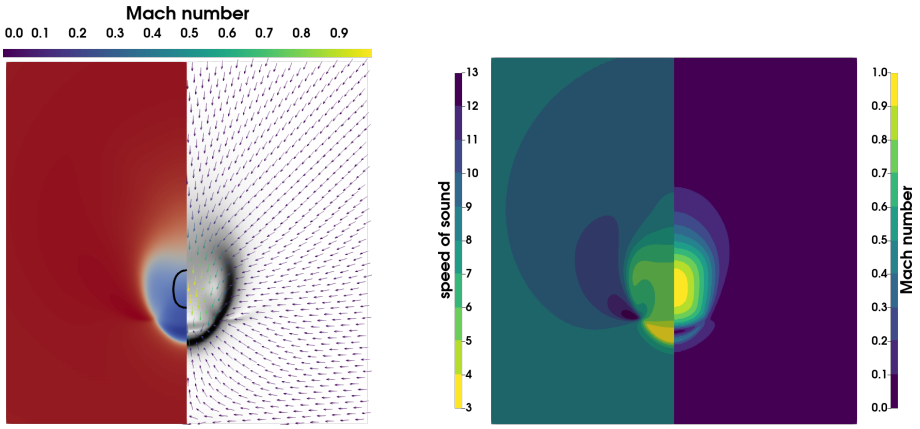

(a) **(b)**

Figure 6.7. ($p^* = \Delta p / p_l^{eq} = 58$) Bubble configuration at $t^* = 14.5$. On the left, liquid jet with Mach number colored vectors to highlight its high velocity, and a solid black contour line delimiting the zone with Ma > 0.9. The fluid in that zone is almost supersonic, but still subsonic. On the right, comparison between speed of sound field from (6.10) and local Mach number from (6.11)

Finally, pictures in Figure 6.8 show the contour plot of the vertical velocity of the fluid. The more energetic case, the one on the right, has a maximum vertical velocity in the field which almost doubles the value of the one on the left

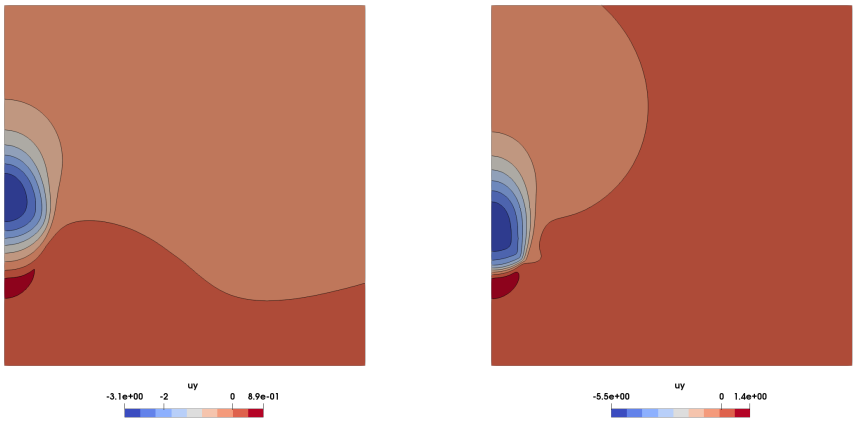

(a) ($p^* = \Delta p / p_l^{eq} = 28.5$) Bubble configuration at time $t^* = 21$, $v_{max} = 810\, m/s$

(b) ($p^* = \Delta p / p_l^{eq} = 58$) Bubble configuration at time $t^* = 14.5$, $v_{max} = 1500\, m/s$

Figure 6.8. Vertical velocity u_z comparison at a similar instant in time

Pressure wave comparison

Following the liquid jet appearance and propagation within the bubble, a pressure wave or shock wave is emitted and starts travelling towards the solid surface.

It is formed as a consequence of the extreme conditions of temperature, density and pressure arising in the bubble during the collapse. As has been mentioned above, the results analyzed in this thesis did not reveal the presence of a proper shock wave, as a consequence of the initial conditions adopted and investigated. We shall therefore refer to these waves as simple pressure waves. A qualitative comparison of the emission and propagation of pressure waves in liquid during and after the collapse stage is presented in the form of Schlieren plots in Figure 6.9 and Figure 6.10, were different time instants are considered. The pressure wave is emitted from the bubble and starts moving towards the solid surface, where it is then reflected. After reflection, it propagates both in the liquid domain as well as along the surface of the wall. Part of the pressure wave reflected interacts with the bubble, which is already moving itself towards the wall, as a consequence of the relative velocity generated during the first collapse phase. From the figure it is evident how much more concentrated and intense the pressure wave is in the more energetic case. The dynamic behavior is somehow similar, and the only relevant difference appears to be the intensity of the collapse and of the density gradients at the wave front.

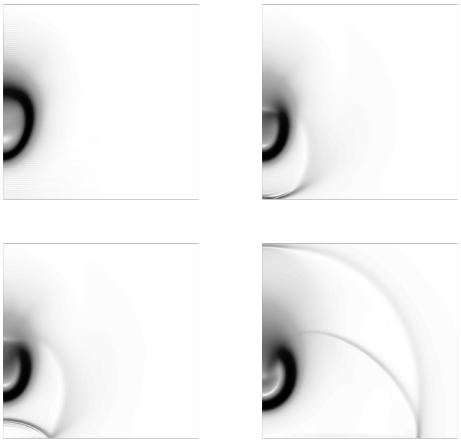

Figure 6.9. Pressure wave visualization in time.
($p^* = \Delta p / p_l^{eq} = 28.5$)

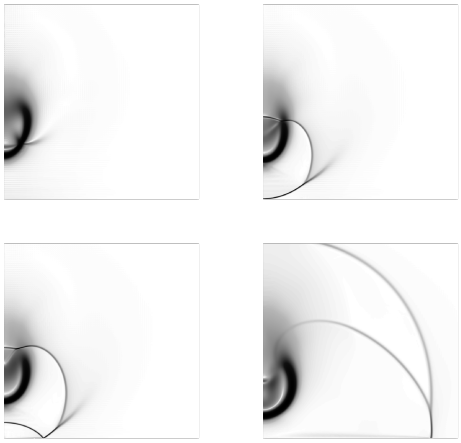

Figure 6.10. Pressure wave visualization in time.
($p^* = \Delta p / p_l^{eq} = 58$)

Vorticity and wave propagation

Once the non-spherical phase of the collapse is triggered, the vorticity in the field starts to play a role, and a vapour torus starts appearing. The vorticity in the field is generated in proximity of the pressure wave emitted by the collapsing bubble, ahead of the bubble itself. The vorticity is then convected and stretched in the domain, by the fluid velocity. The vorticity dynamics is regulated by the

following evolution equation, derived in Chapter 2,

$$\frac{D}{Dt}\left(\frac{\omega}{\rho}\right) = \left(\frac{\omega}{\rho}\cdot\nabla\right)\mathbf{u} - \frac{1}{\rho}\nabla\left(\frac{s}{\rho}\right)\times\nabla\theta + \frac{1}{\rho}\nabla\times\left(\frac{1}{\rho}\nabla\cdot D(\mathbf{u})\right). \tag{6.12}$$

The last term in (6.12) is related to the dissipative term, therefore is responsible for vorticity dissipation in the domain. The first term of the rhs of (6.12) is the stretching and tilting term, responsible for the geometric modification of vortices. The only term that relates to vorticity production is then the second term in the rhs, which assumes the form of a standard baroclinic term, but involves the entropy field s. It can be further developed as follows, considering that the entropy, being a state function, depends solely on the thermodynamic state of the system $s(\rho,\theta)$:

$$\begin{aligned}
-\frac{1}{\rho}\nabla\left(\frac{s}{\rho}\right)\times\nabla\theta &= -\frac{1}{\rho^2}\nabla s\times\nabla\theta + \frac{s}{\rho^3}\nabla\rho\times\nabla\theta \\
&= -\frac{1}{\rho^2}\left(\frac{\partial s}{\partial\rho}\nabla\rho\times\nabla\theta + \frac{\partial s}{\partial\theta}\nabla\theta\times\nabla\theta\right) + \frac{s}{\rho^3}\nabla\rho\times\nabla\theta \\
&= -\frac{1}{\rho}\left(\frac{1}{\rho}\frac{\partial s}{\partial\rho} - \frac{s}{\rho^2}\right)\nabla\rho\times\nabla\theta \\
&= -\frac{1}{\rho}\frac{\partial s/\rho}{\partial\rho}\nabla\rho\times\nabla\theta.
\end{aligned} \tag{6.13}$$

As a consequence of (6.13), the vorticity in the domain is produced in those places where the density contour lines and temperature contour lines intersect each other, or form a different local angle. This condition in well expressed in Figure 6.11, where white lines (density contours) intersect black lines (temperature contours) ahead of the bubble and behind it.

Once the vorticity is produced in the domain, it is stretched and tilted, and dissipated by the remaining terms in eq. (6.12). This evolution is synthesized in Figure 6.12, where snapshots of the pressure wave propagation are compared with pictures of the vorticity field taken at the same time instants.

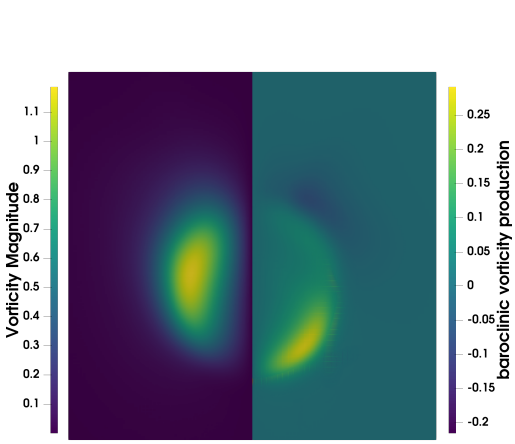

(a) Vorticity magnitude on the left and baroclinic vorticity production from eq. (6.13). Vorticity is produced ahead and behind the bubble.

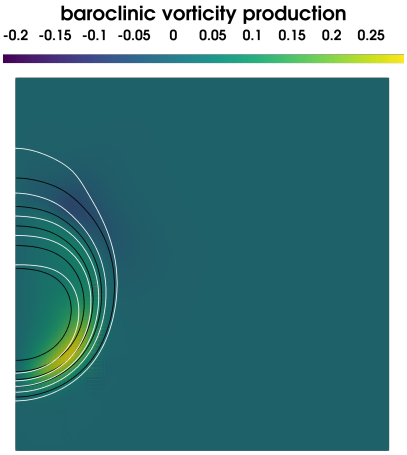

(b) Vorticity is produced ahead and behind the bubble, in those places where the density and temperature contour lines intersect.

Figure 6.11. Vorticity field and vorticity production for the case with $p^* = \Delta p / p_l^{eq} = 42.8$, $Z_c^* = 1.5$.

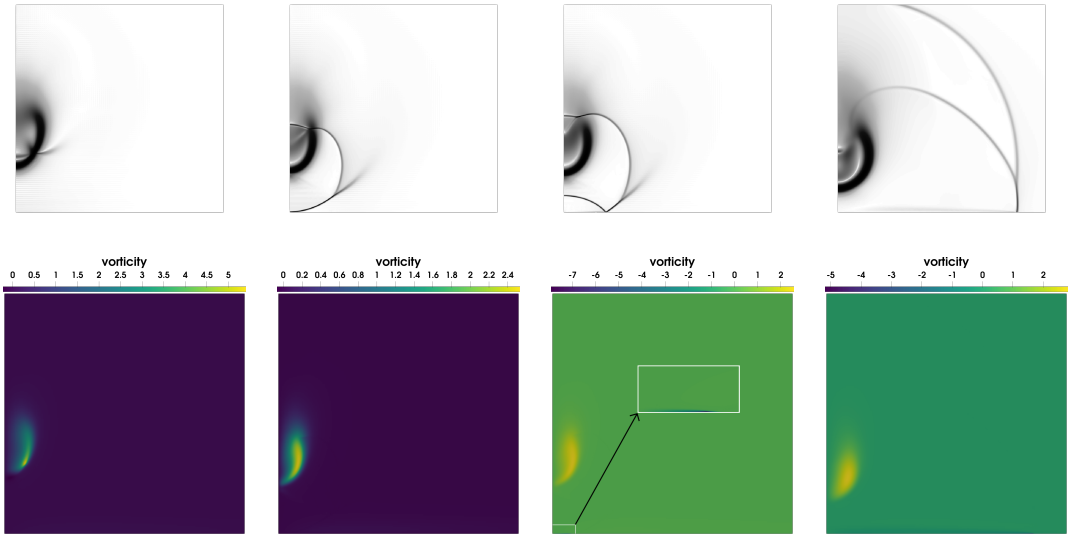

Figure 6.12. Above, pressure wave propagation. Below, corresponding vorticity field evolution. During the collapse, vorticity is always concentrated on the lower interface of the bubble. When the wave hits the wall, and start travelling along the solid surface, an additional vorticity at the wall arises, due to the no-slip condition for the fluid at the boundary; this phenomenon is represented in the inset of the third picture in the second row.

Pressure profiles at the wall

The pressures arising at the wall as a consequence of the wave emission and travelling towards the solid boundary, are the starting point for our analysis of the loads exerted by the fluid dynamics on the solid structures, with the known consequences of high damage and plastic deformation. The maximum pressure at the wall can even be of the order of magnitude of GPa, far above the yield limit of every ductile metal of use in engineering application. Figure 6.13 represents the moment at which the wave hits the wall for the first time. On the right of each image, the contour plot of the thermodynamic pressure, together with the velocity field vectors are depicted. The development of the above described liquid jet on the axis is clearly visible, as well as the pressure wave radiated. It should be noted though, that the thermodynamic pressure is not the only contribution to the normal stress at the wall, and indeed is not the only one considered in the following analysis. The complete stress is the component of the stress tensor normal to the wall surface, namely T_{zz}, which embeds the thermodynamic pressure as well as the capillary contributions and the viscous stresses (This component is represented in (A.23), in the appendix regarding the cylindrical formulation of the NSK equations A.2). In cylindrical coordinates, that component, which is the one used as a input for the solid mechanics simulation, reads

$$\begin{aligned} T_{zz} = &- p(\rho,\theta) + \frac{\lambda}{2}\left[\left(\frac{\partial\rho}{\partial r}\right)^2 - \left(\frac{\partial\rho}{\partial z}\right)^2\right] + \frac{\rho\lambda}{r}\left[\frac{\partial}{\partial r}\left(r\frac{\partial\rho}{\partial r}\right) + r\frac{\partial^2\rho}{\partial z^2}\right] \\ &- \frac{2}{3}\mu\nabla\cdot\mathbf{u} + 2\mu\frac{\partial u_z}{\partial z} \end{aligned} \tag{6.14}$$

In Figure 6.14, the pressure profiles at the wall are presented, for different times, taking into account the whole stress tensor component T_{zz} in (6.14) It is clear how the first impact acts on a very narrow spot, with extremely high pressures and for a very small period of time. These pressures, as function of time and radial distance from the axis of symmetry of the simulation, are then used as natural boundary conditions for the solid mechanics simulation involving plasticity models.

For the case $p^* = \Delta p / p_l^{eq} = 58$, $Z_c^* = 1.2$, the mean velocity at which the pressure wave propagates along the solid surface spanning the whole domain can be calculated as follows,

$$v_{pw} = \frac{\Delta x}{\Delta t} = \frac{L^* \times L_{ref}}{(t_f^* - t_0^*) \times t_{ref}} = \frac{100}{(25.36 - 14.91)} \times v_{ref} = 9.57\, v_{ref} = 2504.9\,\frac{m}{s}, \tag{6.15}$$

where

$$v_{ref} = \sqrt{\frac{p_c}{\rho_c}} = 261.77\,\frac{m}{s}. \tag{6.16}$$

Since this velocity is very high, it may not always be a good approximation to model the solid surface response to these loads as quasi-static, as it is usually

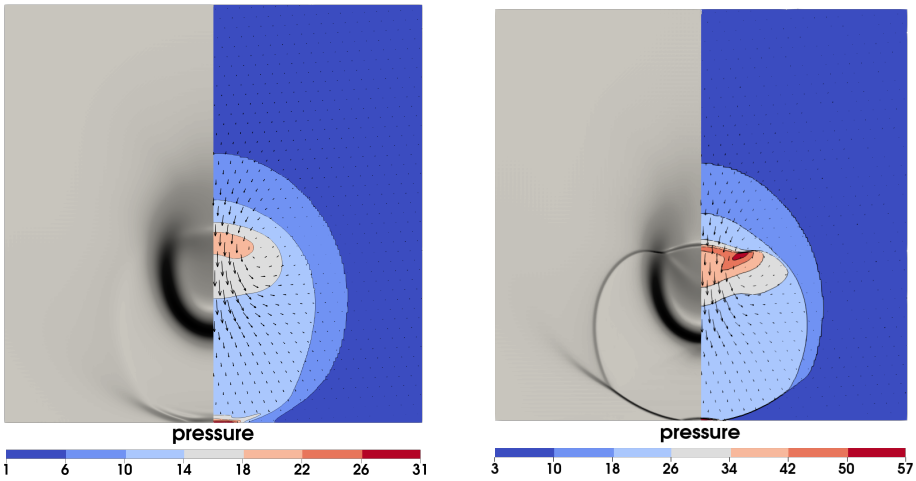

(a) $p^* = \Delta p / p_l^{eq} = 28.5$, $Z_c^* = 1.2$, $t^* = 21.86$, $p_{max} = 660\,MPa$

(b) $p^* = \Delta p / p_l^{eq} = 58$, $Z_c^* = 1.2$, $t^* = 14.91$, $p_{max} = 1.2\,GPa$

Figure 6.13. On the left of each picture, pressure wave visualization, on the right pressure field contour plot at the same instant, with scatter plot of velocity vectors. Pictures taken the first time the pressure wave hits the wall.

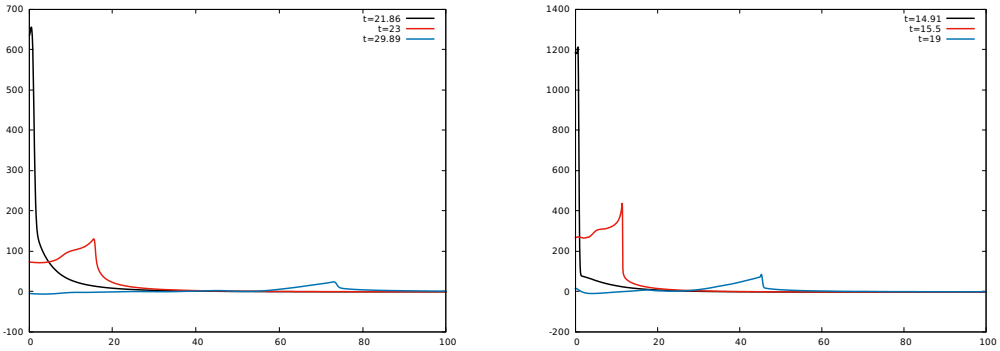

(a) $p^* = \Delta p / p_l^{eq} = 28.5$, $Z_c^* = 1.2$, $p_{max} = 660\,MPa$

(b) $p^* = \Delta p / p_l^{eq} = 58$, $Z_c^* = 1.2$, $p_{max} = 1.2\,GPa$

Figure 6.14. Pressure profiles at the wall (MPa), taken at different times, showing how the load propagates along the surface of the solid. It is clear that the case with $p^* = \Delta p / p_l^{eq} = 58$ is much more powerful.

assumed in solid mechanics application. In these cases in fact, the rate at which the load varies on the wall may be higher then the rate at which elastic and elastoplastic waves propagate in the solid, thus leading to possible interaction between waves in the solid, and results that differ from the ones obtained in the quasi-static case. In such cases, the complete model with inertial term should be considered. This analysis, even though the appropriate equations are already implemented in the codes written, is not presented in this thesis, since requires additional testing and benchmarks. Until now, only 1D and 2D test cases have

been studied, and the work is still in progress. The reasons why this aspect has to be investigated are explained in the concluding Section 7, where some preliminary results are presented.

6.4 Plastic deformation

The pressure profiles at the wall from the case at $p^* = 42.8$ have been extracted and used as boundary conditions for a quasi-static elastoplastic solid solver to study the effects of cavitation on solid objects. This pressure profile has been chosen as representative of all the profiles obtained from the fluid dynamic problem solution, and is the only one presented here as input for the solid simulations, because the attention will be focused more on the variation of the solid response in dependence of the elastoplastic properties. The set of solid properties adopted in the study is composed by some fixed parameters,

$$G = 1\,GPa, \quad \nu = 0.33, \quad E = 2.66\,GPa, \tag{6.17}$$

the shear modulus G, the poisson ratio ν and the elastic or Young modulus E; and some other parameters which are varied through the study, to assess their influence in the mechanical response. The tensile strength or yield stress σ_y assumes the following values,

$$\sigma_y = 390,\, 400,\, 450,\, 480,\, 500\,MPa; \tag{6.18}$$

the thickness of the specimen plate is varied between $h = 10\,L_{ref}$ and $h = 5\,L_{ref}$, and finally two type of elastoplastic model are investigated, the perfectly plastic material with no hardening, and the linear isotropic hardening material model with a hardening modulus $k_1 = 1\,GPa$ (for a discussion on these models, *cf.* Section 3.4.3). No kinematic hardening (Bauschinger effect) model has been used, due to the lack of cyclic traction and compression loads. The plastic deformation induced by fluid pressures is indeed totally caused by compression stresses on the top solid surface. To give an idea of how the isotropic hardening modulus in linear isotropic hardening influences the plastic behavior of the solid, it is important to note that in a simplified one-dimensional elastoplastic model, the slope of the σ-ϵ curve in the plastic regime is given by

$$\text{slope} = \frac{Ek_1}{E + k_1} \approx 0.73\,GPa, \tag{6.19}$$

such that the bi-linear behavior of the system is characterized by the Young modulus below the tensile strength and by the slope (6.19) above the yield strength (in the one-dimensional simplification).

By analyzing the set of properties adopted, it is evident how it is not representative of any actual metal. Plastic quantities such as the yield stress or the models implied are in fact a good approximation for the plastic response of ductile metals such as Aluminium or Tin, but the elastic properties used are way lower than the

actual ones. This choice has been made to allow for an easier visualization of the results, in terms of displacement and strain field in the solid.

The pressure profiles applied at the boundary, and the configuration of the simulation are represented in Figure 6.15. The simulation is performed on a three-dimensional cartesian grid representing one fourth of the material specimen, with its center in the bottom left corner, in correspondence with the axis of the fluid dynamic simulation, so that the top surface is considered the one in contact with the fluid, where the pressures are exerted. The bottom surface is fully constrained, meaning that all the components of displacement are null. The two surfaces that would be in contact with the other portions of the solid have boundary conditions expressing the symmetry of the material, whereas the two remaining outer surfaces are free. No automatic grid refinement has been used in these simulations, but the code was still written with the general purpose finite element library deal.II (Arndt et al. 2020). The red highlighted plane in Figure 6.15 (a) is the one represented is subsequent Figure 6.16 and Figure 6.17. The pressure profiles used in the simulations are reproduced, in three particular time instants of their evolution, in Figure 6.15 (b), with a black dashed line highlighting the value of yield stress for the case depicted in Figure 6.16 and Figure 6.17.

The solver used in the numerical implementation of plasticity models is CG (conjugate gradient method) with an Eisenstat preconditioner. The solution to the linear system is considered at convergence once a tolerance of 10^{-21} is met, whereas the Newton iteration is considered at convergence once the residual vector norm is less than 10^{-8}. The tolerance required on the plastic corrector algorithm (return mapping algorithm for plasticity) is 10^{-10}.

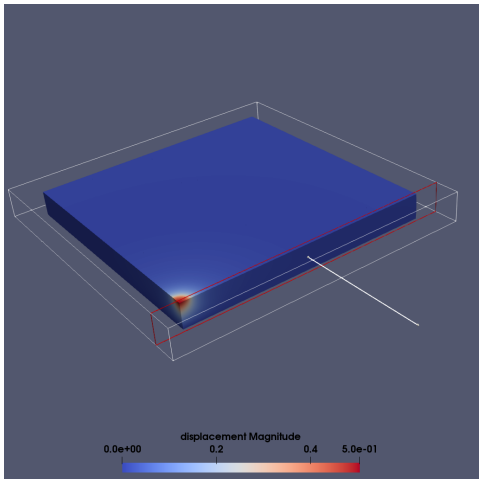

(a) Configuration

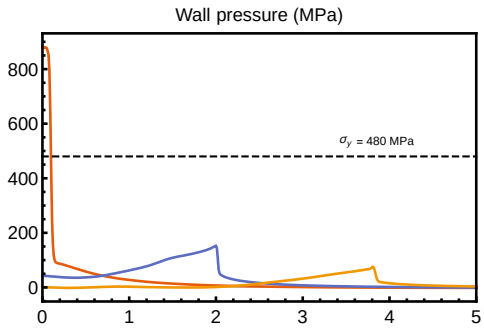

(b) Pressure profiles at the wall (MPa) for different times

Figure 6.15. Case of study

The results presented in Figure 6.16 and Figure 6.17 are concerning the case of a perfectly plastic material with no hardening, and a yield stress $\sigma_y = 480$, with

specimen thickness (the height of the specimen in the figures) of $10\,L_{ref}$. In both the figures, from top to bottom, the fields of displacement, accumulated plastic strain and von Mises stress are represented, together with arrows indicating the displacement vectors. We recall here that the accumulated plastic strain (3.138) is the integral over time of the norm of the plastic strain field, hence it gives a measure of the places where plasticity occurred over time, and where it had a larger influence. Its expression is

$$\alpha^p(t) = \int_0^t \sqrt{\frac{2}{3}}\,\|\boldsymbol{\epsilon}^p(\tau)\|\,\mathrm{d}\tau \tag{6.20}$$

In Figure 6.16, these quantities are plotted at the time the pressure wave coming from the fluid impacts on the wall with its maximum power, thus corresponding to the maximum value of pressure reached at the wall, the red line in Figure 6.15 (b). The impact produces a large displacement, concentrated in a very narrow spot, and a small plastic deformation, located where the accumulated plastic strain is non-zero. The accumulated plastic strain is still very confined, because it's the first time the elastic limit has been overcome. The von Mises stress allows the identification of those places where the stress concentration is higher. The maximum value attained and attainable corresponds to the yield limit, since the model adopted is perfectly plastic. The stress is obviously concentrated in the zone hit by the pressure wave. Figure 6.17 represents the same quantity at the end of the simulation, when no actual stress at the boundary is prescribed, and the top surface is free. In this condition, a permanent indentation, as a consequence of the occurred plastic deformation, is observed, limited to a very narrow spot in the center of the specimen. The accumulated plastic strain instead has taken a larger part of the domain, meaning that during the simulations, other points have undergone plastic permanent deformation. Finally, there is a small portion of stress accumulated in the sub-superficial zone where plastic deformation has occurred.

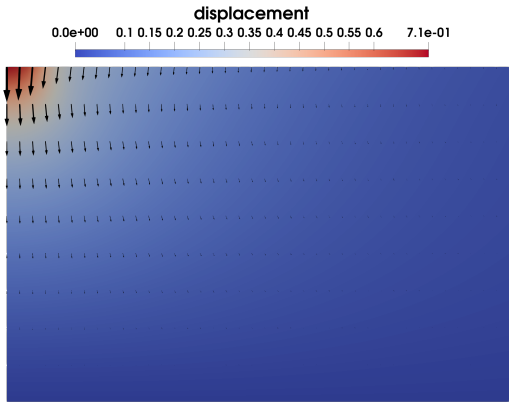

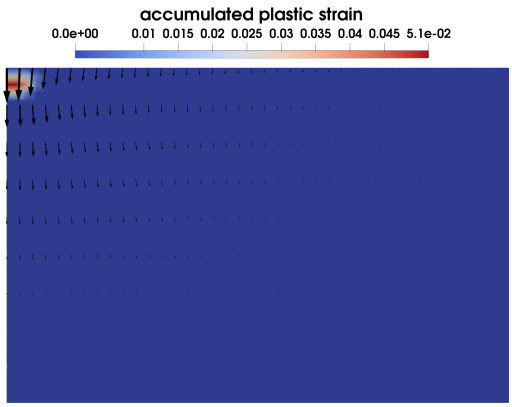

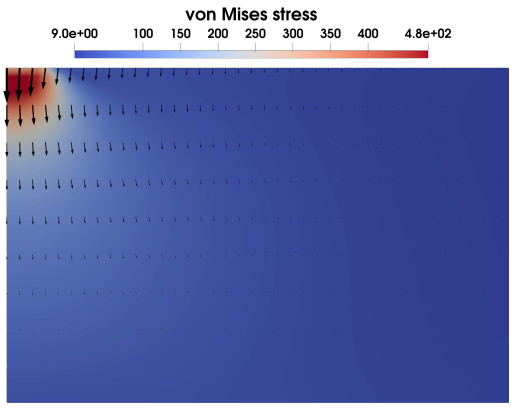

Figure 6.16. From top to bottom, displacement magnitude, accumulated plastic strain and von Mises stress field in the material, at the time of the first impact.

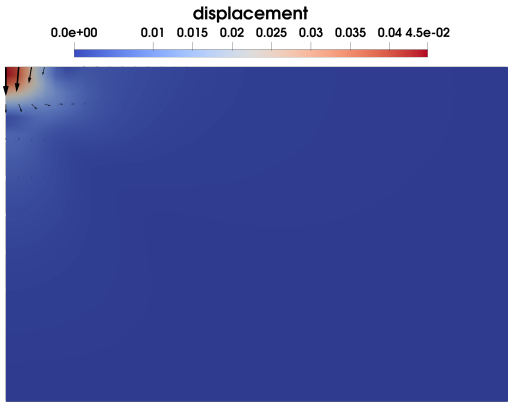

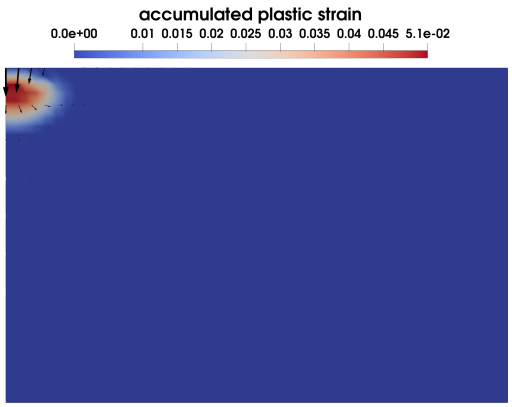

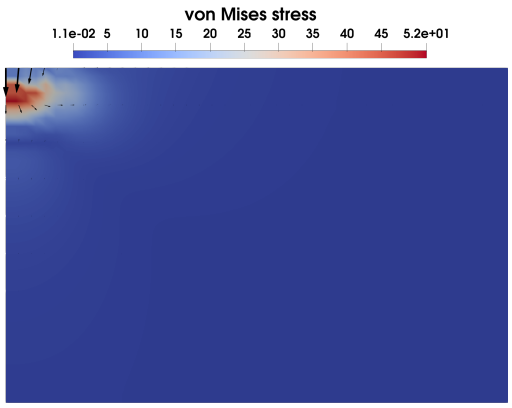

Figure 6.17. From top to bottom, displacement magnitude, accumulated plastic strain and von Mises stress field in the material at the end of the simulation, when no load is applied.

The load at the wall is then repeated multiple times to assess the influence of these repetitions on the final indentation observed as consequence of the plastic permanent deformation. In Figure 6.18, the vertical displacement resulting after one application (solid line) and five repetition of the same load (dashed line) is plotted. It can be noted the increase in depth of the indentation. The same increase

can be evaluated in Figure 6.19, where the progressive increase in indentation depth is represented as a function of the number of times the same load is applied at the wall. After few cycles, the material seems to have saturated its potential to be plastically deformed again, and the maximum attainable pit depth has been reached in this conditions.

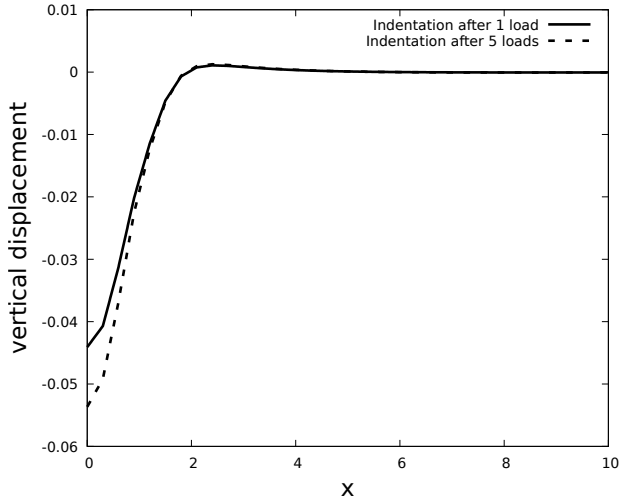

Figure 6.18. Residual plastic indentation after one and five cyclic loads ($L_{ref} = 0.1\,\mu$m). It is evident how the pit depth has increased.

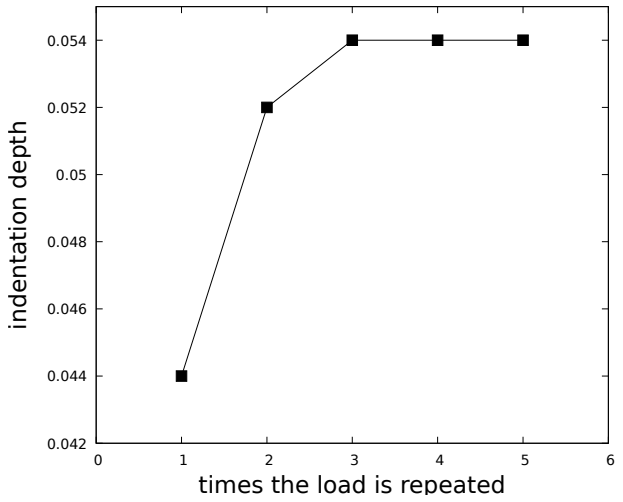

Figure 6.19. Progressive increase of the indentation depth in dependence of the number of times the same load has been applied on the material surface ($L_{ref} = 0.1\,\mu$m).

The case thus far analyzed is only a single configuration of the ones simulated and introduced in the initial part of this section. The other results are gathered in the form of the following figures, where relevant quantities of the different cases are plotted together in dependence of the yield stress. In Figure 6.20 (a) the maximum value of displacement in the field is plotted, as a decreasing function

of increasing yield stress. This is to be expected, since higher yield stress means higher strength of the material. The solid lines represent the perfectly plastic case, with no hardening function, whereas the dashed line is representative for the case with linear hardening. The hardened material is stronger than the perfectly plastic one, and this justifies the fact that the dashed curves lie below the solid lines, allowing for less displacement to be achieved in the material. The blue lines refer to data obtained at the time of the first impact, when the displacements are larger, as a result of the high pressure exerted on the wall; while red lines refer to the end of the simulation, and are therefore representative of the final indentation depth, or permanent deformation. In Figure 6.20 (b) instead, the maximum accumulated plastic strain in the domain is plotted, that is a decreasing function of increasing yield stress as well. The perfectly plastic case is compared with the linear hardening model, and considerations similar to the previous paragraph hold.

In Figure 6.21 the influence of thickness of the metal plate is analyzed. In particular, it is found that the maximum displacement at the impact is lower in the case with thickness 5 if compared to the case with thickness 10, but the same quantity is higher for the case with lower thickness if we look at the permanent deformation. This can be justified by the fact that, even though the displacement at the impact is less for the case with lower thickness, the plastic deformation is actually higher, because the smaller domain allows for higher stress concentration, and when the load is relieved, the residual displacement is actually generated by that permanent plastic deformation. This observation is corroborated by the fact that the same discussion applies to Figure 6.21 (b), where the accumulated plastic strain is compared in the two cases. This quantity is clearly larger in the lower thickness case, as a result of the fact that more plastic deformation has occurred in the domain due to higher stress concentrations.

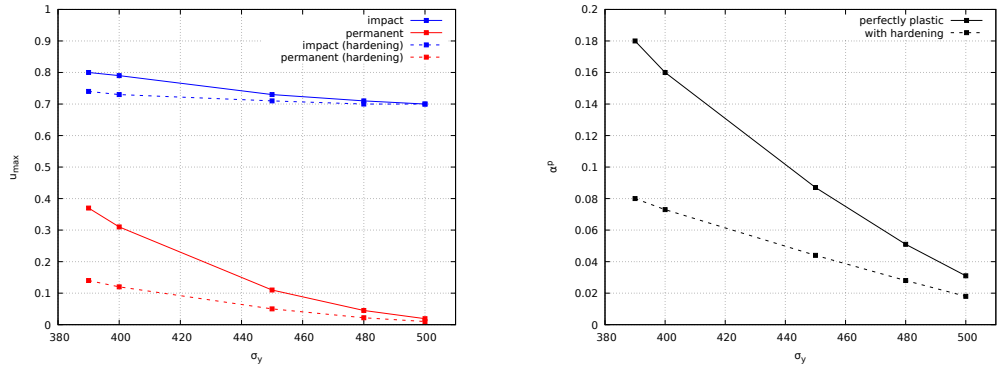

(a) **(b)**

Figure 6.20. Comparison of the results obtained in the simulations. On the left, the maximum value of the displacement in the field is plotted in dependence of the yield stress values adopted. Different cases (perfect plasticity and linear hardening) are compared depending on the yield strength of the material. On the right, comparison between the perfectly plastic and linear hardening model in terms of maximum accumulated plastic strain in the domain, once the load is relieved.

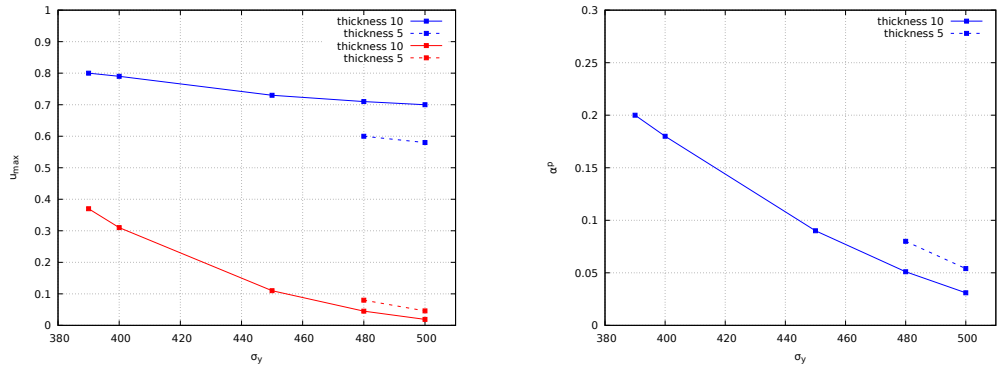

(a) **(b)**

Figure 6.21. The results of two configurations with different thickness of the specimen plate are compared. On the left, the maximum value of the displacement in the field is plotted in dependence of the yield stress values adopted, for different simulation times. On the right, the maximum accumulated plastic strain at the end of the simulation, for the same two configurations, are compared.

Chapter 7

Conclusions and further developments

The study carried out during this Ph.D. program, and the codes developed lead to the promising results obtained and described in previous chapter. The diffuse interface model for fluid dynamics has been shown, again, to be a good framework to study cavitation phenomenon and its applications, in particular those requiring a mesoscale approach. It was suitable for the study of bubble expansion due to high energy spots released in the domain, bubble collapse dynamics, and all the physical phenomena related to them, such as topology change, emission and radiation of pressure waves, phase changes, transitions to and from supercritical states, vorticity dynamic, interaction with solids.

At the same time, the interaction of the fluid dynamic results with a solid solver, to simulate the behavior of an elastoplastic material subject to the loads imposed by the dynamic of the fluid, was successful, leading to qualitative and quantitative analysis regarding the state of stress, deformation and plastic variables occurring in the solid. The macroscopic classical plasticity models have been shown to qualitatively agree with experimental observation on material specimens deformed by the action of cavitation, and is a good and extendible framework for the study of the problem, in particular for those applications in which macroscopic quantities are of interest.

The development of numerical codes with the aid of the finite element library deal.II (Arndt et al. 2020) and its community took large part of the Ph.D. program of the candidate, but is believed to be a good choice, in view of the fact that allowed the simulation of systems that otherwise would not have been possible to investigate with the mathematical and physical models used in this thesis.

That being said, there are still lots of questions to answer, and technical advances to make. Speaking about the latter, in particular, the development of two-dimensional axisymmetric codes to simulate the elastoplastic behavior of structures is required, to decrease the cost of the simulations and allow for a two-way coupling interaction between the fluid solver and the solid one. In a two-way coupling regime, the fluid output is taken as input for the solid simulation, and at the

same time the solid output, in terms of stress and displacements, is taken as an input for the solution of the fluid dynamics. This is something that has been done recently in some relevant researches, even though it was limited to elastic material behaviors and less refined fluid models (Cao et al. n.d.). We believe this approach would be the next one, to assess how these two very complicated physical phenomena interact and influence the behavior of each other. To this aim though, a complete description in terms of dynamics of the solid is needed, and is the one developed and described in Section 4.4.2. Although this aspect has not been fully described and analyzed in the thesis, it was the object of the later months of work of the author. The codes developed already embed the description of the dynamics of solid structures, for both elastic and plastic material models. The role of plastic stress wave and inelastic wave propagation has been studied in the past by many famous scientists (Cristescu 2012; Kolsky 1963; Lubliner 2008; Nowacki 2018; Von Karman and Duwez 1950), but has been abandoned in recent years, to the best of the author knowledge. Nevertheless, it is our belief that inelastic wave propagation may play a relevant role in the dynamics of structures, and in the resulting stress concentration and final plastic deformation, as well as in the full interaction with the fluid dynamics, since the timescales at which the two phenomena take place can overlap in many practical situations.

To give some details about the actual state of the implementation of what constitutes the most immediate further development of our study, few preliminary results regarding the propagation of elastoplastic stress waves are presented. The basis of stress wave propagation within inelastic media have been posed by the work of von Karman and Duwez (Von Karman and Duwez 1950), where the authors derived the analytical one-dimensional solution to the problem. When a displacement or tension is applied to one end of a one-dimensional specimen, and it overcomes the elastic limits, a precursor wave, the actual elastic wave, travelling with the longitudinal wave speed mentioned in Section 3.1.2, is followed by a *plastic stress wave*, which travels slower than the elastic one, with a speed related to plastic quantities such as the isotropic hardening modulus (k_1 in this thesis). The elastic stress wave has an amplitude equal to the elastic limit, while the plastic wave carries all the additional stress, and propagates the plastic deformation in the material. This phenomenology is captured by the one-dimensional simulations presented in Figure 7.1, where it is clear that two wave fronts are propagating, with different speed. The elastic wave has an amplitude equal to the value of yield stress $\sigma_y = 0.5$, while the plastic wave, which has just started its propagation, carries a higher stress, and plastic deformation. A second simulation is carried out in a two-dimensional cartesian framework, and the qualitative results are showed in Figure 7.2, where the bottom case represents an elastoplastic material, while the top case an elastic one. The image is instructive to show the influence of plastic wave propagation. The bottom case presents in fact a plastic wave front, which contributes to a larger stress accumulation in the zone where the load was applied (an initial gaussian load is used to trigger the dynamics). The

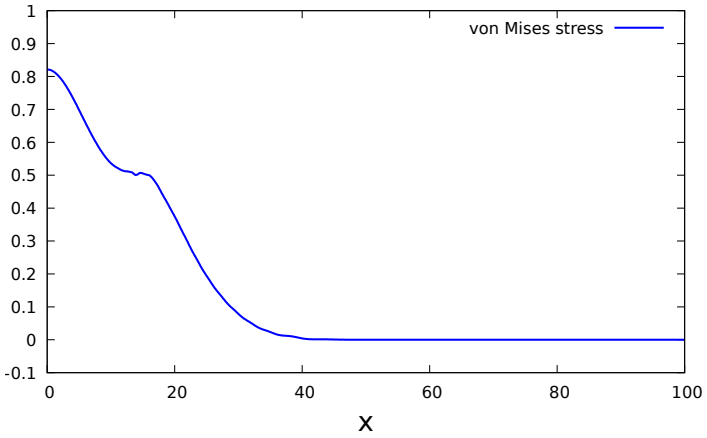

Figure 7.1. Stress waves propagation in an elastoplastic material with hardening, with yield stress $\sigma_y = 0.5$. The results are in good qualitative agreement with the ones proposed by von Karman and Duwez (Von Karman and Duwez 1950). The elastic wave travels with higher speed, the one of *P-waves* (3.21), while the plastic one is slower.

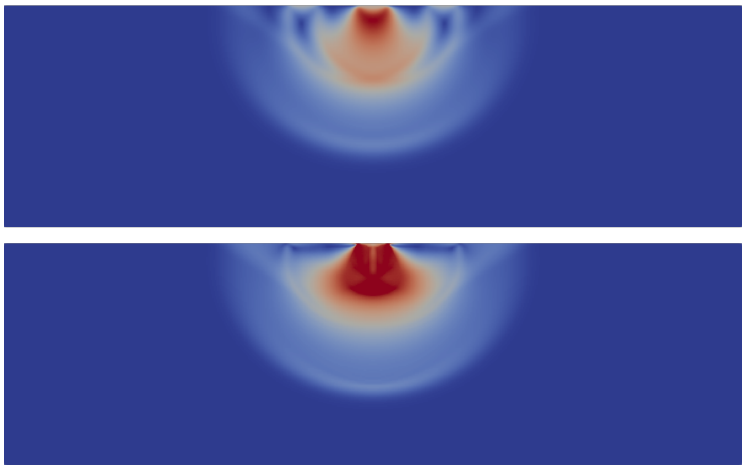

Figure 7.2. Equivalent von Mises stress waves in two materials, elastic (top one) and elastoplastic (bottom one). The place where the stresses are accumulated (red zones) is wider in the case of the elastoplastic material, as a result of the propagation of plastic deformation through the plastic wave.

study of this complicated dynamical behavior may lead to important discoveries in the field of cavitation induced plastic deformation and cavitation interaction with solid materials.

Appendix A

Navier-Stokes with capillarity equations in spherical and cylindrical coordinates

A.1 Equations in spherical coordinates

The spherical system of coordinates, expressed with respect to the standard orthonormal cartesian basis, is

$$\hat{\mathbf{r}} = \sin\theta(\cos\varphi\,\hat{\mathbf{x}} + \sin\varphi\,\hat{\mathbf{y}}) + \cos\theta\,\hat{\mathbf{z}}, \tag{A.1}$$

$$\hat{\boldsymbol{\theta}} = \cos\theta(\cos\varphi\,\hat{\mathbf{x}} - \sin\varphi\,\hat{\mathbf{y}}) + \cos\theta\,\hat{\mathbf{z}}, \tag{A.2}$$

$$\hat{\boldsymbol{\varphi}} = -\sin\varphi\,\hat{\mathbf{x}} + \cos\varphi\,\hat{\mathbf{y}}. \tag{A.3}$$

In those cases where it is possible to adopt the approximation of 1D spherical symmetry, the velocity vector is considered to be composed by a single term, the one along the radial direction, namely the radial velocity,

$$\mathbf{u}(r,\theta,\varphi) = u_r(r)\hat{\mathbf{r}}. \tag{A.4}$$

Moreover, all the derivatives with respect to the angles φ and θ are considered to be negligible, therefore no variable depends on the angles φ and θ. The Navier-Stokes equations with capillary terms, in this framework, read

$$\frac{\partial\rho}{\partial t} + \frac{1}{r^2}\frac{\partial(r^2\rho u_r)}{\partial r} = 0, \tag{A.5}$$

$$\frac{\partial(\rho u_r)}{\partial t} + \frac{1}{r^2}\frac{\partial(r^2\rho u_r^2)}{\partial r} = \frac{1}{r^2}\frac{\partial(r^2 T_{rr})}{\partial r} - \frac{(T_{\theta\theta} + T_{\varphi\varphi})}{r}, \tag{A.6}$$

$$\frac{\partial E}{\partial t} + \frac{1}{r^2}\frac{\partial}{\partial r}\left[r^2\left(Eu_r - T_{rr}u_r + q_e\right)\right] = 0; \tag{A.7}$$

where the stress tensor T has the following structure

$$T = T_{rr}\,\hat{\mathbf{r}}\otimes\hat{\mathbf{r}} + T_{\theta\theta}\,\hat{\boldsymbol{\theta}}\otimes\hat{\boldsymbol{\theta}} + T_{\varphi\varphi}\,\hat{\boldsymbol{\varphi}}\otimes\hat{\boldsymbol{\varphi}}, \tag{A.8}$$

with components

$$T_{rr} = -p + \lambda \left[-\frac{1}{2} \left(\frac{\partial \rho}{\partial r}^2 \right) + \frac{\rho}{r^2} \frac{\partial}{\partial r} \left(r^2 \frac{\partial \rho}{\partial r} \right) \right] + 2\mu \left[\frac{\partial u_r}{\partial r} - \frac{1}{3r^2} \frac{\partial (r^2 u_r)}{\partial r} \right], \quad \text{(A.9)}$$

$$T_{\theta\theta} = -p + \lambda \left[\frac{1}{2} \left(\frac{\partial \rho}{\partial r}^2 \right) + \frac{\rho}{r^2} \frac{\partial}{\partial r} \left(r^2 \frac{\partial \rho}{\partial r} \right) \right] + 2\mu \left[\frac{u_r}{r} - \frac{1}{3r^2} \frac{\partial (r^2 u_r)}{\partial r} \right], \quad \text{(A.10)}$$

$$T_{\varphi\varphi} = T_{\theta\theta}; \quad \text{(A.11)}$$

and the energy flux q_e assumes the form

$$q_e = -k \frac{\partial \theta}{\partial r} + \frac{\lambda \rho}{r^2} \frac{\partial \rho}{\partial r} \frac{\partial (r^2 u_r)}{\partial r}. \quad \text{(A.12)}$$

A.2 Equations in cylindrical coordinates

The cylindrical system of coordinates, expressed with respect to the standard orthonormal cartesian basis, is

$$\hat{\mathbf{r}} = \cos\theta\, \hat{\mathbf{x}} + \sin\theta\, \hat{\mathbf{y}}, \quad \text{(A.13)}$$

$$\hat{\boldsymbol{\theta}} = -\sin\theta\, \hat{\mathbf{x}} + \cos\theta\, \hat{\mathbf{y}}, \quad \text{(A.14)}$$

$$\hat{\mathbf{z}} = \hat{\mathbf{z}}. \quad \text{(A.15)}$$

In those cases where it is possible to adopt the approximation of 2D cylindrical axisymmetry, the velocity vector is considered to be a two-dimensional vector with components along the radial and vertical directions $\hat{\mathbf{r}}$ and $\hat{\mathbf{z}}$

$$\mathbf{u}(r, \theta, z) = u_r(r, z)\hat{\mathbf{r}} + u_z(r, z)\hat{\mathbf{z}}. \quad \text{(A.16)}$$

Moreover, all the derivatives with respect to the angle θ are considered to be negligible, therefore no variable depends on the angle θ. The Navier-Stokes equations with capillary terms, in this framework, read

$$\frac{\partial \rho}{\partial t} + \frac{1}{r} \frac{\partial (r \rho u_r)}{\partial r} + \frac{\partial (\rho u_z)}{\partial z} = 0, \quad \text{(A.17)}$$

$$\frac{\partial (\rho u_r)}{\partial t} + \frac{1}{r} \frac{\partial (r \rho u_r^2)}{\partial r} + \frac{\partial (\rho u_r u_z)}{\partial z} = \frac{1}{r} \frac{\partial (r T_{rr})}{\partial r} + \frac{\partial T_{rz}}{\partial z} - \frac{T_{\theta\theta}}{r}, \quad \text{(A.18)}$$

$$\frac{\partial (\rho u_z)}{\partial t} + \frac{\partial (\rho u_z^2)}{\partial z} + \frac{1}{r} \frac{\partial (r \rho u_r u_z)}{\partial r} = \frac{\partial T_{zz}}{\partial z} + \frac{1}{r} \frac{\partial r T_{rz}}{\partial r}, \quad \text{(A.19)}$$

$$\frac{\partial E}{\partial t} + \frac{1}{r} \frac{\partial}{\partial r} \left[r \left(E u_r - T_{rr} u_r - T_{rz} u_z + q_e^r \right) \right] + \frac{\partial}{\partial z} \left[E u_z - T_{zr} u_r - T_{zz} u_z + q_e^z \right] = 0; \quad \text{(A.20)}$$

where the stress tensor T has the following structure (symmetric rank-2 tensor)

$$T = T_{rr}\, \hat{\mathbf{r}} \otimes \hat{\mathbf{r}} + T_{rz} \left(\hat{\mathbf{r}} \otimes \hat{\mathbf{z}} + \hat{\mathbf{z}} \otimes \hat{\mathbf{r}} \right) + T_{zz}\, \hat{\mathbf{z}} \otimes \hat{\mathbf{z}} + T_{\theta\theta}\, \hat{\boldsymbol{\theta}} \otimes \hat{\boldsymbol{\theta}}, \quad \text{(A.21)}$$

with components

$$T_{rr} = -p + \frac{\lambda}{2}\left[-\left(\frac{\partial\rho}{\partial r}\right)^2 + \left(\frac{\partial\rho}{\partial z}\right)^2\right] + \frac{\rho\lambda}{r}\left[\frac{\partial}{\partial r}\left(r\frac{\partial\rho}{\partial r}\right) + r\frac{\partial^2\rho}{\partial z^2}\right] \tag{A.22}$$
$$- \frac{2}{3}\mu\left(\frac{1}{r}\frac{\partial(ru_r)}{\partial r} + \frac{\partial u_z}{\partial z}\right) + 2\mu\frac{\partial u_r}{\partial r},$$

$$T_{zz} = -p + \frac{\lambda}{2}\left[\left(\frac{\partial\rho}{\partial r}\right)^2 - \left(\frac{\partial\rho}{\partial z}\right)^2\right] + \frac{\rho\lambda}{r}\left[\frac{\partial}{\partial r}\left(r\frac{\partial\rho}{\partial r}\right) + r\frac{\partial^2\rho}{\partial z^2}\right] \tag{A.23}$$
$$- \frac{2}{3}\mu\left(\frac{1}{r}\frac{\partial(ru_r)}{\partial r} + \frac{\partial u_z}{\partial z}\right) + 2\mu\frac{\partial u_z}{\partial z},$$

$$T_{rz} = -\lambda\frac{\partial\rho}{\partial r}\frac{\partial\rho}{\partial z} + \mu\left(\frac{\partial u_r}{\partial z} + \frac{\partial u_z}{\partial r}\right), \tag{A.24}$$

$$T_{\theta\theta} = -p + \frac{\lambda}{2}\left[\left(\frac{\partial\rho}{\partial r}\right)^2 + \left(\frac{\partial\rho}{\partial z}\right)^2\right] + \frac{\rho\lambda}{r}\left[\frac{\partial}{\partial r}\left(r\frac{\partial\rho}{\partial r}\right) + r\frac{\partial^2\rho}{\partial z^2}\right] \tag{A.25}$$
$$- \frac{2}{3}\mu\left(\frac{1}{r}\frac{\partial(ru_r)}{\partial r} + \frac{\partial u_z}{\partial z}\right) + 2\mu\frac{u_r}{r};$$

and the two components of the energy flux $\mathbf{q}_e = q_e^r\,\hat{\mathbf{r}} + q_e^z\,\hat{\mathbf{z}}$ take the form

$$q_e^r = -k\frac{\partial\theta}{\partial r} + \lambda\rho\frac{\partial\rho}{\partial r}\left(\frac{1}{r}\frac{\partial(ru_r)}{\partial r} + \frac{\partial u_z}{\partial z}\right), \tag{A.26}$$

$$q_e^z = -k\frac{\partial\theta}{\partial z} + \lambda\rho\frac{\partial\rho}{\partial z}\left(\frac{1}{r}\frac{\partial(ru_r)}{\partial r} + \frac{\partial u_z}{\partial z}\right). \tag{A.27}$$

Bibliography

Adewuyi, Yusuf G (2005). "Sonochemistry in environmental remediation. 1. Combinative and hybrid sonophotochemical oxidation processes for the treatment of pollutants in water". In: *Environmental science & technology* 39.10, pp. 3409–3420.

Ainsworth, Mark and Oden, J Tinsley (2011). *A posteriori error estimation in finite element analysis*. Vol. 37. John Wiley & Sons.

Arndt, Daniel et al. (2020). "The deal.II Library, Version 9.2". In: *Journal of Numerical Mathematics* 28.3, pp. 131–146. DOI: 10.1515/jnma-2020-0043. URL: https://dealii.org/deal92-preprint.pdf.

Blander, Milton and Katz, Joseph L (1975). "Bubble nucleation in liquids". In: *AIChE Journal* 21.5, pp. 833–848.

Boffi, Daniele, Brezzi, Franco, Fortin, Michel, et al. (2013). *Mixed finite element methods and applications*. Vol. 44. Springer.

Boukharfane, Radouan, Ribeiro, Fábio Henrique Eugênio, Bouali, Zakaria, and Mura, Arnaud (2018). "A combined ghost-point-forcing/direct-forcing immersed boundary method (IBM) for compressible flow simulations". In: *Computers & Fluids* 162, pp. 91–112.

Brems, S, Hauptmann, M, Camerotto, E, Pacco, A, Kim, T-G, Xu, X, Wostyn, K, Mertens, P, and De Gendt, Stefan (2013). "Nanoparticle removal with megasonics: a review". In: *ECS Journal of Solid State Science and Technology* 3.1, N3010.

Brennen, Christopher E (2014). *Cavitation and bubble dynamics*. Cambridge University Press.

Brennen, Christopher Earls (2015). "Cavitation in medicine". In: *Interface focus* 5.5, p. 20150022.

Brujan, EA, Keen, GS, Vogel, A, and Blake, JR (2002). "The final stage of the collapse of a cavitation bubble close to a rigid boundary". In: *Physics of fluids* 14.1, pp. 85–92.

Brujan, Emil-Alexandru, Nahen, Kester, Schmidt, Peter, and Vogel, A (2001). "Dynamics of laser-induced cavitation bubbles". In: *Journal of Fluid Mechanics* 433, pp. 283–314.

Cao, S, Wang, G, Coutier-Delgosha, O, and Wang, K (n.d.). "Shock-induced bubble collapse near solid materials: effect of acoustic impedance". In: *Journal of Fluid Mechanics* 907 ().

Chahine, Georges L and Hsiao, Chao-Tsung (2015). "Modelling cavitation erosion using fluid–material interaction simulations". In: *Interface focus* 5.5, p. 20150016.

Cole, Robert H and Weller, Royal (1948). "Underwater explosions". In: *PhT* 1.6, p. 35.

Coleman, Bernard D and Gurtin, Morton E (1967). "Thermodynamics with internal state variables". In: *The Journal of Chemical Physics* 47.2, pp. 597–613.

Coleman, Bernard D and Noll, Walter (1974). "The thermodynamics of elastic materials with heat conduction and viscosity". In: *The Foundations of Mechanics and Thermodynamics*. Springer, pp. 145–156.

Coussios, Constantin C and Roy, Ronald A (2008). "Applications of acoustics and cavitation to noninvasive therapy and drug delivery". In: *Annu. Rev. Fluid Mech.* 40, pp. 395–420.

Cristescu, Nicolae (2012). *Dynamic plasticity*. Elsevier.

Cueto-Felgueroso, Luis and Peraire, Jaume (2008). "A time-adaptive finite volume method for the Cahn–Hilliard and Kuramoto–Sivashinsky equations". In: *Journal of Computational Physics* 227.24, pp. 9985–10017.

Dell'Isola, Francesco, Gouin, Henri, and Rotoli, Giacomo (2009). "Nucleation of spherical shell-like interfaces by second gradient theory: numerical simulations". In: *arXiv preprint arXiv:0906.1897*.

Diehl, Dennis (2007). "Higher order schemes for simulation of compressible liquid-vapor flows with phase change". PhD thesis. Verlag nicht ermittelbar.

Doinikov, Alexander A, Dollet, Benjamin, and Marmottant, Philippe (2018). "Model for the growth and the oscillation of a cavitation bubble in a spherical liquid-filled cavity enclosed in an elastic medium". In: *Physical Review E* 97.1, p. 013108.

Drucker, Daniel Charles (1957). *A definition of stable inelastic material*. Tech. rep. BROWN UNIV PROVIDENCE RI.

Drysdale, Catherine, Doinikov, Alexander A, and Marmottant, Philippe (2017). "Radiation dynamics of a cavitation bubble in a liquid-filled cavity surrounded by an elastic solid". In: *Physical Review E* 95.5, p. 053104.

Du, Qiang and Nicolaides, Roy A (1991). "Numerical analysis of a continuum model of phase transition". In: *SIAM Journal on Numerical Analysis* 28.5, pp. 1310–1322.

Dular, Matevž, Delgosha, Olivier Coutier, and Petkovšek, Martin (2013). "Observations of cavitation erosion pit formation". In: *Ultrasonics sonochemistry* 20.4, pp. 1113–1120.

Dular, Matevž, Požar, Tomaž, Zevnik, Jure, et al. (2019). "High speed observation of damage created by a collapse of a single cavitation bubble". In: *Wear* 418, pp. 13–23.

Elliott, Charles M, French, Donald A, and Milner, FA (1989). "A second order splitting method for the Cahn-Hilliard equation". In: *Numerische Mathematik* 54.5, pp. 575–590.

Gallo, Mirko, Magaletti, Francesco, and Casciola, Carlo Massimo (2018). "Thermally activated vapor bubble nucleation: The Landau-Lifshitz–Van der Waals approach". In: *Physical Review Fluids* 3.5, p. 053604.

Gallo, Mirko, Magaletti, Francesco, Cocco, Davide, and Casciola, Carlo Massimo (2020). "Nucleation and growth dynamics of vapour bubbles". In: *Journal of Fluid Mechanics* 883.

Glowinski, Roland (2008). *Lectures on numerical methods for non-linear variational problems*. Springer Science & Business Media.

Gomez, Hector, Bures, Miguel, and Moure, Adrian (2019). "A review on computational modelling of phase-transition problems". In: *Philosophical Transactions of the Royal Society A* 377.2143, p. 20180203.

Gomez, Hector, Hughes, Thomas JR, Nogueira, Xesús, and Calo, Victor M (2010). "Isogeometric analysis of the isothermal Navier–Stokes–Korteweg equations". In: *Computer Methods in Applied Mechanics and Engineering* 199.25-28, pp. 1828–1840.

Gomez, Hector and Zee, Kristoffer G van der (2018). "Computational phase-field modeling". In: *Encyclopedia of Computational Mechanics Second Edition*, pp. 1–35.

Gómez, Héctor, Calo, Victor M, Bazilevs, Yuri, and Hughes, Thomas JR (2008). "Isogeometric analysis of the Cahn–Hilliard phase-field model". In: *Computer methods in applied mechanics and engineering* 197.49-50, pp. 4333–4352.

Gurtin, ME (1972). *The linear Theory of Elasticity, in (Flugge ed.) Encyclopedia of Physics, Volume VIa/2*.

Gurtin, Morton E (1982). *An introduction to continuum mechanics*. Academic press.

Gurtin, Morton E, Fried, Eliot, and Anand, Lallit (2010). *The mechanics and thermodynamics of continua*. Cambridge University Press.

Hadjadj, A and Kudryavtsev, A (2005). "Computation and flow visualization in high-speed aerodynamics". In: *Journal of Turbulence* 6, N16.

Han, Weimin and Reddy, B Daya (2012). *Plasticity: mathematical theory and numerical analysis*. Vol. 9. Springer Science & Business Media.

Hughes, Thomas JR, Franca, LP, and Mallet, M (1986). "A new finite element formulation for computational fluid dynamics: I. Symmetric forms of the compressible Euler and Navier-Stokes equations and the second law of thermodynamics". In: *Computer Methods in Applied Mechanics and Engineering* 54.2, pp. 223–234.

Jamet, D, Lebaigue, O, Coutris, N, and Delhaye, JM (2001). "The second gradient method for the direct numerical simulation of liquid–vapor flows with phase change". In: *Journal of Computational Physics* 169.2, pp. 624–651.

Jamet, Didier (2001). "Diffuse interface models in fluid mechanics". In: *GdR CNRS documentation, see pmc. polytechnique. fr/mp/GDR/docu/Jamet. pdf*.

Jamet, Didier, Torres, David, and Brackbill, JU (2002). "On the theory and computation of surface tension: the elimination of parasitic currents through energy conservation in the second-gradient method". In: *Journal of Computational Physics* 182.1, pp. 262–276.

Johnsen, Eric and Colonius, TIM (2009). "Numerical simulations of non-spherical bubble collapse". In: *Journal of fluid mechanics* 629, pp. 231–262.

Joshi, Shrey (2018). "Cavitation erosion modelling using SPH". PhD thesis. Université Grenoble Alpes.

Karush, William (1939). *Minima of Functions of Several Variables with Inequalities as Side Constraints*.

Kelly, DW, De SR Gago, JP, Zienkiewicz, OC, and Babuska, I (1983). "A posteriori error analysis and adaptive processes in the finite element method: Part I—error analysis". In: *International journal for numerical methods in engineering* 19.11, pp. 1593–1619.

Kodama, Tetsuya and Takayama, Kazuyoshi (1998). "Dynamic behavior of bubbles during extracorporeal shock-wave lithotripsy". In: *Ultrasound in medicine & biology* 24.5, pp. 723–738.

Kolsky, Herbert (1963). *Stress waves in solids*. Vol. 1098. Courier Corporation.

Kou, Jisheng and Sun, Shuyu (2018). "Thermodynamically consistent modeling and simulation of multi-component two-phase flow with partial miscibility". In: *Computer Methods in Applied Mechanics and Engineering* 331, pp. 623–649.

Kudryashov, Nikolay A and Sinelshchikov, Dmitry I (2014). "Analytical solutions of the Rayleigh equation for empty and gas-filled bubble". In: *Journal of Physics A: Mathematical and Theoretical* 47.40, p. 405202.

Kuhn, Harold W and Tucker, Albert W (2014). "Nonlinear programming". In: *Traces and emergence of nonlinear programming*. Springer, pp. 247–258.

Le Beau, Gerald John and Tezduyar, Tayfun E (1991). "Finite element computation of compressible flows with the SUPG formulation". In.

Le Gac, Séverine, Zwaan, Ed, Berg, Albert van den, and Ohl, Claus-Dieter (2007). "Sonoporation of suspension cells with a single cavitation bubble in a microfluidic confinement". In: *Lab on a Chip* 7.12, pp. 1666–1672.

Lechner, Christiane, Koch, Max, Lauterborn, Werner, and Mettin, Robert (2017). "Pressure and tension waves from bubble collapse near a solid boundary: A numerical approach". In: *The Journal of the Acoustical Society of America* 142.6, pp. 3649–3659.

Lechner, Christiane, Lauterborn, Werner, Koch, Max, and Mettin, Robert (2020). "Jet formation from bubbles near a solid boundary in a compressible liquid. Numerical study of distance dependence". In: *arXiv preprint arXiv:2005.05733*.

Li, ZG, Luo, KQ, Ohl, CD, Zhang, JB, and Liu, AQ (2011). "A single-cell membrane dynamic from poration to restoration by bubble-induced jetting flow". In: *15th International Conference on Miniaturized Systems for Chemistry and Life Sciences*, pp. 94–96.

Liu, Ju, Landis, Chad M, Gomez, Hector, and Hughes, Thomas JR (2015). "Liquid–vapor phase transition: Thermomechanical theory, entropy stable numerical formulation, and boiling simulations". In: *Computer Methods in Applied Mechanics and Engineering* 297, pp. 476–553.

Liu, Robin Hui, Lenigk, Ralf, Druyor-Sanchez, Roberta L, Yang, Jianing, and Grodzinski, Piotr (2003). "Hybridization enhancement using cavitation microstreaming". In: *Analytical Chemistry* 75.8, pp. 1911–1917.

Lubliner, Jacob (1972). "On the thermodynamic foundations of non-linear solid mechanics". In: *International Journal of Non-Linear Mechanics* 7.3, pp. 237–254.

— (2008). *Plasticity theory*. Courier Corporation.

Luenberger, David G, Ye, Yinyu, et al. (1984). *Linear and nonlinear programming*. Vol. 2. Springer.

Lutsko, James F (2011). "Density functional theory of inhomogeneous liquids. IV. Squared-gradient approximation and classical nucleation theory". In: *The Journal of chemical physics* 134.16, p. 164501.

Magaletti, Francesco, Gallo, Mirko, Marino, Luca, and Casciola, Carlo Massimo (2016). "Shock-induced collapse of a vapor nanobubble near solid boundaries". In: *International Journal of Multiphase Flow* 84, pp. 34–45.

Magaletti, Francesco, Marino, Luca, and Casciola, Carlo Massimo (2015). "Shock wave formation in the collapse of a vapor nanobubble". In: *Physical Review Letters* 114.6, p. 064501.

Mises, R v (1913). "Mechanik der festen Körper im plastisch-deformablen Zustand". In: *Nachrichten von der Gesellschaft der Wissenschaften zu Göttingen, Mathematisch-Physikalische Klasse* 1913, pp. 582–592.

Newmark, Nathan M (1959). "A method of computation for structural dynamics". In: *Journal of the engineering mechanics division* 85.3, pp. 67–94.

Noll, Walter (2012). *The foundations of mechanics and thermodynamics: selected papers*. Springer Science & Business Media.

Nowacki, Wojciech Krzysztof (2018). *Stress waves in non-elastic solids*. Elsevier.

Onsager, Lars (1931). "Reciprocal relations in irreversible processes. I." In: *Physical review* 37.4, p. 405.

Peng, Chi, Tian, Shouceng, Li, Gensheng, and Sukop, Michael C (2019). "Simulation of multiple cavitation bubbles interaction with single-component multiphase Lattice Boltzmann method". In: *International Journal of Heat and Mass Transfer* 137, pp. 301–317.

— (2020). "Simulation of laser-produced single cavitation bubbles with hybrid thermal Lattice Boltzmann method". In: *International Journal of Heat and Mass Transfer* 149, p. 119136.

Peraire, Jaime, Peiro, Joaquin, Formaggia, Luca, Morgan, Ken, and Zienkiewicz, Olgierd C (1988). "Finite element Euler computations in three dimensions". In: *International Journal for Numerical Methods in Engineering* 26.10, pp. 2135–2159.

Pereira, Francisco, Avellan, François, and Dupont, Ph (1998). "Prediction of cavitation erosion: an energy approach". In.

Peruzzi, Giovanna, Sinibaldi, Giorgia, Silvani, Giulia, Ruocco, Giancarlo, and Casciola, Carlo Massimo (2018). "Perspectives on cavitation enhanced endothelial layer permeability". In: *Colloids and Surfaces B: Biointerfaces* 168, pp. 83–93.

Petter Langtangen, Hans and Pedersen, Geir K (2016). *Scaling of differential equations*. Springer Nature.

Philipp, A and Lauterborn, W (1998). "Cavitation erosion by single laser-produced bubbles". In: *Journal of Fluid Mechanics* 361, pp. 75–116.

Plesset, Milton S (1949). "The dynamics of cavitation bubbles". In: *Journal of applied mechanics* 16, pp. 277–282.

Prandtl, Ludwig (1925). *Spannungsverteilung in platischen korpern*. Waltman.

Rajagopal, Amirtham, Fischer, Paul, Kuhl, Ellen, and Steinmann, Paul (2010). "Natural element analysis of the Cahn–Hilliard phase-field model". In: *Computational mechanics* 46.3, pp. 471–493.

Reuss, A (1932). "Fließpotential oder Gleitebenen?" In: *ZAMM-Journal of Applied Mathematics and Mechanics/Zeitschrift für Angewandte Mathematik und Mechanik* 12.1, pp. 15–24.

Robinson, PB, Blake, JR, Kodama, T, Shima, A, and Tomita, Y (2001). "Interaction of cavitation bubbles with a free surface". In: *Journal of Applied Physics* 89.12, pp. 8225–8237.

Scholz, Reinhard (1978). "A mixed method for 4th order problems using linear finite elements". In: *RAIRO. Analyse numérique* 12.1, pp. 85–90.

Shan, Ming-lei, Zhu, Chang-ping, Zhou, Xi, Yin, Cheng, and Han, Qing-bang (2016). "Investigation of cavitation bubble collapse near rigid boundary by lattice Boltzmann method". In: *Journal of Hydrodynamics* 28.3, pp. 442–450.

Simo, Juan C and Hughes, Thomas JR (2006). *Computational inelasticity*. Vol. 7. Springer Science & Business Media.

Simo, Juan C and Taylor, Robert Leroy (1985). "Consistent tangent operators for rate-independent elastoplasticity". In: *Computer methods in applied mechanics and engineering* 48.1, pp. 101–118.

Sinibaldi, G, Occhicone, A, Alves Pereira, F, Caprini, D, Marino, L, Michelotti, F, and Casciola, CM (2019). "Laser induced cavitation: Plasma generation and breakdown shockwave". In: *Physics of Fluids* 31.10, p. 103302.

Souza Neto, Eduardo A de, Peric, Djordje, and Owen, David RJ (2011). *Computational methods for plasticity: theory and applications*. John Wiley & Sons.

Sukop, Michael C and Or, Dani (2005). "Lattice Boltzmann method for homogeneous and heterogeneous cavitation". In: *Physical Review E* 71.4, p. 046703.

Sun, Tao, Samiotaki, Gesthimani, Wang, Shutao, Acosta, Camilo, Chen, Cherry C, and Konofagou, Elisa E (2015). "Acoustic cavitation-based monitoring of the reversibility and permeability of ultrasound-induced blood-brain barrier opening". In: *Physics in Medicine & Biology* 60.23, p. 9079.

Thomas, James William (2013). *Numerical partial differential equations: finite difference methods*. Vol. 22. Springer Science & Business Media.

Tian, Lulu, Xu, Yan, Kuerten, JGM, and Vegt, Jaap JW van der (2015). "A local discontinuous Galerkin method for the (non)-isothermal Navier–Stokes–Korteweg equations". In: *Journal of computational physics* 295, pp. 685–714.

Tomita, Y and Shima, A (1986). "Mechanisms of impulsive pressure generation and damage pit formation by bubble collapse". In: *Journal of Fluid Mechanics* 169, pp. 535–564.

Truesdell, Clifford (1969). "Rational thermodynamics: a course of lectures on selected topics". In.

— (1984). "Historical Introit The origins of rational thermodynamics". In: *Rational Thermodynamics*. Springer, pp. 1–48.

Van Gorder, Robert A (2016). "Dynamics of the Rayleigh–Plesset equation modelling a gas-filled bubble immersed in an incompressible fluid". In: *Journal of Fluid Mechanics* 807, pp. 478–508.

Voce, E (1955). "A practical strain hardening function". In: *Metallurgia* 51, pp. 219–226.

Vogel, Alfred et al. (1999). "Energy balance of optical breakdown in water at nanosecond to femtosecond time scales." In: *Applied Physics B: Lasers & Optics* 68.2.

Von Karman, Theodore and Duwez, Pol (1950). "The propagation of plastic deformation in solids". In: *Journal of Applied Physics* 21.10, pp. 987–994.

Waals, Johannes Diederik van der (1979). "The thermodynamic theory of capillarity under the hypothesis of a continuous variation of density (English translation JS Rowlinson)". In: *Journal of Statistical Physics* 20.2, pp. 200–244.

Ward, CA, Johnson, WR, Venter, RD, Ho, S, Forest, TW, and Fraser, WD (1983). "Heterogeneous bubble nucleation and conditions for growth in a liquid–gas system of constant mass and volume". In: *Journal of applied physics* 54.4, pp. 1833–1843.

Wells, Garth N, Kuhl, Ellen, and Garikipati, Krishna (2006). "A discontinuous Galerkin method for the Cahn–Hilliard equation". In: *Journal of Computational Physics* 218.2, pp. 860–877.

Xu, Hangxun, Zeiger, Brad W, and Suslick, Kenneth S (2013). "Sonochemical synthesis of nanomaterials". In: *Chemical Society Reviews* 42.7, pp. 2555–2567.

Zhang, Sheguang, Duncan, James H, and Chahine, Georges L (1993). "The final stage of the collapse of a cavitation bubble near a rigid wall". In: *Journal of Fluid Mechanics* 257, pp. 147–181.

Zhao, Nanrong, Mentrelli, Andrea, Ruggeri, Tommaso, and Sugiyama, Masaru (2011). "Admissible shock waves and shock-induced phase transitions in a van der Waals fluid". In: *Physics of fluids* 23.8, p. 086101.

Zhong, Pei (2013). "Shock wave lithotripsy". In: *Bubble dynamics and shock waves*. Springer, pp. 291–338.

Zhu, Songlin, Cocks, Franklin H, Preminger, Glenn M, and Zhong, Pei (2002). "The role of stress waves and cavitation in stone comminution in shock wave lithotripsy". In: *Ultrasound in medicine & biology* 28.5, pp. 661–671.

Zienkiewicz, Olek C and Taylor, Robert L (2005). *The finite element method for solid and structural mechanics*. Elsevier.